Karlsruhe Institute of Technology

Simulation and analysis of source-related effects for KATRIN

Zur Erlangung des akademischen Grades eines
DOKTORS DER NATURWISSENSCHAFTEN
von der Fakultät für Physik
des Karlsruher Instituts für Technologie
genehmigte
DISSERTATION
von

Diplom-Physiker Markus Hötzel
aus Karlsruhe

Referent:	Prof. Dr. G. Drexlin Institut für Experimentelle Kernphysik, KIT
Korreferent:	Prof. Dr. G. Quast Institut für Experimentelle Kernphysik, KIT

Tag der mündlichen Prüfung: 23. November 2012

Hiermit versichere ich die vorliegende Arbeit selbstständig und nur unter Verwendung der angegebenen Hilfsmittel und Quellen verfasst zu haben.

Ich erkläre, dass die wörtlichen oder dem Sinne nach anderen Veröffentlichungen entnommenen Stellen von mir kenntlich gemacht wurden.

Karlsruhe, den 23. Oktober 2012

Contents

Introduction

Neutrinos are part of the standard model of particle physics, but their nature may go beyond the scope of this model. Originally, they were supposed to have vanishing mass, but in fact they do have a small mass. And neutrinos may be Majorana particles that means their own antiparticles. They play an important role in cosmology since they are assumed to have contributed to the formation of our universe and – as weakly interacting particles – they are messengers from astrophysical processes. This versatility makes neutrinos interesting in many areas of physics.

Postulated in 1930 by Pauli to save spin, energy and momentum conservation in recently discovered β-decays, it took 26 more years until the neutrino was finally detected by Cowan and Reines. The reason is that neutrinos only interact weakly with ordinary matter. They pass easily through almost everything and therefore are hard to detect. Even today, large neutrino fluxes and sophisticated methods are required to measure at least some interactions of neutrinos within a detector.

On the other hand, this weak interaction can be regarded as an advantage in astroparticle physics since the universe is full of neutrinos ($\approx 340/\mathrm{cm}^3$) and they carry information from distant objects of the universe to the earth without being disturbed on their way. For example, neutrinos are emitted in fusion processes of the sun and help to investigate its interior. Cosmic events like supernova explosions are accompanied by neutrinos that act as messengers and help to understand the underlying processes.

But the neutrino itself has to be understood first, since neutrino experiments discovered a mysterious nature during the recent decades: Neutrinos seemed to disappear since one measured fewer neutrinos than expected when investigating solar and atmospheric neutrino fluxes. After thorough investigations and several generations of experiments, the solution was found to be neutrino oscillations: A neutrino can change its flavour and become 'invisible' for certain types of experiments. One important implication of the evidence of neutrino oscillations is that neutrinos have mass although they were expected to be massless in the standard model. The oscillation experiments are sensitive to determine small mass differences between different neutrino mass eigenstates, but the absolute mass scale remains inaccessible.

Therefore, other approaches were focused to determine the mass of the neutrino. These experiments were able to set upper limits, for example on the effective mass of the electron antineutrino

$$m_{\bar{\nu}_e} < 2\,\mathrm{eV}/c^2\,(95\%\,\mathrm{C.L.}). \tag{1}$$

In this context, the KArlsruhe TRItium Neutrino experiment KATRIN (see chapter 2) will determine the mass $m_{\bar{\nu}_e}$ of the electron antineutrino in a direct, model-

independent measurement. The tritium β-decay spectrum will be measured close to the spectral endpoint energy where a non-vanishing neutrino mass influences the spectral shape. For that purpose, KATRIN will use a windowless gaseous tritium source WGTS (see chapter 3) to produce β-electrons. The WGTS is a large, complex cryostat operated at 30 K. Strict requirements on the WGTS parameters are necessary to achieve low systematic effects on the neutrino mass. The retarding spectrometer of KATRIN will analyse the electrons' energies with an energy resolution of $\Delta E < 0.93\,\mathrm{eV}$. Only electrons with energies above the analysing retarding energy can pass in this integral spectrum measurement. A silicon detector will allow detecting the high energy part of the electron spectrum and determining the rate depending on the set retarding energy of the spectrometer. Within three years measurement time KATRIN will reach a sensitivity of $m_\nu < 200\,\mathrm{meV}/c^2$ (90% C.L.).

For this ambitious goal it is important to increase the statistics of the experiment, to understand the whole experimental system and to identify and quantify systematic uncertainties. These tasks immediately put the focus on the WGTS of KATRIN, since on the one hand it provides the high β-electron flux and on the other hand induces systematic effects. To investigate these implications of the source, dedicated simulations of the WGTS are presented in chapter 4. They comprise detailed descriptions of the physical processes in the source like the density and temperature distributions, the tritium β-decay spectrum and scattering processes. Special emphasis is given to gas dynamics simulations (see chapter 5) that consider the geometry and the tritium circulation to describe the velocity distribution function of the system.

Then, in chapter 6, developed analysis routines are presented to determine the statistical uncertainty of KATRIN and to investigate the influence of several source parameters on the analysed neutrino mass. These methods use the previously explained spectrum calculation to generate KATRIN-like measurements and statistical methods based on Monte-Carlo simulations and maximum likelihood estimation for their evaluation.

The results of statistical analyses respectively sensitivity studies at KATRIN are presented in chapter 7. This comprises results of ensemble (Monte-Carlo) methods and the concept of profile likelihood to estimate the variance on the neutrino mass of KATRIN. Feldman-Cousins unified approach is then used to translate the statistical uncertainty into upper limits or claims.

The influence of various source parameters on the neutrino mass measurement at KATRIN is evaluated and discussed in chapter 8. Again, ensemble methods and the concept of profile likelihood with constraints on parameters is used to quantitatively determine the effect of systematic uncertainties of key parameters on the analysed neutrino mass.

The concluding part of this thesis, chapter 9, explains the measurements at the 'demonstrator', a test experiment of the WGTS. There, a temperature profile has been measured and has been used as realistic input for the source simulations. All results of the test measurement were investigated with respect to their implications on KATRIN.

1. Neutrino physics

1.1 Neutrinos: Historical

In 1930, Wolfgang Pauli postulated a new particle to explain the measured β-spectrum [1]. At that time, the decay of a nucleus with mass A and charge number Z under emission of an electron was observed

$$(A, Z) \longrightarrow (A, Z + 1) + e^{-}. \tag{1.1}$$

Without a third particle, the spectrum would be a monoenergetic line at the decay energy Q. The new particle, Pauli called it "neutron" first, was supposed to be neutral, have spin 1/2 and carry away energy and momentum to explain the continuous electron spectrum. This new particle was hard to detect due to its electrical neutrality and since it interacts only very weakly with matter. In 1956, Cowan and Reines [2] discovered the new particle – the electron antineutrino $\bar{\nu}_\mathrm{e}$ – by inverse β-decay

$$\bar{\nu}_e + p \longrightarrow e^{+} + n. \tag{1.2}$$

In this type of experiment, the positron annihilates with an electron and creates two photons that are recorded immediately by scintillators. The neutron is captured by a Cadmium nucleus that emits a photon during de-excitation after a characteristic time delay. The coincidence of these two photon signals proves the reaction of $\bar{\nu}_\mathrm{e}$ with the target. The determined cross-section of the inverse β-decay was published as $\sigma = (1.2^{+0.7}_{-0.4}) \cdot 10^{-43}\mathrm{cm}^2$ [2], a typical cross-section for weakly interacting particles.

1.2 Neutrino properties

Today, in the Standard Model (SM) (see figure 1.1), neutrinos belong to the three generations: ν_e that was discovered as described above by Cowan and Reines, ν_μ that was shown to be different from ν_e in 1962 [3] and ν_τ discovered in 2000 [4]. Neutrinos are weakly interacting particles and are treated massless in the SM (see section 1.4). This makes them excellent messengers in astroparticle physics, for example for observations of the sun. Only the surface of the sun can be observed by

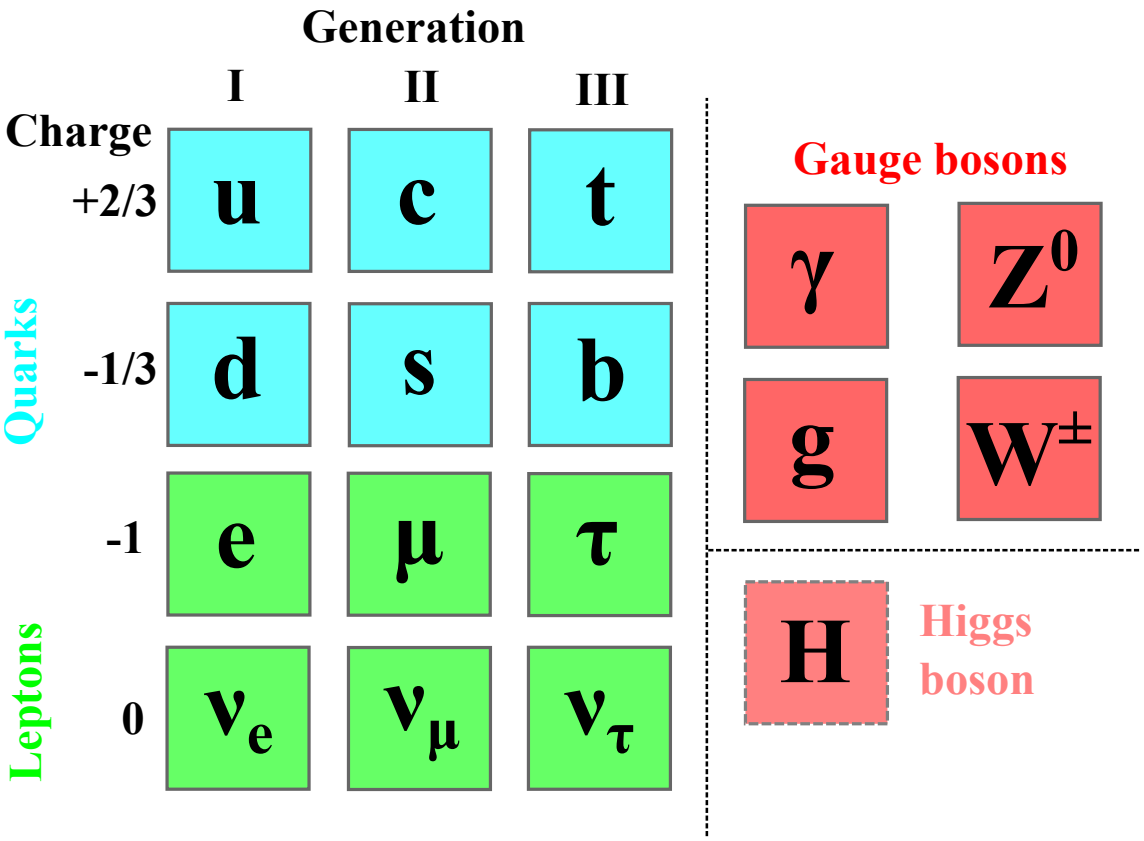

Figure 1.1: **The Standard Model of particle physics.** The quarks (up, down, charm, strange, top, bottom) and leptons (electron, electron neutrino, muon, muon neutrino, tau and tau neutrino) have a spin of 1/2 and belong to 3 generations. The gauge bosons, photon γ as mediator of the electromagnetic force, gluon g for the strong force and Z^0 and W-Bosons for the weak interaction carry spin 1. The Higgs boson H as part of the Standard Model generates the masses of particles.

photons, since the interior is so dense that photons scatter permanently. But during fusion processes, neutrinos are also created (see section 1.3). Due to their weak interaction, they can leave the sun undisturbed. A measurement of solar neutrinos therefore offers information on the interior of the sun.

Another messenger function of neutrinos happens during supernova (type II) explosions. This brief description follows [5]: If a heavy star passes the Chandrasekhar limit, the gravitational attraction is so strong that the star collapses. The density at the centre increases drastically and neutronisation $e^- + p \rightarrow n + \nu_e$ happens; a neutron star is created. Additionally, neutrinos are created by $e^+ + e^- \rightarrow \nu + \bar{\nu}$. The core of the supernova is too dense, so it is opaque for neutrinos; they "diffuse" to outer regions and leave the supernova earlier than photons, before a shock wave causes the big supernova explosion. Therefore, neutrinos are the first message from a supernova and could be used to understand early phases of the supernova explosion mechanism and to adjust telescopes for the observation of photons.

1.3 Neutrino oscillations

In the previous section, three types of neutrinos ν_e, ν_μ and ν_τ (and their antiparticles) have been discussed. These flavours are eigenstates of the weak interaction that

means a neutrino (antineutrino), which is produced by a W-boson together with an electron (positron) is a ν_e ($\bar{\nu}_\mathrm{e}$), together with a muon (antimuon) is a ν_μ ($\bar{\nu}_\mu$), etc. [6]. But these flavour states are no eigenstates of the mass operator M. Instead, each flavour eigenstate $|\nu_\alpha\rangle$ with $\alpha = \mathrm{e}, \mu, \tau$ is composed of a superposition of the mass eigenstates $|\nu_j\rangle$ with $j = 1, 2, 3$

$$|\nu_\alpha\rangle = \sum_{j=1}^{3} U_{\alpha j} |\nu_j\rangle \tag{1.3}$$

with the elements $U_{\alpha j}$ of the Pontecorvo-Maki-Nakagawa-Sakata (PMNS) matrix. A typical representation is given in [6]

$$U = \begin{pmatrix} c_{12}c_{13} & s_{12}c_{13} & s_{13}e^{-\mathrm{i}\delta} \\ -s_{12}c_{23} - c_{12}s_{23}s_{13}e^{\mathrm{i}\delta} & c_{12}c_{23} - s_{12}s_{23}s_{13}e^{\mathrm{i}\delta} & s_{23}c_{13} \\ s_{12}s_{23} - c_{12}c_{23}s_{13}e^{\mathrm{i}\delta} & -c_{12}s_{23} - s_{12}c_{23}s_{13}e^{\mathrm{i}\delta} & c_{23}c_{13} \end{pmatrix} \cdot \mathrm{diag}(1,\, e^{\mathrm{i}\frac{\alpha_{21}}{2}}, e^{\mathrm{i}\frac{\alpha_{31}}{2}}), \tag{1.4}$$

where c_{ij} (s_{ij}) denote $\cos\theta_{ij}$ ($\sin\theta_{ij}$) of the mixing angles θ_{ij} with $i, j = 1, 2, 3$ and δ denotes the Dirac CP violation phase, α_{n1} the possible Majorana CP violating phases.

This neutrino mixing has the following implications: A neutrino with energy E is produced in initial flavour state $|\nu_l\rangle$ and is travelling along distance L within time t from the source to the detector. Since $E_j^2 = p_j^2c^2 + m_j^2c^4$ and the masses m_j are assumed to be different, the different states $|\nu_j\rangle$ propagate with different momentum p_j. In quantum mechanics, a propagation is written as $\exp(-\mathrm{i}(Et - p_jL)/\hbar)$. Therefore, after time t at the detector the initial state has changed to

$$|\nu(t)\rangle = \sum_i U_{\alpha j} \cdot e^{-\mathrm{i}(Et - p_jL)/\hbar} |\nu_j\rangle \tag{1.5}$$

If one asks for the probability P to measure a flavour $|\nu_\beta\rangle$ after propagation time t of neutrinos in state $|\nu_\alpha\rangle$, one calculates (with $\hbar = c = 1$) [5, 6]

$$P(\alpha \longrightarrow \beta) = |\langle\nu_\beta|\nu(t)\rangle|^2 = \sum_j |U_{\beta j}U_{\alpha j}^*|^2 + 2\sum_{j>k} U_{\beta j}U_{\alpha j}^* U_{\alpha k}U_{\beta k}^* \cos\left(\frac{\Delta m_{jk}^2}{2p}L + \phi\right). \tag{1.6}$$

with the squared mass differences

$$\Delta m_{jk}^2 = m_j^2 - m_k^2 \tag{1.7}$$

and phase ϕ. The cosine term causes oscillatory behaviour in the probability to measure different states $|\nu_\beta\rangle$ after propagation length $L \approx c \cdot t$ with energy $E \approx pc$ for relativistic neutrinos. For example, after

$$L = \frac{2E\hbar}{\Delta m_{jk}^2 c^3} \cdot 2\pi k, \text{ with } k \in N \tag{1.8}$$

a measurement of a pure beam of ν_e would yield only ν_e again. At other distances, also ν_μ or ν_τ could occur. Their individual contributions are determined by the matrix elements U_{ej} respectively by the mixing angles θ_{ij}, often stated as $\sin^2(2\theta_{ij})$.

Eq. (1.6) shows that observations of neutrino oscillations can only deduce Δm^2_{jk}; the absolute mass scale remains unknown.

In the history of neutrino oscillation experiments, different lengths L and energies E were required to test for unknown Δm^2_{jk}. Therefore, various neutrino sources have been used and appropriate detector concepts have been developed. Some major results are presented in the following.

1.3.1 Solar neutrinos

The fusion reactions in the sun create electron neutrinos within the net equation of the proton-proton cycle [6]

$$4p + 2e^- \longrightarrow {}^4\mathrm{He} + 2\nu_e + 26.73\mathrm{MeV} - E_\nu \tag{1.9}$$

with released thermal energy of 26.73 MeV minus the energy E_ν that the neutrino carries away. In various steps of the CNO-cycle additional ν_e are produced. Their energies are below 2 MeV for most processes of the cycles (below 18.8 MeV for the ^{8}B-neutrinos and neutrinos the hep-cycle) [5]. These cycles are described by the standard solar model (SSM) e.g. [7] that predicts fluxes of solar electron neutrinos from the various reactions, which reach the earth.

Early neutrino experiments like the Homestake experiment [8] measured only fluxes of about one third of the theoretical prediction of the SSM. This was called the "solar neutrino problem". It could be solved by the theory of neutrino oscillations, namely by $\nu_e \longrightarrow \nu_\mu$ disappearance where ν_μ was not able to be detected.

Further experiments followed, for example the "Sudbury Neutrino observatory SNO" [9]. It consisted of 1000 tons of ultra pure heavy water D_2O [1]. Electron neutrinos can scatter on deuterium by charged current weak interaction

$$\nu_e + d \longrightarrow e^- + p + p \tag{1.10}$$

whereas neutral current interaction

$$\nu_\alpha + d \longrightarrow \nu_\alpha + p + n. \tag{1.11}$$

and elastic scattering

$$\nu_\alpha + e \longrightarrow \nu_\alpha + e \tag{1.12}$$

are possible for every neutrino flavour α. Therefore, the experiment was sensitive to all neutrinos and was able to show that the total flux of measured solar ^{8}B neutrinos is in good agreement with predictions of the SSM.

In combination with other solar neutrino experiments and results from reactor experiments (see below), a global analysis of the particle data group in [6] results in

$$\Delta m_\mathrm{S} = 7.58^{+0.22}_{-0.26} \cdot 10^{-5}\,\mathrm{eV}^2. \tag{1.13}$$

[1] In later phases of the experiment NaCl respectively neutron counters were added to increase its sensitivity [10, 11].

1.3.2 Atmospheric neutrinos

Interactions of cosmic rays with molecules of the atmosphere create pions and muons that decay into electrons and (anti-)neutrinos

$$\pi^{\pm} \longrightarrow \mu^{\pm} + \nu_{\mu}(\bar{\nu_{\mu}}) \tag{1.14}$$

$$\mu^{\pm} \longrightarrow e^{\pm} + \nu_{e}(\bar{\nu_{e}}) + \bar{\nu_{\mu}}(\nu_{\mu}). \tag{1.15}$$

It is expected to measure twice as many muon neutrinos as electron neutrinos.

The Super-Kamiokande experiment [12], a 50kt water Cherenkov detector detected and discriminated electron and muon neutrinos by scattering with nuclei producing leptons that then emit Cherenkov light. It measured an asymmetry between the number of neutrinos from top with a distance of only few km from the atmosphere and from the bottom where the neutrinos have travelled 10000 km through the earth. This asymmetry can be explained by neutrino oscillations because neutrinos from top have no time to oscillate, to disappear whereas neutrinos that travelled through the earth oscillate into τ neutrinos that were not detectable. A global analysis of various experiments [6] yields

$$|\Delta m_{\mathrm{A}}| = 2.35^{+0.12}_{-0.09} \cdot 10^{-3}\,\mathrm{eV}^2. \tag{1.16}$$

1.3.3 Accelerator neutrinos

With eq. (1.8) and expected mass splittings of eq. (1.13) or eq. (1.16), accelerator experiments can be designed with appropriate energy E and baseline length L, for example the MINOS long-baseline neutrino experiment [13]. In this experiment, a disappearance of a muon neutrino beam from Fermilab was detected in an underground detector at the Soudan mine in a distance of 735 km. Its results are

$$|\Delta m^2_A| = 2.32^{+0.12}_{-0.08} \cdot 10^{-3}\,\mathrm{eV}^2 \tag{1.17}$$

$$\sin^2(2\theta_A) > 0.90\,(90\%\,\mathrm{C.L.}). \tag{1.18}$$

The mixing angle is accessible, since a near detector at the accelerator measured the initial flux of muon neutrinos that can be compared with the detected muon flux.

1.3.4 Reactor neutrinos and determination of θ_{13}

Similar to accelerator neutrinos, $\bar{\nu}_{\mathrm{e}}$ from nuclear power plants can be used to study neutrino oscillations. In recent years, a tandem detector setup proved to be successful. One detector is placed close to the reactor core where no oscillations have happened yet to determine the initial flux of neutrinos. A second detector is placed under consideration of eq. (1.8) in distance L from the reactor to determine the disappearance $\bar{\nu}_{\mathrm{e}} \longrightarrow \bar{\nu}_{\mu}$. The Daya Bay experiment [14] is mentioned here as representative for many successful reactor neutrino experiments. With 4 near and 2 far detectors it was able to detect neutrino disappearance from 6 nuclear power plants and measure the last unknown mixing angle θ_{13} as

$$\sin^2(2\theta_{13}) = 0.092 \pm 0.016\,(\mathrm{stat.}) \pm 0.005\,(\mathrm{syst.}) \tag{1.19}$$

Other experiments [15, 16] with similar setup achieved compatible results.

Table 1.1: **Best fit values for neutrino oscillation parameters from [6].**

parameter	best-fit ($\pm 1\sigma$)
Δm^2_{S}	$7.58^{+0.22}_{-0.26} \cdot 10^{-5}\,\mathrm{eV}^2$
$\lvert\Delta m^2_{\mathrm{A}}\rvert$	$2.35^{+0.12}_{-0.09} \cdot 10^{-3}\,\mathrm{eV}^2$
$\sin^2\theta_{12}$	$0.306^{+0.018}_{-0.015}$
$\sin^2\theta_{23}$	$0.42^{+0.08}_{-0.03}$
$\sin^2\theta_{13}$	0.0251 ± 0.0034

Summary neutrino oscillations

The neutrino oscillation experiments were very successful in recent years and completed the mixing matrix with the measurement of θ_{13} in 2012. A summary of the determined parameters is given in table 1.1.

Although the oscillation data only allows for determination of the mass splittings, not for the absolute scale of the neutrino masses, two cases of neutrino mass ordering are possible [6]:

- Normal hierarchical ordering $m_1 < m_2 < m_3$. This means one can connect $\Delta m^2_{\mathrm{A}} = \Delta m^2_{31} > 0$ and $\Delta m^2_{\mathrm{S}} = \Delta m^2_{21} > 0$.
- Inverted hierarchical ordering $m_3 < m_1 < m_2$ with $\Delta m^2_{\mathrm{A}} = \Delta m^2_{32} < 0$ and $\Delta m^2_{\mathrm{S}} = \Delta m^2_{21} > 0$.
- Quasi-degenerate case $m_1 \approx m_2 \approx m_3$ where all masses m_j are larger than the splittings: $m_j^2 \gg |\Delta m^2_{\mathrm{A}}|$.

1.4 Neutrino masses

1.4.1 Particle physics

In the Standard Model SM (see figure 1.1), neutrinos are massless like photons. But the observation of neutrino oscillations (section 1.3) shows that at least 2 neutrino mass eigenstates have non-zero masses. On the other hand, the masses are very small, in the sub-eV range, at least 5-6 orders of magnitude smaller than the lightest particle of the SM, the electron [6]. Besides other theories based on supersymmetry or Grand Unified Theories GUT, the seesaw mechanism can explain why the mass of the neutrinos is small but nonzero and is presented briefly in the following.

The seesaw mechanism requires a heavy right-handed Majorana-Neutrino[2] N_R and a left-handed light neutrino ν_L [5]. The mass term of the Lagrangian is then

$$-\mathcal{L}_{DM} = \frac{1}{2}\begin{pmatrix}\bar{\nu}_L & \bar{N}^c_L\end{pmatrix}\begin{pmatrix}0 & m_D\\ m_D & m_R\end{pmatrix}\begin{pmatrix}\nu^c_R\\ N_R\end{pmatrix} + \mathrm{h.c.} \tag{1.20}$$

[2] A Majorana particle is its own antiparticle.

with a Dirac mass m_D and Majorana mass m_R.

Diagonalizing the matrix yields eigenvalues for the mass of the light neutrino m_ν and the heavy neutrino m_N

$$m_\nu = \frac{m_D^2}{m_R} \ll m_D \tag{1.21}$$

$$m_N \approx m_R \tag{1.22}$$

The mass m_ν depends on the values for m_D and m_R that are used in the specific model. Typically m_D is a fermion mass (lepton or quark) and m_R is on the GUT scale ($10^{16}\,\mathrm{GeV}$) what results in small m_ν [5].

1.4.2 Cosmology

Cosmic microwave background

After the Big Bang, the temperature was so high that the particles of the standard model were in thermal equilibrium [17, 18]. For example, pair annihilation and pair production $e^+ + e^- \rightleftharpoons \gamma + \gamma$ happened as well as Thomson scattering $e^- + \gamma \to e^- + \gamma$. The universe was opaque for photons. Then, the universe expanded and cooled. About 380,000 years after the Big Bang, the temperature was low enough that electrons and protons were able to build neutral hydrogen and the photons had insufficient energies to break it up again. This process is called recombination. The photons decoupled from the interactions and were able to stream freely. They kept their original spectrum, a black-body spectrum. During the expansion of the universe, the wavelength was redshifted, so that we expect a temperature of $T \approx 3\,\mathrm{K}$ of this so called cosmic microwave background (CMB) from all directions of space today.

Modern experiments like the "Cosmic Microwave Background Explorer" (COBE) determined $T = 2.72548 \pm 0.00057\,\mathrm{K}$ [19] and discovered small anisotropies. Today, these anisotropies have been measured with highest precision by the "Wilkinson Microwave Anisotropy Probe" (WMAP) [20] and are shown in figure 1.2a. A multipole analysis of the autocorrelation function that compares the temperature from different directions of the sky is a main result and is shown in figure 1.2b.

The anisotropy occurs due to several effects:

- Baryonic acoustic oscillations (BAO): Primordial density fluctuations attract more matter. An overdense region grows, compresses and heats up until the photon pressure dominates and drives the baryons apart again. This procedure repeats itself. This is called BAO. When the photons finally decouple after 380,000 years, they carry information about the primordial density fluctuations [17].
- Sachs-Wolfe effect: Photons that escaped from denser regions during recombination have to overcome a stronger gravitational potential and are redshifted compared to photons from regions with low density that are blueshifted [17].
- Silk damping: Photons from hotter, denser regions of the early universe stream to colder regions and equalize the differences, reducing the anisotropy [18].

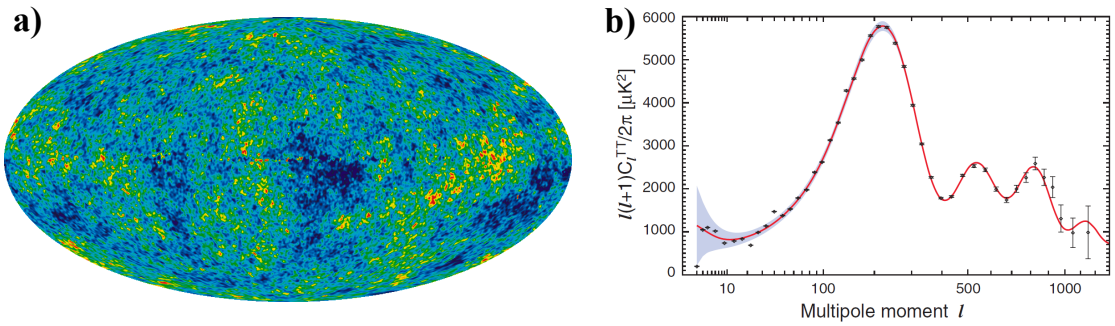

Figure 1.2: **a) Seven-year sky map of the CMB anisotropy from [21]. b) Power spectrum of the CMB anisotropies from [20].** The multipole analysis results in the black dots, the best fit to the ΛCDM model is drawn as red line.

These effects can be treated in physical models and simulations. The resulting CMB pattern depends on the different contributions of baryons Ω_b, dark matter Ω_DM and dark energy Ω_Λ within the concordance model ΛCDM. Various cosmological parameters can be varied so that the power spectrum matches the measured one [20].

Analogous to the CMB, relic neutrinos are expected. The mechanisms are similar: "As the universe cools, the weak interaction rate Γ_ν falls below the expansion rate given by the Hubble parameter H and one says that neutrinos decouple from the rest of the plasma" [22]. Since then, the neutrinos stream freely and are redshifted due to the expansion of the universe.

Relic neutrinos have not been measured so far, but there is a close correlation

$$n_\nu = \frac{3}{11} n_\gamma \tag{1.23}$$

between the relic neutrino density n_ν and the CMB photon density n_γ. This results in "113 neutrinos and antineutrinos of each flavour per cm^3" [22]. The contribution of the neutrino energy density ρ_ν to the critical energy density ρ_crit constrains the sum of all neutrino masses $\sum m_\nu$ to

$$\Omega_\nu = \frac{\rho_\nu}{\rho_\mathrm{crit}} = \frac{\sum m_\nu}{93.14 \cdot h^2\,\mathrm{eV}} \tag{1.24}$$

with the Hubble parameter h in $100\,\mathrm{km\,s^{-1}\,Mpc^{-1}}$. Analyses from WMAP [20] within the ΛCDM model result in

$$\sum m_\nu < 1.3\,\mathrm{eV}\,(95\%\,\mathrm{C.L.}). \tag{1.25}$$

Structure formation

Observations of the structure of the universe also constrain the neutrino mass. As an example, the "Sloan Digital Sky Survey (SDSS-III)" [23] observed structures of galaxies showing the filament structure of the universe. These structures can be reproduced by extensive simulations (e.g. [24]) for example within the ΛCDM model. Therein, one of the parameters is the sum of the neutrino masses, since neutrinos can stream freely in the early universe and erase primordial density fluctuations.

The heavier neutrinos are, the better they were able to equalize fluctuations on small scales. Comparing simulations with measured structures of the universe allows constraining the neutrino masses, for example in [24]

$$\sum m_\nu < 0.61\,\mathrm{eV}\,(95\%\,\mathrm{C.L.}). \tag{1.26}$$

In combination with results from WMAP (see above) this has been reduced in [25] to

$$\sum m_\nu < 0.58\,\mathrm{eV}\,(95\%\,\mathrm{C.L.}). \tag{1.27}$$

1.5 Neutrinoless double β-decay

Next to the single β-decay that will be explained in the final section 1.6 of this chapter, the observation of neutrinoless double β-decay is an approach to determine the absolute mass scale of neutrinos. This approach is promising on the one hand, because if successful, it would prove that neutrinos are Majorana particles that means their own antiparticle $\bar{\nu}_\mathrm{e} = \nu_e = \nu^\mathrm{M}$. On the other hand, this approach is model-dependent, since the calculation of nuclear matrix elements depends on underlying models.

First of all, a double β-decay ($2\nu\beta\beta$-decay) is a simultaneous decay of two neutrons

$$2n \longrightarrow 2p + 2e^- + 2\bar{\nu}_\mathrm{e}. \tag{1.28}$$

It is accompanied by two electrons and two electron antineutrinos $\bar{\nu}_\mathrm{e}$. The sum of the electron energies is a continuous spectrum below two times the decay energy Q, since the two $\bar{\nu}_\mathrm{e}$ carry away kinetic energy.

Double β-decays can happen in every β-emitter, but are rare compared to single β-decays. Electrons from single β-decays conceal any signal from $2\nu\beta\beta$-decay in a typical measurement. Therefore, material is chosen where single β-decays are energetically forbidden, but a $2\nu\beta\beta$-decay is possible[3]. Germanium-76 or Xenon-136 are promising candidates for double β-decay experiments.

Instead of $2\nu\beta\beta$-decay the neutrinoless double β-decay ($0\nu\beta\beta$-decay)

$$2n \longrightarrow 2p + 2e^- \tag{1.29}$$

is investigated to determine the neutrino mass. No neutrinos are emitted, since it is assumed that a common virtual neutrino is exchanged between both β-decays (see figure 1.3a). This is a process beyond the standard model, since it requires:

- **Lepton number violation:** There are no antineutrinos emitted, but two electrons. That violates the lepton number L by $\Delta L = 2$.

[3]The energy state of a nucleus with even number of protons Z and neutrons $A-Z$ is energetically lower than the state of the daughter nucleus in a β^--decay with $Z-1$ and $A-Z+1$, both odd. Therefore, the single β-decay is forbidden. Instead, a double β-decay is possible, since it reaches $Z-2$ protons and $A-Z+2$ neutrons, that is even-even again and energetically lower than the initial state.

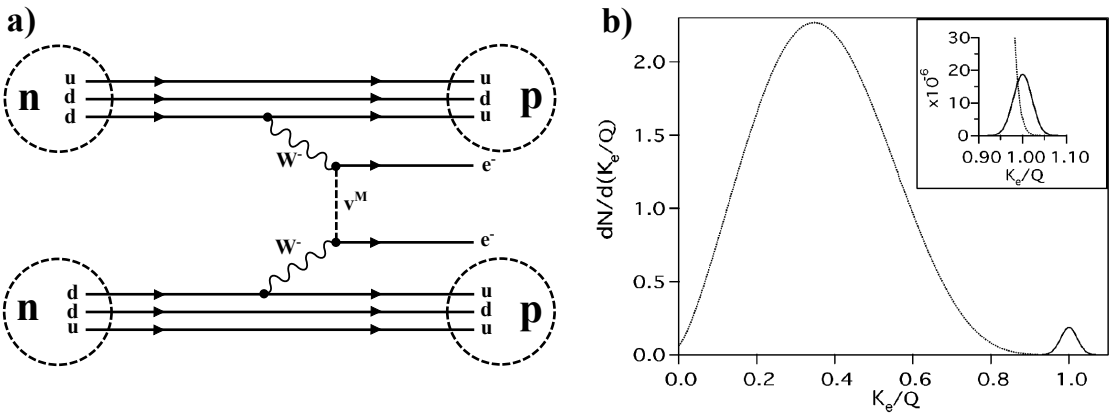

Figure 1.3: **a) Feynman diagram of a neutrinoless double β-decay.** Two neutrons decay simultaneously into two protons and two electrons. They exchange a Majorana neutrino ν^{M}.
b) "Illustration of the spectra of the sum of the electron kinetic energies K_e (Q is the endpoint) for the $\beta\beta(2\nu)$ normalized to 1 (dotted curve) and $\beta\beta(0\nu)$ decays (solid curve). The $\beta\beta(0\nu)$ spectrum is normalized to 10^{-2} (10^{-6} in the inset). All spectra are convolved with an energy resolution of 5%, representative of several experiments." [26].

- **Helicity flip:** The emitted neutrino at the first β-decay is – as usual in weak interactions – a right-handed (anti)neutrino with helicity[4] $H = +1$ if $m_\nu = 0$ and absorbed as left-handed neutrino with $H = -1$ if $m_\nu = 0$. This is not possible. If $m_\nu > 0$, the helicity is not fixed [5], so that there is a probability to emit left-handed antineutrinos respectively absorb right-handed neutrinos. Another possibility is right-handed currents that would allow the same behaviour.

The neutrino mass that is connected to the $0\nu\beta\beta$-decay is an effective mass, the coherent sum

$$\langle m_\nu \rangle = \left| \sum_i U_{ej}^2 m_j \right| . \tag{1.30}$$

Since the U_{ej} of eq. (1.4) contain Majorana phases α_i, this can cause $\langle m_\nu \rangle$ to be smaller than the contributing m_j; even a vanishing $\langle m_\nu \rangle$ is possible. To obtain $\langle m_\nu \rangle$ from $0\nu\beta\beta$-decay, the half-life $T_{1/2}^{0\nu}$ is measured with the relation

$$(T_{1/2}^{0\nu})^{-1} = G^{0\nu}(Q, Z) \cdot |M^{0\nu}|^2 \left(\frac{\langle m_\nu \rangle}{m_e} \right)^2 \tag{1.31}$$

with phase space integral $G^{0\nu}(Q, Z)$ depending on decay energy Q and charge number Z, nuclear transition matrix elements $M^{0\nu}$ and the electron mass m_e [5]. The matrix elements can be calculated, but they depend on the underlying calculation model and carry uncertainties of up to a factor of 10 [26].

The $0\nu\beta\beta$-decay experiments share a common strategy: They have a well-known target mass of suited $0\nu\beta\beta$-material and measure the sum spectrum of both emitted

[4]The helicity H is the projection of the spin $\vec{s}$ on the (unit) momentum vector $\vec{p}$: $H = \vec{s} \cdot \frac{\vec{p}}{|\vec{p}|}$.

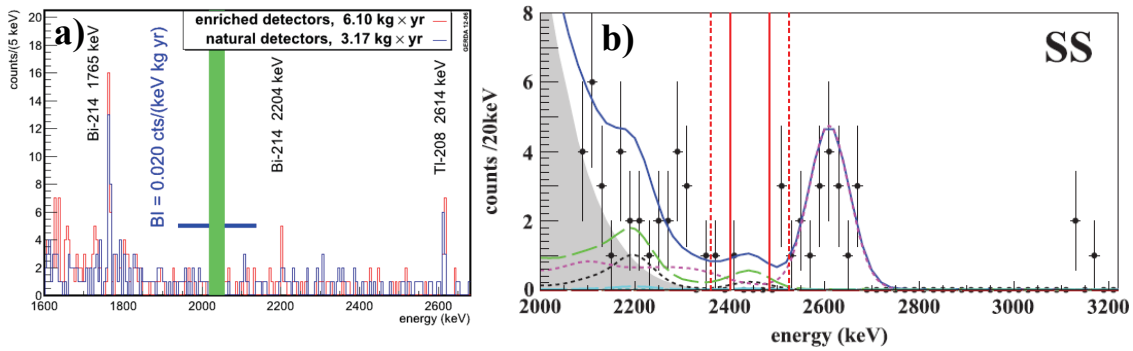

Figure 1.4: **a) Measured GERDA spectrum from [29].** The count rates are shown for detectors with natural Ge and enriched Ge. The region where the $0\nu\beta\beta$-peak is expected $E = 2 \cdot Q$ is blinded for blind analysis.
b) Measured EXO-200 spectrum from [30]. The measured counts are drawn as black dots, the best-fit as blue line with the fits to various background components (dashed coloured lines). The vertical red lines (1 and 2σ) show the expected region of a $0\nu\beta\beta$-peak.

electrons (see figure 1.3b). The $0\nu\beta\beta$ signal is a peak above the endpoint of the $2\nu\beta\beta$-spectrum at an energy of $2 \cdot Q$. Since very low count rates are expected, a major effort of these experiments is the reduction of background events.

The experiments on double β-decay have long-term goals to measure with detector material on the ton-scale. With this statistical power, determining neutrino masses down to 50 meV is feasible. The status of two of many experiments on their way to the ton-scale is presented in the following.

GERDA

The "Germanium Detector Array (GERDA)" [27] consists of ^{76}Ge detectors. It is located in the underground laboratory of Gran Sasso to reduce background events from cosmic rays. Surrounding copper and a water tank with photomultipliers shield respectively monitor background from natural radiation. The aim of GERDA in a first phase with a detector mass of 18 kg of ^{76}Ge and an expected background rate of 0.01 counts/(keV·kg·yr) is to confirm or disprove the measurements of the Heidelberg-Moscow experiment [28]. A measured spectrum is shown in figure 1.4a. In a second phase, enriched detector material (+20 kg) will be installed and the background will be reduced further to 0.001 counts/(keV·kg·yr) [29].

EXO

The "Enriched Xenon Observatory (EXO)" uses enriched liquid Xenon ^{136}Xe as $0\nu\beta\beta$ material. It is planned to run with 1t Xenon; currently EXO-200 with 200 kg is measuring as a prototype [30]. Xenon is used as source and detector of the created β-electrons simultaneously: The energy of the two β-electrons creates an ionisation and scintillation signal whose characteristics are used to discriminate background events. EXO-200 achieved a background rate of 0.0015 counts/(keV·kg·yr), published the spectrum in figure 1.4b and was able to state a lower limit

$$T^{0\nu}_{1/2}(^{136}\mathrm{Xe}) > 1.6 \cdot 10^{25}\,(90\%\,\mathrm{C.L.}) \tag{1.32}$$

that can be translated to

$$\langle m_\nu \rangle < (140 - 380)\,\mathrm{meV}, \tag{1.33}$$

depending on the used matrix elements.

1.6 Beta-decay

In a β-decay, the charge Z of a nucleus with mass A changes by 1:

$$\begin{aligned} \beta^- : &\quad (A,Z) \longrightarrow (A,Z+1) + e^- + \bar{\nu}_\mathrm{e} \\ \beta^+ : &\quad (A,Z) \longrightarrow (A,Z-1) + e^+ + \nu_e \end{aligned} \tag{1.34}$$

$$\mathrm{EC} : \quad (A,Z) + e^- \longrightarrow (A,Z-1) + \nu_e. \tag{1.35}$$

In a β^- (β^+)-decay, the released energy is shared by electron (positron) and neutrino. The electron capture EC causes an excited daughter molecule and emitted neutrino. Restricting to the β^- decay in the following, the electron energy spectrum is continuous up to the maximal possible energy, the endpoint energy E_0, since the electron and neutrino share the available decay energy Q. The shape of the spectrum $\mathrm{d}N/\mathrm{d}E$ is described by Fermi's β-decay theory [31] that considers the available phase space for the electron as well as energy and momentum conservation [32]:

$$\frac{\mathrm{d}N}{\mathrm{d}E} = C \cdot F(Z,E) \cdot p_e (E + m_e c^2)(E_0 - E)\sqrt{(E_0 - E)^2 - m_\nu^2 c^4} \cdot \Theta(E_0 - E - m_\nu c^2). \tag{1.36}$$

The Fermi function $F(Z,E)$ considers the interaction between emitted lepton and nucleus with charge $+Z$. Here E denotes the kinetic energy of the electron, p_e the momentum and the neutrino mass squared m_ν^2. The Heaviside function Θ ensures energy conservation. The energy independent constant $C = (G_F^2 \cos^2\theta_C |M|^2)/(2\pi^3 \hbar^7 c^5)$ consists of Fermi's coupling constant G_F, the Cabibbo angle θ_C and the nuclear matrix element M. In contrast to double beta decay matrix elements, M for single β-decays especially for tritium (see section 1.6.2), a superallowed decay with M independent of E, is well known. So the description of the process is model-independent from the viewpoint of nuclear matrix element calculation. The resulting β-spectrum is shown in figure 1.5.

The influence of m_ν^2 on the spectrum is only significant close to E_0 and causes an earlier end of the spectrum due to energy conservation, but more importantly a different spectral shape in this region (figure 1.5b). A precise measurement of the spectrum at the endpoint region allows comparing the expected spectral shape with it and extract a best-fit m_ν^2.

Although an electron antineutrino $\bar{\nu}_\mathrm{e}$ is created in every β^--decay, three neutrino mass eigenstates $|m_j\rangle$ contribute to the spectrum, since neutrino oscillations (section 1.3) showed that neutrinos mix. Then the phase space of eq. (1.36) results in

$$\frac{\mathrm{d}N}{\mathrm{d}E} \propto \sum_j |U_{ej}|^2 \sqrt{(E_0 - E)^2 - m_j^2 c^4}\,\Theta(E_0 - E - m_j), \tag{1.37}$$

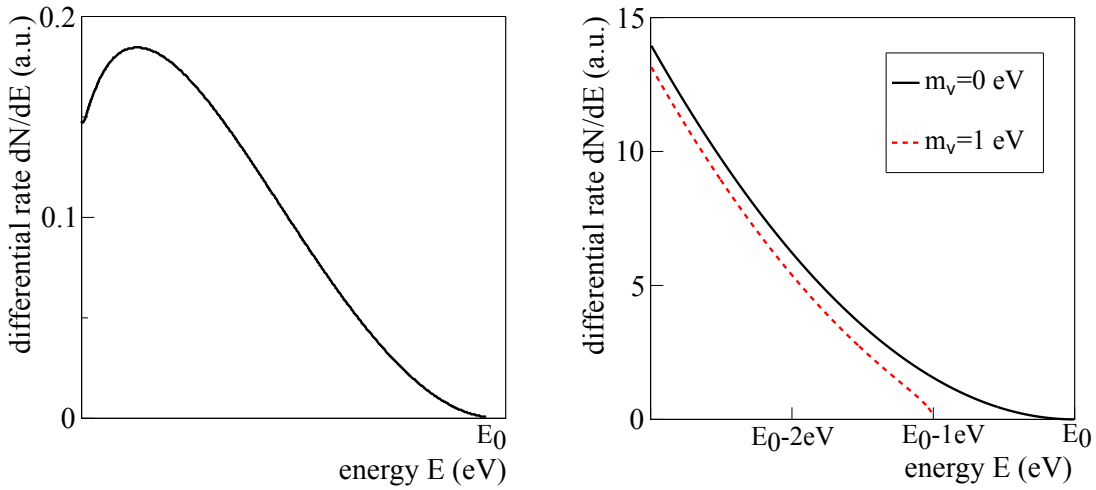

Figure 1.5: **Differential β-spectrum.** Full range (*left*) and zoom to the region below the endpoint energy E_0 (*right*) where the influence of non-vanishing m_ν^2 is evident.

a superposition of β-spectra weighted according to the contribution $|U_{ej}|^2$ of ν_j to $\bar{\nu}_\mathrm{e}$. Since the mass differences Δm_{jk}^2 are small (see table 1.1), one can define the effective mass of the electron antineutrino $\bar{\nu}_\mathrm{e}$, the incoherent sum

$$m_{\bar{\nu}_e}^2 = m_\nu^2 = \sum_j |U_{ej}|^2 m_j^2 \tag{1.38}$$

to quantify the influence of a neutrino mass on the shape of the β-spectrum and use eq. (1.36). In contrast to double β-decay where possible Majorana phases could reduce the observable $\langle m_\nu \rangle$ of eq. (1.30), m_ν^2 is equal or larger than a single m_j and accessible in a direct β-decay experiment in a model-independent approach.

1.6.1 Rhenium and Holmium experiments

As in the search for $0\nu\beta\beta$ one of the first tasks is to choose an appropriate β-emitter for a direct neutrino mass measurement and to develop a suitable experimental setup. A promising candidate is Rhenium ^{187}Re due to its low endpoint energy of $E_0 = 2.47\,\mathrm{keV}$ that is a benefit for the measurement (see discussion in section 1.6.2). ^{187}Re can be used as a crystal and acts as β-electron source and detector at the same time: A β-electron created in the material transfers its energy E to phonons of the crystal. These can be measured calorimetrically as a small temperature increase proportional to E. The MILANO experiment [33] used an array of 10 microcalorimeters operated between 5 and 65 mK [34] where each contained 250-300 μg of $AgReO_4$ and published an upper limit

$$m_{\bar{\nu}_e} < 15\,\mathrm{eV}\,(90\%\,\mathrm{C.L.}). \tag{1.39}$$

The power of a calorimetric approach is its scalability. The Rhenium source-detector arrays can be extended by further microcalorimeters to increase the mass and improve the sensitivity. This extension is proposed by the "Microcalorimeter Arrays for a Rhenium Experiment (MARE)" [35]. It is planned to improve the calorimetric technique and the number of the calorimeters to 10^4 to reach a statistical sensitivity on m_ν of 0.2 eV.

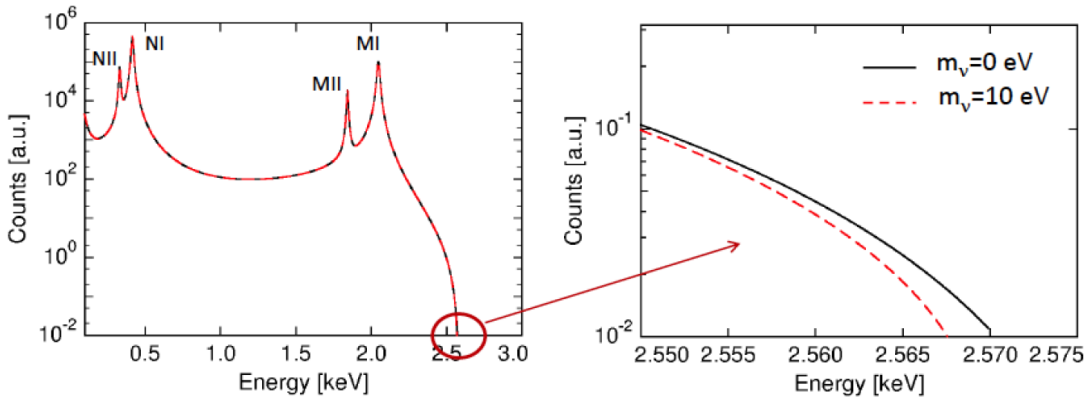

Figure 1.6: **Spectrum of ^{163}Ho from [38].** It is a "sum of Lorentzian peaks, centred at the binding energy E_H of the captured electron, where H represents the hole left in the orbitals" [37]. On the right, the endpoint region is shown where a non-vanishing neutrino mass reduces the maximal possible energy.

Another possibility to determine the neutrino mass in a direct kinematic approach is the precise measurement of electron capture, for example of Holmium-163 [36]:

$$\mathrm{EC}: {}^{163}\mathrm{Ho} + e^- \longrightarrow {}^{163}\mathrm{Dy}^* + \nu_e \tag{1.40}$$

$$ {}^{163}\mathrm{Dy}^* \longrightarrow {}^{163}\mathrm{Dy} + E_\mathrm{C}. \tag{1.41}$$

The released energy $Q = 2.56\,\mathrm{keV}$ [37] is split between emitted neutrino and the excitation energy E_C of Dysprosium. The following de-excitation happens by emission of X-rays, Auger electrons or Coster-Kronig transitions and can be measured in a calorimetric approach. The energy spectrum is shown in figure 1.6 and shows the dependence on m_ν close to the endpoint energy.

An experimental approach is the "Electron Capture HOlmium experiment (ECHO)" [38] that comprises two steps: On the one hand, calorimeters will measure the holmium spectrum E_C and deduce the endpoint E_0. On the other hand, a Penning trap [39] will be used to determine the Q-value, the mass difference between ^{163}Ho and ^{163}Dy. Then, the difference $E_\nu = Q - E_C$ determines m_ν. It is planned to reach a sensitivity of a few eV [37].

1.6.2 Tritium as β-emitter

Tritium is one of the most promising candidates in direct neutrino mass measurements and has already been used for decades. Its advantages are:

- **Low endpoint energy E_0.** The endpoint energy of tritium is $E_0 = 18.6\,\mathrm{keV}$, the second lowest of all β-emitters [32, 40]. The region of the β-spectrum that is most sensitive to m_ν^2 is the endpoint region, typically a few tens of eV below E_0. There, the number of decays N is proportional to $1/E_0^3$, favouring low E_0 with high N in the endpoint region at reasonable overall activity. Additionally, low E_0 only needs a low, technically achievable retarding potential U (see section 2.1) to measure the integrated spectrum.

- **Short half-life.** The half-life of tritium with $t_{1/2} = (4500 \pm 8)\,\mathrm{d}$ ($\approx 12.3\,\mathrm{y}$) [41] is short compared to many other β-emitters. To reach a high source activity, i.e. adequate statistics, only small amounts of tritium are needed[5].

- **Superallowed decay.** In case of tritium β-decay, parent atom ^{3}H and daughter atom ^{3}He have identical wave-functions. The calculation of the nuclear matrix element $|M|$ needed for the theoretical description of the decay simplifies, since no intermediate states have to be included. $|M|$ is independent of the energy of the emitted electron.

- **Low interaction between β-electron and nucleus.** This interaction is described by Fermi's function [42]. In case of tritium β-decay the daughter nucleus ^{3}He only has two protons that attract the emitted β-electron. This modification of the spectrum can be calculated or measured [43].

- **Gaseous hydrogen isotope.** As a hydrogen isotope many physical and chemical properties of tritium are similar to the well-known hydrogen. This simplifies the description of several processes, of course besides strict rules for safety due to its radioactivity. Storage of tritium gas is feasible and adjusting the pressure in a volume allows varying the activity of a gaseous tritium source.

Besides all the advantages, there is a disadvantage: Gaseous tritium is molecular (T_2) and its decay is

$$T_2 \rightarrow {}^3\mathrm{HeT}^+ + \mathrm{e}^- + \bar{\nu}_\mathrm{e}. \tag{1.42}$$

The daughter ion $^3\mathrm{HeT}^+$ can be excited electronically as usual, but due to the molecular structure also rotationally and vibrationally. These energies constitute a final state distribution with energies between 0 and 4 eV for the ro-vibrational excitations and energies above 20 eV for the first electronic excitation. The final state energy remains at the daughter ion, thus modifies the spectrum of the β-electrons and has to be considered for the neutrino mass analysis. Details on the calculation of the theoretical spectrum like the final state distribution can be found in section 4.2.3.

The Mainz experiment and the Troitsk experiment

Two recent tritium β-decay experiments are the "Mainz neutrino mass experiment" [44] that was finished in 2001 and the still running "Troitsk neutrino mass experiment" [45]. At both experiments, a spectrometer of MAC-E type (see section 2.1.1) was used to measure the β-electron spectrum, but the tritium source followed different approaches.

At Mainz, a quench-condensed tritium source was used. This avoids the final state distribution of gaseous molecular T_2 (see above), but also has to deal with charging of the substrate due to the remaining $^3\mathrm{He}^+$ ions. The final results of the Mainz experiment are published in [46]

$$\begin{aligned} m^2_{\bar{\nu}_\mathrm{e}} &= (-0.6 \pm 2.2(\mathrm{stat}) \pm 2.1(\mathrm{syst}))\,\mathrm{eV}^2 \\ m_{\bar{\nu}_\mathrm{e}} &< 2.3\,\mathrm{eV}\,(95\%\mathrm{C.L.}). \end{aligned} \tag{1.43}$$

[5] KATRIN uses 40 g tritium that cycles through the source.

The Troitsk experiment used a windowless gaseous tritium source, a concept that will also be used at KATRIN and will be explained in detail in chapter 3. The final results published in [47] are

$$\begin{aligned} m^2_{\bar{\nu}_e} &= (-0.67 \pm 1.89(\text{stat}) \pm 1.68(\text{syst}))\,\text{eV}^2 \\ m_{\bar{\nu}_e} &< 2.05\,\text{eV}\ (95\%\text{C.L.}). \end{aligned} \tag{1.44}$$

2. The KATRIN experiment

The KArlsruhe TRItium Neutrino experiment KATRIN is designed to directly determine the mass of the electron antineutrino $\bar{\nu}_e$ in a model-independent way. A non-vanishing neutrino mass square m_ν^2 influences the spectral shape of a β-electron spectrum (see section 1.6.2). KATRIN uses a high luminosity gaseous tritium source to accumulate high statistics and a precise spectrometer to analyse the β-electron energies from tritium decay. KATRIN is currently under construction at the Karlsruhe Institute of Technology (KIT), Germany. Within three years of measurement time and envisaged low systematic uncertainties, KATRIN will reach a sensitivity of $m_\nu < 200\,\mathrm{meV}$ @90%C.L. [48]. This will at least improve the upper limits on m_ν of its predecessors [46, 47] by a factor of 10 or may allow claiming a non-vanishing directly measured neutrino mass if $m_\nu > 350\,\mathrm{meV}$[1]. The following chapter briefly explains the measurement principle (section 2.1), as well as the different components (sections 2.2-2.6) of the experimental setup (see figure 2.1).

2.1 Measurement principle

KATRIN uses an integrating measurement system, a so-called MAC-E filter (see below) to measure the β-spectrum of tritium and thereby the influence of the neutrino mass square m_ν^2. At different retarding energies qU the integrated β-spectrum is

$$N(qU) \propto t_{qU} \int_0^{E_0} \frac{\mathrm{d}N}{\mathrm{d}E}(E_0, m_\nu^2) \cdot R(E, qU)\mathrm{d}E \tag{2.1}$$

with measuring time t_{qU} (see figure 2.2). The measurement reveals information about the differential spectrum $\mathrm{d}N/\mathrm{d}E$ (see section 1.6.2) that again depends on the wanted m_ν^2 and the spectrum endpoint energy E_0. Additionally, it is modified by the influence of the whole experimental system, comprised in the response function $R(E, qU)$ (see section 4.2). For example, the transmission probability for electrons with kinetic energies below qU is zero, so that only the high energetic part of the spectrum is measured.

[1] Since the observable is m_ν^2, the improvement will even be a factor of 100.

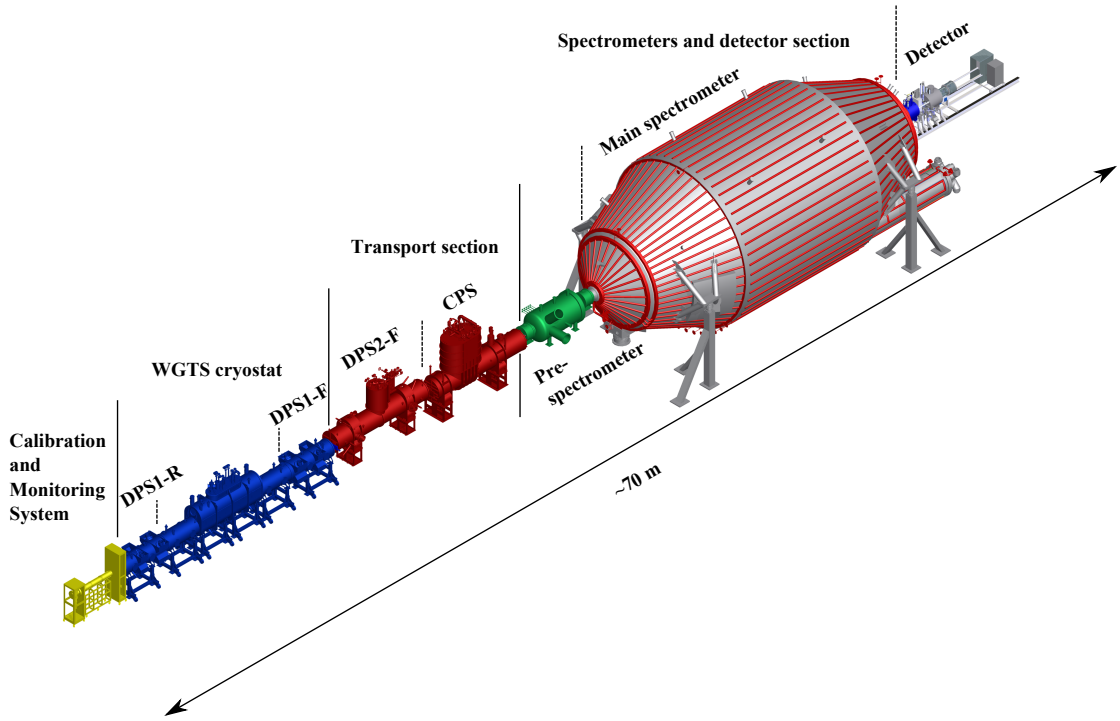

Figure 2.1: **The KATRIN experiment.** Detailed explanation of sub-components in main text.

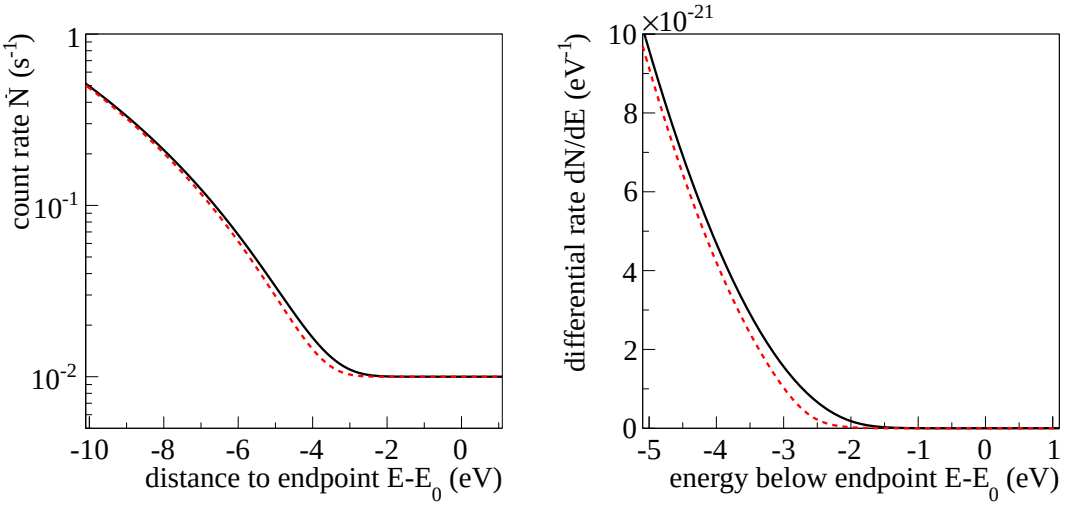

Figure 2.2: **a) Integrated β-spectrum at KATRIN.** The count rate $\dot{N}$ depends on the retarding energy $E = qU$ respectively the distance to the endpoint energy E_0. Here, a background rate of $10^{-2}\,\mathrm{s}^{-1}$ is assumed. The influence of a neutrino mass $m_\nu = 1\,\mathrm{eV}$ is shown as red dashed line compared to a spectrum with vanishing m_ν in black.
b) Differential β-spectrum. Includes the final state distribution of tritium. Again, the effect of a 1 eV neutrino mass is drawn in red, dashed compared to vanishing m_ν in black.

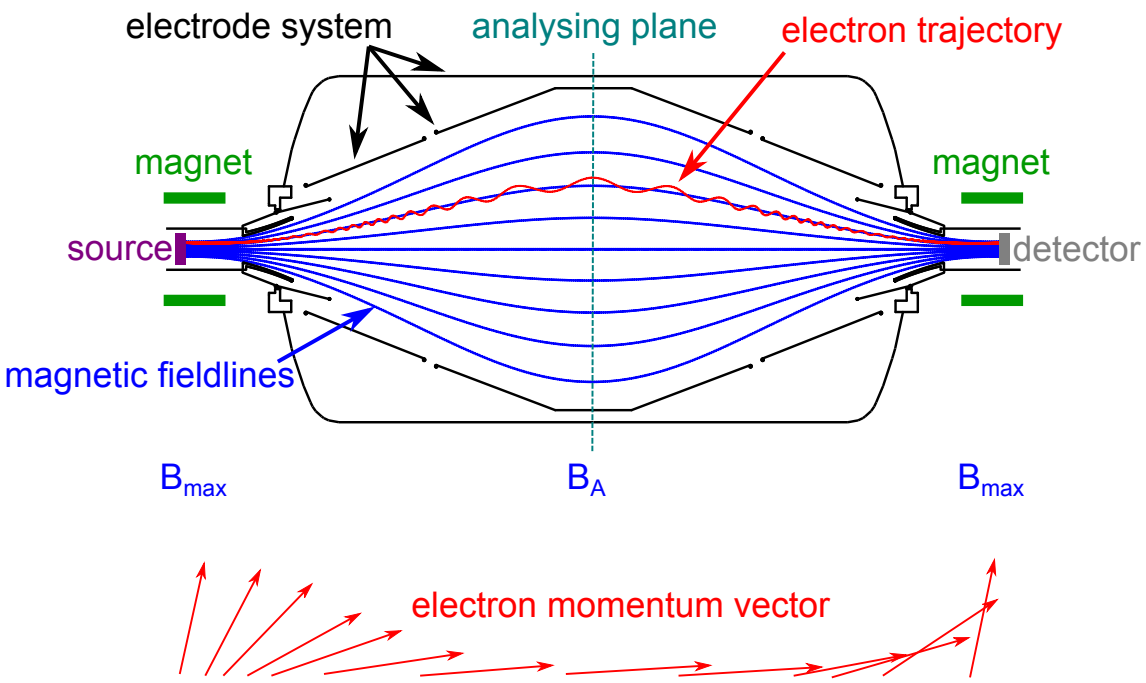

Figure 2.3: **Principle of a MAC-E filter from [51], modified.** Here, in case of the KATRIN pre-spectrometer. Detailed explanation in main text.

The neutrino mass square m_ν^2 will then be obtained by adapting a theoretical, expected spectrum with fit parameter m_ν^2 to the measured integrated spectrum (see section 6.2.5 and 6.2.6).

If an expected spectrum is fitted to the measurement, this expectation should be as exact as possible. Therefore, eq. (2.1) shows that the description of $\mathrm{d}N/\mathrm{d}E$ must consider standard β-decay theory (see chapter 1.6) and various corrections from experiment and theory like the Fermi function or radiative corrections. Additionally, knowledge of the response function, that means the influence of the whole experiment on the measurement, is mandatory to analyse the measured spectrum. Therefore, great efforts are taken to control and monitor all important experimental parameters. Important in this context means that they critically influence the measurement at KATRIN respectively the neutrino mass determination as a systematic effect. The work at hand is – amongst other subjects – responsible for investigating these systematics.

2.1.1 MAC-E filter

MAC-E filter stands for Magnetic Adiabatic Collimation with an Electrostatic filter [45, 49, 50]. A scheme is shown in figure 2.3.

The principle is to probe the electrons' kinetic energy by a retarding potential. Only electrons with sufficient energy can overcome the potential; the system works as a high-pass filter. A closer look shows that electrons in case of a β-decay, created within the source field B_S, are emitted isotropically with azimuthal angle θ to the magnetic field line. Their kinetic energy E is composed of a longitudinal component $E_\parallel$, causing a translation along the field line, and a transversal component $E_\perp$, creating the cyclotron motion around the field line. When applying an electric retarding potential difference U along the field line, only $E_\parallel$ can be analysed. Therefore, a

mechanism is needed that converts $E_\perp$ to $E_\parallel$ adiabatically, without changing the electrons' total energy.

That is accomplished by the magnetic adiabatic collimation. It uses that the magnetic moment $\mu = \frac{E_\perp}{B}$ is constant in non-relativistic adiabatic approximation [32]. If the magnetic field strength is lowered adiabatically from the source with $B_S = 3.6\,\mathrm{T}$ to the analysing plane with $B_A = 3 \cdot 10^{-4}\,\mathrm{T}$, $E_\perp$ is reduced, $E_\parallel$ is increased. This is visualized by a turning momentum vector in figure 2.3. Vice versa, if B increases, the momentum vector is erected again. The maximal magnetic field in the KATRIN setup $B_{max} = 6.0\,\mathrm{T}$ is reached at the detector pinch magnet. This causes electrons that are emitted in the source with an azimuthal angle θ larger than the maximal opening angle θ_{max} [48]

$$\sin\theta_{max} = \sqrt{B_S/B_{max}} \tag{2.2}$$

to be reflected magnetically. Electrons with starting angles between 0 and θ_{max} can be analysed due to the magnetic collimation and reach the detector afterwards, if their kinetic energy is sufficient. But this is not working perfectly, since the ratio B_S/B_A (or rather B_{max}/B_A) is finite; the maximal $E_\perp$ that an electron can still possess in the analysing plane defines the energy resolution ΔE of a MAC-E filter. For the electromagnetic design of the KATRIN main spectrometer (section 2.4), for electrons near the endpoint energy of 18.6 keV, it is [48]

$$\Delta E = \frac{B_A}{B_{max}} \cdot E = 0.93\,\mathrm{eV}. \tag{2.3}$$

2.2 Tritium source

As β-electron source, KATRIN uses a windowless gaseous tritium source WGTS, a concept that has been developed at the Los Alamos experiment [52] and was also successful in various other β-decay experiments for direct neutrino mass determination [45, 53]. The advantages of tritium have already been outlined in chapter 1.6.2. In the WGTS, gaseous molecular tritium T_2 is injected at the center of a beam tube and pumped out by turbomolecular pumps at both ends. The pumped-out gas is collected and reinjected in a closed cycle. This pumping concept avoids closing windows at the beam tube ends, so that β-electrons that are created inside the source can leave it without losing energy besides scattering processes with the low pressure gas. The WGTS in KATRIN has a beam tube length of 10 m and a diameter of 90 mm. On each end, a pumping section with 12 turbomolecular pumps in total is attached, increasing the length to 16 m. A gas flow reduction factor of 10^2 is estimated for this setup. The whole system is embedded in a cryostat, since it will be operated at $T = 30\,K$, to achieve reasonable densities ($\rho \approx 5 \cdot 10^{14}\,\mathrm{cm}^{-3}$) and thereby a high source activity ($A \approx 10^{11}$Bq) at reasonably low injection pressure ($p_{in} \approx 3\,\mu$bar). Furthermore, low temperatures cause a low Doppler broadening of the measured β-spectrum due to the low thermal movement of the β-emitting T_2.

Inside the cryostat, superconducting solenoids provide a source magnetic field of $B_S = 3.6\,\mathrm{T}$ to guide the created β-electrons out of the source towards the spectrometers (see section 2.4) for energy analysis.

Various tests of WGTS sub-systems, for example the demonstrator tests (see section 3.4) or tests of the magnets are finished, so that the WGTS can be assembled. Planned date of delivery and commissioning is 2015.

A detailed discussion of the WGTS, its physical concepts, technical challenges and its implications for KATRIN are presented in the dedicated chapter 3 due to its importance for this work at hand.

2.3 Transport section

Since the WGTS has no terminating windows and the turbomolecular pumps in the WGTS are not sufficient to capture all T_2, further efforts are needed to collect all neutral gas as well as unwanted ions. At the same time, the β-electrons should be transported towards the spectrometers without altering the electrons' energy, otherwise the measured spectrum would be distorted.

The first module of the transport section is the Differential Pumping Section DPS2-F. It is an almost 7 m long cryostat at 77 K, with 5 beam tube elements of 1 m length, arranged in a chicanery and 4 turbomolecular pumps in between (see figure 2.4a). The chicanery avoids that neutral T_2 molecules would be able to pass the DPS2-F without hitting the walls respectively the pumps at least once; the pumping is more efficient. Commissioning measurements showed an extrapolated gas flow reduction factor of $1.8 \cdot 10^4$ for gases of atomic mass 4 like tritium with the potential to improve it to the requested 10^5 [54].

The β-electrons are not affected by the pumping. As charged particles they follow the magnetic field lines through the whole chicanery – adiabatically due to the slowly varying fields. This is also true for ions, so special electric dipole elements are used to remove the heavy ions from the beam [55].

To monitor the flux of ions from the WGTS towards the spectrometers and the performance of the electric dipoles to remove them, Fourier transform ion cyclotron resonance (FT-ICR) is used. Ions are trapped inside the FT-ICR-modules (penning traps) of the DPS2-F and their cyclotron frequency is analyzed to determine the ion concentration in the system [56].

The second part of the transport section is the 7 m long Cryogenic Pumping Section CPS. Almost all molecules that have overcome the previous pumps are adsorbed by argon frost at 4 K on the inner surface of the CPS beam tube chicanery (see figure 2.4b). This concept yields an estimated reduction factor of 10^7 [48]. Together with the pumps in the WGTS and the DPS2-F, a total reduction factor of 10^{14} will be obtained, allowing for very low partial pressures of T_2 at the end of the complete source and transport section.

2.4 Spectrometers

KATRIN uses a tandem spectrometer setup, consisting of the pre-spectrometer and the main spectrometer.

Pre-spectrometer

All β-electrons that have crossed the transport section reach the pre-spectrometer ($l = 3.4$ m, $d = 1.7$ m). It is working as a MAC-E filter (see section 2.1.1) with its retarding energy at a few 100 eV below the spectrum endpoint energy E_0 [48]. This prevents a large number of low-energetic electrons from entering the large volume

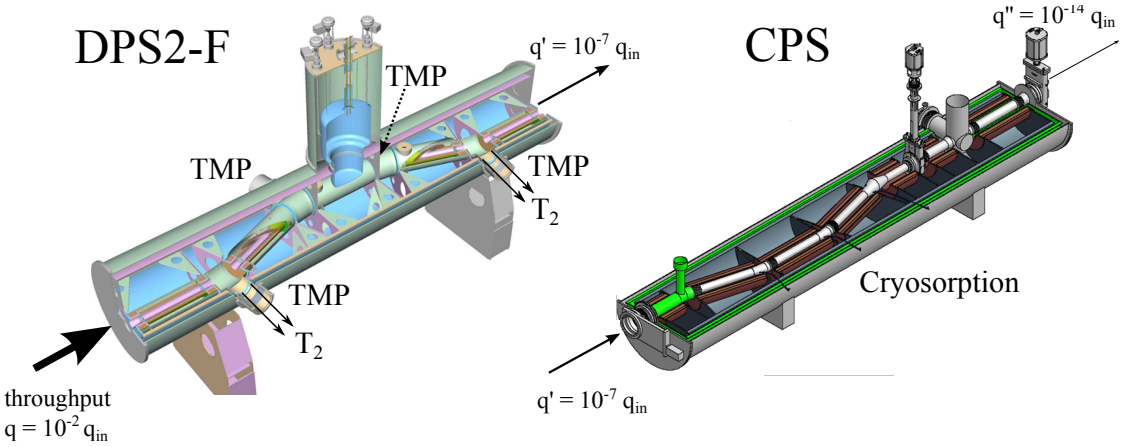

Figure 2.4: **a) Technical drawing of the DPS2-F.** The gas flow q that leaves the WGTS and arrives at the DPS2-F is the WGTS injection throughput q_{in} reduced by a factor 10^2 due to the DPS1-F. The turbomolecular pumps (TMP) in the DPS reduce the gas flow further by 10^5.
b) Technical drawing of the CPS. Cryosorption allows for a final gas flow reduction of 10^7.

of the main spectrometer, causing background electrons (see below). This cut does not disturb the high-energetic part of the spectrum – the last 50 eV below E_0 – that is used for the KATRIN analysis.

Main spectrometer

The KATRIN main spectrometer is responsible for the energy analysis of the β-electrons. Technically, it is a vacuum tank of length $l = 23.3\,\mathrm{m}$ and central diameter $d = 9.8\,\mathrm{m}$. To compose a MAC-E filter two superconducting magnets on both sides of the spectrometer create a strong magnetic field up to $B_{\mathrm{max}} = 6.0\,\mathrm{T}$. The field strength drops towards the center of the spectrometer, the so-called analysing plane, by a factor of 20000 to $B_{\mathrm{A}} = 3{\cdot}10^{-4}\,\mathrm{T}$. The dimensions and magnetic fields limit the magnetic flux ϕ that is transported through the spectrometer. As a reference [48]

$$\phi = \int B\,\mathrm{d}A = B_{\mathrm{A}} A_{\mathrm{A}} = 192\,\mathrm{Tcm}^{-2} \tag{2.4}$$

is chosen, with an effective area of the analysing plane $A_{\mathrm{A}} = 63.6\,\mathrm{m}^2$.

Metal electrodes and a sophisticated inner wire electrode system provide the retarding potential to analyse the energies of the β-electrons. The wires are mounted inside the spectrometer in a distance of a few centimetres to the walls [57]. They are arranged in two layers and have a potential difference of $\Delta U \approx -100\,\mathrm{eV}$ with respect to the spectrometer walls. If cosmic rays hit the wall and create electrons, these electrons cannot overcome the negative potential of the wires and will be reflected towards the wall. This prevents additional background events at the detector.

The main spectrometer is operated at UHV conditions of $p \approx 10^{-11}\,\mathrm{mbar}$ [48]. This is necessary, since on the one hand, β-electrons can scatter on residual gas molecules in the spectrometer vessel, lose energy and therefore influence the measured spectrum. On the other hand, T_2 molecules could decay directly inside the spectrometer and create β-electrons that would not experience any retarding potential and that would directly disturb the measurement as background electrons.

2.5 Detector

The electrons that were able to pass the spectrometer are guided to the KATRIN focal plane detector FPD. The detector is a silicon PIN-diode with a diameter of the sensitive region $d = 90\,\text{mm}$, segmented into 148 pixels [58]. This segmentation allows distinguishing between electrons that were emitted in different parts of the source and have passed the spectrometers on different radii and azimuthal angles. The measured energy resolution $\Delta E = 1.637 \pm 0.004\,\text{keV}$ [58] is sufficient for KATRIN, since the energy of signal electrons is determined by the precise main spectrometer with $\Delta E = 0.93\,\text{eV}$; the detector just has to count the electrons and reject background events.

A background contribution is caused by cosmic muons, passing the detector system. Therefore, a veto system is used that rejects events when they coincide with a cosmic muon. With this veto and other measures to suppress background from the spectrometers it is intended to reach a total background rate of only 0.01 cps [48].

2.6 Monitoring systems

Next to the main components, several monitoring systems are used at KATRIN. Their general task is to monitor crucial parameters of the source and spectrometers. Uncertainties in these parameters cause systematic uncertainties on the analysed neutrino mass and have to be minimized to reach KATRIN's sensitivity (see section 3.2). The major monitoring systems are listed here:

- **The Laser Raman System** is used to monitor the tritium purity of the source [59]. Its working principle as well as its importance for KATRIN are discussed in detail in section 3.3.
- **The rear section** is connected to the WGTS on its rear end. Electrons that are emitted towards the rear end or that are reflected by the spectrometer retarding potential due to their insufficient kinetic energy, hit the rear wall. This can possibly be used to monitor the overall activity of the WGTS by a Faraday cup or β-induced X-ray spectroscopy. The studies are ongoing and their status is summarized in [60]. Additionally, an electron gun will be installed at the rear section. Sending a stable beam of electrons through the whole WGTS and analysing the fraction of scattered to unscattered electrons with the spectrometers and detector allows monitoring the column density (see section 3.1 and 4.2.2).
- **The Forward Beam Monitor** was tested with a silicon PIN-diode [60]. It is brought into the beam tube of the CPS (section 2.3) to monitor the source activity outside the transported magnetic flux in eq. (2.4) without disturbing the neutrino mass measurement.
- **The monitor spectrometer** is operated at the same retarding voltage as the main spectrometer. Monitoring of the line width and position of the krypton K-32-line (17.8 keV) determines fluctuations or drifts of the retarding potential [61].

3. Windowless gaseous tritium source

The windowless gaseous tritium source WGTS has already been outlined in the previous chapter in the context of the KATRIN experiment. This chapter will focus on a detailed characterisation of the instrument in terms of its key parameters and will highlight the importance of the WGTS with respect to systematic effects on the determination of m_ν^2. In section 3.1, the general physical concept of the source is discussed together with the definition of the key parameters. Using sophisticated gas dynamics models that are presented in detail later (see chapter 5), requirements on the key parameters are inferred in section 3.2. The technical realisation in terms of precise controlling and monitoring of the key parameters follows in section 3.3. Since the temperature stability and homogeneity of the WGTS was known to be challenging right from the beginning, the demonstrator experiment has been performed with the aim to characterize the WGTS with regard to its thermal behaviour before the full WGTS assembly. In preparation of the results of the demonstrator experiment in chapter 9, the demonstrator is introduced here in section 3.4.

3.1 Key parameters

It has already been discussed in chapter 1.6, why experiments for direct neutrino mass determination measure the tritium β-decay spectrum and why the approach of a windowless gaseous tritium source has been used in the past and is the choice at KATRIN. In the following, the key parameters of a gaseous tritium source are discussed.

Column density

Describing a gaseous tritium source, the different molecule species i are distributed according to density profiles

$$\rho_i(\vec{r}) = \rho_i(\vec{r}, p_{\mathrm{in}}, p_{\mathrm{ex}}, T(\vec{r})) \tag{3.1}$$

as a function of the injection pressure p_{in}, the exit pressure p_{ex} and the beam tube temperature $T(\vec{r})$ [1].

The most fundamental parameter of a gaseous tritium source is the column density

$$\rho d = \rho d(p_{\mathrm{in}}, p_{\mathrm{ex}}, T(\vec{r})) = \sum_i \int_{-L/2}^{+L/2} \rho_i(\vec{r}, p_{\mathrm{in}}, p_{\mathrm{ex}}, T(\vec{r}))\mathrm{dz}. \tag{3.2}$$

It is obtained by integrating the densities $\rho_i(\vec{r})$ along the beam axis z with a source length L. ρd is also a function of p_{in}, p_{ex} and $T(\vec{r})$ [2]. The column density is directly connected to the source activity S as

$$S \propto \rho d \cdot A_{\mathrm{S}} \cdot \varepsilon_{\mathrm{T}} \tag{3.3}$$

with source cross section A_{S} and tritium purity ε_{T} that is explained below. Increasing ρd obviously increases S in total. But there is a drawback: Increasing the amount of molecules in the source increases the probabilities for inelastic scattering of the β-electrons. Fewer electrons can leave the source unscattered; this increases the systematic uncertainties connected with scattering (see section 4.2.2).

Tritium purity

When using molecular T_2, the other hydrogen isotopologues DT, HT, D_2, HD and H_2 in the source are inevitable due to exchange processes. The tritium purity ε_{T} is defined as the fraction of tritium nuclei among all other constituents in the source. If we denote the fraction of all isotopologues X as $c(\mathrm{X})$ with $\sum_{\mathrm{X}} c(\mathrm{X}) = 1$, then ε_{T} will be

$$\varepsilon_{\mathrm{T}} = c(\mathrm{T_2}) + 0.5 \cdot \mathrm{c(DT)} + 0.5 \cdot \mathrm{c(HT)}. \tag{3.4}$$

Obviously a high tritium purity is desirable to have a high activity; impurities only contribute to ρd and increase the scattering probabilities of out-going electrons. This demands for a system that provides highly pure T_2 and removes impurities reliably. Because such a system usually cannot remove all impurities perfectly, the remaining contributions should be monitored. This is especially true for the tritiated hydrogen isotopologues T_2, DT and HT in a neutrino mass experiment: They contribute differently to the measured β-spectrum as will be explained in section 4.2.3, causing a systematic uncertainty.

Source temperature

Low temperature operation of a gaseous tritium source is advisable, since this allows for a high density and therefore column density, respectively source activity, at a reasonable injection pressure. In addition, the broadening of the β-spectrum due to the Doppler effect is weaker for low temperatures, since the thermal movement of the β-emitting T_2 molecules is lower (see also section 4.2.5.4). In both cases, very low temperatures might look promising, but below 27 K molecule clusters T_n

[1] In chapter 5, $\rho_i(\vec{r})$ is obtained by integrating the velocity distribution function over the velocity space.

[2] In general, ρd depends on the coordinates x and y, but this is negligible in the case of the WGTS at KATRIN as will be shown in section 5.4.

emerge and tritium freezes on surfaces. Both effects lead to different spectra of the β-electrons emitted from clusters or frozen T_2 at walls, disturbing the measurement of the free T_2 β-spectrum. For a gaseous source, temperatures between 27 and 33 K should be used [48]. The exact temperature can be chosen when fully operating the source; in the following 30 K is used as reference temperature.

Additionally, a homogeneous source is required to ensure equal conditions for electrons emitted at different parts of the source.

Source magnetic field

For the energy analysis in a MAC-E setup (see section 2.1.1), the β-electrons have to be guided to the spectrometers. Therefore, the source needs a magnetic field B_S; the isotropically emitted electrons then follow the magnetic field lines out of the source towards the spectrometers. A strong B_S is practical in two ways: First, considering eq. (2.2), a strong B_S allows to analyse a large fraction of all electrons that have been emitted in the source. Additionally, eq. (2.4) shows that a strong source magnetic field allows for a reasonable area of the source A_S that is seen by the spectrometer and the detector. A homogeneous magnetic field is desirable, because it allows for equal starting conditions for electrons that are created in different parts of the source. In context of the magnetic field strength, this means that the maximal opening angle of eq. (2.2) is constant for all electrons. This has an impact on the mean path length of the electrons and the mean scattering probabilities (see eq. (4.8)) that are crucial for the analysis of measured spectra at KATRIN.

Source electric potential

The electric potential difference between the point of electron creation and the analysing plane in the spectrometer is used to determine the electrons' kinetic energies. For that purpose, the WGTS can either be grounded and the potential of the main spectrometer can be varied or the WGTS gets a bias potential up to -1 kV that can be varied with respect to a fixed potential $U = -18.6\,\mathrm{keV}$ of the spectrometers [48]. In both cases, if the electric potential of the source varied locally, the energy measurement would be inaccurate. The aim is to have an equipotential source.

The β-electrons, the remaining positively charged ions and secondary electron-ion pairs due to ionisation constitute a plasma in the source [48]. The magnetic field along the beam axis confines the charged particles in radial direction. "Therefore, the plasma potential along any field line is set by the first conducting surface the field line intersects" [62]. For that purpose, the so-called rear wall is placed between the WGTS end and the rear section. It is required to have a stable, homogeneous surface potential to generate a homogeneous WGTS potential.

3.2 Source-related systematic uncertainties

The physics of a tritium source has been defined above. Before constructing the source, requirements on stability, homogeneity and the required accuracy of source parameters and their monitoring have to be defined.

Table 3.1: **Identified systematic uncertainties connected with unaccounted shifts of WGTS key parameters [48].** There, the requirements and systematic influences on m_ν^2 were already reported. They are re-evaluated in chapter 8 with more sophisticated models and methods that are explained in the chapters 4, 5, 6. The demonstrated achievements are reported in [60] with the exception of the temperature stability reported in [63].

source of syst. uncertainty	**requirements**	**syst. shift** $\Delta m_\nu^2\,(10^{-3}\,\mathrm{eV}^2)$	**achievements**
variations of			
column density	$\Delta\rho d/\rho d < 2\cdot10^{-3}$	< 1.5	
injection pressure	$\Delta p_{\mathrm{in}}/p_{\mathrm{in}} < 2\cdot10^{-3}$		$1.3\cdot10^{-4}$
exit pressure	$\Delta p_{\mathrm{ex}}/p_{\mathrm{ex}} < 0.06$		$1\cdot10^{-4}$
temperature	$\Delta T/T < 2\cdot10^{-3}$		$5\cdot10^{-5}$
tritium purity	$\Delta\epsilon_{\mathrm{T}}/\epsilon_{\mathrm{T}} < 2\cdot10^{-3}$		$1\cdot10^{-3}$
WGTS magnetic field	$\Delta B_{\mathrm{S}}/B_{\mathrm{S}} < 2\cdot10^{-3}$	< 2	
WGTS potential	$\Delta U < 10\,\mathrm{mV}$	< 1.2	

Uncertainties in the description of the source lead to systematic uncertainties on the analysed neutrino mass squared m_ν^2; they cause a systematic shift Δm_ν^2 from the unknown true m_ν^2.

During the design phase of KATRIN, the most important systematic effects have been identified in [48]. It is remarkable that 4 out of 5 major systematic uncertainties are connected with the WGTS. Therefore, dedicated analyses and test experiments presented in [60, 63] report the already achieved control and monitoring of source parameters. They are shown in table 3.1.

One of the major contributions to the systematic uncertainty is the stability of the column density ρd (see eq. (3.2)). Changes of ρd change the source activity. This could lead to differences when scanning the integrated spectrum (see section 2.1), imitating the effects of m_ν^2, disturbing the measurement. This is true since changes of ρd alter the scattering probabilities P_i (see section 4.2.2). If the ratio of the probability P_0 of unscattered electrons and the probability P_1, that electrons have scattered once, changes, the analysis of the measured spectrum will be executed with wrong assumptions. The unaccounted shifts of ρd inevitably lead to shifts of m_ν^2. In other words, not knowing the changes of ρd results in a systematic uncertainty on m_ν^2.

According to [48], the influence of ρd on m_ν^2 is significant and therefore a strict requirement on ρd-variations is demanded

$$\frac{\Delta\rho d}{\rho d} < 2\cdot10^{-3}. \tag{3.5}$$

Since ρd is determined by various parameters, the requirement in eq. (3.5) translates to the same requirements on variations of injection pressure Δp_{in} and tritium purity $\Delta\varepsilon_{\mathrm{T}}$. The influence of the exit pressure of a windowless source p_{ex} on ρd is weaker [64], so this requirement can be relaxed to $\Delta p_{\mathrm{ex}}/p_{\mathrm{ex}} < 0.06$.

Table 3.2: **Requirements on parameter trueness.** The trueness is the difference between the expectation of a measured observable and the (unknown) true value [60].

source of syst. uncertainty	**reference value**	**required trueness**
absolute temperature	(27 - 30) K	0.5 K
tritium purity	>0.95	10^{-2}

Temperature variations ΔT of table 3.1 are also named ΔT_{stab} in the following to distinguish temporal variations from temperature gradients along the source that are named as ΔT_{hom}. The requirement

$$\frac{\Delta T_{\mathrm{stab}}}{T} < 2 \cdot 10^{-3}, \tag{3.6}$$

on the temperature stability within a KATRIN run of two hours [48] at 30 K operational temperature at KATRIN is then translated to

$$\Delta T_{\mathrm{stab}} < 30\,\mathrm{mK/h}. \tag{3.7}$$

The physical motivation for a desired temperature homogeneity of

$$\Delta T_{\mathrm{hom}} < 30\,\mathrm{mK} \tag{3.8}$$

is different. A homogeneous temperature of the source ensures equal starting conditions for all electrons. Especially the thermal movement of the β-emitting T_2 molecules would vary, if the temperature distribution of the source were inhomogeneous. This would lead to position-dependent modifications of the spectrum due to the Doppler effect. It would cause an uncertainty on the description of the source. For KATRIN, the requirement in eq. (3.8) is asked for the inner 9.5 m of the source [48]. The only heat influx is from the end of the source (see section 3.3), increasing the temperature there. But since the densities there will be small, the effect of higher temperature near the ends will be small, too. A temperature gradient can be accepted up to 3 K there, if the main part of the source obeys eq. (3.8).

The same reason as for the temperature homogeneity is also true for the magnetic field variation and the source potential variation, shown in table 3.1. Variations in these parameters would alter the starting conditions of electrons generated in different parts of the source, influencing the spectrum measurement and thereby the analysis of m_ν^2.

Besides requirements on parameter stability, there are some requirements on the trueness of parameters that means knowledge of absolute values is needed. One of them is the tritium purity ε_{T}. Not knowing ε_{T} that means the fractions of tritiated hydrogen isotopologues T_2, DT and HT in the gas mixture results in an uncertainty on the description of the final state distribution (FSD) of the measured β-spectrum. It has already been explained in chapter 1.6.2 that the daughter molecule $(^3\mathrm{HeT})^+$ of a molecular decay of T_2 retains energy due to rotational, vibrational or electronic

excitations. The resulting FSD with probabilities for different excitation energies has been calculated for different hydrogen isotopologues in [65–68]. But since these calculations have no experimental verification, there is an uncertainty on m_ν^2 connected with them. To parameterize its effect on m_ν^2, in [48] a 1% broadening of the typical first 4 eV peak of the FSD was examined (see section 4.2.5.3), resulting in a systematic shift of $\Delta m_\nu^2 = 6 \cdot 10^{-3}\,\mathrm{eV}^2$. This can only state qualitatively what an uncertainty in the description of the final states means for KATRIN, but clearly shows that the influence of the FSD should not be underestimated. A similar effect is caused by an uncertainty of the absolute temperature T that determines the probabilities of parent molecules to have initial angular momentum J. This distribution influences the FSD similar to ε_T. This demands for requirements on the trueness that are presented in table 3.2. Additionally, section 8.3 deals with various analyses to further investigate the influence of the FSD on m_ν^2.

To summarize, all mentioned uncertainties contribute considerably to the total systematic uncertainty in KATRIN. When designing the tritium source, special emphasis is given to the stability and homogeneity of the system. Reducing the uncertainties by having a very stable, homogeneous source and accurately monitoring its parameters is of utmost importance to reach the KATRIN design sensitivity on m_ν^2.

3.3 Technical realisation

KATRIN uses a windowless gaseous tritium source WGTS, meeting the physical concepts and requirements on systematics discussed above. A 10 m long tube with diameter $D = 90\,\mathrm{mm}$ made of stainless steel, the so-called beam tube, is the recipient for gaseous tritium. To avoid energy losses of the generated β-electrons, there are no windows at the exits of the beam tube. Tritium leaving the tube is captured by in total twelve turbomolecular pumps distributed over four pumping chambers at the beam tube ends, the DPS1-R and DPS1-F (see figure 3.1). The gas that is not pumped out reaches further pumping sections adjacent to the WGTS (see section 2.3). To maintain an adequate, time-independent tritium content inside the windowless volume, a continuous gas injection at the center is needed. The injection pressure p_in and the gas throughput q, next to the exit pressure p_ex and the temperature distribution $T(\vec{r})$ determine the amount of tritium in the source.

The inner tritium loop

The whole injection and part of the pumping system of KATRIN is called “inner loop” system in figure 3.2a. It ensures a steady stable circulation of tritium gas through the WGTS by injecting in the center and pumping at the ends of the WGTS. This is essential to maintain a stable column density of $\rho d = 5 \cdot 10^{17}\,\mathrm{cm}^2$. In the inner loop, more than 99% of all tritium that is pumped out in the DPS1-R and DPS1-F is directly reinjected into a buffer vessel after passing a permeator. It can then be reinserted into a pressure controlled buffer vessel and from there into the WGTS. The missing 1% – together with the gas that is pumped out at the DPS2-F – is transferred to an outer loop where the facilities of the Tritium Laboratory Karlsruhe provide purification processes, which remove nearly all non-hydrogen contributions. Reinserting the highly pure tritium gas into a buffer vessel of the inner loop system ensures high tritium purity of the WGTS.

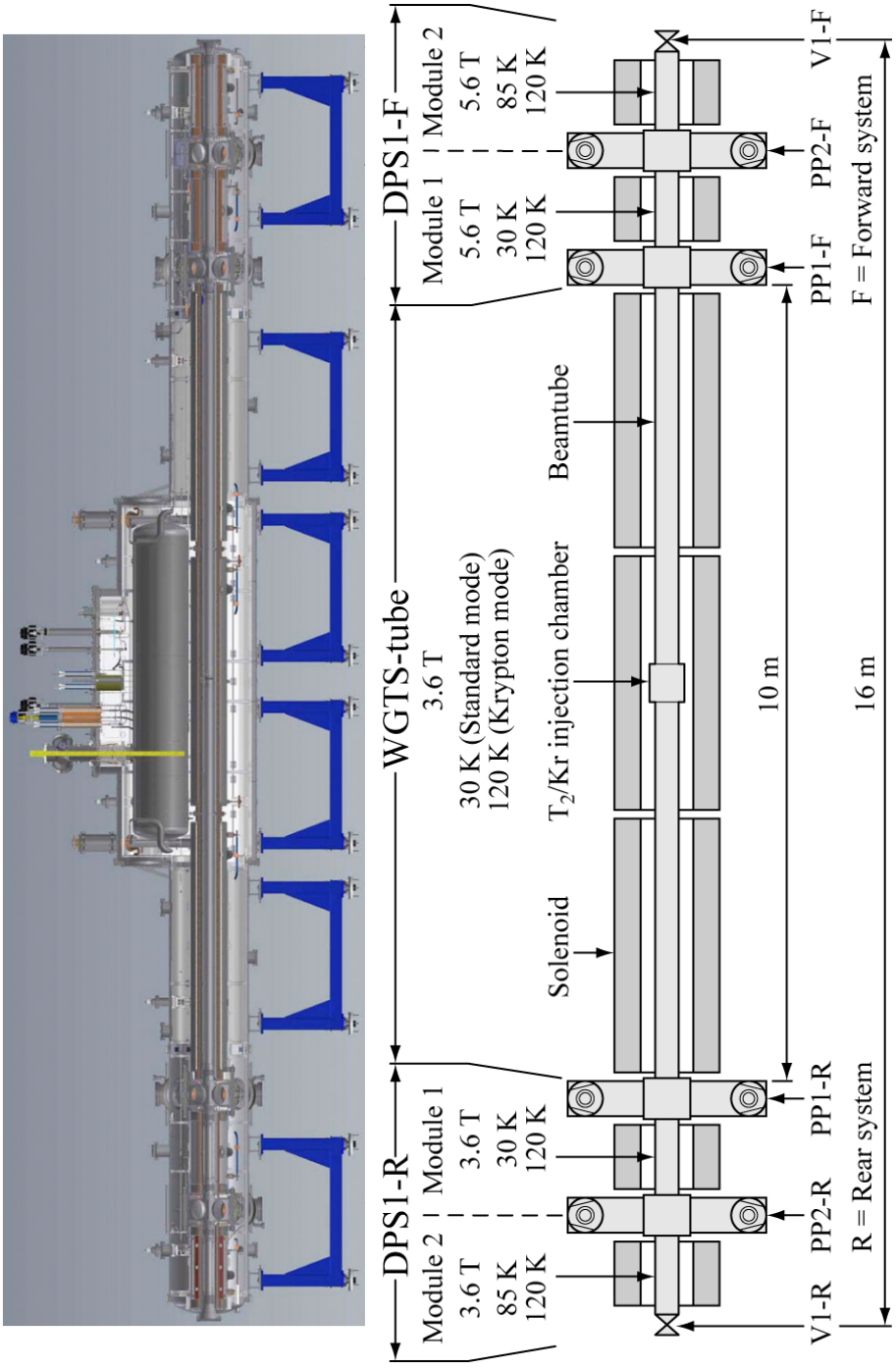

Figure 3.1: **CAD view of the WGTS and scheme of its main parts.** The 16 m source cryostat consists of the WGTS-tube as central part and two differential pumping sections, DPS1-R and DPS1-F. The temperatures vary from 4 K at the superconducting solenoids to 30 K at the beam tube and to 85 K at parts of the DPS1-R and DPS1-F. The tritium gas is injected in the center and diffuses along the beam tube to the turbomolecular pumps in the pumping chambers PP1 and PP2. The magnetic field of $B_S = 3.6\,\mathrm{T}$ is provided by superconducting solenoids (seven main magnets). It adiabatically guides the created β-electrons towards the spectrometers. In a special operation mode, the so-called krypton mode (see appendix A), gaseous krypton will be added to the tritium gas for calibration purposes. This requires a different temperature range of 120 K.

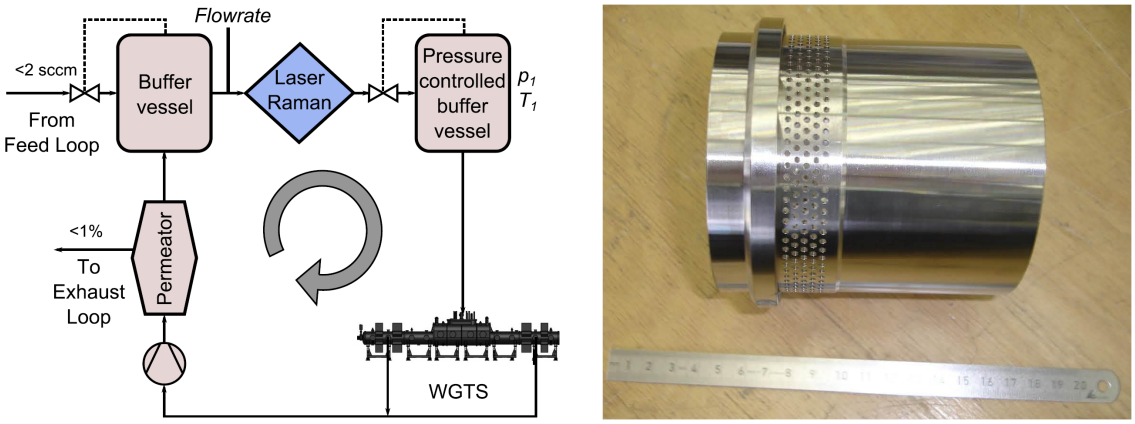

Figure 3.2: **a) Scheme of the inner loop from [60].** It shows the circulation of tritium from the buffer vessel (upper left) through the Laser Raman cell where the purity is determined to the pressure controlled buffer vessel (upper right). A temperature stabilized transfer line is used to insert the tritium into the WGTS beam tube. The tritium that is pumped out is collected and passes a permeator that blocks impurities. **b) Photo of the inner part of the tritium injection chamber [70].** The 415 holes have a diameter of 2 mm and avoid turbulences when injecting the tritium gas into the beam tube.

A major part of the inner loop system is the pressure controlled buffer vessel, operated at up to 20 mbar. From this vessel, a temperature controlled transfer line transports the tritium to the WGTS cryostat. The pipe enters the cryostat and is guided along 5 m of the 30 K beam tube to adapt its temperature until the tritium reaches the injection chamber. 415 holes with a diameter of 2 mm, arranged in 5 adjacent rings (see figure 3.2b) are used to insert the tritium to the beam tube. This concept works at small pressure gradients with reasonable tritium throughput without creating turbulences or severe density deviations [69]. In fact, due to the stabilized connection tube from the buffer vessel to the injection chamber, the pressure in the buffer vessel defines p_{in} and keeps it stable. The success of the stabilization is reported in [60]: Within 200 hours of operation the pressure inside the buffer vessel is kept at $p_{\mathrm{B}} = (15.024 \pm 0.002)$ mbar. Together with the temperature stabilized transfer line from the buffer vessel to the injection chamber, the performance of stabilizing p_{in} is better than the KATRIN requirements of 0.1%.

The pressure p_{ex} at the pumping chambers (figure 3.3) depends on the pumping efficiency of the turbomolecular pumps. The pumping speed is expected to be constant on the 10^{-4} level due to the constant rotation speed of the turbomolecular pump that is monitored. This will ensure that p_{ex} will meet the stability requirement [60].

The Laser Raman system

The tritium purity ε_{T} (see eq. (3.4)) is monitored by the Laser Raman System LARA. A cell between two buffer vessels of the inner loop system is passed by all tritium that is injected into the WGTS later. A laser irradiates the molecules, also producing Raman scattered light that is collected by an optical system and analysed by a spectrometer and recorded by a CCD [59]. Since Raman scattering depends on the molecule species due to their inherent ro-vibrational states, characteristic wavelength shifts between laser light and scattered photons can be used to distinguish between

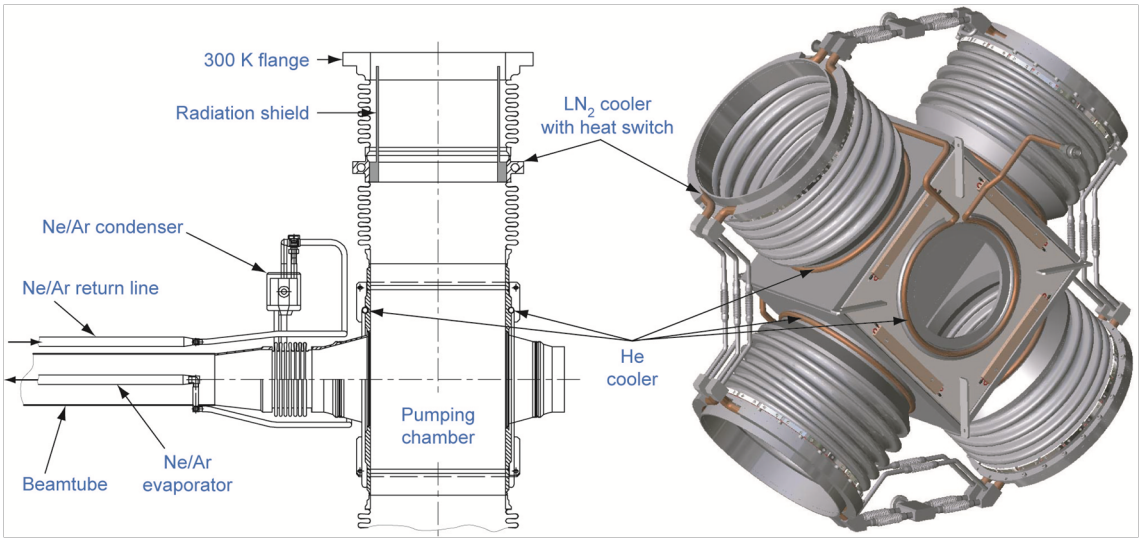

Figure 3.3: **Drawing of beam tube front end and CAD view of a pumping chamber.** A conical part connects the 10 m beam tube at 30 K and the pumping chamber. The inner box of the chamber is cooled by gaseous helium at 30 K. Towards the pump ports with turbomolecular pumps intermediate bellow coolers at liquid nitrogen level and a radiation shield are installed. This cooling cascade is needed to reduce the incoming thermal radiation from the pump ports that lasts on the beam tube.

different hydrogen isotopologues. The intensity of the Raman scattered light can be used to recognize changes in the tritium purity. In addition, absolute numbers for the amount of different hydrogen isotopologues in a gas mixture at KATRIN can be obtained with dedicated calibration efforts [71].

Intermediate results of the LARA performance are given in [60], stating a statistical uncertainty on the tritium purity of $\Delta\varepsilon_T/\varepsilon_T = 0.3\%$ within 250 s acquisition time for a measurement with low pressures. Extrapolating to KATRIN conditions yields the designated $\Delta\varepsilon_T/\varepsilon_T = 0.1\%$ within 60 seconds. Additionally, the status of efforts to determine absolute values of contributions from the different hydrogen isotopologues is stated as trueness of ε_T of $< 3\%$ [72].

Cooling concept

To achieve and keep a low temperature, the WGTS is a cryostat with its central part, the beam tube, operated at 30 K [73–75]. For this temperature range cryogenic helium is standard, but in section 3.2 it was shown that the system has to be stable on the 10^{-3} level. This is not possible for a conventionally cooled cryogenic system with dimensions of the WGTS. Therefore the two-phase neon system is used for cooling: A two-phase mixture is ideal to compensate heat influxes. Any heat entering the system is used to bring atoms from the liquid phase to the gaseous phase, keeping the temperature constant. The same is true for the reverse process; an external temperature drop leads to condensation instead of changing the temperature. Neon fulfils the two-phase condition in a temperature range around 30 K and a corresponding saturation pressure of $p_{sat} \approx 2$ bar [76]. At the WGTS, two small tubes with diameter $d = 16$ mm are brazed to the beam tube along the whole 10 m. They are filled partially with liquid neon, establishing a gas phase with pressure p_{sat}

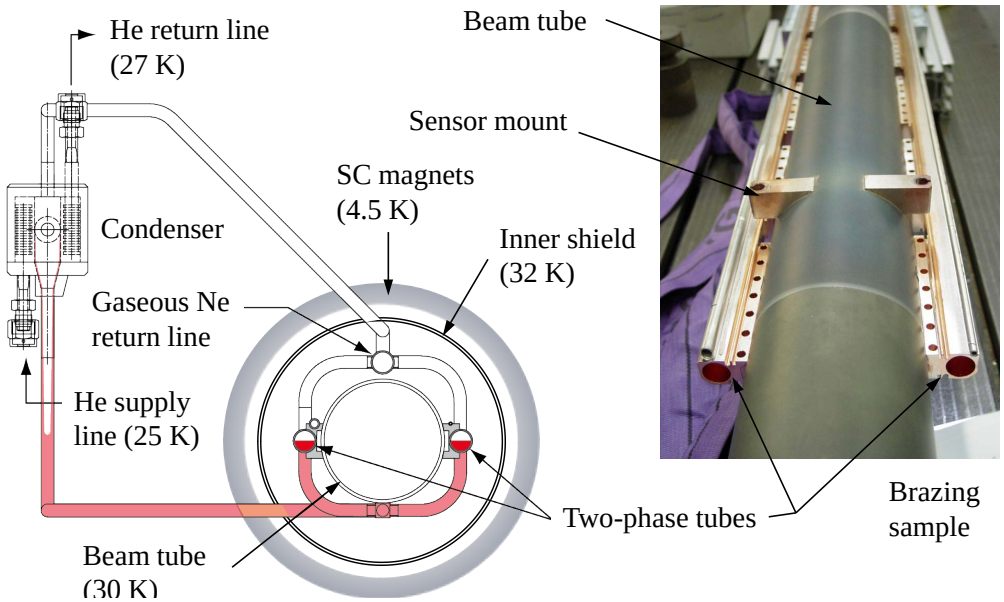

Figure 3.4: **The two-phase neon cooling principle of the WGTS.** The system works as a thermosiphon. If there is a heat influx, two-phase neon in the cooling tubes, which are braced to the beam tube on both sides along the whole 10 meters, will evaporate, but the temperature will remain constant. The gaseous neon then flows to the condenser, is cooled by helium from the cryogenic facility of KATRIN, is liquefied again and flows back to the neon tubes by gravity.

between 1 bar and 10 bar that can be adjusted to correspond to a temperature between 27 K and 33 K. The full system is shown in figure 3.4. It contains a condenser as heat exchanger that is cooled by gaseous helium at 25 K to liquefy the gaseous neon again and cool the beam tube.

The two-phase neon system is embedded into the overall cooling concept of the WGTS, depicted in figure 3.5. For different domains in the source, shields in between to separate them and different cooling liquids are used. The beam tube at 30 K, cooled by the two-phase neon system, is shielded by the inner shield, which is cooled by gaseous helium. This is necessary because the next layer are superconducting magnets (see below) at liquid helium temperatures of 4.5 K. The cryostat vessel, an insulating vacuum and an additional outer radiation shield at 77 K protect the inner parts against thermal radiation from the outside at room temperature. For the special cooling cascade of the pumping chambers please see figure 3.3. To avoid heat conduction crucial parts of the WGTS are suspended. Thin stainless steel wires hold the beam tube (see figure 3.6) and other parts of the source, completing the sophisticated WGTS cooling concept.

Magnetic field

As shown in section 3.1, a magnetic field is needed to adiabatically guide the created β-electrons along the magnetic field lines to the spectrometer for energy analysis. The field should be homogeneous to ensure equal starting conditions for all electrons.

The choice at KATRIN is superconducting solenoids, which create a constant, homogeneous magnetic field of $B_S = 3.6\,\mathrm{T}$. In the WGTS three main modules with a

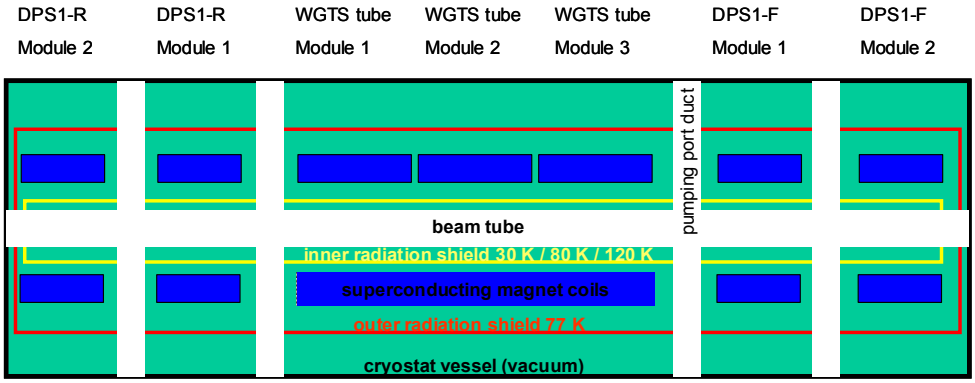

Figure 3.5: **Magnet layout and shielding concept of the WGTS [77].** The central part of the WGTS contains three main solenoids with 3.3 m length each and two smaller correction coils (not shown in the scheme) to avoid strongly reduced fields at the gaps between the main modules. Each part of the DPS1-R and DPS1-F has a 1 m solenoid, again with correction coils to transport the magnetic flux through the pumping chambers. Superconductivity requires liquid helium temperature of 4 K for the magnets. Therefore, the 30 K beam tube is separated from the magnets by an inner radiation shield cooled by 30 K gaseous helium. 85 K are realized at the last parts of the DPS1-R and DPS1-F, and 120 K would be needed for the special calibration mode, the krypton mode (see appendix A). To the outside part of the cryostat an outer radiation shield at 80 K cooled by gaseous and liquid nitrogen and the cryostat vessel protect the magnets and the beam tube from the ambient environment.

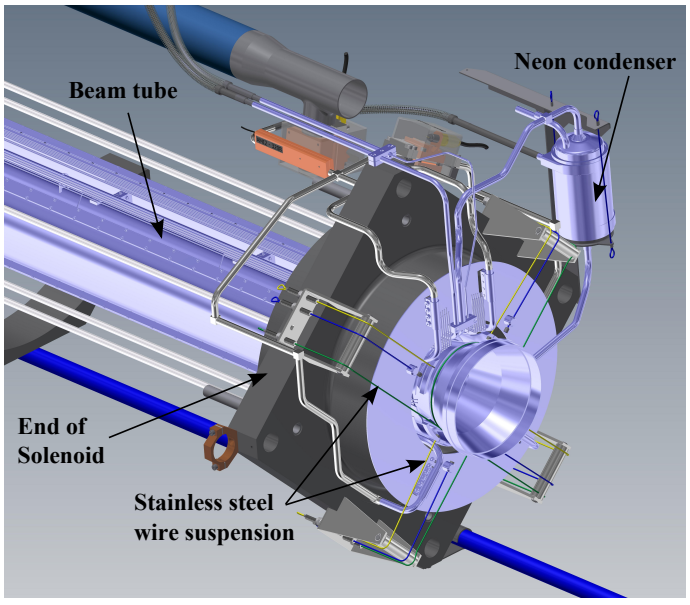

Figure 3.6: **Stainless steel wire suspension of the beam tube.** Adjustable wires (yellow, green, blue) hold the beam tube ends relative to the solenoids, minimizing heat conduction. Additional suspensions near the beam tube center avoid significant sagging.

length of 3.3 m are used. Each main solenoid has one correction coil with increased diameter at each end to compensate for the magnetic field drop at the gap between different modules. The remaining drop between the main modules is <1.5%. This concept is repeated at the DPS1-R and DPS1-F, which both have a 1 m solenoid and correction coils. The DPS1-R solenoids are operated at 3.6 T like the central beam tube magnets to form the magnetic field on its way to the rear section (see section 2.6), whereas the DPS1-F has a field of 5.0 T that then continues in the transport section[3] (see section 2.3).

Due to problems with the superconducting magnets of the DPS2-F, the operating mode of the WGTS magnets was also changed: Instead of the foreseen persistent mode, the magnets will be operated in driven-mode. "Air-cooled ultra stabilized power supplies"' [78] will be connected permanently to the magnets to ensure stable currents and thereby magnetic field strengths. Additionally, the quench-detection system will be improved [78].

3.4 The demonstrator test experiment

The demonstrator test experiment (figure 3.7) is performed to test crucial properties of the WGTS. Its main goal is to test the beam tube cooling system, the two-phase neon system (see section 3.3). This cooling technique has never been used before on a large scale like the WGTS. Section 3.2 showed that there are strict requirements on the temperature stability, so a dedicated test is appropriate to prove the functionality or refine the design. In addition, the whole cooling concept is tested, including the cooling of the pumping chambers, the shields and the cryostat itself. Since the WGTS is one of the most important parts of KATRIN, the demonstrator test reduces risks. It is an acceptance test of the mechanical and thermomechanical integrity [79]. The demonstrator tests started in autumn 2010 and were finished in December 2011.

Demonstrator components

An important feature of the demonstrator is its components: They are mainly original components that are also used later, when converting the demonstrator to the WGTS. The original central 10 m part of the WGTS beam tube and the first attached pumping chambers are tested at the demonstrator. This defines the total length of 12 m of the test cryostat. The demonstrator vessel is also built from original parts, namely the end parts of the WGTS vessel; the characteristic WGTS central dome is not needed. All transfer lines that will enter the WGTS there temporarily enter the demonstrator at unused pump ports.

To test the cooling principle at the demonstrator no magnets are needed. They are replaced by an equivalent dummy cold mass, made of aluminium, cooled by cryocoolers on the 4.5 K level. This mock-up simulates the thermal behaviour of the superconducting solenoids in the LHe baths at the WGTS later. It allows to test the functionality of the inner shield to protect the beam tube from the 4.5 K magnets and vice versa.

[3] Original design value was 5.6 T. Due to insufficient performance of the DPS2-F solenoids, the magnetic field in the DPS2-F will be reduced to 5.0 T. The DPS1-F will follow to match the DPS2-F.

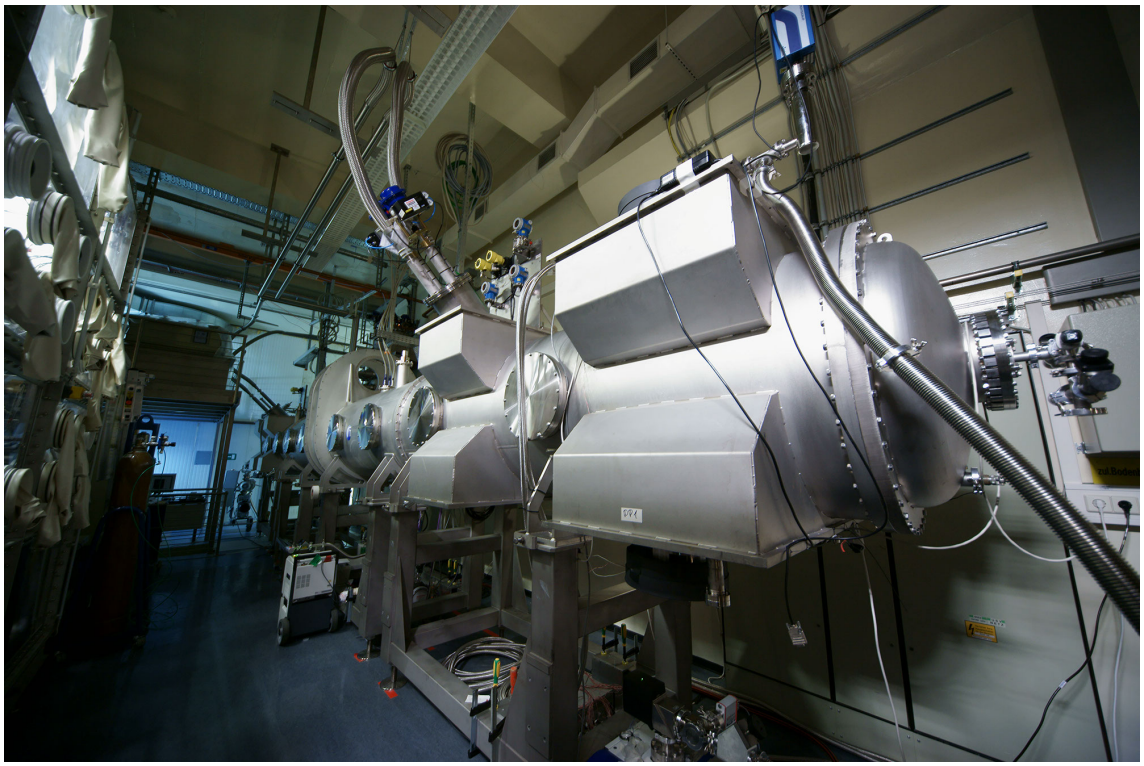

Figure 3.7: **The demonstrator test experiment.** The tests are performed inside the Tritium Laboratory Karlsruhe at KIT.

Since there is no need for gas circulation at the demonstrator, the whole test is executed without any tritium. No turbomolecular pumps are installed at the pump ports; only a few other pumps are needed to maintain the insulating vacuum. To simulate the additional thermal radiation from the pumps that are operated later in strong magnetic fields of the WGTS and reach temperatures more than 60°C due to eddy currents [80], electrical heaters are installed on top of the pump port blank flanges. These heaters are only operated during dedicated measurements to determine the effects of additional heat load on the stability of the system.

The cooling liquids and pipes that are used at the demonstrator will also be used at the WGTS with slight modifications as well as the KATRIN refrigerating plant: The beam tube is cooled by the 30 K two-phase neon system (see section 3.3). The neon condenser and the inner shield are cooled by gaseous helium at around 30 K as well as the inner part of the pumping chambers. The outer shield and the outer parts of the pumping chamber including their radiation shields are cooled by liquid and gaseous nitrogen (see figure B.1 in the appendix for details).

Temperature sensors

The sensors used to measure temperatures at the demonstrator are mostly original sensors of the WGTS. On the beam tube 24 metallic resistance thermometers (Pt500 sensors) are used to continuously measure the temperature. Their characteristics and measurement uncertainties are discussed in [75] stating a total uncertainty of 0.125 K @30 K. This mainly arises from the strong magnetic field dependence of a resistance measurement. It prevents from reliable and precise temperature monitoring on the 30 mK level that is required by KATRIN. Therefore, 24 vapour pressure

sensors (VPS) are used additionally. Partially filled with neon, the measured saturation pressure can be converted to temperatures using a vapour pressure chart [76]. In [75] is shown again that the uncertainty of such a VPS is only 4 mK @30 K, since this measurement is insensitive to magnetic fields. A disadvantage of the VPS is that it cannot be used continuously during several days of KATRIN measurements, since the filling level of the sensors may vary [75]. Therefore the reliable, but imprecise Pt500 sensors are calibrated in-situ (see appendix C) by an adjacent, very precise VPS between KATRIN measurement intervals, reducing the uncertainty of the temperature measurement to 4 mK. This is sufficient to continuously monitor the temperature for its required stability of $\Delta T_{\mathrm{stab}} < 30\,\mathrm{mK}$ (see section 3.2) until the next calibration cycle.

To get a spatial temperature distribution of the source, the 24 sensor pairs – a Pt500 sensor and a VPS – are distributed over the beam tube as shown in figure 3.8. The largest temperature fluctuations are expected near both beam tube exits, so the sensors are concentrated on the last 0.5 m near each end; in the central part only few sensors measure in larger distances. Most sensors pairs are mounted either on top (90°) or on bottom (270°) of the beam tube – here again the sensors have mirrored sensors with identical longitudinal positions – while the two-phase tubes are brazed to the beam tube on 0° and 180° (see figure 3.9). It is expected to see the largest temperature fluctuations on top and bottom of the beam tube, where the sensors are located. To examine the azimuthal temperature distribution along the beam tube wall, in total 4 sensor pairs are mounted at a 45° respectively 225° angle.

In the demonstrator as well as in the WGTS, the Pt500 sensors and the VPS are controlled by a dedicated temperature acquisition system. It allows to read out all beam tube Pt500 sensors in a 5 second cycle and to calibrate them with the VPS (see appendix C).

Expectations on the demonstrator tests

Regarding important key characteristics, the demonstrator tests will determine, if the requirements on the temperature stability of $\Delta T_{\mathrm{stab}} < 30\,\mathrm{mK/h}$ and the temperature homogeneity of $\Delta T_{\mathrm{hom}} < 30\,\mathrm{mK}$ (see section 3.2) can be achieved.

Simulations of the temperature stability in [74] examined the performance of the neon condenser and the beam tube temperature behaviour. A result is shown in figure 3.10a, expecting to meet the requirements.

Expectations on the temperature homogeneity are motivated by figure 3.10b. At the demonstrator, the pump ports remain on room temperature first, causing thermal radiation. Due to the special pumping chamber geometry, only the end parts of the beam tube can be hit by photons, increasing the heat load there and creating a longitudinal temperature profile. Dedicated heat load measurements with heated pump ports have been performed during the demonstrator measurements to simulate turbomolecular pumps in strong magnetic fields. An increased heat influx is expected that results in an intensified longitudinal temperature profile and possibly larger temperature fluctuations. The results of the demonstrator measurements are presented and discussed in detail in chapter 9.

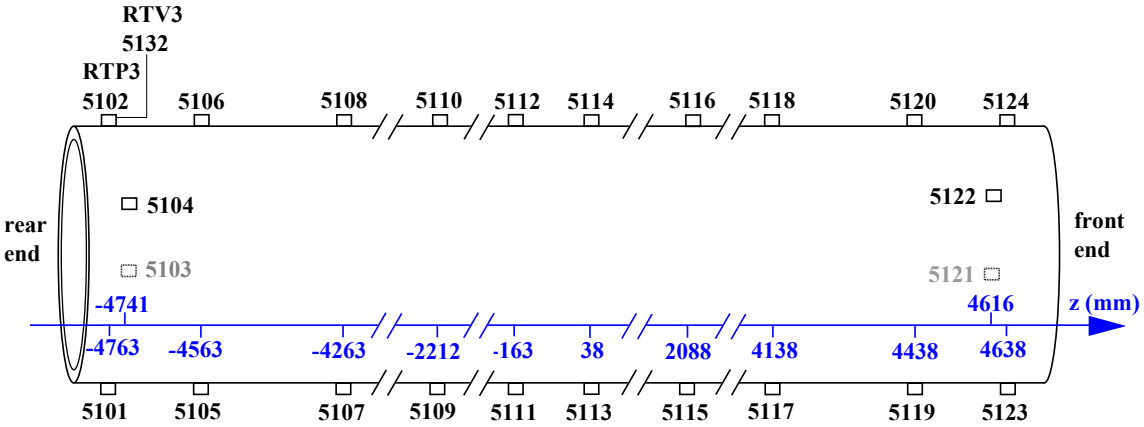

Figure 3.8: **Positions of the temperature sensors at the demonstrator beam tube (not to scale).** The sensors are concentrated at the ends, to measure a longitudinal temperature gradient. At each denoted position a pair of sensors is measuring: A Pt500 sensor (RTP-3-5101 to 5124) and a vapour pressure sensor (RTV-3-5131 to 5154, not shown). Odd numbered sensors measure at the bottom except for sensor pairs 5103/5133 and 5121/5151 that are located on the side of the beam tube. Even numbered sensors measure at the top with sensor pairs 5104/5134 and 5122/5152 again at a different azimuthal position (see also figure 3.9). The positions are given relative to the origin of the CAD model that is shifted by 62.5 mm from the geometrical center of the WGTS due to the dimensions of the injection chamber.

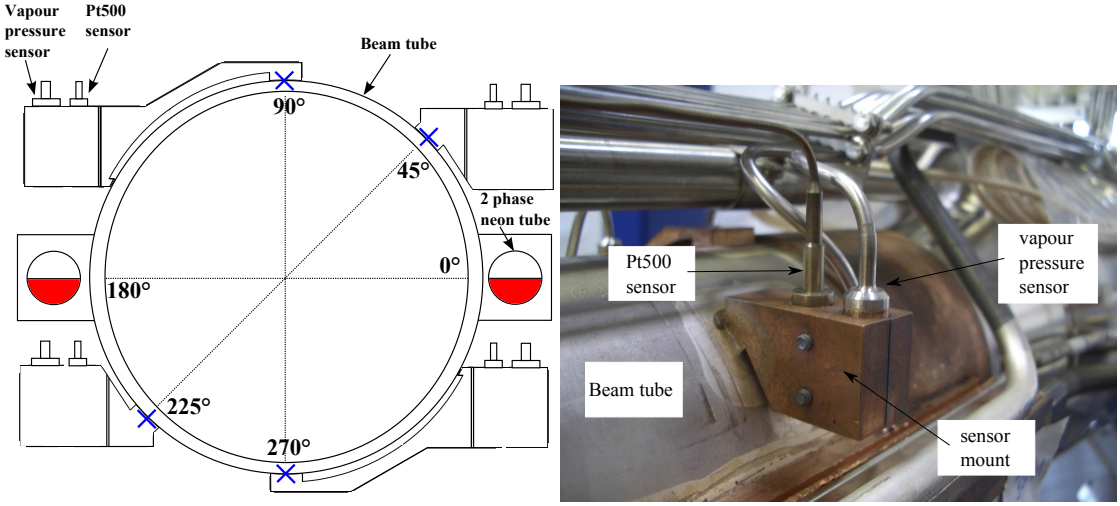

Figure 3.9: **a) Azimuthal positioning of the beam tube temperature sensors (not to scale).** Looking from the rear end of the source, this sensor layout can be observed. Twenty sensor pairs, mounted by a common sensor holder, measure on top (even sensor numbers) or on the bottom (odd sensor numbers) of the tube. A total of four sensor pairs measure at a 45° respectively 225° angle. The measurement positions are highlighted by a blue cross, all other parts of the sensor holders are not connected to the beam tube.
b) Sensor mounting. One of the sensor holders at 45°, containing a Pt500 sensor and a vapour pressure sensor, is brazed to the beam tube. Connection lines for readout of the Pt500 and for pressure measurements of the VPS are also visible. They are collimated at the top and guided out of the source at the front end.

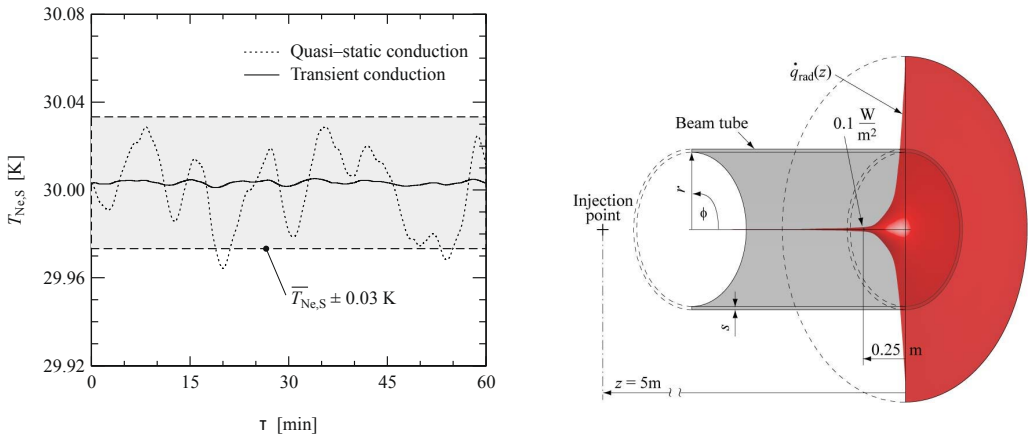

Figure 3.10: **a) Simulations of the neon respectively the beam tube temperature stability from [74].** The neon saturation temperature was simulated using two different heat conduction models for the neon condenser with measured fluctuations of 0.3 K of the helium to cool the condenser. The maximum deviations in the model with transient conduction are ±2 mK.
b) Expected thermal radiation from the pump ports on the beam tube from [74]. Warm pump ports at room temperature or above emit photons that may hit the beam tube inner surface near its end. Requirements on this heat influx are set by a requested temperature homogeneity of ±30 mK at the inner 9.5 m of the beam tube. View-factor considerations yield a maximal heat influx of 0.1 W/m^2 at 0.25 m distance from the beam tube end and a maximal overall thermal heat load of 0.25 W [74].

4. Simulations of the tritium source

Since many systematic uncertainties on the measured neutrino mass occur due to uncertainties of source parameters (see section 3.2), understanding the tritium source in all its aspects is necessary. For this reason, dedicated measurements and analyses of source properties are performed in advance and during the KATRIN measurements. This has to be supported by detailed simulations of the source, on the one hand to understand the processes itself and on the other hand to determine their influence on the neutrino mass analysis. These simulations must include the full description of hydrodynamical gas simulations, electro-magnetic particle tracking and particle interactions within a detailed 3D-geometry.

For this purpose, the general KATRIN simulation package Kassiopeia is introduced in section 4.1. This work at hand has significantly contributed to the source simulations in section 4.2. The conceptual aspects like the voxelization and the spectrum calculation are presented in sections 4.2.1-4.2.4. Finally, in section 4.2.5, the significant improvement for the description of the crucial physical processes like the Doppler effect and the final state distribution is presented.

4.1 Simulation framework Kassiopeia

The KATRIN experiment as a whole is a complex system with several subcomponents (see chapter 2), each with different tasks and various physical processes connected with it. For example, the key parameter column density of the WGTS is described by macroscopic simulations of gas dynamics of injected and pumped tritium molecules. On the other hand, a description of the tritium β-spectrum is needed, since that is measured by KATRIN. These are completely different processes and both are needed to describe the source. Going even further, the transport section and the spectrometers deal with electron transport in electric and magnetic fields. Finally, at the detector, interactions of electron with matter happen. Again, these processes are versatile; there are different specialized models to describe them, known from theory and experiments. Simulations at KATRIN reach from Monte-Carlo simulations of single particles to macroscopic simulations for example of the whole source system.

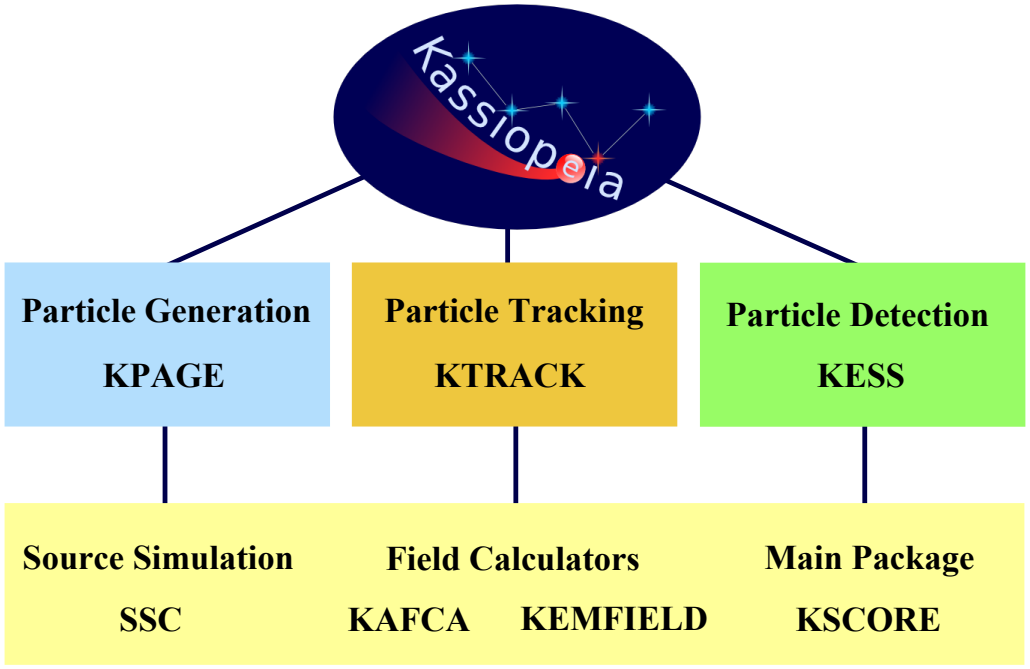

Figure 4.1: **The KATRIN Monte-Carlo simulation software Kassiopeia.** Kassiopeia can be divided into three main modules: The particle generation, the particle tracking and the particle detection. The responsible module names are given as well and are described in the text. Further components of Kassiopeia are the Source Simulation and the Field Calculators, which are used in various parts. A general part, the KSCore, is responsible for a unified program structure, connecting all modules.

For a long time, specialized small program packages for the different processes in KATRIN have been used, either available software adapted to KATRIN conditions or newly developed, highly specialized code. In fact, this was successful and sufficient for some time. But then, connections between the different programs were requested. For example one wanted to execute a Monte-Carlo simulation: Generate a large number of particles in the source, follow their trajectory through the whole experiment and investigate their events on the detector. This was possible with some efforts to pass results from one simulation module to the other, but it was very inconvenient and error-prone. Therefore, in spring 2010 the KATRIN software developers decided to merge all existing (Monte-Carlo) simulation software to the new package Kassiopeia [81]. Within this framework, the different modules can communicate. The user of Kassiopeia can deal with a unified system to initialize and execute the simulation as well as interpret the results. The code is written in C++ and developed and supported for Linux and Mac OS. Kassiopeia is planned to be accessible to people outside the KATRIN collaboration. Its dependencies are only program libraries that can be used free of charge.

The structure of Kassiopeia and its modular design is shown in figure 4.1. The various modules are briefly introduced in the following:

Particle Generator KPAGE

The KATRIN Particle Generator KPAGE is responsible for the event generation of Monte-Carlo simulations. The configuration of a generator is modular [82], the user assembles different parts of the generator:

- **The particles' type and properties.** Each generator typically generates particles of a certain type, for examples electrons or ions. For the simulation, the generated particles are defined by their charge and mass that are needed to calculate the particles' trajectories later.

- **The starting positions.** Particles can be emitted from a "point" source like the tip of an electron gun, from a surface like background electrons generated at the spectrometer walls or inside a volume like β-electrons in the WGTS. In the latter case, the density distribution of molecules in the source, provided by the module SSC (see section 4.2), is used to randomly start electrons according to this distribution.

- **The energy distribution.** The user can define the energy spectrum of the particles to be generated. For KATRIN, electrons from the tritium β-decay are created according to the β-spectrum provided by SSC (see section 4.2). Other tasks are to generate electrons from an electron gun with a Gaussian energy distribution or fixed energies that can be used for test purposes.

- **The angular distribution.** The particles' initial direction can be isotropically distributed like in a β-decay or can have a preferred direction like for an electron gun that emits electrons in a very narrow solid angle. Arbitrary angular distributions can be defined, even allowing for energy-direction dependencies [82].

- **The timing distribution.** For special simulations, timing information can be important. KPAGE allows the user to define life times of a decay or dedicated time distributions.

Particle Tracking KTRACK

Having generated charged particles with KPAGE, these particles propagate due to their initial conditions and present electric and magnetic fields in the experiment. This is the task of the KATRIN Tracking module KTRACK. It numerically solves the Lorentz equation of motion to describe the trajectories of a charged particle in vacuum inside electric and magnetic fields. Details on these methods can be found in [83]. Features during tracking that are important for this work on hand are the description of scattering processes with elastic and inelastic cross sections from [84–87] and synchrotron radiation as energy losses. The tracking can be executed with different level of detail, for example tracking the particles adiabatically along the magnetic field lines or using the most accurate tracking that considers the cyclotron motion of the particle around the field lines.

Particle Detection KESS

Particles entering the silicon of the detector (see section 2.5) switch the responsible simulation code from KTRACK that was used for tracking in vacuum to the KATRIN Electron Scattering in Silicon KESS module [88]. This newly developed simulation code tracks electrons in silicon simulating their energy deposition there. It also considers effects of back-scattered electrons and the behaviour inside the detector dead layer. The description of the required elastic and inelastic double differential cross sections has been optimized for electrons from 1-30 keV.

Source Simulation SSC

The Source Spectrum Calculation SSC [82], [89] contains descriptions of all physical processes of the source. Its features are explained in detail in section 4.2; here only its contribution to the particle generation and tracking is highlighted: SSC provides a detailed description of the β-spectrum, containing radiative corrections, the final state distribution and the Doppler broadening (all in section 4.2.3). It can be used as energy distribution to generate β-electrons with KPAGE (see above). In addition, to randomly choose the starting positions of electrons in the WGTS, the density profile can be used as input for a random number generator. The same information on the density is also used during tracking with KTRACK (see above) to account for scattering of electrons on T_2 molecules in the source.

Field Calculators KAFCA and KEMFIELD

Kassiopeia includes two modules KAFCA [83] and KEMFIELD [90] that can both calculate electric as well as magnetic fields. They provide various field calculation methods for different, specialized tasks, for example axially symmetric fields or fields of complicated geometries like wire electrodes of the spectrometer. The user can choose appropriate methods depending on his tasks and use them by a unified interface, independent of the underlying field calculator.

Main package KSCore

The general part of the Kassiopeia code is called KSCore [81]. It contains classes that are used by several other modules like common physical constants or random number generators. It also provides routines to initialize the different modules in a unified way by configuration text files. Other important parts are the sophisticated geometry system for various tasks and a management system that connects the different modules and allows to run them, communicating with each other.

4.2 Source Spectrum Calculations SSC

Simulations of the WGTS are needed for the Monte-Carlo simulation Kassiopeia as described above to generate electrons according to the tritium β-spectrum and according to a density distribution in the source. The developed Source Spectrum Calculation SSC [82], [89] contains these features. In a unified program structure all available models to describe the source from spectrum calculation to gas dynamics are combined to give a complete, detailed simulation of the KATRIN WGTS.

Although the focus is on the source, SSC allows going beyond the border of the WGTS, including a spectrometer and detector response, finally calculating the integrated β-spectrum that KATRIN will be measuring. This is no Monte-Carlo simulation, just numerical integration of the differential spectrum, considering the detailed model of the WGTS and general models for other parts of KATRIN. Together with analysis and fitting algorithms (see chapter 6) this allows investigating the influence of parameters – especially source parameters – on the neutrino mass determination. To do so, SSC with its components is explained in the following, in sections 4.2.1-4.2.4 the status of the program at the end of the work [89] in 2009, then its extensions and modifications in section 4.2.5.

4.2.1 Main concept: "Voxelization"

Previous simulations of the WGTS treated it as a totally homogeneous system. The source indeed is homogeneous to a certain degree, but especially along the 10 m of the beam tube small inhomogeneities are inevitable as can be seen in the discussion of the magnetic field or the gas dynamics in the following. Therefore, in a detailed model the source is divided into small volumes, so-called voxels. Local physical properties like the density, temperature or magnetic field strength, provided by a model for the specific source parameter, can then be assigned separately to each voxel.

To do this "voxelization", a division of the 10 m beam tube in small slices is useful to account for longitudinal inhomogeneities. The degree of segmentation depends on the parameter profile, but 1000 slices of equal length, that means 1 cm per slice, seemed sufficient for most investigations so far. In general, the program is flexible to allow for special segmentations with fine slices in regions of severe inhomogeneities, for example near the pumping chambers, and large slices for homogeneous parts of the source in the centre.

Each slice can then be divided in radial and azimuthal direction creating a ring structure, each with several segments (see figure 4.2), the voxel structure. This cylindrical division is based on the detector segmentation, so that the source voxels are mapped to specific detector pixels. During KATRIN measurements, the measured spectra recorded by different detector pixels can be compared with rates calculated by SSC. This is useful to understand radial inhomogeneities like the additional gas flow bulk-velocity (see section 5.1) or azimuthal asymmetries like an azimuthal temperature gradient of the beam tube (see temperature profile in the following) and its implications on the density profile.

Classes implementing this voxelization concept in SSC are `SSCSlice`, `SSCRing` and `SSCSegment`. The overall WGTS is described by a vector of objects of type `SSCSlice`. For many simulations, this longitudinal division is sufficient to account for source inhomogeneities. If further divisions are needed, each slice can be divided radially due to the cylindrical structure into a vector of rings, objects of type `SSCRing`. Finally, each ring can be divided in a vector of objects of type `SSCSegment`. These segments have access to its dimensions and all physical properties like density and field strengths stored individually, corresponding to the voxel structure described above.

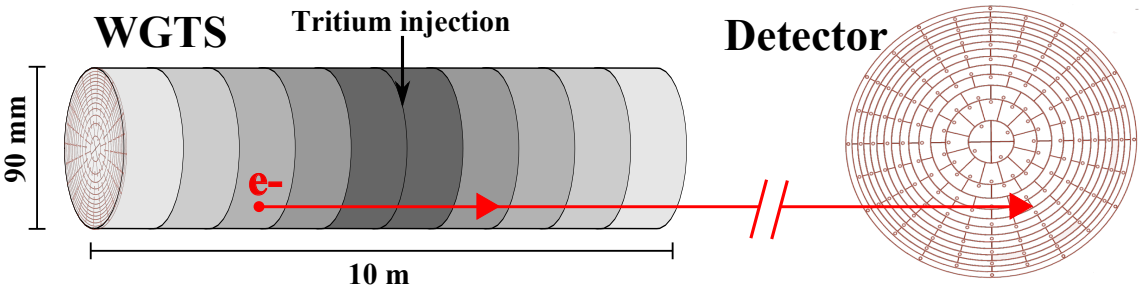

Figure 4.2: **Schematic "voxelization" of the WGTS.** The 10 m beam tube is divided into longitudinal slices to account for inhomogeneities of the density, temperature and magnetic field. Each slice can then be divided into rings and segments, creating a "voxel" structure. The segmentation of the source is chosen here to fit the detector with its 12 rings, each containing 12 coextensive segments. Electrons emerging from certain parts of the source contribute to the events hitting a corresponding segment of the detector.

Magnetic field

The magnetic field in the WGTS is needed to guide the produced β-electrons from the source to the spectrometers. It has several influences on the measurement and needs to be considered in SSC:

- The source field strength B_S together with other magnetic fields in the spectrometer and at the detector determines which part of the source is mapped to the detector. Using eq. (2.4) with nominal strength $B_S = 3.6\,\mathrm{T}$, this results in an effective source area $A_{S,\mathrm{eff}} = 53.1\,\mathrm{cm}^2$ and a radius of $r_{S,\mathrm{eff}} = 4.1\,\mathrm{cm}$.

- Using a MAC-E filter, eq. (2.2) defines the maximal opening angle $\theta_{\max}$. If the magnetic field is axially symmetric, but longitudinally inhomogeneous (see figure 4.3), $\theta_{\max}$ will depend on the longitudinal position z. Electrons from different parts of the source experience different starting conditions, modifying the total spectrum. Mean scattering probabilities P_i (eq. (4.8)) are also influenced by $\theta_{\max}$, since averaging over all electrons contributing to the signal requires integration up to $\theta_{\max}$.

- The amount of synchrotron radiation[1] E_{syn}, that a charged particle emits, depends on the magnetic field strength B, on the particle's energy $E_\perp$ transversal to the field and also on the time t (respectively path length) it moves in the field (non-relativistic approximation) [48]

$$E_{\mathrm{syn}} = 0.4 E_\perp B^2 t. \tag{4.1}$$

  The path length itself also depends on B_S, since higher B_S increases the cyclotron motion, creating longer path lengths. This effect again influences the scattering probabilities P_i (see eq. (4.6)).

[1] Energy losses due to synchrotron radiation have not yet been included in calculations of SSC.

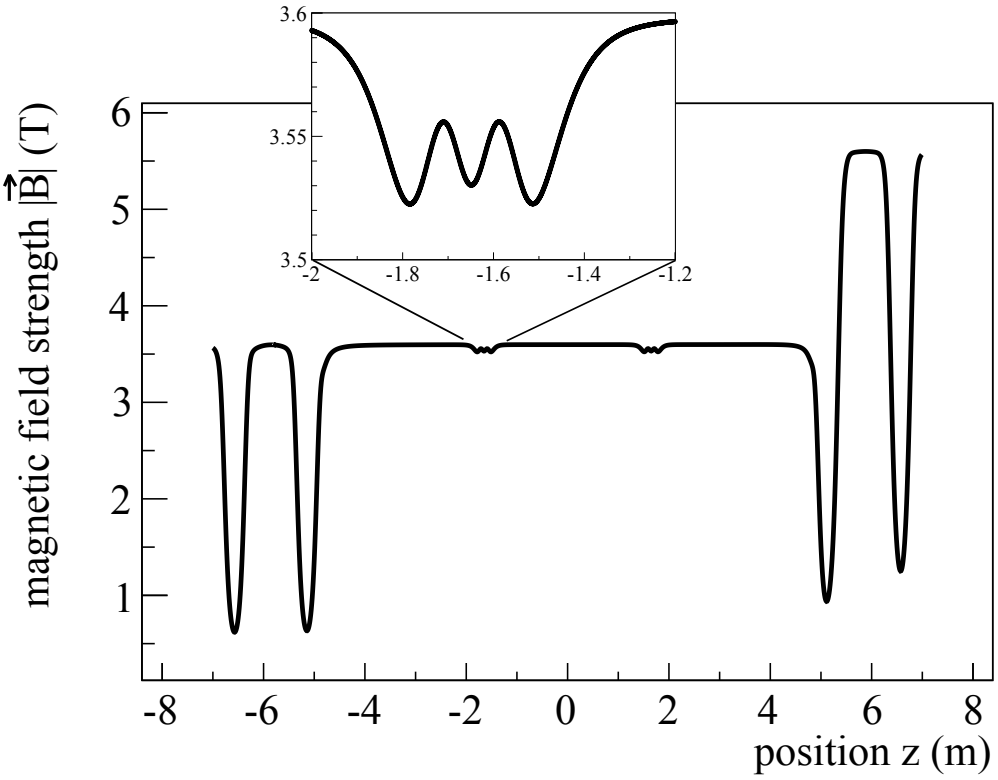

Figure 4.3: **Magnetic field strength in the WGTS.** The field in the central part is provided by three solenoids with a nominal strength of 3.6 T. The behaviour shown in the inset is due to attached correction coils in between that avoid a severe drop of the field strength. The large drop of the field at ±5 m and ±6.5 m is due to the gap, where the pumping chambers are installed.

The magnetic field in SSC is provided by one of Kassiopeia's field calculators, which the user can choose. Then, for every source voxel j the magnetic field strength B_{S}^{j} is calculated and stored, defining $\theta_{\mathrm{max}}^{j}$ and P_{i}^{j}.

Density profile

Injecting tritium gas in the WGTS centre and pumping at the beam tube ends will create a density profile. For that purpose, dedicated gas dynamics simulations have been developed and will be summarized in chapter 5. In general, any information on the density distribution can be used with SSC. The density for each source voxel can be set according to the underlying density calculator. Then the density can be used to

- provide density information for the Monte-Carlo simulations when generating particles or when considering scattering of electrons on T_2 molecules (see section 4.1).
- correctly calculate scattering probabilities (see section 4.2.2).
- account for the number of molecules, respectively the activity of each voxel and its contribution to the total KATRIN spectrum (see section 4.2.4).

The present implementation in SSC consists of a base class `SSCDensityBase` with a general method `GetDensity(TVector3& r)`[2] to obtain the density at position $\vec{r}$. Special derived classes provide access to existing gas dynamics simulations in chapter 5, for example `SSCDensityAsymmetric` that uses a fit to a calculated one-dimensional density profile (see eq. (5.13)) or `SSCDensity3DSharipov` that uses the present pseudo-3D calculations described in section 5.3.

The velocity profile of molecules is closely connected to the density profile and will be discussed in section 4.2.5.2 as an extension of SSC.

Temperature profile

The temperature of the beam tube directly influences the density distribution in the WGTS (see chapter 5), thus considering the temperature in a source simulation is inevitable. Since these density calculations usually are performed in dedicated programs outside SSC, a detailed temperature model in SSC is not needed at first sight. But there is another influence of the beam tube temperature: It defines the thermal movement of the T_2 molecules and therefore the Doppler broadening of emitted β-electrons. Setting the temperature for each source voxel in SSC, the Doppler effect can be handled correctly for electrons emerging from different parts of the source (see section 4.2.5.4).

A base class `SSCTemperatureBase` has been implemented. In conformity with the density profile, a method `GetTemperature(TVector3& r)` returns the temperature at position $\vec{r}$. Special temperature profiles are already predefined or can easily be added by the user. At the moment, the most suitable one is `SSCTemperatureAsymmetric` based on the demonstrator measurements (see section 9.4). By this kind of implementation, it will be straight forward to obtain the temperature profile determined by the measuring sensors during WGTS measurements later.

4.2.2 Response function

The response function comprises effects of the experimental setup of KATRIN that modify the measured integrated β-spectrum. It convolutes energy losses due to inelastic scattering of β-electrons on tritium molecules in the source and the transmission properties of the KATRIN main spectrometer.

Energy loss function

KATRIN is designed to avoid energy losses of signal β-electrons, using a windowless source and adiabatic guidance of electrons. If any energy loss cannot be avoided, these losses will have to be known precisely and will be included in the neutrino mass analysis. Inelastic scattering of electrons on T_2 molecules is one of these energy losses. It depends on the inelastic scattering cross section σ_{inel} and the detailed energy loss function $f(\epsilon)$, normalized and related to the differential cross section by

$$f(\epsilon) = \frac{1}{\sigma_{\text{inel}}} \frac{\mathrm{d}\sigma}{\mathrm{d}\epsilon} \tag{4.2}$$

$$\int_0^\infty f(\epsilon)\mathrm{d}\epsilon = 1 \tag{4.3}$$

[2] TVector3 is a vector with three components, provided by ROOT [91].

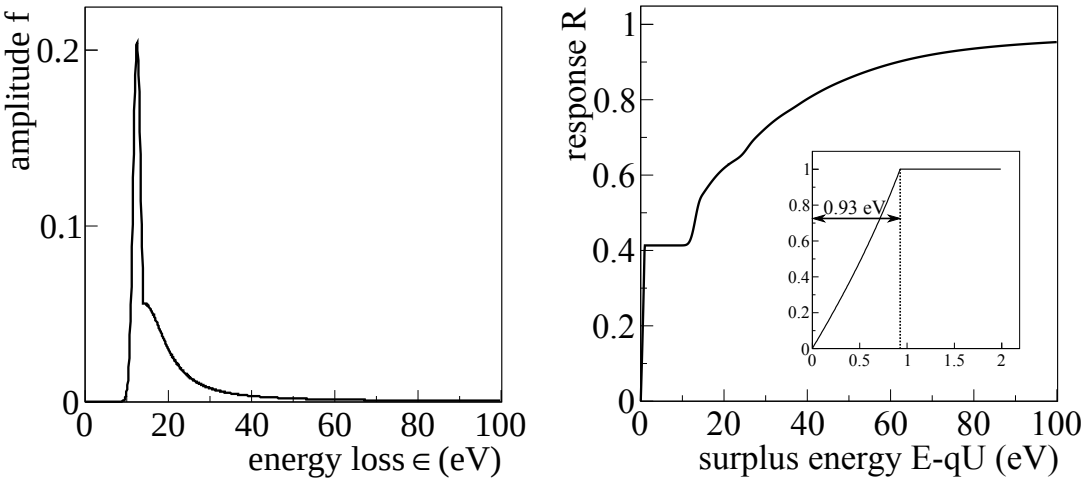

Figure 4.4: **a) Energy loss function of electrons scattering on gaseous T_2.** The distribution was measured in [92]. A prominent feature is that inelastic scattering implies an energy loss of at least 10 eV.
b) KATRIN response function and spectrometer transmission function (inset). The response function is drawn for a fixed electron energy of $E = 18.6\,\mathrm{eV}$, varying the retarding potential energy qU. The other parameters here were chosen for the WGTS that means $P_0 = 0.41$ as can be seen from the plateau between 1 and 10 eV and a spectrometer energy resolution of 0.93 eV.

Both quantities have been determined in a measurement [92] for electrons scattering on gaseous T_2 with results

$$\sigma_{\mathrm{inel}} = (3.40 \pm 0.07) \cdot 10^{-18}\,\mathrm{cm}^2 \tag{4.4}$$

and

$$f(\varepsilon) = \begin{cases} A_1 \exp\left(-\frac{2(\epsilon-\epsilon_1)^2}{\omega_1^2}\right) & \text{for } \epsilon < \epsilon_c \\ A_2 \frac{\omega_2^2}{\omega_2^2+4(\epsilon-\epsilon_2)^2} & \text{for } \epsilon \geq \epsilon_c \end{cases} \tag{4.5}$$

with fitted parameters $A_1 = 0.204 \pm 0.001$, $\omega_1 = 1.85 \pm 0.02$, $A_2 = 0.0556 \pm 0.0003$, $\omega_2 = 12.5 \pm 0.1$ and $\epsilon_2 = 14.30 \pm 0.02$, using a fixed $\epsilon_1 = 12.6$. Additionally, $\epsilon_c = 14.09$ was chosen to obtain a continuous function. The function is shown in figure 4.4a. In this parameterisation, the Gaussian part describes the energy loss due to excitation, the Lorentzian part accounts for ionisation [92]. To obtain the energy loss of multiple inelastic scatterings, the function can be convoluted with itself, for example $(f \otimes f)(\epsilon)$ for a twofold scattering.

Eq. (4.4) states that the accuracy of σ_{inel} is only $\approx 2\%$ and the description of $f(\varepsilon)$ is quite coarse. To reach the planned KATRIN sensitivity, both quantities have to be known on the 10^{-3} level (see section 3.2), demanding for a new, dedicated measurement of the energy loss function at KATRIN: For different column densities in the WGTS, the response function (see below) is measured with the rear section electron gun (see section 2.6). Together with the transmission function and scattering probabilities (see the following sections), a deconvolution will give $f(\epsilon)$. Details on this procedure can be found in [93–95].

The implementation of $f(\epsilon)$ and σ_{inel} in SSC follows the usual way: A base class `SSCEloss` provides a function to obtain the probability f for an energy loss ϵ. This can then be specified by derived classes, at present the measured function of eq. (4.5) or later by a measurement and deconvolution of the energy loss function at KATRIN.

Scattering probabilities

To describe the complete energy losses in the WGTS, probabilities P_i for i-times inelastic scattering are needed next to the already discussed energy loss function. For an electron emitted at longitudinal position z in the WGTS under an angle θ relative to the magnetic field line, the P_i are Poisson-distributed [92]

$$P_i(z,\theta) = \exp\left(-\lambda(z,\theta)\cdot\sigma_{\text{inel}}\right)\frac{(\lambda(z,\theta)\cdot\sigma_{\text{inel}})^i}{i!}. \tag{4.6}$$

They are determined by the inelastic cross section σ_{inel} in eq. (4.4) and the number of tritium molecules or effective column density $\lambda(z,\theta)$ that an electron passes when leaving the source at $+L/2$ [92]

$$\lambda(z,\theta) = \frac{1}{\cos\theta}\int_{z}^{+L/2}\rho(z)\mathrm{d}z. \tag{4.7}$$

The factor $1/\cos\theta$ accounts for an increased path length of the electron due to its helix cyclotron motion in the source magnetic field. Radial and azimuthal inhomogeneities can be considered by treating λ as a function of r and ϕ, respectively the density as $\rho(r,\phi,z)$.

From eq. (4.6) and eq. (4.7) it is obvious that electrons from the rear side of the WGTS scatter more often – P_0 decreases – than electrons emitted from the front. Therefore, if the electrons' starting conditions differ throughout the WGTS, they influence the spectrum differently: Electrons from the front side of the WGTS are generally contributing stronger to the overall spectrum than those from the rear side.

To encompass different effects in few numbers, mean scattering probabilities P_i^{WGTS} can be calculated [96]

$$P_i^{\text{WGTS}} = \frac{1}{\rho d(1-\cos\theta_{\max})}\int_{-L/2}^{+L/2}\mathrm{d}z\int_{0}^{\theta_{\max}}\mathrm{d}\theta\ \rho(z)P_i(z,\theta)\sin\theta. \tag{4.8}$$

This is an average of the $P_i(z,\theta)$ in eq. (4.6) weighted with the density distribution, averaging over all possible emission angles[3] between 0 and $\theta_{\max}$. It should be noted that this method does not account for changes in angle during scattering. Currently, Monte-Carlo simulations that consider changes in angle are used to verify the P_i of eq. (4.8) [95].

Nevertheless, SSC can calculate the P_i^{WGTS} for given magnetic field and density profile, but it can do more: Like for all other physical properties, SSC can calculate

[3] Isotropic emission, therefore $\sin\theta$ enters the averaging.

and store the local scattering probabilities. For each voxel the probabilities are determined that electrons from this voxel scatter i-times when passing the molecules between their starting position and the spectrometer. This can be done by constraining the z-average in eq. (4.8) to the dimensions of the specific voxel $[z_1,\, z_2]$ and by replacing the θ-integration limits by the local $\theta_{\max}$. This procedure is more accurate than eq. (4.8), because it considers local inhomogeneities. It is a further step towards calculating the contribution of each voxel to the whole KATRIN spectrum.

Transmission function

The properties of a MAC-E filter (see section 2.4) can be summarized in a transmission function $T(E, qU)$. It states the probability that an electron with energy E can overcome the spectrometer retarding potential energy qU. An analytical formula for an isotropic source in derived in [48]

$$T(E,qU) = \begin{cases} 0 & E - qU \leq 0 \\ \frac{1-\sqrt{1-\frac{E-qU}{E}\frac{B_\mathrm{S}}{B_\mathrm{A}}}}{1-\sqrt{1-\frac{\Delta E}{E}\frac{B_\mathrm{S}}{B_\mathrm{A}}}} & 0 < E - qU \leq \Delta E \\ 1 & E - qU > \Delta E, \end{cases} \tag{4.9}$$

where B_S and B_A are the magnetic field strengths of the source and of the analysis plane of the main spectrometer. The energy resolution of the setup (see section 2.4) is denoted as ΔE. The inset of figure 4.4b shows the analytical transmission function. Strictly speaking, the transmission properties are not part of a source simulation. Nevertheless, SSC in the present status contains the analytical shape to calculate the response function that also contains inelastic scattering, clearly connected with the source. This is required to obtain a calculated integrated spectrum. In the future, the transmission function will be removed from the SSC package. It will remain accessible by dedicated code that can calculate realistic transmission functions from electric and magnetic fields [97] and that can actually use measured transmission functions during main spectrometer commissioning [98].

Response function

The response R is the probability that an electron with starting energy E overcomes the retarding potential energy qU when emitted in the WGTS, undergoing inelastic scattering with specific probabilities P_i, losing energy according to the energy loss function $f(\epsilon)$:

$$R(E,qU) = \int_0^E T(E-\epsilon, qU) \cdot (P_0\delta(\epsilon) + P_1 f(\epsilon) + P_2(f \otimes f)(\epsilon) + \cdots)\mathrm{d}\epsilon. \tag{4.10}$$

The shape for standard KATRIN parameters ($\rho d = 5 \cdot 10^{17}\,\mathrm{cm}^{-2}$ and $\Delta E = 0.93\,\mathrm{eV}$) is shown in figure 4.4b. Since the energy loss function, shown in figure 4.4a, is zero below 10 eV, the response function is flat for the first 10 eV, except for the steep rise of the transmission function within the first eV. The visible plateau corresponds to the probability of unscattered electrons $P_0 = 0.41$. Therefore, in the last 10 eV below the endpoint – the region that is most sensitive to the neutrino mass – the measured integrated spectrum of KATRIN is not influenced by scattering. Then

consecutively, when further lowering qU, electrons that have scattered once, twice and so on can pass and contribute to the spectrum.

Experimental influences on the spectrum, that means the response function, need to be understood and monitored precisely to avoid systematic effects on the neutrino mass analysis (see section 3.2). As said above, the energy loss function is determined at KATRIN by a preceding measurement of the response function with an electron gun (see section 2.6) and following deconvolution algorithms. Regarding monitoring, it is planned to use the electron gun between neutrino mass measurements, typically every two hours. Observed changes in the rates of inelastically scattered electrons indicate changes in the column density and allow adjusting the response function that is used for analysis of the following neutrino mass measurement.

In SSC, the voxelization concept provides all information to separately calculate the response function for each voxel j: The specific P_i^j, the magnetic field strengths B_S^j [4] and the universal energy loss function.

4.2.3 Differential β-spectrum

The differential β-spectrum has already been discussed in the chapter 1.6, focussing on Fermi's theoretical description in eq. (1.36). All ingredients of this equation are implemented in SSC with free parameters endpoint energy E_0 and the quantity to measure, the neutrino mass squared m_ν^2. This valid description is refined by several modifications that are important to include, since the effect of a non-vanishing neutrino mass is comparable to these small modifications.

Fermi function

The Fermi function $F(Z, E)$ describes the interaction of the daughter nucleus in a β-decay with charge Z and the emitted particle with kinetic energy E. In a β^--decay, the outgoing electron is attracted by the positively charged nucleus; the energy spectrum is shifted slightly towards lower energies. In a β^+-decay, the emitted positron is repelled, leading to increased energies in the spectrum.

For the tritium β^--decay with $Z = 2$, the modified non-relativistic Fermi function can be considered according to [43] by

$$F(Z,E) = \frac{x}{1-\exp(-x)}\left(a_0 + a_1 \cdot \frac{v_\mathrm{e}}{c}\right); \quad x = \frac{2\pi Z\alpha}{v_\mathrm{e}/c} \tag{4.11}$$

with fine-structure constant α and electron velocity v_e. a_0 and a_1 are empirical values

$$\begin{aligned} a_0 &= 1.002037 \\ a_1 &= -0.001427, \end{aligned} \tag{4.12}$$

that are a "phenomenological modification which makes the non-relativistic expression yield the same values as the relativistic calculation [...] over the energy range of interest." [43].

[4] B_S^j is used for the transmission function and scattering probabilities. Other magnetic field values like B_A in the analysis plane and B_max, the strongest field in the setup, can also be used in a segmented way as B_A^j and B_max^j to consider inhomogeneities.

Radiative corrections

The emitted β-decay electron experiences corrections due to interactions with virtual and real photons, the radiative corrections. A calculation in [99] is used in SSC to apply this correction, adding an energy dependent factor $f_{\mathrm{rad}}(E)$ to the spectrum calculation, respectively eq. (1.36).

Nuclear recoil

In eq. (1.42), the parent molecule T_2 is resting in the centre-of-momentum frame. After the decay, the daughter molecule with mass $M_{^3\mathrm{HeT}}$ carries a small momentum respectively kinetic energy, the nuclear recoil energy E_{rec}. In [48], an equation for E_{rec} is derived. Since the nuclear recoil p_{rec} and the electron momentum p_{e} are equal,

$$E_{\mathrm{rec}} = \frac{p_{\mathrm{rec}}^2}{2M_{^3\mathrm{HeT}}} = \frac{p_{\mathrm{e}}^2}{2M_{^3\mathrm{HeT}}} = E\frac{m_{\mathrm{e}}}{M_{^3\mathrm{HeT}}} + \frac{E^2}{2M_{^3\mathrm{HeT}}} \approx E\frac{m_{\mathrm{e}}}{M_{^3\mathrm{HeT}}} \tag{4.13}$$

with kinetic energy E of the electron. The approximation in eq. (4.13) is valid, since the first term containing m_{e} is larger by at least a factor of 50 in case of tritium and its low endpoint energy E_0 of 18.6 keV (see section 1.6.2). The energy dependence is linear. Constraining the interesting part of the spectrum to a region only a few eV below E_0 yields a nearly constant $E_{\mathrm{rec}} \approx 1.7\,\mathrm{eV}$. E_{rec} does not enter eq. (1.36) directly, because it is considered for practical reasons within the final state distribution, described in the following and especially in section 4.2.5.3. Due to its energy-independence, E_{rec} can be absorbed in an effective endpoint energy $E_0' = E_0 - E_{\mathrm{rec}}$, since the true value of E_0 is of no interest for KATRIN.

Final State Distribution

When tritium is bound in a molecule like T_2 and decays, the daughter molecule, here $(^3\mathrm{HeT})^+$, can be excited. Since it is a molecule, rotational, vibrational and electronic excitations are possible. These excitation states are represented by a final state distribution (FSD) with excitation energies E_f and probabilities P_f, specific for each molecule species. E_f is not available for the electron, thereby the FSD modifies the spectrum[5]

$$\begin{aligned}\frac{\mathrm{d}N}{\mathrm{d}E} = C \cdot F(Z,E) \cdot p \cdot (E + m_{\mathrm{e}}c^2) \cdot f_{\mathrm{rad}}(E) \cdot \sum_f [P_f \cdot (E_0 - E_f - E) \cdot \\ \sqrt{(E_0 - E_f - E)^2 - m_\nu^2 c^4} \cdot \Theta(E_0 - E_f - E - m_\nu c^2)\,].\end{aligned} \tag{4.14}$$

The β-spectrum of a molecular decay is a summation over all final states with index f. It adds single spectra with effective endpoint energies $E_{0,f} = E_0 - E_f$ weighted with probabilities P_f. In SSC, the differential spectrum is available as `SSCDifferentialSpectrumFSD` with a detailed description of the FSD (see section 4.2.5.3).

[5] Radiative corrections f_{rad} are included here.

4.2.4 Integrated β-spectrum

KATRIN measures the integrated β-spectrum (see section 2.1) to determine the parameters of the differential spectrum $\mathrm{d}N/\mathrm{d}E$, especially the neutrino mass squared m_ν^2. The signal count rate $\dot{N}_\mathrm{S}$ at the detector depends on the applied retarding energy qU

$$\dot{N}_\mathrm{S}(qU) = N_\mathrm{T}(\varepsilon_\mathrm{T}) \cdot \varepsilon_\mathrm{det} \cdot \frac{\Omega}{4\pi} \int_{qU}^{E_0} \frac{\mathrm{d}N}{\mathrm{d}E}(E_0, m_\nu^2) \cdot R(E, qU)\mathrm{d}E \tag{4.15}$$

accounting for the experimental effects combined in the response function R, the total number of tritium nuclei N_T as a function of the tritium purity ε_T and the detector efficiency $\varepsilon_\mathrm{det} = 0.9$ [48]. The solid angle

$$\Omega = 2\pi(1 - \cos\theta_\mathrm{max}) \tag{4.16}$$

accounts for the fact that electrons emitted with angles larger than θ_max (see eq.(2.2)) will be reflected at the pinch magnet and cannot reach the detector. Eq. (4.15) is equivalent to eq. (2.1) and already considers the information that electrons with kinetic energies below qU will be reflected and electrons above E_0 do not occur in the spectrum.

The implementation in SSC is called `SSCIntegratedSpectrum`. It contains a user-specified differential spectrum and response function as class members. A connection with the voxelization approach allows to calculate the integrated spectrum $\dot{N}_\mathrm{S}^j$ for each voxel j: In eq. (4.15), N_T is replaced by the number of tritium nuclei N_T^j in voxel j and the correct solid angle Ω^j with θ_max^j as well as the scattering probabilities P_i^j are used to obtain the voxel dependent response function $R^j(E, qU)$. The contributions of single voxels can be used individually to consider the rate at different detector pixels or can be summed up again to obtain the total rate of the integrated spectrum

$$\dot{N}_\mathrm{S}(qU) = \sum_j N_\mathrm{T}^j \cdot \varepsilon_\mathrm{det}^j \cdot \frac{\Omega^j}{4\pi} \int_{qU}^{E_0} \frac{\mathrm{d}N}{\mathrm{d}E}(E_0, m_\nu^2) \cdot R^j(E, qU)\mathrm{d}E. \tag{4.17}$$

With this flexibility, on the one hand SSC allows investigating asymmetries in the count rate, for example between top and bottom of the source. On the other hand, the total rate of the integrated spectrum can be calculated accurately using the detailed source model and its voxelization.

The obtained "total" spectrum can then be used in a next step to simulate a KATRIN measurement including a measurement time distribution and background effects. Analysis routines then allow investigating the effects of (source) parameters as systematic effects on m_ν^2 or to (re-)evaluate the sensitivity of KATRIN for specific modifications. Details on these tools are presented in section 6.2 and results of these investigations in chapters 7 and 8.

4.2.5 Extensions and modifications

4.2.5.1 General modifications

Since 2009, SSC as described in the previous section has been extended and has been subject to considerable improvements. Kassiopeia was started in 2010 and SSC was

decided to be part of it. Thus, SSC was adapted to the general structure that Kassiopeia offered (see section 4.1). This implementation into Kassiopeia was successful, the interfaces were established and tested: On the one hand, SSC can use magnetic fields from Kassiopeia's field calculators, on the other hand Kassiopeia's particle generator KPAGE is able to ask SSC for the β-spectrum or density distribution in the WGTS.

In addition, the connection of SSC to the KATRIN analysis tool KaFit (see section 6.2) was established that allows simulating the complete KATRIN experiment. It considers detailed measuring plans, the measurement time distribution [48] as well as background processes disturbing the measurement. With this connection it was possible to generate KATRIN "measurements" with a detailed source model of SSC and investigate the sensitivity on m_ν^2 as well as the systematic influence of experiment parameters on the analysis respectively the m_ν^2 determination.

4.2.5.2 Velocity profile

An extension to the existing SSC code is the completed implementation of velocity profiles. The velocities of the T_2 molecules in the WGTS are governed by the thermal movement with most probable speed [100]

$$v_\mathrm{m} = \sqrt{2k_\mathrm{B}T/M_{\mathrm{T}_2}} \tag{4.18}$$

with Boltzmann constant k_B, temperature T and molecule mass M_{T_2}. Additionally, a net gas flow with velocity $\vec{u}$ due to the injection and pumping at the tube ends has to be considered. Calculations in [101], that are also presented in chapter 5, show that the resulting velocity distribution is described well by a shifted Maxwellian

$$f(\vec{r},\vec{v})\mathrm{d}r\mathrm{d}v \approx \frac{\rho(\vec{r})}{(\sqrt{\pi}v_\mathrm{m})^3}\exp\left[-\frac{v_r^2+v_\phi^2+(v_z-u_z(\vec{r}))^2}{v_\mathrm{m}^2}\right]\mathrm{d}r\mathrm{d}v, \tag{4.19}$$

with velocity components v_r, v_ϕ and v_z in cylindrical coordinates and density $\rho(\vec{r})$. $f(\vec{r},\vec{v})\mathrm{d}r\mathrm{d}v$ is the probability of finding a molecule in volume $[\vec{r},\vec{r}+\mathrm{d}\vec{r}]$ within the velocity interval $[\vec{v},\vec{v}+\mathrm{d}\vec{v}]$. Thereby, $\vec{u}$ has already been reduced to the z-component $u_z(\vec{r})$, the so-called bulk velocity, since the net gas flow through the source occurs from the injection centre towards the tube ends. It should be emphasized that u_z is not constant; it depends on the position $\vec{r}$ in the source as shown in figure 5.2.

In SSC, a base class `SSCVelocityBase` handles the velocity distribution with the typical method `GetVelocity(TVector3& r)`. A derived class that considers results of chapter 5 contains a detailed model of the velocities in the WGTS. Especially, the obtained values of $u_z(\vec{r})$ are stored in the voxel structure to use the local u_z for the description of the Doppler effect (see section 4.2.5.4).

4.2.5.3 Final State Distribution

As already explained in section 4.2.3, the decay of tritium bound in a molecule causes a rotationally, vibrationally and possibly electronically excited final state of the daughter molecule. Since the molecule masses influence the discrete energies of these excitations, different parent molecules in the WGTS, the tritiated hydrogen isotopologues T_2, DT, HT, decay into the daughter molecules $(^3\mathrm{HeT})^+$, $(^3\mathrm{HeD})^+$ and $(^3\mathrm{HeH})^+$ that have different final state distributions (FSD). Detailed calculations

have been reported in [65–67] to obtain these FSD[6]. Two FSD are shown in figure 4.5a for $(^3\mathrm{HeT})^+$ and $(^3\mathrm{HeD})^+$, composed again by different distributions for different initial states respectively initial angular momentum J with $J = 0, 1, 2, \ldots$ as reported in [65]. The dependence on J is shown in figure 4.5b. The probability P_J to find a molecule in state J is given by a Boltzmann distribution [102]

$$P_J(T) = \frac{g_S g_J \exp\left(-\Delta E_J/(k_\mathrm{B}T)\right)}{Q_T} \tag{4.20}$$

with nuclear spin-degeneracy factor g_S, rotational degeneracy factor $g_J = (2J + 1)$, Boltzmann's constant k_B and temperature T; ΔE_J is the distance to the ground state. The level energies E_J can be found in table 4.1. Q_T is a normalizing sum

$$Q_T = \sum_J g_S g_J \exp\left(-\Delta E_J/(k_\mathrm{B}T)\right). \tag{4.21}$$

Dealing with T_2 as homonuclear molecule, $g_S = 1$ for even J and $g_S = 3$ for odd J; the heteronuclear DT and HT have no spin-degeneracy, therefore $g_S = 1$ [103].

To obtain the needed FSD for KATRIN, the simple FSD for different J have to be weighted according to their probability $P_J(T)$ that depends on the source temperature T and according to the fraction of the specific hydrogen isotopologue, in a way according to the tritium purity ε_T (see section 3.1). For that procedure SSC has two implemented possibilities, similar but with different (dis-)advantages:

- Possibility 1 is the class `SSCFinalStates`. The FSD for $(^3\mathrm{HeT})^+$ and $(^3\mathrm{HeD})^+$ is combined from available distributions [65], [66] for different J with appropriate weights (eq. (4.20)), resulting in an "effective" FSD. The FSD of $(^3\mathrm{HeH})^+$ is only available as a single effective distribution at $T = 30\,K$ [67]. Then, these three effective distributions are weighted according to the abundance of their parent molecule T_2, DT and HT in the WGTS, related to ε_T or later in KATRIN the results from the LARA measurement (see section 3.3). The resulting FSD is then used to calculate the differential β-spectrum. This approach is useful, when simulating a static source, fixing ε_T and T. When these quantities are dynamic, possibility 2 is appropriate.

- Possibility 2 is to store all available FSD individually, that means every distribution for $(^3\mathrm{HeT})^+$, $(^3\mathrm{HeD})^+$ and $(^3\mathrm{HeH})^+$, for every J, and weight them dynamically when calculating the β-spectrum. The class `SSCFinalStatesNew` is responsible to store such a vector of single FSD for all isotopologues and all J, together with appropriate weights. These weights can be adjusted for all temperatures and arbitrary ε_T, providing the most accurate FSD for the spectrum calculation. The disadvantage is that the calculation needs more time when using many separate distributions, especially in case of the Doppler effect (see section 4.2.5.4).

[6] All calculated FSD used in SSC and in this work are brought to the same energy scale, namely the T_2 scale. This means, the lower nuclear recoil energies (see section 4.2.3) of $(^3\mathrm{HeD})^+$ and $(^3\mathrm{HeH})^+$ compared to the 1.7 eV of $(^3\mathrm{HeT})^+$ have been absorbed in the FSD. On that scale, negative final state energies E_f can occur.

Table 4.1: **Non-adiabatic eigenvalues for levels J of the ground states ($\nu = 0$) of T_2, DT and HT from [104], also converted to eV.**

	T_2		DT		HT	
J	E_J (cm^{-1})	E_J(eV)	E_J (cm^{-1})	E_J(eV)	E_J (cm^{-1})	E_J(eV)
0	-37028.481	-4.59095	-36881.271	-4.57269	-36512.166	-4.52693
1	-36988.418	-4.58598	-36831.336	-4.56650	-36432.713	-4.51708
2	-36908.415	-4.57606	-36731.657	-4.55414	-36274.295	-4.49744
3	-36788.716	-4.56122	-36582.614	-4.53567	-36037.874	-4.46813
4	-36629.686	-4.54150	-36384.771	-4.51114	-35724.869	-4.42932
5	-36431.803	-4.51697	-36138.869	-4.48065	-35337.128	-4.38125

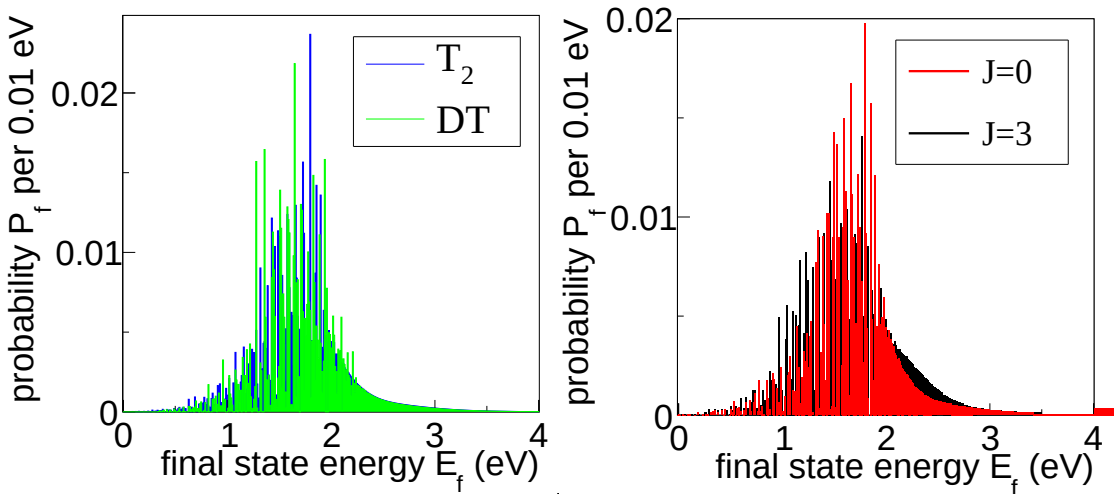

Figure 4.5: **a) Final state distribution of $(^3HeT)^+$ and $(^3HeD)^+$ at $T = 30\,K$.** Due to the different masses, the final state distributions differ slightly. These "effective" FSD are composed of a temperature dependent mixture of different states J (see figure b) and main text.)
b) Final state distribution of $(^3HeT)^+$ for different angular momentum J of the T_2 parent molecule. For clarity reasons, only $J = 0$ and $J = 3$ are plotted. The initial angular momentum influences the final state distribution: Higher J results in a slightly broadened peak. Considering this effect, to obtain the "effective" FSD for a specific molecule, each distribution for different J has to be weighted by its abundance according to a Boltzmann distribution.

4.2.5.4 Doppler effect

If a β-emitting T_2 molecule is moving, the β-electron energy in the laboratory frame is increased or decreased due to the Doppler effect. A classical treatment, simply adding the velocities of the electron $\vec{v}_e$ and the T_2 molecule $\vec{v}_{T_2}$, yields an energy shift of

$$\Delta E = E_f - E_i = \frac{1}{2} m_e \left(\vec{v}_e + \vec{v}_{T_2}\right)^2 - \frac{1}{2} m_e \vec{v}_e^2 = m_e \vec{v}_e \vec{v}_{T_2} + \frac{1}{2} m_e \vec{v}_{T_2}^2. \tag{4.22}$$

The last term in this equation is negligible for source temperatures of $T = 30\,\mathrm{K}$ because $\vec{v}_{T_2}$ in the order of $v_m = 290\,\mathrm{m/s}$ in eq. (4.18) is small compared to $\vec{v}_e$ in the order of $10^7\,\mathrm{m/s}$ for tritium β-electrons near the endpoint energy. Assuming that the direction of T_2 movement and electron emission coincide ($\vec{v}_e || \vec{v}_{T_2}$), this results in an exemplary shift of

$$\Delta E \approx 130\,\mathrm{meV}. \tag{4.23}$$

This value is comparable to a neutrino mass that KATRIN wants to measure and can even be higher for molecules that move faster. Thus, the Doppler effect has to be considered when analysing a measured KATRIN spectrum.

The Doppler effect is described by a broadening of the emitted β-spectrum $\mathrm{d}N/\mathrm{d}E$. It can be described mathematically by a convolution [105]

$$\frac{\mathrm{d}N'}{\mathrm{d}E}(E_f) = (g \otimes \frac{\mathrm{d}N}{\mathrm{d}E})(E_f) = \int_{-\infty}^{\infty} g(\Delta E) \cdot \frac{\mathrm{d}N}{\mathrm{d}E}(E_i)\mathrm{d}E_i \tag{4.24}$$

with a broadening function $g(\Delta E)$ and the initial and final kinetic energies of the β-electron E_i and E_f. The energy shift is $\Delta E = E_f - E_i$ as before.

To obtain the broadening function, the T_2 movement is considered as a Maxwellian distribution (cf. eq. (4.19)). Therefore, each T_2 molecule has a random velocity component v_s along the emission direction $\vec{v}_e$ of the electron. This defines a Gaussian distribution

$$g(v_s) = \frac{1}{\sigma_v \sqrt{2\pi}} \exp\left(-\frac{1}{2}\left(\frac{v_s - u_z}{\sigma_v}\right)^2\right) \tag{4.25}$$

centred around the bulk velocity u_z (see section 4.2.5.2) and width $\sigma_v = \sqrt{k_B T / M_{T_2}}$. In a non-relativistic approach, eq. (4.22) yields

$$\Delta E = E_f - E_i = m_e v_e v_s. \tag{4.26}$$

Substituting v_s in eq. (4.25) by eq. (4.26) and using $v_e = \sqrt{2E_i/m_e}$ leads to the wanted broadening function

$$g(\Delta E) = N \cdot \exp\left(-\frac{1}{2}\left(\frac{\Delta E}{\sigma_E}\right)^2\right). \tag{4.27}$$

Again, this is a Gaussian distribution with width

$$\sigma_E = \sqrt{2E_i k_B T m_e / M_{T_2}} \tag{4.28}$$

and $N = \frac{1}{\sigma_E \sqrt{2\pi}}$ as normalization. Please note the energy dependence of σ_E.

When describing the Doppler broadening relativistically, eq. (4.22) does not hold; the correct relativistic addition of velocities obeys the Lorentz transformation [106]

$$v_{\mathrm{e,f}} = \frac{v_{\mathrm{e,i}} + v_{\mathrm{s}}}{1 + \frac{v_{\mathrm{e,i}} \cdot v_{\mathrm{s}}}{c^2}}. \tag{4.29}$$

Using the relativistic γ factor

$$\gamma_\alpha = \frac{1}{\sqrt{1 - v_{\mathrm{e},\alpha}^2/c^2}} \quad \text{with } \alpha = \mathrm{i}, \mathrm{f} \tag{4.30}$$

$$\gamma_\alpha = \frac{E_\alpha}{m_{\mathrm{e}} c^2} + 1 \tag{4.31}$$

the Doppler energy shift can be written as

$$\Delta E = E_f - E_i = (\gamma_f - \gamma_i) m_{\mathrm{e}} c^2. \tag{4.32}$$

Replacing v_{s} in eq. (4.25) by eq. (4.29) and using eq. (4.31) yields

$$g(E_f, E_i) = N \cdot \exp\left(-\frac{1}{2} \left(\frac{(v_{\mathrm{e},f} - v_{\mathrm{e}i})}{(1 - v_{\mathrm{e},f} v_{\mathrm{e},i}/c^2)\sigma_v} \right)^2 \right) \tag{4.33}$$

with $v_{\mathrm{e},}\alpha = c \cdot \sqrt{1 - 1/\gamma_\alpha^2}$. This resembles a Gaussian, but it is not easy to read-off the width σ_E or the normalization N of the broadening function.

In SSC, the routines to broaden the β-spectrum according to eq. (4.24) are implemented as class `SSCDifferentialSpectrumDoppler`. The broadening function can be defined by the user; in the following the non-relativistic function (eq. (4.27)) has been used if not stated otherwise. In figure 4.6a, the small difference between original β-spectrum and Doppler broadened spectrum is shown.

The described representation of the Doppler effect can get time consuming in a program, when the spectral shape is changed frequently, for example when fitting the spectrum parameters E_0 and m_ν^2 to a measurement: The whole convolution of eq. (4.24) has to be repeated for all needed energies E_f. Therefore, in the non-relativistic case a further approximation can be used to speed up the calculations, namely applying the Doppler broadening to the Final State Distribution (see section 4.2.5.3)

$$P'(E_f) = \int_{-\infty}^{\infty} g(\Delta E) \cdot P(E_i) \mathrm{d}E_i. \tag{4.34}$$

$P(E_i)$ is the usual FSD, $g(\Delta E)$ the favoured broadening function with a small modification: σ_E from eq. (4.28) is fixed to the energy of the spectrum endpoint energy of $E_0 = 18.6\,\mathrm{keV}$, since the final state energies are on the eV-scale. The Doppler broadened spectrum $\left(\frac{\mathrm{d}N}{\mathrm{d}E}\right)'_{\mathrm{FSD}}$, implemented in SSC as `SSCDifferentialSpectrumFSD-Doppler`, is the same as eq. (4.14), but uses $P'(E_f)$

$$\begin{aligned} \left(\frac{\mathrm{d}N'}{\mathrm{d}E}\right)_{\mathrm{FSD}} \propto \sum_f [P'(E_f) \cdot (E_0 - E_f - E) \cdot \sqrt{(E_0 - E_f - E)^2 - m_\nu^2 c^4} \\ \cdot \Theta(E_0 - E_f - E - m_\nu c^2)\,]. \end{aligned} \tag{4.35}$$

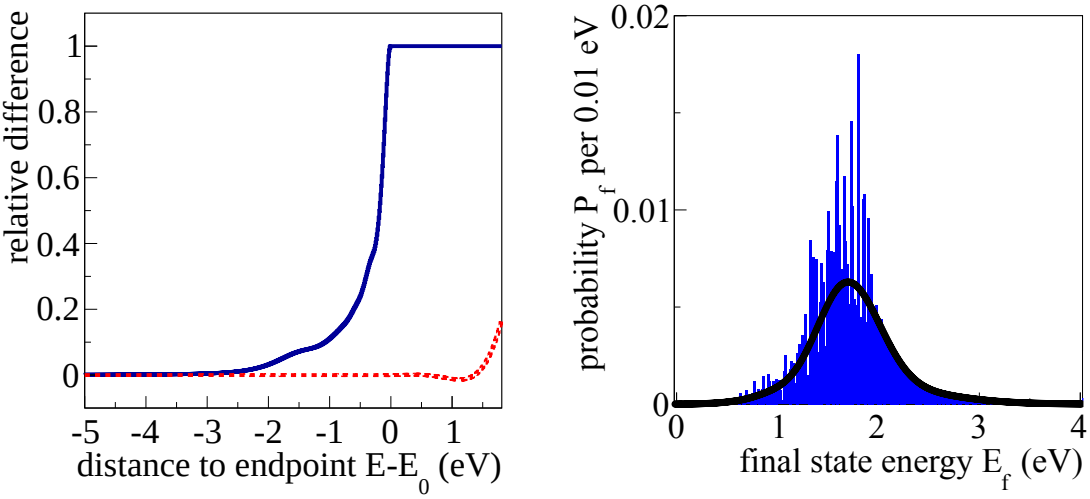

Figure 4.6: **a) Influence of Doppler effect on spectrum.** The blue, solid line shows the relative difference $1-(\mathrm{d}N/\mathrm{d}E)/(\mathrm{d}N/\mathrm{d}E)'$ between the tritium β-spectrum $(\mathrm{d}N/\mathrm{d}E)'$ with applied Doppler broadening at 30 K to a spectrum $(\mathrm{d}N/\mathrm{d}E)$ without the Doppler effect. The broadened spectrum has clearly increased count rates, also above the endpoint energy E_0. The visible structure in this curve results from the different final states contributing to the spectral shape. The red, dashed line shows the relative difference $1-(\mathrm{d}N/\mathrm{d}E)_{\mathrm{FSD}}/(\mathrm{d}N/\mathrm{d}E)'$ between the Doppler broadened spectrum using eq. (4.24) and the approximation $(\mathrm{d}N/\mathrm{d}E)'_{\mathrm{FSD}}$ when smearing the final state distribution with eq. (4.34) and (4.35). The agreement is very good; only a few eV above the endpoint energy E_0, the rates differ slightly.
b) Effect of Doppler broadening on final state distribution. The final state distribution for a tritium purity of 95% is shown in blue, the Doppler broadened distribution (black) at 30 K has lost all prominent peaks, resembling a Gaussian distribution with width of eq. (4.28).

A comparison of this approximation and the Doppler broadened β-spectrum is shown in figure 4.6a. The differences are marginal. The approximation is especially useful and saves time, if an easy FSD comprised from already weighted different contributions of T_2, DT and HT is used, so that the Doppler broadening only has to be applied once. This procedure is shown in figure 4.6b for a FSD of 90% T_2 and 10% DT. Otherwise, if the different contributions of the FSD are stored separately, the smearing has to be applied to every distribution consecutively, annihilating the gain in computation time.

5. Modelling of gas dynamics

The column density ρd was introduced in section 3.1 as a key parameter of a windowless gaseous tritium source. Furthermore, its essential systematic influence on the KATRIN measurements was explained in section 3.2, demanding for a detailed understanding, control and monitoring of ρd.

For that purpose extensive gas dynamics simulations have been developed during the past 10 years. These simulations comprise the experimental parameters of the source that determine ρd: injection pressure p_{in}, exit pressure p_{ex}, temperature distribution $T(\vec{r})$ and the source geometry including the injection and pumping systems (see section 3.3).

To determine the type of required simulations it is useful to calculate the free path l [100] that is defined as

$$l = \frac{\mu v_{\mathrm{m}}}{p} \tag{5.1}$$

with pressure p, viscosity of tritium μ and most probable speed v_m (see eq. (4.18)). The rarefaction parameter δ

$$\delta = \frac{a}{l} \tag{5.2}$$

is used to characterize the gas dynamics in the WGTS, where a denotes a characteristic size of the system, in case of the WGTS the tube radius R. Then δ is defined as in [107]

$$\delta(z) = \frac{R \cdot p(z)}{\mu v_m} = \frac{R \cdot \rho(z)}{\mu v_{\mathrm{m}}} \cdot k_{\mathrm{B}} T \tag{5.3}$$

with pressure $p(z)$ respectively density $\rho(z)$ at longitudinal coordinate z and constant temperature T. Near the injection chamber pressures of several μbar are expected. This allows using Navier-Stokes equations of continuum mechanics. Within this hydrodynamical regime, collisions between gas molecules happen on scales that are small compared to the dimensions R of the system: $\delta \gg 1$. On the other hand, near the pumping chambers the pressure is expected to be small, within only few percent of the injection pressure. Here, in the free-molecular regime with $\delta \ll 1$ intermolecular collisions are absent, the molecules only interact with the wall of the tube. The difficulty arises from the transitional regime with $\delta \approx 1$ in between the

hydrodynamical and free-molecular regime. To treat this problem in a unified way, the Boltzmann equation

$$\frac{\partial f}{\partial t} + v_i \frac{\partial f}{\partial r_i} + \frac{\partial F_i f}{\partial v_i} = J(f, f) \tag{5.4}$$

has to be solved. f is the velocity distribution function [100, 108]

$$f(\vec{r}, \vec{v}) = \frac{\mathrm{d}N}{\mathrm{d}^3\vec{r}\,\mathrm{d}^3\vec{v}} \tag{5.5}$$

with the number of molecules $\mathrm{d}N$ around $\vec{r}$ and $\vec{v}$ inside the phase space volume $\mathrm{d}^3\vec{r}\,\mathrm{d}^3\vec{v}$. Furthermore, F_i denotes an external force on the molecules and $J(f, f)$ is the collision integral that considers intermolecular collisions of molecules and their gains or losses in velocity space. The specific type of $J(f, f)$ is determined by the problem to be solved and is discussed in detail e.g. in [100, 108]. Determining f solves the gas dynamics considerations for the WGTS; it defines the density profile $\rho(z)$ and the column density ρd. This can be used in a source simulation like SSC (see section 4.2) to simulate the expected β-spectra at KATRIN. Considering (density) inhomogeneities in the source, SSC can determine their influence on the neutrino mass measurements in combination with the KaFit package (section 6.2). Additionally, the gas dynamics simulations itself can determine the influence of source parameters on ρd to specify requirements on stability and monitoring. And when considering the Doppler effect, information on the gas velocities is needed that can be obtained again by the velocity distribution function f.

The following chapter summarizes all efforts to model the WGTS gas dynamics. It is based on various reports of Sharipov et al. [64, 69, 101, 107, 109–111] which have been worked out in close cooperation with the KATRIN collaboration. Section 5.1 shows the general concepts towards the calculation of a one-dimensional density profile and the column density of the source. In section 5.2 the velocity distribution of the molecules in the WGTS is determined. Section 5.3 investigates the effects of a radially/azimuthally non-uniform source. In section 5.4 these former approaches are combined to obtain a preliminary pseudo-3D model and an outlook towards a full 3D gas dynamics simulation is presented.

5.1 One-dimensional calculations

With a WGTS tube of length $L = 10\,\mathrm{m}$ and a radius of only $R = 0.045\,\mathrm{m}$ "the gas flow can be considered as one-dimensional" from the injection at the tube centre towards its ends and "no density variation in a given cross section of the source is taken into account" [107]. In these first considerations, an isothermal source at $T = 30\,\mathrm{K}$ is assumed, so that the density profile and the column density ρd of the WGTS are defined by the injection pressure p_{in} at the source tube centre and the exit pressure p_{ex} at the tube ends due to the pumping of turbomolecular pumps.

The following steps allow determining the density profile: For a tube of length L and radius R the reduced flow rate G can be connected to the constant mass flow rate $\dot{M}$ through a source cross section as

$$G = \frac{v_{\mathrm{m}}}{\pi R^3} \frac{(L/2)}{p_{\mathrm{in}}} \dot{M} \tag{5.6}$$

with the most probable speed v_m of eq. (4.18). The molecule movement is driven by the pressure difference between injection and tube end. The local pressure drop ξ_p is defined as

$$\xi_p(z) = \frac{R}{p(z)} \frac{\mathrm{d}p(z)}{\mathrm{d}z}. \tag{5.7}$$

This results in the local reduced flow rate G_p

$$G_p = -\frac{1}{\pi R^2} \frac{v_\mathrm{m}}{p \cdot \xi_p(z)} \dot{M}, \tag{5.8}$$

where G_p depends on the local conditions, which mean the pressure or equivalently the rarefaction parameter $\delta(z)$ of eq. (5.3). Since the mass flow rate $\dot{M}$ is constant, equations (5.6) and (5.8) can be combined to

$$G_p \frac{(L/2)}{\delta_\mathrm{in}} \frac{\mathrm{d}\delta}{\mathrm{d}z} = -G. \tag{5.9}$$

Separation of variables and integration from the centre of the tube with rarefaction parameter δ_in to a position z yields

$$\frac{1}{\delta_\mathrm{in}} \int_{\delta_\mathrm{in}}^{\delta} G_p(\delta) \mathrm{d}\delta = -\frac{z}{(L/2)} G. \tag{5.10}$$

$G_p(\delta)$ can be obtained by solving the kinetic Boltzmann equation, as well as G can be related to $G_p(\delta)$ again (for details see [107, 112, 113]). In fact, eq. (5.10) is a function $z(\delta)$ that can be inverted to obtain $\delta(z)$ or with eq. (5.3) the desired density profile $\rho(z)$.

The final step is to calculate the column density ρd by the usual integration over the whole source length as in eq. (3.2).

Further investigations account for a longitudinal temperature profile $T(z)$. Eq. (5.3) becomes

$$\delta(z) = \frac{R \cdot p(z)}{\mu(T) v_\mathrm{m}(T)} \frac{T_0}{T(z)} \tag{5.11}$$

with nominal temperature $T_0 = 30\,\mathrm{K}$, temperature dependent viscosity $\mu(T)$ and most probable speed $v_\mathrm{m}(T)$. Additional to the previously described problem with the pressure gradient as driving force, now the temperature gradient causes molecule movement. This extends the contributions to the mass flow rate $\dot{M}$ in eq. (5.8) by a term proportional to

$$G_T(\delta) \frac{p(z)}{T(z)} \frac{\mathrm{d}T(z)}{\mathrm{d}z} \tag{5.12}$$

with the reduced flow rate $G_T(\delta)$ due to the temperature gradient, but the general concepts remain the same (see [114] for details). The results are numerical values $\delta(z)$.

5.1.1 Density interpolation formula

In [101] a phenomenological interpolation formula for the expected density profile in the WGTS is stated

$$\begin{aligned} \frac{\delta(z)}{\delta_\mathrm{in}} = \frac{\rho(z)}{\rho_\mathrm{in}} = \left[B_0 + B_1(1-z') + B_2(1-z')^2\right] \left[1 - \exp(5z')\right] \\ + \left[1 + B_3 z'^2 + B_4 z'^4\right] \cos(\pi z'/2) \end{aligned} \tag{5.13}$$

with injection rarefaction δ_{in} respectively density ρ_{in} and $z' = z/(L/2)$. The coefficients B_i can be obtained by adapting the interpolation formula to numerical data obtained by eq. (5.10) for specific boundary conditions p_{in}, p_{ex} and $T(z)$. The coefficient B_0 has been introduced later to account for non-vanishing p_{ex} [115]. The agreement of eq. (5.13) with the numerical values is good (see also figure 5.1), "the uncertainty [...] does not exceed 0.5%" [101] and the influence on ρd is even weaker.

Further refinements of the simulations were obtained in [111] where a slight asymmetry of the injection chamber and therefore different lengths $L_{\text{front}} = 5.0075\,\text{m}$ and $L_{\text{rear}} = 5.0745\,\text{m}$ of the front and rear side of the tube were considered[1]. Additionally, the exit pressures on both sides as well as the temperature profile can differ. The routines to calculate the density profile for both sides of the tube are executed simultaneously. Finally, the interpolation formula in eq. (5.13) can be used again with different coefficients for front and rear side and with $z' = z/L_{\text{front}}$ respectively $z' = z/L_{\text{rear}}$. Figure 5.1 shows the numerical results of the gas dynamics calculations with an asymmetric WGTS as well as the used interpolation formula.

5.1.2 Discussion of systematic uncertainties

The following list summarizes systematic uncertainties on the column density calculation that arise from the discussed methods [107]:

- The use of a one-dimensional calculation neglects the non-zero radius-to-length ratio $R/(L/2)$. This means that the influence of end effects is neglected.
- Using coefficients G_p and G_T from a linearized kinetic Boltzmann equation induces small uncertainties for the transitional regime of the source.
- The viscosity of tritium μ at $T = 30\,\text{K}$ is unknown. An extrapolation from measured viscosities of deuterium (and hydrogen) is used to get

$$\mu = 0.95\sqrt{3/2}\mu_{\text{D}} = 2.425 \cdot 10^{-6}\,\text{Pa s}. \tag{5.14}$$

- The accommodation coefficient α with $(0 \leq \alpha \leq 1)$ describes the boundary condition of the gas, in case of the WGTS tube the interaction of the tritium molecules with the wall. "The case $\alpha = 1$ is called the diffuse-reflection condition, and $\alpha = 0$ the specular-reflection condition." [108]. In case of tritium at low temperatures α is unknown.

All uncertainties are in the order of 1% and sum up to a total uncertainty of 4.6% [107]. Possibilities to reduce this uncertainty are measurements of the viscosity and the accommodation coefficient at 30 K and considerations of the end effects (see section 5.4).

5.1.3 Influence of source parameters on the column density

In section 3.2 was discussed that unrecognized changes in the WGTS column density ρd of only 0.2% cause intolerably high systematic shifts on the analysed neutrino mass squared. The report [64] investigates the influence of source parameters on ρd and therefore sets requirements for a KATRIN measurement. Its results are summarized in table 5.1.

[1] These lengths arise from technical drawings of the WGTS in 2008 and do not consider the planned inversion of the beam tube and modifications of the design within this context.

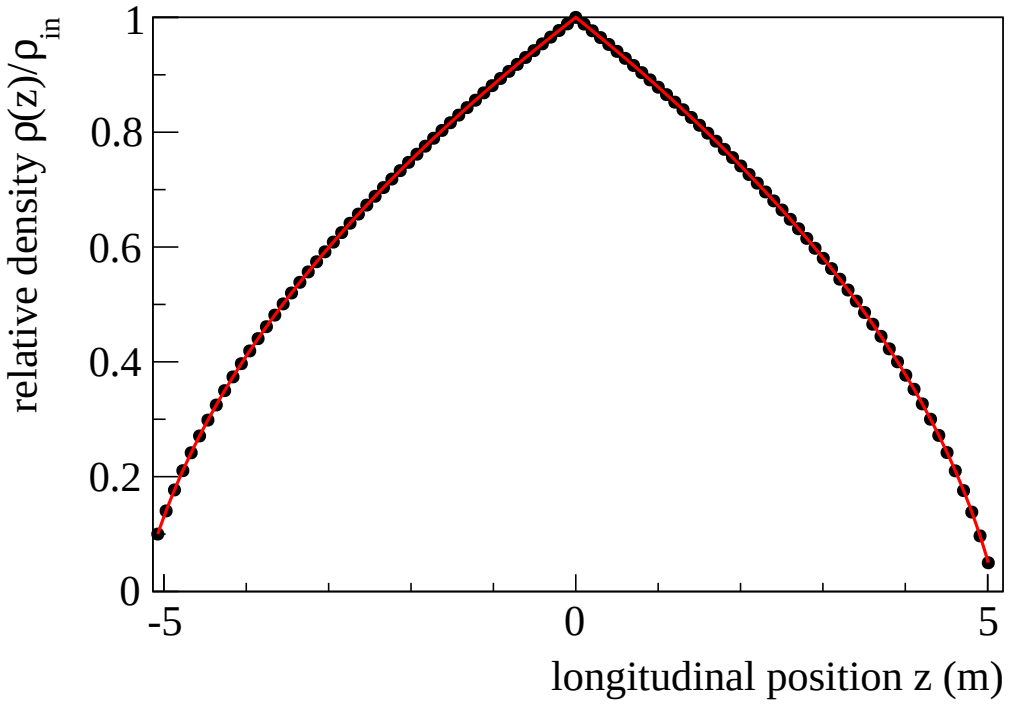

Figure 5.1: **Calculated density profile $\rho(z)$ of the WGTS, relative to the injection density ρ_{in}.** In this case a homogeneous temperature of $T = 30\,K$ was assumed. The profile for both sides of the tube is calculated in a combined approach, since the two parts are slightly asymmetric due to the injection chamber that is shifted from the geometrical centre of the tube by 67 mm towards the front end within a total tube length of 10.082 m. Additionally, two different exit pressures have been assumed for both ends, $p_{\text{ex,rear}} = 0.10 \cdot p_{\text{in}}$ and $p_{\text{ex,front}} = 0.05 \cdot p_{\text{in}}$. The interpolation formula of eq. (5.13), drawn as red line, can be applied to both sides separately and is in good agreement with the numerical results.

Table 5.1: **Systematic influence of source parameters X on ρd and requirements on parameter stability.** The numbers α_X denote the proportionality constants between changes of the parameter X and the column density: $\Delta\rho d/\rho d = \alpha_X \cdot \Delta X/X$.

parameter X	α_X	stability requirement
temperature T	-1.2	$\Delta T/T \leq \pm 0.2\%$
injection pressure p_{in}	1.1	$\Delta p_{\text{in}}/p_{\text{in}} \leq \pm 0.2\%$
exit pressure p_{ex}	0.03	-

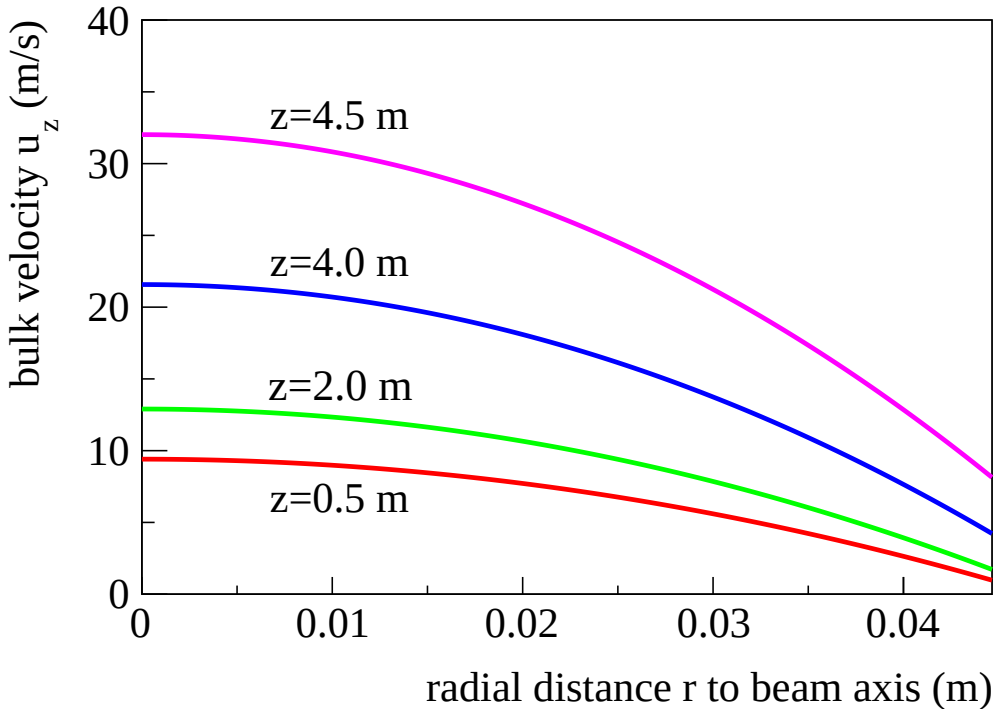

Figure 5.2: **Bulk velocities in the WGTS.** The bulk velocity decreases from the beam tube centre towards the wall at $r = 0.045\,\mathrm{m}$. The velocity increases with increasing z from the injection chamber at $z = 0\,\mathrm{m}$ towards the pumping chambers at $z = 5\,\mathrm{m}$.

5.2 The velocity distribution function

The calculations so far were responsible to determine $\rho(z)$ as a part of the velocity distribution function $f(\vec{r},\vec{v})$ of eq. (5.5). To obtain the full velocity distribution function, the approach of a linearized kinetic equation is used again in [101] with

$$f(\vec{r},\vec{v}) = \frac{\rho(z)}{(\sqrt{\pi}v_\mathrm{m})^3}\exp\left(-\frac{v^2}{v_\mathrm{m}^2}\right)\left[1+2\xi_p(z)\frac{v_z}{v_\mathrm{m}}\Phi(x,y,v_x,v_y)\right] \tag{5.15}$$

with the local pressure gradient $\xi_p(z)$ as in eq. (5.7). The perturbation function $\Phi(x,y,v_x,v_y)$ is obtained by the discrete velocity method (see [116] for details). The results can be approximated by local Maxwellians

$$f(\vec{r},\vec{v}) \approx \frac{\rho(z)}{(\sqrt{\pi}v_\mathrm{m})^3}\exp\left[-\frac{v_x^2+v_y^2+(v_z-u_z(\vec{r}))^2}{v_\mathrm{m}^2}\right]. \tag{5.16}$$

The problem reduces to the determination of the bulk velocity $u_z(\vec{r})$. It describes the net movement of molecules from the injection towards the pumping chamber. The bulk velocity profile is shown in figure 5.2.

The dependence of u_z on the longitudinal position z along the beam axis and the radial distance r to the axis can be parameterized as

$$u_z(r,z) = -v_\mathrm{m}\xi_p(z)\left[a(\delta)-c(\delta)\left(\frac{r}{R}\right)^2\right] \tag{5.17}$$

with pressure gradient $\xi_p(z)$ accessible by differentiating eq. (5.13) and with coefficients $a(\delta)$ and $c(\delta)$. These coefficients have been calculated numerically and can be interpolated[2] by

$$a(\delta) = \left[0.894 - 0.1048 \cdot \delta(1 - \frac{\ln \delta}{4})\right] \frac{1+\delta}{1+1.963 \cdot \delta} + \frac{\delta(\delta + 2.036)}{2.593 + 4 \cdot \delta} \tag{5.18}$$

$$c(\delta) = \left[0.295 - 0.0536 \cdot \delta(1 - \frac{\ln \delta}{4})\right] \frac{1+\delta}{1+0.7599 \cdot \delta} + \frac{\delta^2}{0.07788 + 4 \cdot \delta}. \tag{5.19}$$

At the end of this procedure, the position dependent bulk velocities together with the obtained density distribution $\rho(z)$ yield eq. (5.16) that completely describes the source gas dynamics at every position in the source.

5.3 Two-dimensional calculations

The one-dimensional calculations of the density profile seem appropriate for KATRIN due to the very long tube with small cross section. But it is worthwhile to check for density variations within a cross section that means inhomogeneities in radial (r) and azimuthal (ϕ) direction. This is important at KATRIN, since the segmented focal plane detector (see section 2.5) can resolve r and φ of electrons that were emitted in the WGTS.

5.3.1 Injection and pumping chambers

Responsible for small deviations of the density distribution are the injection as well as the pumping chambers of KATRIN (see figure 3.2). In [69], these end effects were studied in a 2D axisymmetric numerical approach. The kinetic Boltzmann equation was solved on a 2D grid near the injection chamber. The result is shown in figure 5.3. Since the sensitive part of the WGTS – the part that is mapped through the spectrometer onto the detector – is specified as the inner part with $r < 0.041\,\mathrm{m}$, the expected local density variations are $< 5\%$. The region of higher density does not extend beyond 2 cm around the injection chamber; this is only 0.2% of the total length. This means that ρd at large radii differs by at most 0.01% from ρd on the beam axis. This small deviation can be considered when using a pseudo-3D model for the WGTS, but is too small to influence the KATRIN measurement. Similar to the injection region, the simulations of the pumping chamber were executed in 2D with a simplified geometry: a tube entering an unlimited volume, neglecting the walls of the pumping chamber and the continuation of the beam tube on the opposite side. The results in figure 5.4 indicate the behaviour of the gas at the pumping chamber, but further simulations (see section 5.4) will be performed to clarify the situation at the WGTS pump ports.

5.3.2 Influence of an azimuthal temperature gradient

The two-phase neon system (see section 3.3) that is responsible for the homogeneous cooling to 30 K along the whole length of the beam tube is brazed to the beam tube at $\varphi = 0°$ and $\varphi = 180°$ (see figure 3.9). The temperature of the beam tube

[2] Here, the results for an accommodation coefficient $\alpha = 1$ are presented.

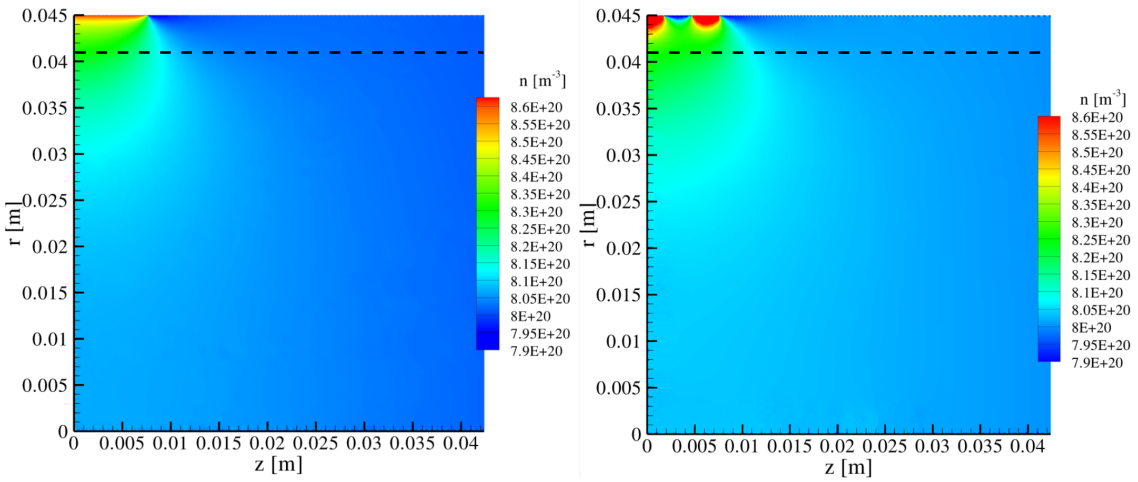

Figure 5.3: **Influence of the WGTS gas injection on the density profile from [69].** Two scenarios are shown to estimate the influence at KATRIN: The left figure shows a central slit injection with small density deviations 10 cm towards the centre and within the dimensions of the slit along the beam axis. Using two slits as in the right figure yields a similar behaviour. At KATRIN, small holes instead of slits are used, arranged in 5 rings (see figure 3.2). The "active" part of the source within the flux tube (see section 4.2.1) is the part below the black dashed line. These results indicate that density perturbations due to the injection are weak and limited to the outermost parts of the beam tube.

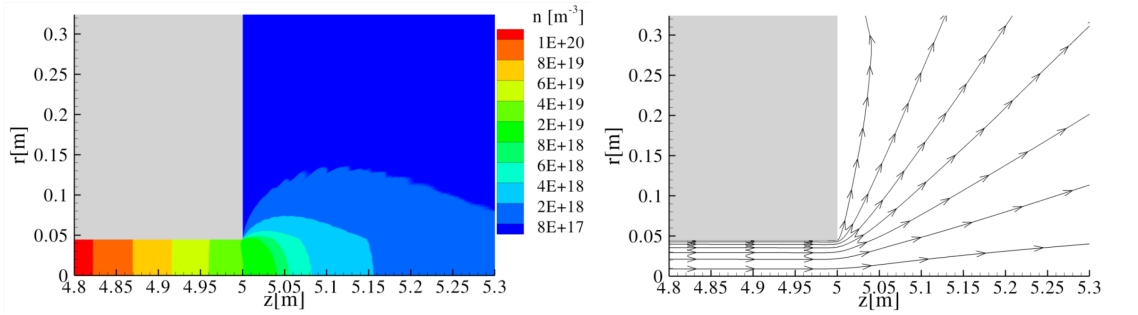

Figure 5.4: **a) Density profile at the WGTS pumping chamber from [69].** In this 2D approach, the general density drop towards the beginning of the pumping chamber is visible. When entering the large pumping chamber the gas stream expands. This can also be seen in **b) Streamlines in the pumping chamber from [69].**

there is fixed to the defining neon temperature. Towards top ($\varphi = 90°$) and bottom ($\varphi = 270°$) of the beam tube, an azimuthal temperature gradient establishes, caused by heat radiation through the pumping chambers onto the inner surface of the beam tube. Since the heat radiation varies for different longitudinal positions z in the source, the strength of an azimuthal temperature profile also depends on z. Due to this temperature profile, it is expected to have gas circulation and inhomogeneities of the density distribution within a cross section of the WGTS.

"Since we consider a weakly disturbed state of the gas, then the longitudinal flow and the circulation of the gas in a cross section can be considered separately." [101]. Then, the problem is simplified to two-dimensional cross sections of the source, and due to symmetry to a quarter of it. An azimuthal temperature profile of the beam tube wall

$$T(\varphi) = T_0 + \Delta T \sin^2 \varphi \tag{5.20}$$

with equilibrium temperature T_0 and maximal temperature difference ΔT between T_0 and the top/bottom of the beam tube was assumed. At different rarefaction parameters δ with $0 < \delta < 22$ for the WGTS, the discrete velocity method is used to solve the linearized Boltzmann equation, e.g. [117]. Figure 5.5 shows the results. With expected relative temperature differences $\Delta T/T = 10^{-3}$ maximal density variations of $\Delta\rho/\rho_0 = 4 \cdot 10^{-4}$ compared to the local density ρ_0 can be expected. The influence on ρd will be discussed in the following section when a pseudo-3D model is created.

5.4 Extension to a pseudo-3D density profile

The final step for the WGTS gas dynamics simulations would be a full three-dimensional modelling of the density profile. Solving the Boltzmann equation in 3D numerically is a difficult task and has not yet been achieved for the WGTS. This is a future task that will be discussed at the end of this section.

But the results that have been obtained so far from the one-dimensional density profile in section 5.1 and the two-dimensional simulations in 5.3 can be combined to an intermediate description of the WGTS gas dynamics: a pseudo-3D density profile. This is allowed since the dominant process is the longitudinal movement of the molecules according to the one-dimensional density profile. The two-dimensional gas circulation and the radial and azimuthal density deviations are small corrections; "both motions of the gas, namely, longitudinal and circulation, can be considered together by a linear superposition." [101]. Technically, this happens as follows:

1. The one-dimensional density profile $\rho(z)$ is calculated according to p_{in}, p_{ex} and $T(z)$ (section 5.1).

2. A series of two-dimensional density profiles for various δ in the range of $0 < \delta < 22$ as expected in the WGTS is calculated (section 5.3). They are calculated with the azimuthal temperature difference ΔT as a free parameter and can be saved and used for other calculations.

3. The obtained two-dimensional density profiles are arranged as shown in figure 5.6 where the inverted $\rho(z)$ yields the required $z(\rho)$ or $z(\delta)$ and determines where to place the profiles. The central density ρ_0 for each 2D profile is determined by δ.

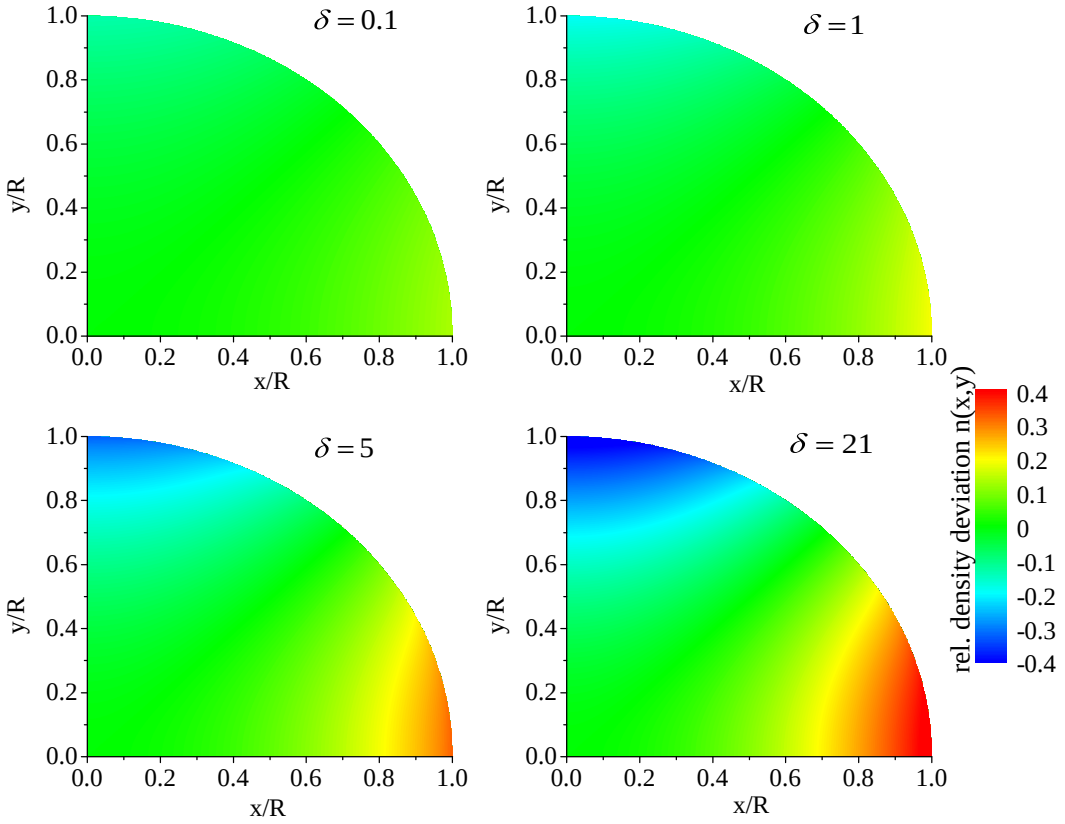

Figure 5.5: **Two-dimensional density profiles.** Numerical data from [101]. Shown is the relative density deviation n for different δ respectively density regimes in the WGTS. The underlying temperature distribution of the wall is given by eq. (5.20) with $T_0 = 30\,\mathrm{K}$ and variable ΔT. The position dependent n can be converted to real densities ρ by $n(x,y) = \frac{\rho(x,y)-\rho_0}{\rho_0}\frac{T_0}{\Delta T}$ with ρ_0 defined by δ. This means, the relative deviations up to $\pm 40\%$ have to be scaled with $\frac{\Delta T}{T_0}$ that is expected to be $< 10^{-3}$. In the centre, where larger 2D density deviations occur, ΔT is expected to be even smaller. Therefore, maximal density variations to $4 \cdot 10^{-4}$ are possible.

4. ΔT is now related to $T(z)$; each density profile can be weighted by the local azimuthal temperature gradient.

5. Between two adjacent 2D density profiles at z_i and z_{i+1} a linear interpolation allows calculating densities for $z_i < z < z_{i+1}$. This procedure allows obtaining the density $\rho(\vec{r})$ at every position $\vec{r} = (r, \varphi, z)$ in the WGTS.

Furthermore, this pseudo-3D model can be used to calculate the column density as a function of r, φ to check for inhomogeneities. This means integrating $\rho(\vec{r})$ along z for every (r, φ) with help of the arrangement in figure 5.6: Each two-dimensional profile i is weighted with the length Δz_i where it is valid. The result of this summation is shown in figure 5.7. It can be seen that the inhomogeneities of ρd are on the 10^{-5} level. These deviations are too small to be resolved in KATRIN.

To conclude this chapter, an outlook towards a complete reliable gas dynamics simulation is given. In [69], the most efficient way to do this is shown: The parts of the WGTS between the injection and the pumping chambers (almost 5 m) do not need a sophisticated three-dimensional simulation. The one-dimensional calculations are sufficient to describe the gas flow along the thin beam tube. Radial and azimuthal deviations there can be superimposed by independently determined two-dimensional density profiles, resulting in the presented pseudo-3D density profile. The results of the 2D simulation of the injection through slits (see figure 5.3) may be satisfactory or might be extended to a 3D simulation in the future. A full 3D simulation of the pumping chambers is proposed by F. Sharipov [118], since the gas flow is not guaranteed to be axisymmetric and the temperature distribution of the pumping chamber is complicated. This simulation will be "based on both kinetic equation and direct simulation Monte Carlo". The combination of these approaches will then provide the most accurate description of the gas dynamics in the WGTS.

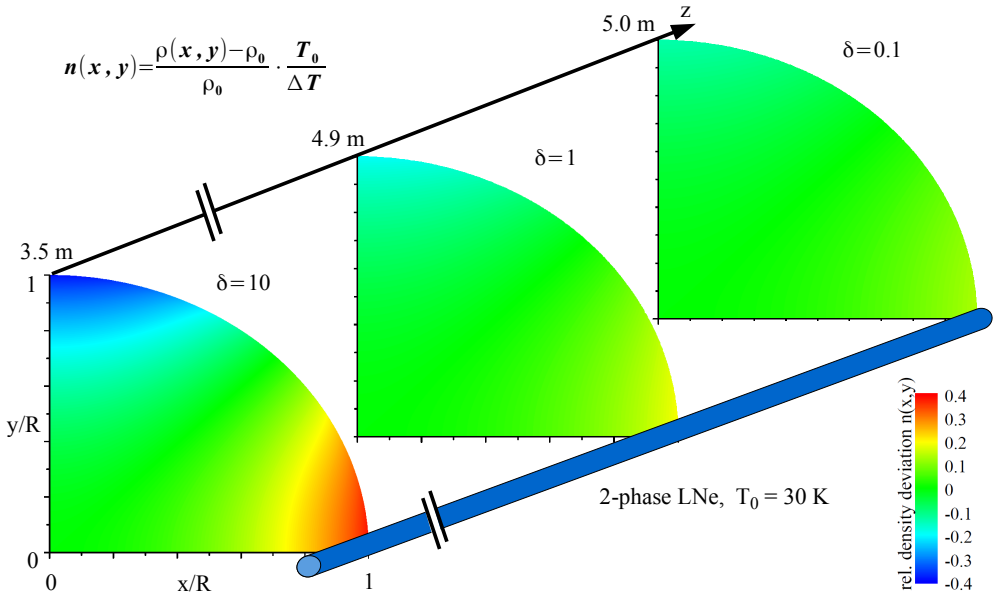

Figure 5.6: **Pseudo-3D density profile.** The 2D density profiles of section 5.3 are positioned along the z-axis according to the inverted 1D density profile $z(\delta)$ of section 5.1.

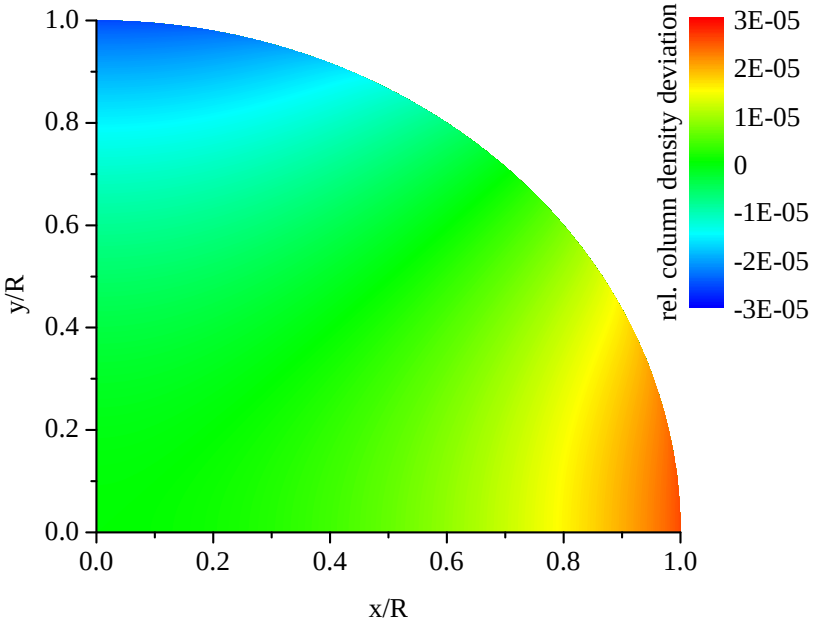

Figure 5.7: **Column density inhomogeneities obtained by integrating the pseudo-3D density profile.** A longitudinal temperature profile $T(z)$ with $\Delta T = 30\,\mathrm{mK}$ was assumed that is translated to $\Delta T(z)$, the maximal azimuthal temperature deviation along the wall of the beam tube. Each 2D profile in figure 5.6 was weighted by $\Delta T(z)$ and assumed to be valid between half the distance to its neighbours on both sides. Summing up over all 2D profiles yields the shown column density deviations.

6. Spectrum analysis

The measured integrated β-spectrum at KATRIN has to be analysed carefully to detect small distortions of its shape due to a non-vanishing neutrino mass m_ν^2 (see section 2.1). This will be done by fitting an expected spectral shape with m_ν^2 as a free parameter next to endpoint energy, signal and background strength to the measured spectrum.

Before analysing a real measured spectrum, simulated spectra, for example from the simulation software SSC (see section 4.2), can be used to validate the analysis software and to study the statistical and systematic uncertainties in determining m_ν^2.

For both purposes, the KASPER analysis toolkit, outlined in section 6.1, was developed. KASPER contains the package KaFit (section 6.2), a newly developed tool to analyse (simulated) measurements of KATRIN and to study the influence of (source) parameters in the analysis of m_ν^2. In the following, it is described how to get from the expected tritium β-spectrum (obtained e.g. by SSC) to a simulated KATRIN measurement. Then, the basic analysis strategy is presented to fit the theoretical expectation to the simulated measurement and deduce m_ν^2 and its uncertainties. Section 6.3 shows more advanced methods that have been implemented into KaFit and are used in this work to determine statistical and systematic uncertainties at KATRIN.

6.1 Analysis toolkit KASPER

The KATRIN analysis software is available in the toolkit KASPER [119], which consists of several tools for simulation, data access and analysis as shown in figure 6.1. The idea is to provide these tools for various types of analysis that any collaboration member of KATRIN may want to do without requiring extensive knowledge of C++ programming or every detail of each KASPER tool. Users are able to use the provided classes and functions in their private analyses, and may add them to KASPER later if they are useful for others. So KASPER that was started in 2011 will grow over the next years when more and more KATRIN analyses will be implemented.

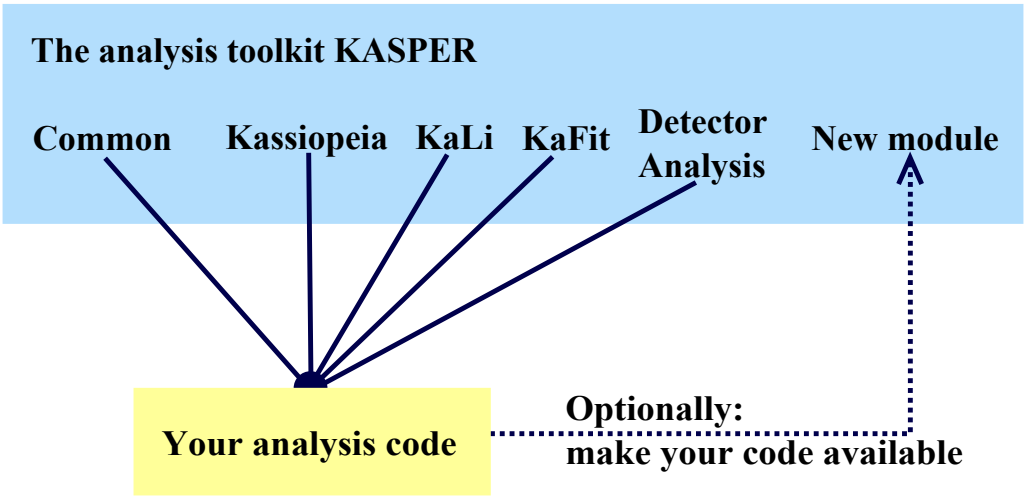

Figure 6.1: **The KATRIN analysis toolkit KASPER (simplified, from [120]).** KASPER consists of simulation and analysis software that is used by the KATRIN collaboration. Any analysis code can refer to the tools provided by KASPER. So far, next to a general package **Common** with utility functions, the KATRIN Monte-Carlo simulation **Kassiopeia** is included (see also figure 4.1). The module **KaLi** is a data access and processing module. **KaFit** is the analysis tool that is presented in this chapter in detail. The module **Detector Analysis** stands for all other developed analysis code that is already available or may be added in the future.

A main feature of KASPER is that simulation results and real data can be treated in a unified way. The Monte-Carlo simulation software Kassiopeia (see section 4.1) that also contains the spectrum calculation SSC is part of KASPER. The same is true for the KATRIN Library KaLi [97, 121], which is used to access different databases where all the measurement data and other parameters, such as the geometric parameters of the KATRIN setup, are stored [122]. These tools allow comparing measurements with expectations from simulations.

During the development and construction of KATRIN, KASPER can be used to guide the refinement of the hardware design by studying the effects of the design changes to the physics sensitivity. This is accomplished by the tool KaFit and will be explained in detail in the following section.

6.2 A tool to study statistical and systematic uncertainties: KaFit

By simulating the integrated spectrum at KATRIN that considers the WGTS and spectrometer properties like SSC (see section 4.2), dedicated analyses can determine the sensitivity of KATRIN and investigate the systematic effects on m_ν^2.

For that purpose, the KaFit package has been developed in 2012 in collaboration with M. Haag [121]. It is based on a program package already described in [82]. It uses the following steps:

- The rates of the integrated β-spectrum, provided by SSC, can be combined with a measurement time distribution (section 6.2.1) – how long KATRIN will

measure at which retarding energy – and background events (section 6.2.2) to simulate a KATRIN "measurement" (section 6.2.3).

- The analysis on m_ν^2 can be performed by fitting an expected β-spectrum with m_ν^2 as one of the fit parameters to the simulated KATRIN measurement, taking into account the effects introduced by the instrument (see sections 4.2) with likelihood/χ^2 fits and adjustable minimization routines (sections 6.2.5 and 6.2.6).

- The errors of the fit parameters in an ensemble of simulated measurements determine the sensitivity and discovery potential of the KATRIN experiment (sections 6.2.7, 6.3.1, 6.3.4 and 6.3.5).

- Systematic effects can be investigated by various methods, explained in sections 6.3.1, 6.3.3 and 6.3.5.

6.2.1 Measurement time distribution

The measurement time distribution defines fractions of measurement time t_{qU} at different spectrometer retarding energies qU_i. The preliminary planned distribution [48] is shown in figure 6.2. It was determined in [123] that by distributing the fixed total measurement time of three years to different voltages around the endpoint energy E_0 the physics reach of KATRIN can be optimized. The distribution shows three prominent regions: The region few eV below E_0 is the most sensitive to the neutrino mass[1], therefore most of the measurement time is spent there. Far below E_0 the signal rate is high due to the steeply rising spectrum, allowing to collect many electrons, accumulating statistics, that helps to constrain E_0 during the analysis. Even above E_0, where no signal events are expected, measurement time is spent to determine the background rate (section 6.2.2). The existing measurement time distribution is included in KaFit as class `KFRuntimeSchedule`. The distribution can easily be scaled or modified by adding or removing measurement points or time.

6.2.2 Background

Background events disturb the measurement of the signal spectrum at KATRIN. Expecting signal count rates of only a few counts per minute near E_0, the background rate is required to be smaller than 0.01 counts per second [48]. Several processes contribute to background at the detector and are presented in [48]. Investigations on active and passive suppression of the backgrounds can be found in [124, 125].

In KaFit, an arbitrary number of different backgrounds, managed by the class `KFBackground` can be added. A typical background is an energy independent, Poissonian background. It is used throughout this work with $\dot{N}_\mathrm{b} = 10^{-2}\,\mathrm{cps}$ by the derived class `KFBackgroundPoisson`. More complicated backgrounds can be added, like energy dependent ones, or non-Poissonian effects like the background cascade from a single nuclear decay in the spectrometer [83], resulting in large fluctuations of the background rate.

[1] In [32] is shown that an optimal sensitivity is given for a signal to background ratio of 2:1.

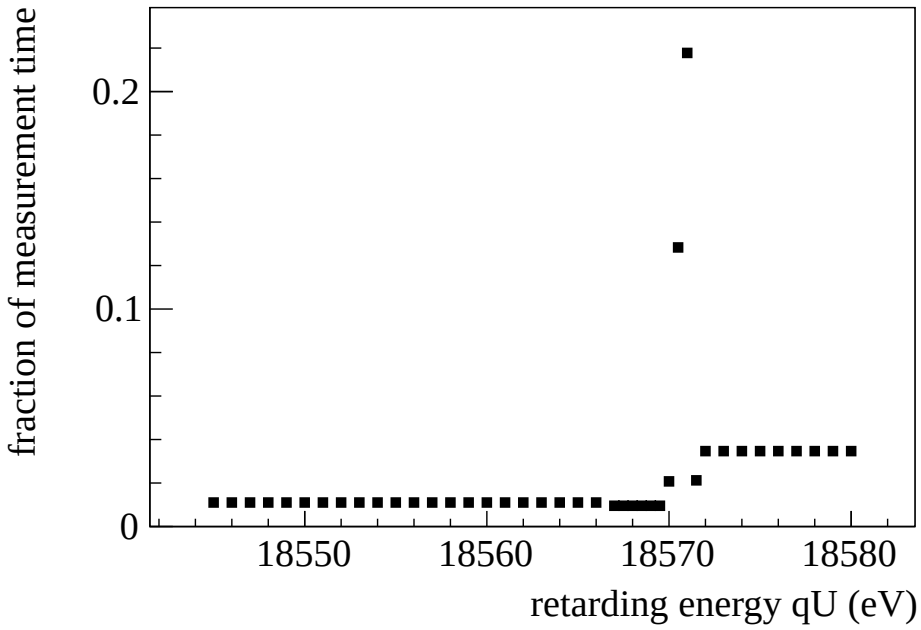

Figure 6.2: **Planned measurement time distribution at KATRIN.** The measurement time is distributed on 41 points with an interval of 1 eV respectively 0.5 eV in the sensitive region on m_ν^2 below the endpoint energy that was set to 18575 eV here.

6.2.3 Generating a KATRIN measurement

At KATRIN, the expected number of events $\tilde{N}$ during measurement time t_{qU} is a function of the retarding energy qU

$$\tilde{N}(qU) = \left(\dot{N}_\mathrm{s}(qU, E_0, m_\nu^2) + \dot{N}_\mathrm{b}\right) \cdot t_{qU}. \tag{6.1}$$

It is composed of signal rate $\dot{N}_\mathrm{s}$ of eq. (4.15) with parameters E_0 and m_ν^2 and the background rate $\dot{N}_\mathrm{b}$. In KaFit, the task of the class `KFRunGenerator` is to implement eq. (6.1), to connect the SSC-simulated spectrum $\dot{N}_\mathrm{S}$ with the background classes to obtain $\dot{N}_\mathrm{b}$ and with the measurement time distribution to get t_{qU} for each measurement point. In addition, to simulate a measurement, the number of counts $N^\mathrm{exp}(qU)$ is obtained by drawing from a Poisson distribution with expectation value $\tilde{N}(qU)$

$$N^\mathrm{exp}(qU) = \mathrm{Poisson}(\tilde{N}(qU)), \tag{6.2}$$

implicitly assuming a statistical uncertainty of $\sigma = \sqrt{\tilde{N}(qU)}$. A simulated KATRIN "measurement" is shown in figure 6.3.

In the program, each adjustment of qU is called a `KFSubrun`. It stores qU, N^exp and t_{qU}. All sub-runs together form a `KFRun`. The program structure of KaFit is intended to process simulated runs the same way as real data later.

6.2.4 Simulation of the theoretical rate

Again, the simulation of the theoretical spectrum is provided by SSC with the class `KFSpectrumSimulator`. In principle, any other spectrum simulation can be used to

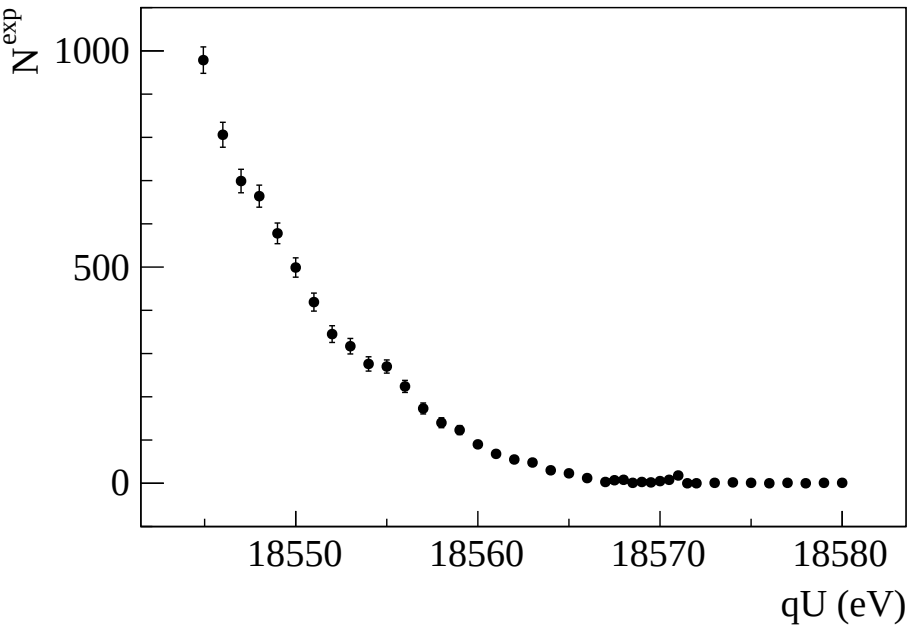

Figure 6.3: **A KATRIN "measurement", simulated by KaFit.** The measurement time distribution of figure 6.2 was used for a 2-hours run, creating the general rising shape of an integrated spectrum with a small peak slightly above 18570 eV due to increased measurement time there.

obtain a theoretical signal rate $\dot{N}_{\mathrm{S}}$ of an integrated β-spectrum. The expected counts N^{theo} are the same as in eq. (6.1), with two additional parameters, signal strength R_{s} and background strength R_{b} that are treated as unknown amplitudes [48]. Therefore, N^{theo} is expressed as

$$N^{\mathrm{theo}}(qU) = \left(R_{\mathrm{s}} \cdot \dot{N}_{\mathrm{s}}(qU, E_0, m_\nu^2) + R_{\mathrm{b}} \cdot \dot{N}_{\mathrm{b}}\right) \cdot t_{qU}. \tag{6.3}$$

Together with the important parameters E_0 and m_ν^2, four parameters are adapted to fit a measured spectrum.

6.2.5 Parameter estimation

The process of obtaining the value of a desired quantity based on a set of experimental observations is called parameter estimation or point estimation [126, 127]. A typical method for parameter estimation is the maximum likelihood method. The likelihood function is defined as

$$L(\vec{\theta}|\vec{X}) = \prod_i p(X_i|\vec{\theta}), \tag{6.4}$$

where $p(X_i|\vec{\theta})$ is the probability density function (p.d.f.) that a measurement X_i will occur, if the underlying parameters $\vec{\theta}$ are realised. A fitting routine can adapt $\vec{\theta}$ to obtain a maximal L, resulting in the best-fit values $\hat{\vec{\theta}}$, the maximum-likelihood estimator. The likelihood function can be written as negative log-likelihood

$$-\log L(\vec{\theta}|\vec{X}) = -\sum_i \log p(X_i|\vec{\theta}), \tag{6.5}$$

since the logarithm is a monotonic function and a summation of $\log p(X_i|\vec{\theta})$ is easier than a multiplication. The minus sign is introduced to minimize $-\log L$. This is not different from finding the maximum, but numerical algorithms are well established to find minima of functions (see e.g. [128]).

At this point, a special type of $-\log L$ is introduced, the Chi-square function

$$\chi^2(\vec{\theta}|\vec{X}) = \sum_i \frac{(X_i - X_i^{\text{theo}}(\vec{\theta}))^2}{\sigma_i^2} \tag{6.6}$$

with measurements X_i, uncertainties σ_i and theoretically expected values $X_i^{\text{theo}}(\vec{\theta})$. χ^2 is obtained by putting a Gaussian distribution

$$p(X_i|\vec{\theta}) = \frac{1}{\sqrt{2\pi}\sigma_i} \exp\left(\frac{(X_i - X_i^{\text{theo}}(\vec{\theta}))^2}{2\sigma_i^2}\right) \tag{6.7}$$

into eq. (6.5), multiplying by a factor of 2 and neglecting additional constant summands. Again, χ^2 can be minimized numerically, in some cases analytically, to get $\hat{\vec{\theta}}$.

In KaFit, several estimation methods are predefined, all deriving from a base class `KFLogLikelihoodKATRIN`. It contains a measurement run, simulated by the `KFRunGenerator` with user-defined, fixed values E_0^{sim} and $m_\nu^{2,\text{sim}}$ and a `KFSpectrumSimulator` with the theoretical description of the spectrum. The χ^2-function in case of a standard KATRIN fit[2] is

$$\chi^2(E_0, m_\nu^2, R_\text{s}, R_\text{b}|\vec{N}) = \sum_i \frac{(N_i^{\text{exp}}(qU_i) - N_i^{\text{theo}}(qU_i, E_0, m_\nu^2, R_\text{s}, R_\text{b}))^2}{\sigma_i^2}. \tag{6.8}$$

Numerically minimizing χ^2 (section 6.2.6) for all measurements[3] results in the four fitted parameters introduced in eq. (6.3), including the best-fit estimator $\hat{m}_\nu^2$.

6.2.6 Minimization

After all the preparations in the previous sections, KaFit comprises several classes derived from the base class `KFCurveFitter` that are responsible for minimizing $-\log L$ or χ^2 and obtaining the point estimation. The implemented derived classes give access to special minimization packages like `KFMinuit2`, which is an interface to the widely-used MINUIT2 in ROOT [91], or a standalone Markov-Chain-Monte-Carlo simulation `KFMCMC` [121]. KaFit can be extended to other user-specified minimization routines with a common interface. All routines are initialized and called in a unified way, and the results are stored in the standard ROOT structure TTree [91]. This allows comparing results from different minimization methods with each other.

[2] In the following sections, extensions of this analysis are discussed, where further parameters can be added to the fit.

[3] The index i stands for all measurements in $\vec{N}$. It does not necessarily stand for only 41 different retarding energies qU_i but also for different measurement periods, or the measured rates at different detector pixels.

In general, the user can define any function with an arbitrary number of parameters [4] to be minimized. For KATRIN, the `KFLogLikelihoodKATRIN` described above is to be minimized when fitting the parameters of eq. (6.3) to a KATRIN measurement.

Another function of the fit is to provide an estimate on the parameter uncertainties. As an example, MINUIT2 provides the routine MINOS that investigates the behaviour of the likelihood function in a multi-parameter space around the minimum to set asymmetric errors on the best fit parameters. Further details on error analysis are described in section 6.3.

6.2.7 Confidence intervals

The frequentist approach, sometimes called classical approach [126], treats probability $P(A)$ as the frequency ratio of an outcome A after N experiments

$$P(A) = \lim_{N\to\infty} \frac{n_A}{N}. \tag{6.9}$$

Classical confidence intervals of α confidence level (C.L.) claim that in an ensemble of measurements each reporting a confidence interval the true unknown value μ_t will be contained in α of these intervals[5] [126].

To determine the classical confidence interval, Neyman's construction of a confidence belt (see figure 6.4) is used [130]. For every possible value μ, an interval $[x_1, x_2]$ is selected, so that

$$P(x \in [x_1, x_2]|\mu) = \alpha \tag{6.10}$$

is fulfilled.[6] This construction creates horizontal line segments. The confidence belt is the union of these line segments. A measurement x_0 then allows reading off the confidence interval $[\mu_1, \mu_2]$ at the intersections of a vertical line at x_0 with the belt borders.

Some important terms that should be clarified here are under- and overcoverage. If a confidence interval of α C.L. contains less than the stated probability α, that means $P(\mu \in [\mu_1, \mu_2]) < \alpha$, it is called "undercoverage". An undercovering interval does not hold its promise of a classical confidence interval (see above). Vice versa, an interval overcovers, if the probability $P(\mu \in [\mu_1, \mu_2]) > \alpha$. A reported overcovering interval is a classical confidence interval, but it is chosen too wide to optimally constrain the measured quantity.

All plots in figure 6.4 are given in units of the standard deviation σ. If the probability distribution function is Gaussian, the area of a Gaussian distribution can be used to calculate the confidence intervals. Typical values that are used in the following are shown in table 6.1.

Several methods that are explained in the following try to determine confidence intervals for KATRIN measurements.

[4] The number of possible fit parameters may be constrained by the used minimization routines.

[5] This is in contrast to the Bayesian, subjective interpretation, where a confidence interval, rather called "credibility interval", of α C.L. is supposed to contain the true value μ_t with probability α [129].

[6] One can choose to state upper limits ($x_1 = -\infty$), central limits ($P(x < x_1|\mu) = P(x > x_2|\mu) = (1-\alpha)/2$) or any other interval that respects eq. (6.10).

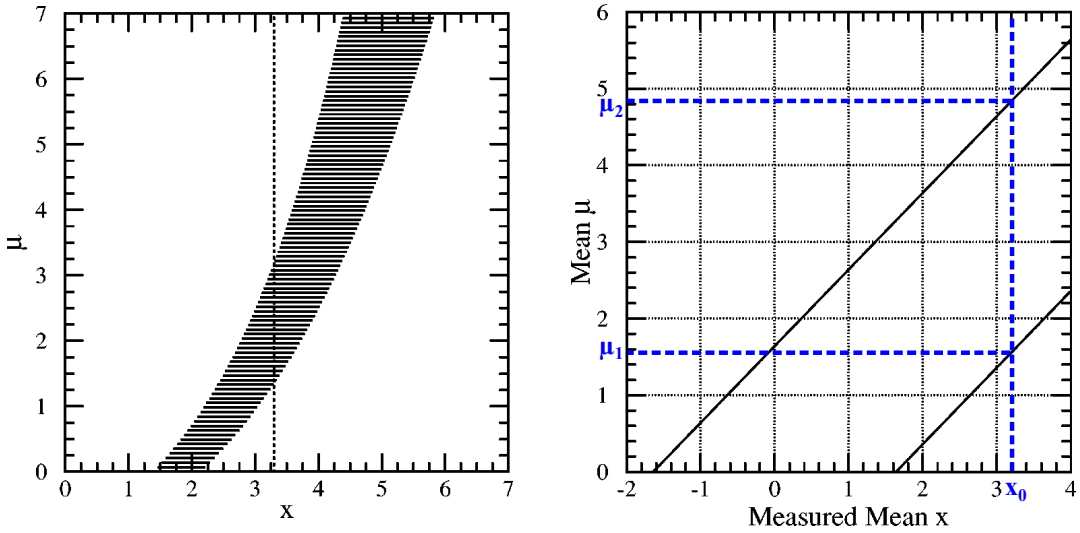

Figure 6.4: **a) Generic confidence belt from [129].** Construct horizontally, read vertically. See text for details.
b) Confidence belt for 90% C.L. for a Gaussian distribution in units of the standard deviation from [129], modified. A measurement x_0 allows drawing a vertical line. The intersections with the borders of the confidence belt define $[\mu_1, \mu_2]$.

Table 6.1: **a)** Integrals α and β of a normal distribution $N(\mu = 0, \sigma = 1)$ for a central interval $[-n \cdot \sigma, n \cdot \sigma]$ and a one-sided interval $[-\infty, m \cdot \sigma]$ respectively.
b) Central interval respectively one-sided interval that contains α,β probability of a normal distribution.

n, m	α	β
1	0.6827	0.8413
2	0.9544	0.9772
3	0.9973	0.9987

α, β	n	m
0.90	1.645	1.282
0.95	1.960	1.645
0.99	2.576	2.326

6.3 Implemented methods

6.3.1 Ensemble simulations

A method to investigate the KATRIN sensitivity and the influence of several nuisance parameters (systematic effects) on m_ν^2 is to simulate an ensemble of complete KATRIN experiments. This Monte-Carlo approach allows estimating the variance of the maximum likelihood estimator $\hat{m}_\nu^2$ [126]. For example 4000 full KATRIN measurements with 3 years measurement time for a fixed, known $m_\nu^{2,\mathrm{sim}}$ are simulated, where statistical variations (and possible systematic effects) are included to pretend a measurement (section 6.2.3). The free parameters of the theoretical expectation (section 6.2.4) are adapted to each "measurement" by fitting routines (section 6.2.6) to obtain the best-fit value $\hat{m}_\nu^2$. The ensemble of $\hat{m}_\nu^2$ is filled into a histogram (figure 6.5). The mean $\overline{m_\nu^2}$ and variance σ_{stat}^2 respectively standard deviation σ_{stat} of the resulting distribution can be used to project the physics sensitivity of KATRIN. In [48], the standard deviation of such a distribution was found to be

$$\sigma_{\mathrm{stat}} = 0.018\,\mathrm{eV}^2. \tag{6.11}$$

Variations of experimental parameters, measurement time or backgrounds affect the sensitivity and can be investigated with the combination of SSC and KaFit. Results on the sensitivity analyses are shown in chapter 7.

In addition, figure 6.5 that uses a Gaussian fitted to the distribution shows another effect: a shift

$$\Delta m_\nu^2 = \overline{m_\nu^2} - m_\nu^{2,\mathrm{sim}} \tag{6.12}$$

of mean $\overline{m_\nu^2}$ from the input value $m_\nu^{2,\mathrm{sim}} = 0.0\,\mathrm{eV}^2$ to $\overline{m_\nu^2} = -0.0075\,\mathrm{eV}^2$. This was obtained exemplarily here, by using a different source parameter for the analysis than for the underlying measurement simulation. In this case the column density ρd^{fit} for the analysis was chosen to be $\rho d^{\mathrm{fit}} = 1.02 \cdot \rho d^{\mathrm{sim}}$, causing a shift on $\overline{m_\nu^2}$ as a systematic effect. This investigation can be repeated for different combinations of experimental parameters and variations to determine their impact on m_ν^2. It allows KATRIN to define the required stability or control on these parameters.

The envisaged systematic uncertainty on m_ν^2 at KATRIN is

$$\sigma_{\mathrm{syst}} \leq 0.017\,\mathrm{eV}^2 \tag{6.13}$$

that means equal contribution of statistical and systematic uncertainties. In [48], the total systematic uncertainty has been divided into five major individual systematic uncertainties, added quadratically with each causing

$$\Delta m_\nu^2 = 0.0075\,\mathrm{eV}^2. \tag{6.14}$$

This is a reference for investigations on systematic effects connected with the WGTS that are presented and discussed in chapter 8.

The statistical (eq. (6.11)) and systematic uncertainties (eq. (6.13)) can be added quadratically and used for example to state an upper limit (see section 6.2.7) of $m_\nu < 0.2\,\mathrm{eV}$ (90% C.L.) if $\hat{m}_\nu^2 = 0.0\,\mathrm{eV}^2$ is measured.

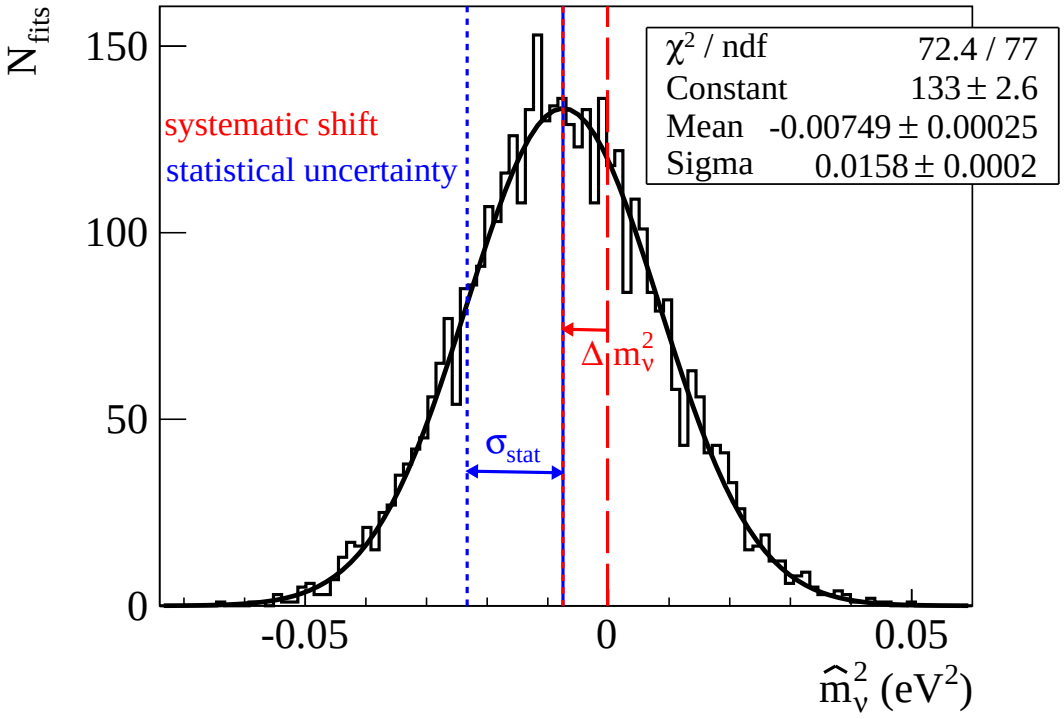

Figure 6.5: **Exemplary distribution of best-fit values $\hat{m}_\nu^2$ in 4000 KATRIN simulations.** Input value was $m_\nu^{2,\mathrm{sim}} = 0.0\,\mathrm{eV}$, the simulated measurement time was 3 years. The fit results $\hat{m}_\nu^2$ are Gaussian distributed with mean $\overline{m_\nu^2}$ and width σ_{stat}. The systematic shift is obtained by the difference between mean and input $\Delta m_\nu^2 = \overline{m_\nu^2} - m_\nu^{2,\mathrm{sim}}$. Here, the shift was induced on purpose by using a different column density ρd for the spectrum generation than for the analysis.

6.3.2 "Graphical methods"

The behaviour of the negative log-likelihood function $-\log L$ around the minimum at the maximum likelihood estimator $\hat{\theta}$ can be used to determine the statistical uncertainty of the experiment. To do so, $-\log L$ is written as a Taylor series around $\hat{\theta}$ [126]

$$-\log L(\theta) = -\log L(\hat{\theta}) - \left[\frac{\partial \log L}{\partial \theta}\right]_{\theta=\hat{\theta}} (\theta-\hat{\theta}) - \frac{1}{2!}\left[\frac{\partial^2 \log L}{\partial \theta^2}\right]_{\theta=\hat{\theta}} (\theta-\hat{\theta})^2 - \dots \quad (6.15)$$

with $-\log L(\hat{\theta}) = -\log L_{\max}$, the minimal value of the negative log-likelihood. The term with the first derivative is zero, since the function is expanded around an extremum. Connecting the second derivatives with the estimated standard deviation $\hat{\sigma}_{\hat{\theta}}$ (see [126] for details), one obtains

$$-\log L(\theta) = -\log L_{\max} + \frac{(\theta-\hat{\theta})^2}{2(\hat{\sigma}_{\hat{\theta}})^2} \quad (6.16)$$

$$-\log L(\hat{\theta} \pm \hat{\sigma}_{\hat{\theta}}) = -\log L_{\max} + \frac{1}{2}. \quad (6.17)$$

This means that $\hat{\sigma}_{\hat{\theta}}$ can be obtained by following the function $-\log L(\theta)$ away from the minimum to the point, where it has increased by 1/2. This method can be used to determine the confidence interval (see section 6.2.7), e.g. the 68.3% central confidence interval $\left[\hat{\theta}-\hat{\sigma}_{\hat{\theta}}, \hat{\theta}+\hat{\sigma}_{\hat{\theta}}\right]$. In case of an asymmetric $-\log L$, $\hat{\sigma}_{\hat{\theta}}$ can be determined to the lower side as $\hat{\sigma}_{\hat{\theta}-}$ and to the upper side as $\hat{\sigma}_{\hat{\theta}+}$, again checking for an increase of $-\log L$ by 1/2, although there are some technical subtleties as discussed in [131].

KaFit allows plotting the negative log-likelihood function for KATRIN and graphically determining statistical uncertainties.

6.3.3 Systematic effects as nuisance parameters

Another method to include systematic effects of some experiment parameters into the analysis is to treat them as additional free fit parameters. As an example, the tritium purity ε_{T} is regarded here, since an uncertainty in ε_{T} leads to a systematic shift of m_ν^2 (see section 3.2). To avoid that, ε_{T} is added to the set of fit parameters of eq. (6.3). Now

$$\vec{\theta} = \{E_0, m_\nu^2, R_{\mathrm{s}}, R_{\mathrm{b}}, \varepsilon_{\mathrm{T}}\} \quad (6.18)$$

needs to be adjusted to fit the model to the measured data. The fitting routines remain unchanged, they just have to consider additional parameters. The fit with additional nuisance parameters usually takes longer to converge and more evaluations of the spectrum calculation are needed. The results of the fit are best-fit values for all parameters, especially $\hat{m}_\nu^2$ and $\hat{\varepsilon}_{\mathrm{T}}$ with uncertainties determined by responsible methods as before. An additional uncertainty in the tritium purity as a free parameter instead of using a fixed value will increase the uncertainty on m_ν^2 compared to the 4 parameter fit (see chapter 8).

This concept of adding systematic effects as nuisance parameters in the likelihood function is scalable; further parameters can be added to $\vec{\theta}$. The procedure is limited

by the number of fit parameters that the minimization routine can deal with and by the number of required steps for convergence that may need too many evaluations of the function to minimize.

A further step is to extend the likelihood function to include external measurements into the analysis what is also called "pull method". In the example of ε_{T}, a LARA measurement (see section 3.3) will give a measured $\overline{\varepsilon_{\mathrm{T}}}$ with an uncertainty $\sigma_{\varepsilon_{\mathrm{T}}}$. This can be added to eq. (6.5)

$$-\log L(\vec{\theta}|\vec{X}) = -\sum_i \log p(X_i|\vec{\theta}) \; - \; \log p(\varepsilon_{\mathrm{T}}|\overline{\varepsilon_{\mathrm{T}}}) \tag{6.19}$$

with $\vec{\theta}$ as in eq. (6.18). In case of a Gaussian distributed measurement of ε_{T} this reduces to

$$-\log L(\vec{\theta}|\vec{X}) = -\sum_i \log p(X_i|\vec{\theta}) \; + \; \frac{(\varepsilon_{\mathrm{T}} - \overline{\varepsilon_{\mathrm{T}}})^2}{2\sigma^2_{\overline{\varepsilon}_{\mathrm{T}}}}. \tag{6.20}$$

The last terms of eq. (6.19) and eq. (6.20) are called constraints in the following. During the fit, ε_{T} is varied to fit to the measurements $\vec{X}$ on the one hand, but also to account for the external measurement $\overline{\varepsilon_{\mathrm{T}}}$. Adding more constraints allows including other parameters that systematically influence m_ν^2 and their external measurements into the analysis.

6.3.4 Unified approach

The motivation for a unified approach is to *avoid* the situation of deciding how to report the result of a measurement, when the result has already been determined. This is especially important when dealing with low signal rates or near a physical boundary and the experimenter has to decide, if he wants to report an upper (or lower) limit or even claim a discovery. This behaviour is called "flip-flopping" and is shown and explained in figure 6.6a.

To avoid that behaviour and problems with empty confidence intervals, Feldman and Cousins (F.C.) proposed to use a unified approach [129] and showed applications for neutrino oscillation experiments. Their concept is summarized in the following and highlighted in the context of KATRIN.

6.3.4.1 Ordering principle

The idea of the F.C. unified approach is to use an ordering principle on the likelihood ratio

$$R = \frac{p(x|\mu)}{p(x|\mu_{\mathrm{best}})}. \tag{6.21}$$

It is the ratio of the usual probability $p(x|\mu)$ of obtaining the measurement x when μ is the true value and $p(x|\mu_{\mathrm{best}})$ that chooses $\mu = \mu_{\mathrm{best}}$ to obtain a maximal probability. As an example, in case of a quantity that is physically constrained to positive values [129], μ_{best} is chosen as

$$\mu_{\mathrm{best}} = \max(0, \mathrm{x}), \tag{6.22}$$

since $p(x|\mu)$ is maximal for the smallest possible μ, that means $\mu = 0$, if x is negative; or $\mu = x$ for any positive x. The construction of a confidence belt (see section 6.2.7) of α confidence level (C.L.) makes use of R.

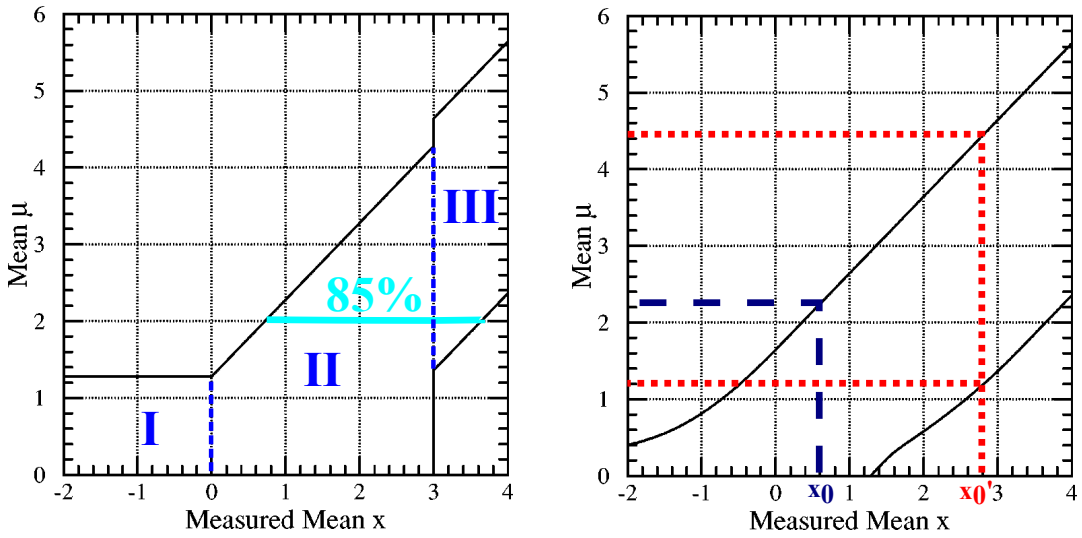

Figure 6.6: **a) Composed 90% "flip-flopping" confidence belt [129], modified.** The underlying probability distribution is a normal distribution around μ, "where only non-negative values for μ are physically allowed" [129]. An experimenter who measures an unphysical value $x < 0$ (region I) can only state an upper limit. The same is true for the attitude that a measurement less than 3σ away from 0.0 cannot rule out a vanishing μ. Therefore, if the measurement falls into region II, an upper limit is stated. But, if the measurement is further than 3σ away from 0.0, the experimenter wants to state a central confidence interval, switching to the confidence belt of region III. This behaviour undermines the concept of a confidence belt, since some intervals show undercoverage (see section 6.2.7). For example, at $\mu = 2$, the belt contains only 85% probability.
b) Confidence belt obtained by the unified approach for Gaussian probability distribution with constraint on non-negative values only [129]. There is a smooth transition between stating an upper limit or a central confidence interval, avoiding undercoverage as in the flip-flopping behaviour.

In case of a discrete p.d.f., for a value μ, R is calculated for all discrete x_i and written in increasing order. Then the probabilities $p(x_i|\mu)$ with highest R are summed up, until the required α is reached. All x_i that have been included in the summation define a horizontal line segment for this specific μ. Repeating this procedure for all μ with reasonable step width yields a confidence belt.

In case of a continuous p.d.f. $p(x|\mu)$, for each μ, the horizontal line segment $[x_\mathrm{L}, x_\mathrm{U}]$ is obtained by solving

$$R(x_\mathrm{L}) = R(x_\mathrm{U}) \tag{6.23}$$

$$\int_{x_\mathrm{L}}^{x_\mathrm{U}} p(x|\mu)\mathrm{d}x = \alpha \tag{6.24}$$

numerically [129]. Again, combining these line segments yields a confidence belt that is shown in figure 6.6b for a normal p.d.f.

Comparing this confidence belt constructed according to F.C. unified approach with figure 6.6a shows that the transitions between the different regions I-III are smooth. This belt can be determined before a measurement or at latest when the statistical uncertainty of the experiment has been evaluated. It allows a consistent reporting of the confidence interval without flip-flopping. By construction, no undercoverage is possible. As usual, a measurement x_0 (x_0') is represented by a vertical line intersecting the belt and allows reading off an upper limit (a central confidence interval). Results of applying F.C. unified approach to KATRIN are shown in section 7.4.

6.3.4.2 Monte-Carlo method to construct F.C. confidence belts

To implement the unified approach into the analysis software KaFit, the methods described in [132] have been realized. There, the logarithm of eq. (6.21) is used

$$-2\log R = \Delta\chi^2 = \chi^2 - \chi^2_\mathrm{best} = \chi^2(x,\mu) - \chi^2(x,\mu_\mathrm{best}) \tag{6.25}$$

with an assumed Gaussian probability distribution $p(x|\mu)$ and χ^2 as in eq. (6.6). μ_best remains as in eq. (6.22) when dealing with a quantity that is constrained to non-negative values only. The general algorithm to obtain a confidence belt of α C.L. by a Monte-Carlo simulation in [132] is:

1. Draw a measurement value x_toy from a Gaussian distribution with expectation value μ and width σ (measurement uncertainty).
2. Compute $\Delta\chi^2$ of eq. (6.25) and arrange the pairs $(x_0, \Delta\chi^2)$ according to increasing $\Delta\chi^2$.
3. Cut the ordered pairs $(x_\mathrm{toy}, \Delta\chi^2)$ at $\Delta\chi^2_c$, such that α of the pairs have $\Delta\chi^2 < \Delta\chi^2_c$.
4. All x_toy with $\Delta\chi^2 < \Delta\chi^2_c$ then belong to the confidence interval of α C.L.

Repeat this procedure for all μ. This method allows easy construction of confidence belts, since it only relies on drawing random numbers and calculating χ^2-terms. Again, the results of this Monte-Carlo approach in KaFit are presented and discussed in chapter 7.4.

Table 6.2: $\Delta\chi^2$ **for confidence level** α **and number of parameters of interest** ν **from [128].** Typical values for α that are related to the standard deviation σ of a Gaussian distribution.

	ν				
α	1	2	3	4	5
$1\sigma = 68.27\%$	1.00	2.30	3.53	4.72	5.89
$2\sigma = 95.45\%$	4.00	6.18	8.02	9.72	11.3
$3\sigma = 99.73\%$	9.00	11.8	14.2	16.3	18.2

6.3.5 Profile likelihood

The concept of profile likelihood [133] is useful to determine uncertainties, both statistical and systematic. It divides the set of fit parameters into parameters of interest

$$\vec{\pi} = \{\pi_1, \ldots, \pi_k\} \tag{6.26}$$

and nuisance parameters

$$\vec{\phi} = \{\phi_1, \ldots, \phi_l\}. \tag{6.27}$$

These nuisance parameters have to be included into the analysis, but are of no real interest for the experimenter. The likelihood function for measurements $\vec{X} = \{X_1, \ldots, X_n\}$ is the same as eq. (6.4)

$$L(\vec{\pi}, \vec{\phi}|\vec{X}) = \prod_i p(X_i|\vec{\pi}, \vec{\phi}), \tag{6.28}$$

just distinguishing between parameters of interest and nuisance parameters. The so-called profile likelihood λ is then defined as [133]

$$\lambda(\vec{\pi}_0|\vec{X}) = \frac{\sup\{L(\vec{\pi}_0, \vec{\phi}|\vec{X}); \vec{\phi}\}}{\sup\{L(\vec{\pi}, \vec{\phi}|\vec{X}); \vec{\pi}, \vec{\phi}\}}. \tag{6.29}$$

λ is a function of the still free parameters of interest of subspace $\vec{\pi}_0$. The numerator for a given, fixed $\vec{\pi}_0$ is the maximum likelihood with respect to optimized nuisance parameters $\vec{\phi}$. The denominator is a normalizing constant, the maximum likelihood, where all parameters $\vec{\pi}$ and $\vec{\phi}$ are optimized. Ref. [133] states that "$-2\log\lambda$ converges in distribution to a χ^2 random variable with k (cf. eq. (6.26)) degrees of freedom". This means, a profile likelihood as shown in figure 6.7 allows the investigation of the behaviour of the likelihood function in the vicinity of the optimum and allows reading off uncertainties by following the standard rules for a χ^2 method (see table 6.2). In contrast to a simple error analysis, for example by gradient methods like MIGRAD in the MINUIT package that usually use the parabolic approximation around the optimum to state symmetric uncertainties, the profile likelihood analysis is more sophisticated. The concept of profile likelihood is also implemented in MINUIT, when using MINOS for error analysis that reports asymmetric errors by investigating the behaviour of the likelihood function around the optimum [134].

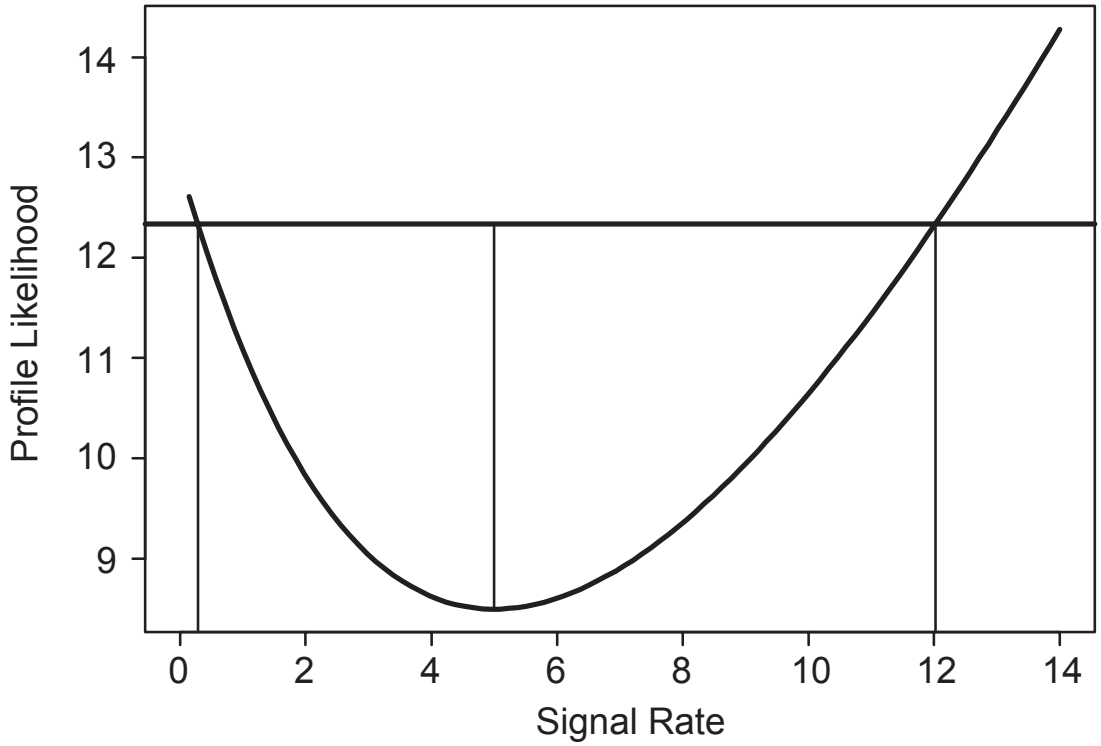

Figure 6.7: **Example profile likelihood from [133]**. The parameter of interest is the signal rate. Shown is the 95% C.L., obtained by an increase of $-2\log\lambda$ by 3.84 (see table 6.2).

Table 6.3: $\Delta\chi^2$ **for confidence level** α **and number of parameters of interest** ν **from [126, 128].**

	ν				
α	1	2	3	4	5
$90\% = 1.645\sigma$	2.71	4.61	6.25	7.78	9.24
$95\% = 1.960\sigma$	3.84	5.99	7.82	9.49	11.1
$99\% = 2.576\sigma$	6.63	9.21	11.3	13.3	15.1
$99.99\% = 3.291\sigma$	15.1	18.4	21.1	23.5	25.7

When applying the profile likelihood approach to KATRIN analyses, m_ν^2 is the only parameter of interest, all other parameters count as nuisance parameters $\vec{\phi} = \{E_0, R_\mathrm{s}, R_\mathrm{b}\}$. The profile likelihood is

$$\lambda(m_{\nu,0}^2|\vec{X}) = \frac{\sup\{L(m_{\nu,0}^2, E_0, R_\mathrm{s}, R_\mathrm{b}|\vec{X}); E_0, R_\mathrm{s}, R_\mathrm{b}\}}{\sup\{L(m_\nu^2, E_0, R_\mathrm{s}, R_\mathrm{b}|\vec{X}); m_\nu^2, E_0, R_\mathrm{s}, R_\mathrm{b}\}}. \tag{6.30}$$

An additional promising possibility of the profile likelihood method is to extend the set of nuisance parameters by (source) parameters that might have systematic influences on m_ν^2 (see section 6.3.3). Furthermore, this can be combined with the use of constraints to the likelihood in eq. (6.19). If an uncertainty on a (source) parameter influences m_ν^2, the profile likelihood will reveal it, creating a broader distribution around the best-fit value of $\hat{m}_\nu^2$.

In KaFit, the profile likelihood approach has been implemented preliminarily to examine its use for KATRIN. The needed likelihood functions in classes `KFLog-LikelihoodKATRIN` are already available, since they are generally used for fitting KATRIN measurements. The same is true for required numerical minimization routines. Section 8.4 shows applications of the profile likelihood method in KATRIN.

7. Statistical analysis and sensitivity studies

With the available analysis tools it is possible to determine the statistical uncertainty of KATRIN by various methods that have been explained in the previous chapter. Together with the systematic uncertainty (see chapter 8) the total uncertainty is determined and statements on KATRIN's sensitivity on m_ν^2 are thus possible. In section 7.1, the new simulation and analysis software is applied to conditions of older simulations of the KATRIN Design report. This comparison is performed to check and verify the results of the new code. The results of new and old simulations regarding the statistical uncertainty of KATRIN are compared and discussed. Section 7.2 evaluates the influence of background on the KATRIN measurement, first the impact of the overall background rate and then fluctuations in time. The power of the full source simulation is used in section 7.3 to determine the physics sensitivity of KATRIN with a detailed, realistic model that for the first time considers inhomogeneities of the source. This approach can be regarded as the state of the art KATRIN model. The chapter concludes in section 7.4 with the applications of Feldman and Cousins unified approach to KATRIN.

7.1 Re-evaluation of the design sensitivity

The spectrum simulation SSC (section 4.2) and the analysis package KaFit (section 6.2) are used to re-evaluate the design sensitivity of KATRIN. Comparing results from the present software with results from the KATRIN Design Report [48] allows one to crosscheck the new routines and to detect the effects of the new, more sophisticated approaches, for example of the minimization routines, the spectrum calculation itself or the treatment of fit values $\hat{m}_\nu^2 < 0$ in the unphysical region.

The KATRIN Design Report (TDR) defined the default KATRIN simulation parameters for the WGTS and other system, shown in table 7.1. A total measurement time of 3 years within a measurement interval of 30 eV below and 5 eV above the endpoint energy E_0 was chosen. The measurement time distribution was optimized for a neutrino mass in the (sub-)eV range (see also section 6.2.1). An ensemble approach "by

Table 7.1: **Parameters for a KATRIN simulation in [48, 135].**

parameter	setting
column density	$\rho d = 5 \cdot 10^{17}\,\mathrm{cm}^{-2}$
scattering probabilities	$P_0 = 0.413339$
	$P_1 = 0.292658$
	$P_2 = 0.167331$
	$P_3 = 0.079129$
	$P_4 = 0.031776$
"active" source cross-section	$A_\mathrm{S} = 53.3\,\mathrm{cm}^2$
magnetic field strengths	$B_\mathrm{S} = 3.6\,\mathrm{T}$
	$B_\mathrm{A} = 3 \cdot 10^{-4}\,\mathrm{T}$
	$B_\mathrm{max} = 6.0\,\mathrm{T}$
tritium purity	$\varepsilon_\mathrm{T} = 0.95$
background rate	$\dot{N}_\mathrm{b} = 0.01\,\mathrm{cps}$
detection efficiency	$\varepsilon_\mathrm{det} = 0.9$
measurement time distribution	$t = 3\,\mathrm{y}$; optimized
measurement interval	$[E_0 - 30\,\mathrm{eV}, E_0 + 5\,\mathrm{eV}]$
Doppler effect	neglected
differential spectrum calculation	includes Fermi function
	includes radiative corrections
	includes extension to negative m_ν^2
tritium endpoint energy	$E_0 = 18575\,\mathrm{eV}$

repeating large samples of simulated experiment-like integral β-spectra" [48] yielded a statistical uncertainty of

$$\sigma_\mathrm{stat} = 0.018\,\mathrm{eV}^2 \tag{7.1}$$

for KATRIN. Together with an assumed systematic uncertainties of in total

$$\sigma_\mathrm{syst} = 0.017\,\mathrm{eV}^2, \tag{7.2}$$

this results in a total uncertainty

$$\sigma_\mathrm{tot} = \sqrt{\sigma_\mathrm{stat}^2 + \sigma_\mathrm{syst}^2} = 0.025\,\mathrm{eV}^2. \tag{7.3}$$

By $m_\nu < \sqrt{1.645 \cdot \sigma_\mathrm{tot}}$ (see table 6.1) it can be converted to a 90% C.L. upper limit of $m_\nu < 200\,\mathrm{meV}$ in the null measurement.

The former calculations of the spectrum are replaced within this work by SSC and the analysis routines by the package KaFit. Both parts are configured to have the same parameters as the default KATRIN simulation in table 7.1. To be as close as possible to the former calculations, SSC does not make use of its ability to treat the WGTS as union of many small voxels with local physical properties. Instead, the WGTS is described as "one volume" by integral quantities only to reproduce former results. In the following, two approaches are presented to determine the statistical uncertainty of KATRIN and deduce the sensitivity on m_ν^2.

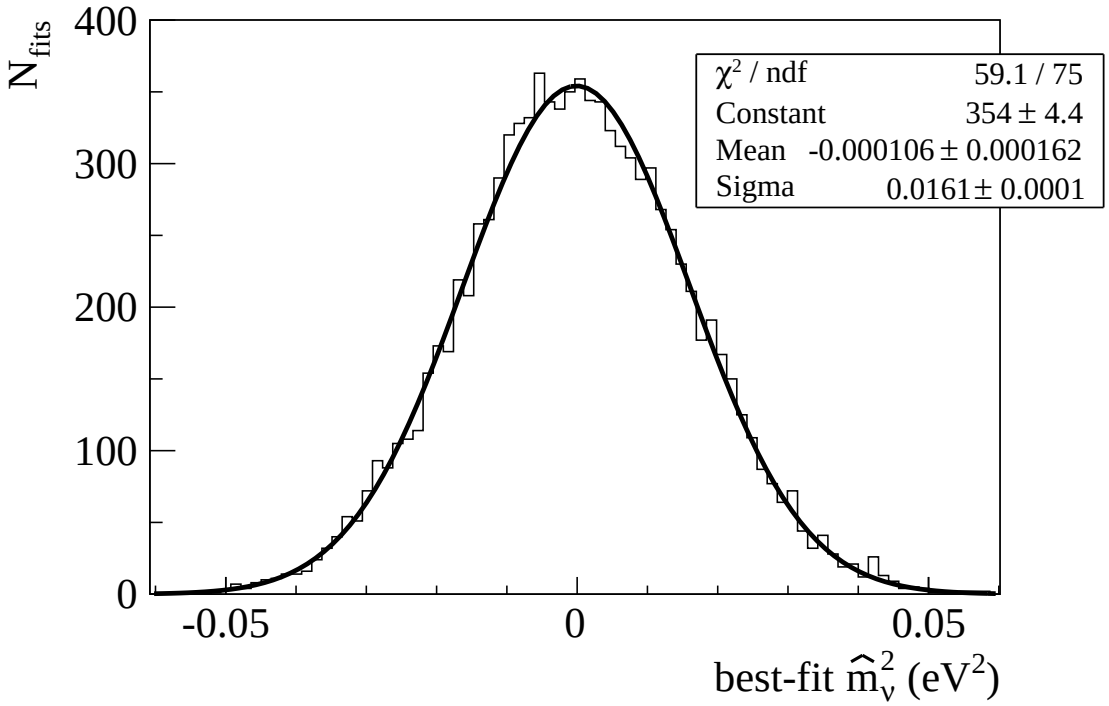

Figure 7.1: **KATRIN ensemble simulation.** 10000 full KATRIN experiments are simulated with simulation input $m_\nu^{2,\mathrm{sim}} = 0.0\,\mathrm{eV}^2$ and analysed. Each time, the best-fit $\hat{m}_\nu^2$ is filled into the histogram. The width of the distribution $\sigma_{\mathrm{stat}} = 0.0161\,\mathrm{eV}^2$ is interpreted as statistical uncertainty of the KATRIN experiment.

7.1.1 Ensemble simulations

The simulation of a large sample of KATRIN experiments and their analysis as described in section 6.3.1 allows the determination of the statistical uncertainty of KATRIN. Figure 7.1 shows the result of these ensemble simulations with

$$\sigma_{\mathrm{stat}} = (0.0161 \pm 0.0001)\,\mathrm{eV}^2. \tag{7.4}$$

7.1.2 Profile likelihood

The profile likelihood approach as discussed in section 6.3.5 allows investigating the curvature of the likelihood function and deducing the statistical uncertainty of a measurement. At KATRIN, eq. (6.30) is used with m_ν^2 as single parameter of interest. In figure 7.2, m_ν^2 is varied, and the nuisance parameters of the spectrum are fitted to minimize the profile likelihood $-2\log\lambda$. For standard KATRIN conditions (see table 7.1) and an assumed true neutrino mass of $m_\nu^2 = 0.0\,\mathrm{eV}^2$, the profile likelihood is slightly asymmetric and yields

$$\begin{aligned} \sigma_{\mathrm{stat}}^- &= (0.0175 \pm 0.0005)\,\mathrm{eV}^2 \\ \sigma_{\mathrm{stat}}^+ &= (0.0165 \pm 0.0005)\,\mathrm{eV}^2 \end{aligned} \tag{7.5}$$

by determining the function increase by 1.0 of $-2\log\lambda$ around the minimum.

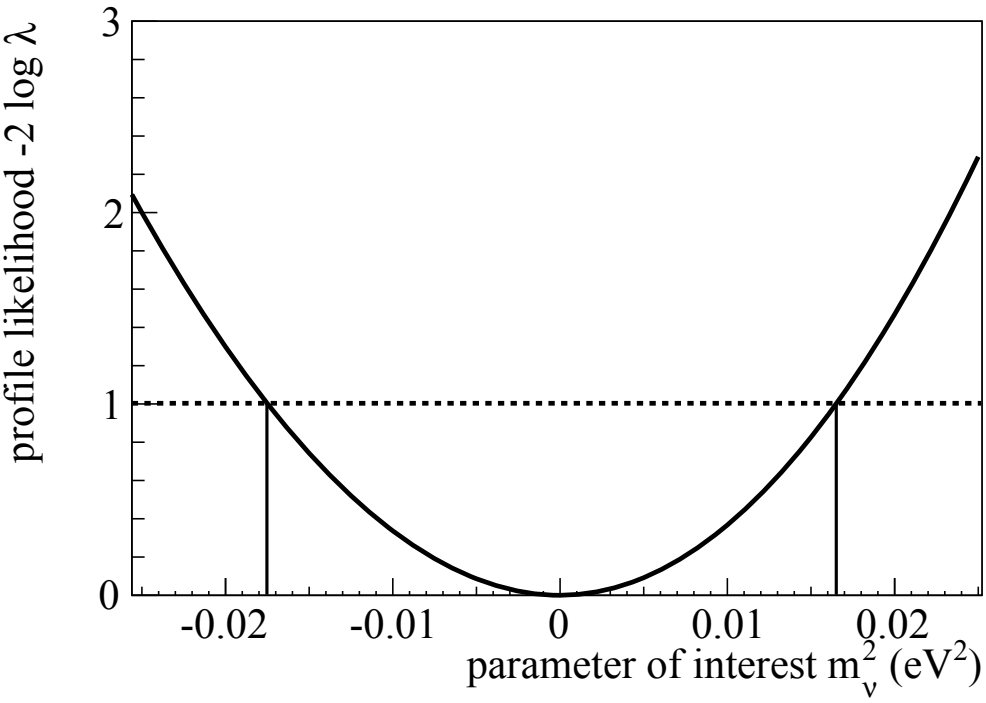

Figure 7.2: **Profile likelihood of KATRIN.** For different values of the parameter of interest m_ν^2, the negative log-likelihood function is minimized with respect to all nuisance parameters. An increase of the function by 1 determines the statistical uncertainty stated in eq. (7.5).

7.1.3 Comparison of statistical uncertainties

The statistical uncertainty obtained in this work in eq. (7.4) and (7.5) are up to 10% smaller that the value of eq. (7.1) from the KATRIN Design Report. Part of the difference can be attributed to the difference in the size of the ensemble used in the respective studies. It can cause fluctuations that are not stated in [48]. Analysing a single raw data file of [135] with an ensemble of only 100 spectra yields $\sigma_{\mathrm{stat}} = (0.0165 \pm 0.0017)\,\mathrm{eV}^2$, that is compatible with eq. (7.4) and (7.5).

Furthermore, the two analyses used different spectrum calculations. Although the new source simulation SSC is adapted to be as close as possible to the experimental configuration that was used before, there are up to 5% differences in the calculated rate of the integrated spectrum. The differences were traced back to the description of the differential β-spectrum. The Fermi function, radiative corrections and calculation of the phase space are identical, so the only remaining difference is the final state distribution (FSD). The FSD is treated differently in the two approaches. It was not possible to use the same description of the FSD that has been used in former calculations within SSC, so small differences in the spectrum calculation have to be accepted. The current calculation uses a more detailed FSD (see section 4.2.5.3).

In addition, differences may be introduced by the respective minimization algorithms in the analyses. The new code KaFit uses TMinuit to minimize χ^2 (or $-\log L$) to determine m_ν^2 whereas the old code calculated χ^2 on a parameter grid, choosing the lowest occurring χ^2-value as minimum. This could lead to a different estimation of σ_{stat} as well.

In summary, the agreement of the statistical uncertainty obtained by different methods with KaFit and of former simulations in [48] is sufficient to investigate new effects on the sensitivity of KATRIN.

7.2 Influence of background

In [136], the influence of the background rate $\dot{N}_{\mathrm{b}}$ on the neutrino mass determination within an integrating measurement is derived analytically. The statistical uncertainty σ_{stat} is related to $\dot{N}_{\mathrm{b}}$ as

$$\sigma_{\mathrm{stat}} \propto \dot{N}_{\mathrm{b}}^{1/6}. \tag{7.6}$$

This is derived by simplifying the measurement to one single hypothetical measurement point (see also eq. (7.7)). In reality, several measurement points are required to use the information on the spectral shape to determine all the fit parameters of eq. (6.3). In fact, eq. (7.6) "underestimates the necessary measurement time about an order of magnitude" [32], but the functional dependence remains.

With the described ensemble methods of KaFit, σ_{stat} on m_ν^2 of a full KATRIN measurement (TDR conditions, see table 7.1) has been determined for various $\dot{N}_{\mathrm{b}}$. The results are presented in table 7.2.

In general, the simulated values of σ_{stat} are higher than those expected by eq. (7.6) when fixing σ_{stat} at $\dot{N}_{\mathrm{b}} = 10^{-2}\,\mathrm{cps}$ as the reference value. This is caused by using the measurement time distribution that was optimized for exactly that reference case. For other background rates, the measurement time would have to be adapted, since

Table 7.2: **Statistical uncertainty σ_{stat} of KATRIN for different background rates $\dot{N}_{\mathrm{b}}$.** In the second column, σ_{stat} is obtained by KaFit. The third column $\sigma_{\mathrm{stat}}^{\mathrm{exp}}$ shows the expectation of eq. (7.6).

$\dot{N}_{\mathrm{b}}$ (10^{-3}cps)	σ_{stat} $(\mathrm{eV})^2$	$\sigma_{\mathrm{stat}}^{\mathrm{exp}}$ $(\mathrm{eV})^2$
1	0.0113 ± 0.0002	0.0109
3	0.0124 ± 0.0002	0.0131
10	0.0160 ± 0.0002	0.0160
30	0.0221 ± 0.0003	0.0192
100	0.0345 ± 0.0004	0.0235

KATRIN is most sensitive to m_ν^2 at a retarding energy qU_{opt} where the rate of the integrated spectrum $\dot{N}_{\mathrm{s}}(qU_{\mathrm{opt}})$ is twice the background rate $\dot{N}_{\mathrm{b}}$ [32]

$$\dot{N}_{\mathrm{s}}(qU_{\mathrm{opt}}) = 2 \cdot \dot{N}_{\mathrm{b}}. \tag{7.7}$$

This shows that it is important on the one hand to keep the background rate low. On the other hand, $\dot{N}_{\mathrm{b}}$ should be estimated and measured early during the neutrino mass measurement to adapt the measurement time distribution right from the start to be as sensitive as possible on m_ν^2.

Additional effects like an energy dependent background rate, that means a slope in the analysed part of the spectrum below the endpoint energy, were already investigated in [48]. Motivated by the time-dependent backgrounds which are discussed in detail in [83, 125], KaFit is used to determine the sensitivity of KATRIN, if the expectation of $\dot{N}_{\mathrm{b}}$ is not constant. For that purpose, a Gaussian distribution around mean $\dot{N}_{\mathrm{b}}$ and width $\sigma = (1\%, 5\%, 10\%) \cdot \dot{N}_{\mathrm{b}}$ is assumed as the fluctuating background rate. Ensemble simulations of full 3-year KATRIN experiments[1] result in figure 7.3. The larger $\dot{N}_{\mathrm{b}}$ and the larger the fluctuation σ, the larger the statistical uncertainty σ_{stat} gets. This indicates the strong impact of background fluctuations on the m_ν^2 determination.

In [83], the impact on m_ν^2 from more complicated time-dependent backgrounds, namely electron cascades from single radon decays in the spectrometer volume, was investigated with the developed analysis tools presented in this work at hand. Events that increase the background rate during a specific time are especially critical for KATRIN. Then, the order of measurement points (retarding energies qU) and the specific length of measurement intervals even influence the sensitivity.

7.3 Sensitivities when using a detailed source model

With the presented spectrum calculation SSC it is now possible to simulate the expected spectra for KATRIN with a detailed source model, which is referred to as the "full source model" in the following. This model is close to the KATRIN model in table 7.1, but makes use of SSC's ability to divide the WGTS into small volumes,

[1] In this case, the measurement is not broken down to several single measurements of few hours, but treated "integrally" as time spend at each retarding voltage U of the spectrometer.

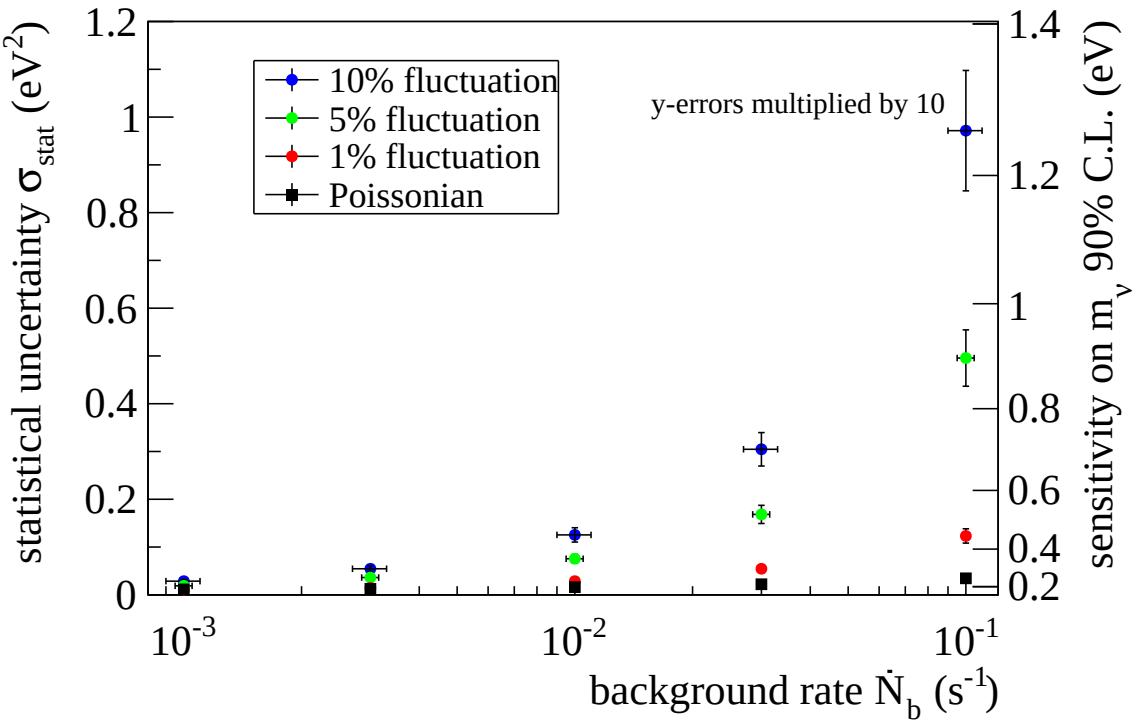

Figure 7.3: **Dependence of the statistical uncertainty of KATRIN on the background rate.** The y-error bars are increased by a factor of 10 for visibility. The Poissonian case stands for a "usual" KATRIN measurement with background events with a constant expectation value $\dot{N}_\mathrm{b}$. The fluctuations of 1, 5 and 10% stand for a varying Gaussian background rate around the mean $\dot{N}_\mathrm{b}$ during a full KATRIN measurement. On the right axis, σ_stat is directly converted to a 90% upper limit for KATRIN assuming a systematic uncertainty of $\sigma_\mathrm{syst} = 0.017\,\mathrm{eV}^2$.

so that effects from changes in the local physical properties and source parameters can be studied. The following parameters are used in simulations with the "full source model":

- Voxelization: This is the main difference to former simulations of KATRIN. Source inhomogeneities can be studied by dividing the source volume into small "voxels" (see section 4.2.1). Since most source parameters only have a longitudinal dependency, azimuthal and radial inhomogeneities are neglected for the moment. Therefore, the source is divided longitudinally into 1000 slices, each with a width of 1 cm. This allows for detailed profiles of the different source parameters. To reduce the necessary calculations later, every 100 bins are then rebinned, weighting the local physical properties. This is more accurate than starting with only 10 slices as was shown in [89], and has the advantage of fast calculations that are required for large ensemble simulations.

- Density profile and column density: The routines that were explained in chapter 5 are used in SSC to set the density profile of the WGTS. The column density (with the default value of $\rho d = 5 \cdot 10^{17}\,\mathrm{cm}^{-2}$) is specified by the user and the program calculates the necessary injection pressure and the resulting density distribution along the source.

- Temperature profile: In contrast to the TDR KATRIN model that used a fixed and homogeneous temperature of $T = 30\,\mathrm{K}$, a temperature profile $T(z)$ is incorporated into SSC. For the following simulations, the profile is flat in the center with $T = 30\,\mathrm{K}$ and rises quadratically towards the pumping chambers by $\Delta T = 30\,\mathrm{mK}$.

- Velocity profile: The gas dynamics simulations in chapter 5 also provide a velocity distribution for T_2 molecules in the source, which describes their thermal movement at $T = 30\,\mathrm{K}$ and the bulk velocity u_z due to injection and pumping.

- Scattering probability: Instead of fixing the scattering probabilities to the mean values of the whole source, each voxel in SSC can have its specific scattering probabilities for electrons emitted within its boundaries. For instance, electrons from the rear side of the source at $z = -5\,\mathrm{m}$ have a probability P_0 of only 15.3% to cross the source without scattering inelastically, whereas $P_0 = 33.8\%$ for electrons from the center at $z = 0\,\mathrm{m}$ and $P_0 > 99\%$ for electrons that are emitted right at the front end of the source at $z = +5\,\mathrm{m}$.

- Magnetic field: SSC uses the field calculation methods provided by Kassiopeia (section 4.1). The calculated magnetic field strength in the WGTS is shown in figure 4.3. In general, the field strength is lower than the previously used standard value $B_\mathrm{S} = 3.6\,\mathrm{T}$. This means the active source area A_S is increased, since the transported magnetic flux $\Phi = B_\mathrm{S} \cdot A_\mathrm{S}$ remains constant. Then, for a constant column density ρd and tritium purity ε_T, the number of signal counts

$$N \propto \rho d \cdot A_\mathrm{S} \cdot \varepsilon_\mathrm{T} \cdot \Omega \cdot P_0 \tag{7.8}$$

  is increased at first sight. But on the other hand, the maximal opening angle θ_max of eq. (2.2) decreases, since more electrons are reflected at the high magnetic field of the pinch magnet $B_\mathrm{max} = 6.0\,\mathrm{T}$. This reduces the solid angle Ω

of eq. (4.16) and thereby the number of electrons that can reach the detector. Additionally, a lower $\theta_{\max}$ increases the mean scattering probabilities P_i of eq. (4.8) for low i. Combining all the effects leads to a smaller count rate for the full source model as can be seen in the first and second column of table 7.3.

- Differential β-spectrum and final state distribution: The calculation of the differential spectrum according to eq. (4.14) remains nearly unchanged. The corrections due to Fermi function and radiative corrections are the same functions that have been used for the simulations in the TDR. The final state distribution is used in an updated version (see section 4.2.3). In the full source model it is possible to (de-)activate the Doppler effect that broadens the β-spectrum due to the thermal movement of molecules at $T = 30\,\mathrm{K}$ and the additional bulk velocity u_z (see above).

- Integrated β-spectrum: In the full source model, the expected integrated spectrum is calculated as in eq. (4.17) by summing up the contributions from all source voxels.

- Other parameters: All other parameters are kept at their value/setting of table 7.1.

The "ensemble method" (see section 6.3.1) with 4000 simulations within the KaFit package allows the evaluation of the statistical uncertainty of KATRIN with the full source model. In the case of neglecting the Doppler effect, the statistical uncertainty was found to be

$$\sigma_{\mathrm{stat}}^{\mathrm{w/o}} = (0.0160 \pm 0.0002)\,\mathrm{eV}^2, \tag{7.9}$$

while that evaluated with the Doppler effect yielded

$$\sigma_{\mathrm{stat}}^{\mathrm{w}} = (0.0153 \pm 0.0002)\,\mathrm{eV}^2. \tag{7.10}$$

First of all, the obtained $\sigma_{\mathrm{stat}}^{\mathrm{w/o}}$ is very close to eq. (7.4), since the expected signal rates shown in table 7.3 are very similar in both models. Applying the Doppler effect to the spectrum increases the count rate around the endpoint by shifting lower energy electrons to higher energies[2]. This results in higher count rates and thus a lower statistical uncertainty. In a way, this seems counter-intuitive, since one would expect that the Doppler effect as an energy uncertainty decreases the power of KATRIN to measure a neutrino mass. To check this, a typical energy shift of the Doppler effect of 130 meV (eq. (4.23)) is added to the energy resolution of the main spectrometer to have a slightly worse energy resolution of $\Delta E = 1.06\,\mathrm{eV}$. This results in a statistical uncertainty of

$$\sigma_{\mathrm{stat}}^{\Delta E} = (0.0161 \pm 0.0002)\,\mathrm{eV}^2 \tag{7.11}$$

that is increased marginally – only within the stated uncertainty – compared to eq. (7.9). This indicates that an additional energy uncertainty like the Doppler effect has no drastic influence on the statistical uncertainty. Nevertheless, further

[2] Although the molecule movement is omnidirectional with a small addition in positive respectively negative z-direction due to the bulk velocity u_z, the steep dropping spectrum near the endpoint energy causes a net effect of shifting the spectrum towards higher energies.

Table 7.3: **Comparison of rates of the integrated spectrum $\dot{N}_s(qU)$ in case of vanishing neutrino mass with different simulation models.** The count rates $\dot{N}_s^{TDR}$ of a WGTS model of [48], presented in table 7.1, are given in the first column. The full source model is described in the main text. Here, the Doppler effect has been switched on ($\dot{N}_s^{w}$) and off ($\dot{N}_s^{w/o}$) for comparison.

qU (eV)	$\dot{N}_s^{TDR}$ (s^{-1})	$\dot{N}_s^{w/o}$ (s^{-1})	$\dot{N}_s^{w}$ (s^{-1})
$E_0 - 30$	23.5	23.4	24.6
$E_0 - 20$	5.83	5.77	6.08
$E_0 - 10$	0.486	0.474	0.500
$E_0 - 5$	0.0236	0.0222	0.0235

investigations regarding systematic shifts due to the Doppler effect are addressed in section 8.2.

The studies in this chapter demonstrated the reliability of the new SSC and KaFit software, which have additional features, such as the treatment of source inhomogeneities and Doppler effect, over the previous codes. The obtained uncertainties are consistent with those of a simplified KATRIN simulation as done in [48]. In view of the required systematic studies following in the next chapter, the WGTS model as presented in this work should be regarded in the future as "standard" KATRIN model.

7.4 Unified approach

Since m_ν^2 is expected to be close to zero (see section 1), negative values are physically forbidden and the effect of non-vanishing m_ν^2 on the β-spectrum is small, it is not guaranteed that KATRIN will be sensitive enough to claim a measurement or that it will only be able to state an improved upper limit. Therefore, the Feldman-Cousins unified approach (see section 6.3.4) is suitable for KATRIN to consistently report its results later.

If the measurement of m_ν^2 is supposed to be obtained with a Gaussian resolution function with the constraint $m_\nu^2 \geq 0$, the typical Feldman-Cousins confidence belt in figure 6.6b can be used. It has to be adapted to KATRIN conditions by considering the statistical uncertainty σ_{stat}: Since figure 6.6b was produced with $\sigma = 1.0$, both axes can be scaled by σ_{stat}, resulting in figure 7.4a. As usual, a measurement result $m_{\nu,0}^2$ of KATRIN can be converted consistently to a 90% confidence interval, independent of a positive or negative value, by reading off the intersections of a vertical line at $m_{\nu,0}^2$ with the belt borders.

Additionally, the question remains, how to include systematics into this method. A simple approach is to add statistical and systematic uncertainties quadratically to obtain σ_{tot}. If this is allowed, remains topic for further investigations. As a first test, this has been done in the following.

To check the consistency of this method, figure 7.4b shows the 5σ-confidence belt with $\sigma_{tot} = 0.025\,eV^2$ that represents a 99.99994267% confidence level. For a measurement of $m_\nu^2 < 0.125\,eV^2$, which corresponds to a neutrino mass of $m_\nu < 0.35\,eV$

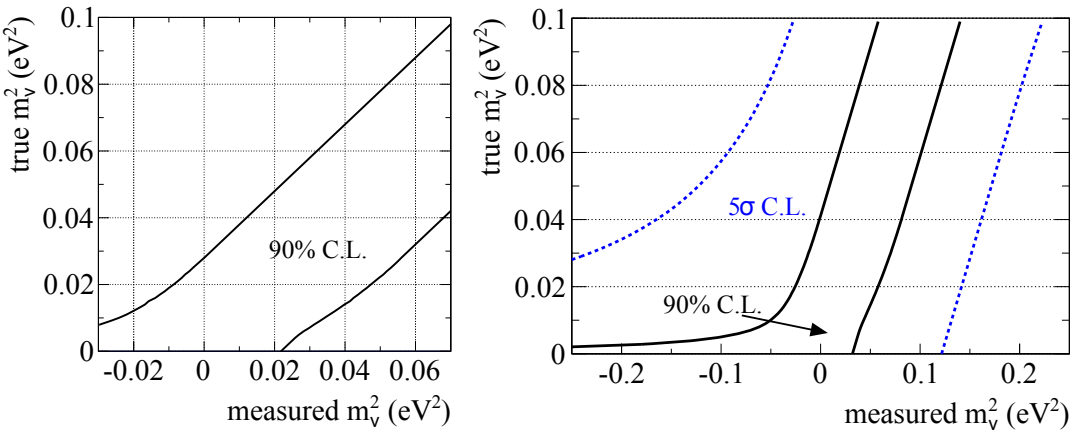

Figure 7.4: **a) Confidence belt of 90% C.L. for KATRIN with** $\sigma_{\text{stat}} = 0.018\,\text{eV}^2$**.** It can either be obtained by scaling the standard Feldman-Cousins confidence belt for a Gaussian p.d.f. of [129] with σ_{stat} or by using the recipe that has been explained in section 6.3.4.1 and implemented into KaFit.
b) 5σ**-confidence belt of KATRIN with** $\sigma_{\text{tot}} = 0.018\,\text{eV}^2$**.** For orientation, the 90% confidence belt also obtained with σ_{tot} has been drawn as well.

KATRIN can only state an upper limit on m_ν^2, but if the measured value were higher, then KATRIN could claim a detection of m_ν^2. These results are consistent with previous results in [48].

The problem of this method is that m_ν^2 is treated as a single parameter, like a directly measured quantity. Instead, KATRIN measures a spectrum and fits several parameters to it, one of them is m_ν^2. The influence of m_ν^2 on the spectrum and correlations between these parameters and m_ν^2 are not considered immediately by the unified approach, they have to be handled within the general analysis strategy. In addition, further difficulties will occur, if the measured m_ν^2 is not distributed according to a Gaussian. The numerical procedures get more complicated, so that the following method may be favoured.

The Monte-Carlo method described in section 6.3.4.2 is independent of the underlying p.d.f. For each possible true value μ of the neutrino mass squared an expected 3y-KATRIN spectrum is calculated. Following the presented recipe, the confidence belt is constructed by repeated drawing of m_ν^2 from the p.d.f. and by calculating the differences $\Delta\chi^2$ of eq. (6.25).

Since m_ν^2 is drawn and kept fixed at that value, the other correlated fit parameters E_0, R_s and R_b (see eq. (6.3)) have to be fitted each time to still minimize χ^2 between the calculated KATRIN spectrum ("measurement") and the theoretical expectation. The difference $\Delta\chi^2$ is then used in the ordering principle to obtain figure 7.5.

Both presented methods produce KATRIN confidence belts that allow reporting the result of the neutrino mass measurement. The advantage of the original approach is that the confidence belt can be calculated by easy numerical methods. But it is only applicable in easy cases like a Gaussian p.d.f. In contrast to that the Monte-Carlo approach can deal with any given p.d.f., but needs extensive simulations to obtain a smooth confidence belt.

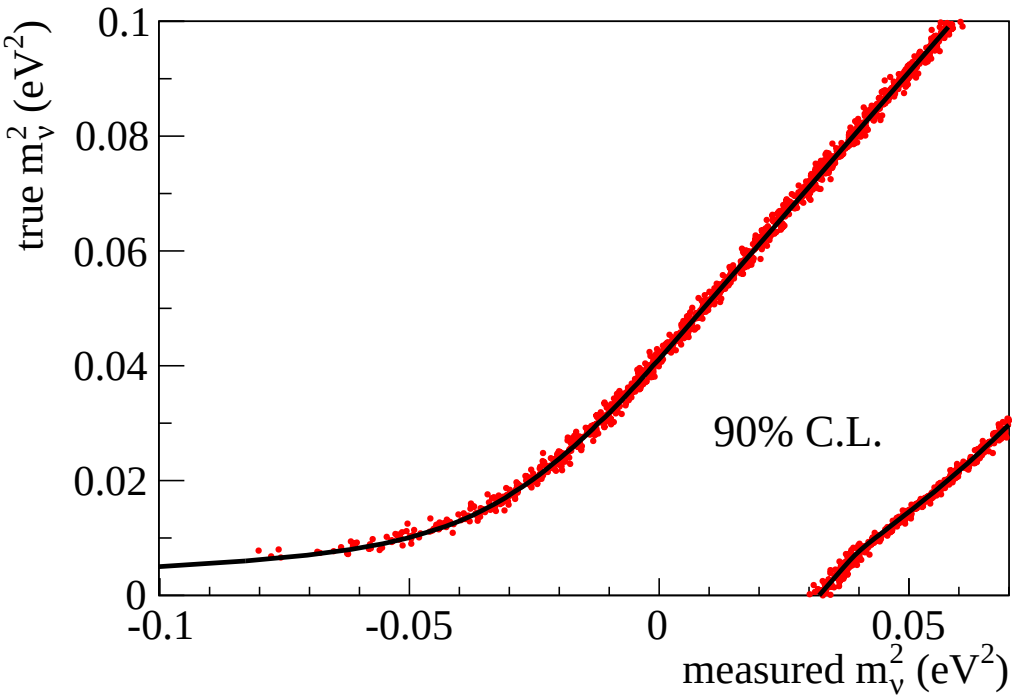

Figure 7.5: **90% confidence belt for KATRIN obtained by the Monte-Carlo construction method of [132].** A Gaussian p.d.f. with total uncertainty $\sigma_{\mathrm{tot}} = 0.025\,\mathrm{eV}^2$ resulting in the red dots is used to compare it with the original Feldman-Cousins confidence belt (solid line). The agreement between Monte-Carlo method and numerical construction is good. The fluctuations of the belt borders occur due to the underlying statistical nature of the Monte-Carlo method. They could be reduced to some extent by increasing the numbers of simulated toy experiments.

8. Analysis of systematic uncertainty

The methods in chapter 6 are also applicable to determine the systematic effects on m_ν^2 at KATRIN. Section 8.1 is treated as test scenario where the systematic effect of column density variations is re-evaluated. Section 8.2 considers the uncertainty of the beam tube temperature on m_ν^2 since that is of special relevance for the demonstrator tests in the final chapter of this work. The influence of the tritium purity on m_ν^2 in section 8.3 completes the investigations of source parameters and is handled as a representative showcase for considering systematics in the KATRIN analysis as shown in section 8.4.

8.1 Re-evaluation of column density variations

Shifts of the column density ρd change the source activity (see eq. (3.3)) and modify the scattering probabilities (see section 4.2.2). If these shifts to lower (higher) ρd remained unaccounted for in the KATRIN analysis, the lower (higher) activity would result in lower (higher) count rates of the integrated spectrum. Since this is exactly the effect of a non-vanishing neutrino mass squared m_ν^2, shifts of ρd cause a shift in m_ν^2.

To quantify this systematic effect, the ensemble method (see section 6.3.1) with the generation of individual trial runs by a combination of SSC and KaFit can be used. As source model, the same detailed description of the source as for sensitivity studies in section 7.3 is used, but without considering the Doppler effect for simplification. Then, 4000 full KATRIN spectra are simulated with the nominal column density $\rho d^{\mathrm{sim}} = 5 \cdot 10^{17}\,\mathrm{cm}^{-2}$. The analysis then assumes $\rho d^{\mathrm{fit}} = (1+\epsilon) \cdot \rho d^{\mathrm{sim}}$ with $\epsilon = \{1, 2, 5, 10\} \cdot 10^{-3}$. The resulting distributions of best-fit values $\hat{m}_\nu^2$ are similar to that in figure 6.5 with Δm_ν^2 for different unaccounted for shifts of ρd. Additionally, Δm_ν^2 is shown in figure 8.1 in comparison to values stated in the KATRIN Design report [48]. The new results show that the influence of ρd is less severe than the old simulations proposed. But this does not change the statement of eq. (3.5) that maximal variations of $\Delta\rho d/\rho d$ of $2 \cdot 10^{-3}$ are allowed.

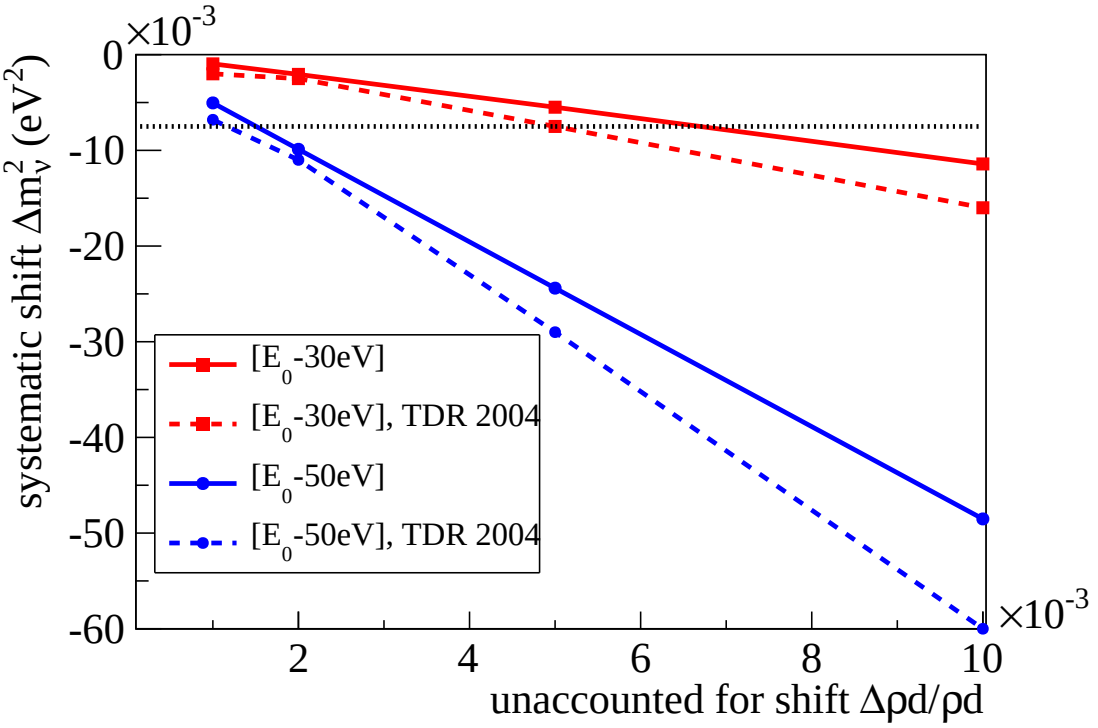

Figure 8.1: **Systematic shift Δm_ν^2 due to unaccounted for shifts $\Delta\rho d/\rho d$ of the column density.** The solid lines show the results from simulations with SSC and KaFit, the dashed lines are from [48]. Two different analysis windows are considered: 30 eV and 50 eV below the spectrum endpoint energy E_0. The dotted black line at $\Delta m_\nu^2 = -0.0075\,\mathrm{eV}^2$ shows the maximum allowable systematic shift of eq. (6.14).

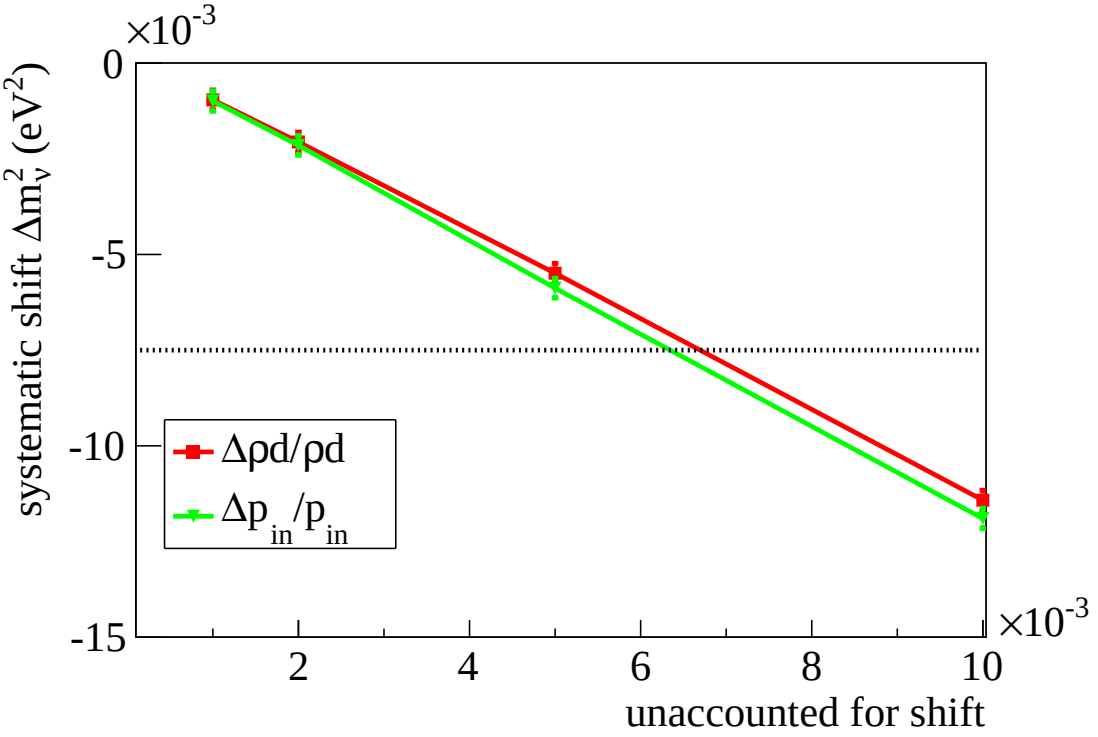

Figure 8.2: **Systematic shift Δm_ν^2 due to unaccounted for shifts.** Either injection pressure shifts $\Delta p_{\text{in}}/p_{\text{in}}$ or column density shifts $\Delta\rho d/\rho d$ (see also figure 8.1) for a KATRIN analysis interval of 30 eV below E_0.

To show the power of the new code, the influence of the injection pressure p_{in} is examined as an example for various parameters that influence ρd (see table 5.1) and therefore the KATRIN measurement. In SSC and KaFit, the gas dynamics routines generate a KATRIN spectrum with a detailed WGTS and nominal $p_{\text{in}}^{\text{sim}}$, and analyse this spectrum with an increased (decreased) $p_{\text{in}}^{\text{fit}}$. Using an ensemble method, the resulting Δm_ν^2 of 4000 simulations for different shifts $\Delta p_{\text{in}}/p_{\text{in}}$ is shown in figure 8.2. It confirms the expectation that changes in p_{in} directly translate to changes on ρd. But it also shows that the influence of experimental observables on m_ν^2 can be determined directly instead of using derived entities like ρd.

8.2 Influence of the beam tube temperature

The absolute temperature T_0 of the beam tube is a systematic effect in the determination of m_ν^2, since it influences the column density in the WGTS. In addition, the temperature influences the final state distribution of the β-decay of molecular tritium and defines the strength of the Doppler effect that broadens the β-spectrum.

Influence on the column density

Similar to the ensemble simulations in section 8.1 that considered changes of the column density or the injection pressure, the beam tube temperature can be shifted in an analysis with respect to the Monte-Carlo truth of $T_0 = 30$ K. Figure 8.3 shows the resulting systematic shifts Δm_ν^2.

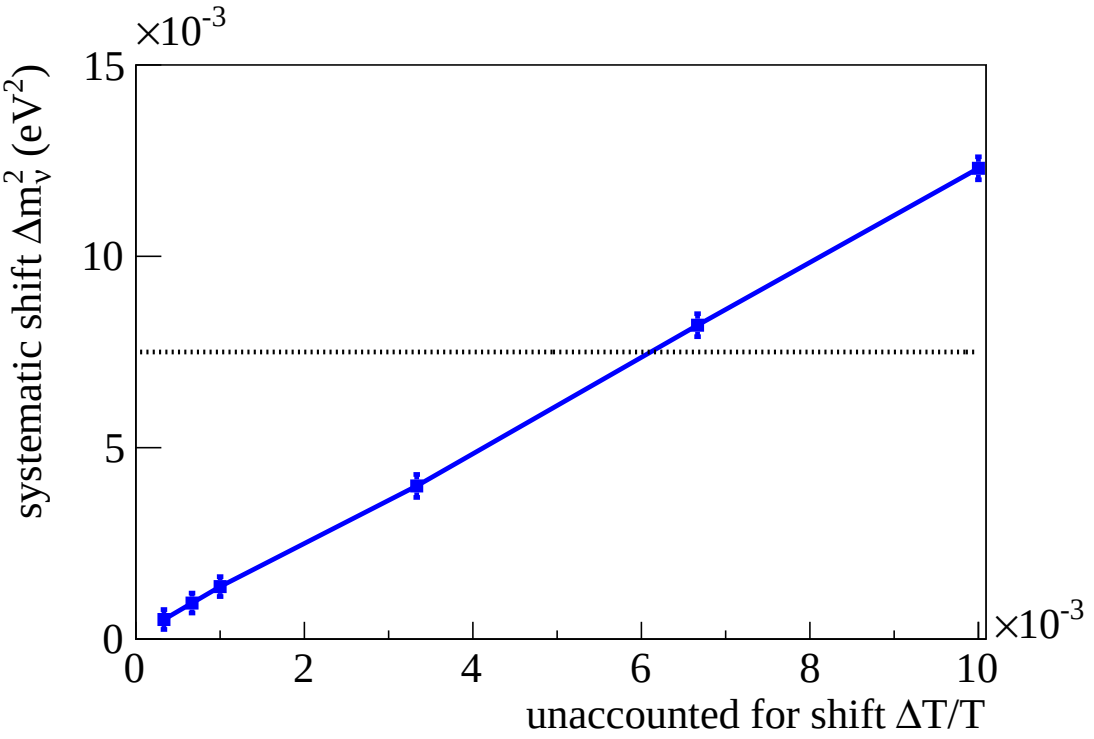

Figure 8.3: **Systematic shift Δm_ν^2 due to an unaccounted for shift of the beam tube temperature T.** The measurements within the typical interval $[E_0 - 30\,\mathrm{eV},\ E_0 + 5\,\mathrm{eV}]$ are simulated with a nominal temperature of $T_0 = 30\,\mathrm{K}$, the analysis is performed with slightly higher temperatures T. The dotted line marks the maximal allowed systematic shift $|\Delta m_\nu^2| = 0.0075\,\mathrm{eV}^2$.

An unaccounted for shift of T_0 by $\approx 0.6\%$ or 180 mK would cause an unacceptable shift of Δm_ν^2. This confirms the impact of changes of T on ρd in table 5.1. For the knowledge of the absolute temperature, this limit can be weakened. If one relied completely on gas dynamics calculations to determine ρd, a very good knowledge of T_0 would be required. Instead, ρd respectively the required scattering probabilities for the analysis will be measured separately with an electron gun (see section 2.6. This avoids a strict requirement on the knowledge of the absolute temperature.

Influence on the final state distribution

The absolute temperature T_0 of the beam tube influences the final state distribution (FSD) as explained in section 4.2.5.3, since T_0 determines the relative population of rotational states J of the tritium parent molecules; if the temperature increases, the contributions from larger J will increase. The FSD of molecules decaying from different states J are different [65]; in general the distributions get broader for higher J.

The influence of an uncertainty in T_0 can be evaluated with ensemble simulations. Since the effect is expected to be small, a temperature of 30 K is used for the simulation of the KATRIN experiments, and a "wrong" temperature of 33 K is used for the analysis. The resulting distribution is shown in figure 8.4. The systematic shift

$$\Delta m_\nu^2 = (6.8 \pm 2.8) \cdot 10^{-4}\,\mathrm{eV}^2 \tag{8.1}$$

is rather small and is compatible with results in [65]. It can be concluded that the knowledge of the absolute temperature due to its small influence on the FSD is not critical, a trueness of ± 3 K is sufficient.

Influence due to the Doppler effect

The absolute temperature T_0 determines the strength of the Doppler effect (see section 4.2.5.4). First of all, one can ask what systematic effect would occur, if the KATRIN analysis neglected the Doppler broadening of the β-spectrum? Figure 8.5 can give a hint on that. To quantify the effect, the usual ensemble simulations with the detailed source model, including the Doppler effect at 30 K were made. The analysis assumed no Doppler effect what resulted in a systematic shift of

$$\Delta m_\nu^2 = (-0.0172 \pm 0.00026)\,\mathrm{eV}^2. \tag{8.2}$$

As absolute value this is clearly above the allowed $0.0075\,\mathrm{eV}^2$ of eq. (6.14) for a single systematic effect. Therefore, the Doppler effect cannot be neglected in the KATRIN analysis.

The next step is to investigate the effect of a wrong assumption on the absolute temperature T_0 in terms of the Doppler broadening. If the simulated measurements in an ensemble method used $T_0^{\mathrm{sim}} = 30$ K as truth and the analysis assumed $T_0^{\mathrm{fit}} = 27$ K, the systematic shift would be

$$\Delta m_\nu^2 = (-0.00158 \pm 0.00026)\,\mathrm{eV}^2. \tag{8.3}$$

This is still within the requirements of eq. (6.14), so again a trueness of ± 3 K is sufficient.

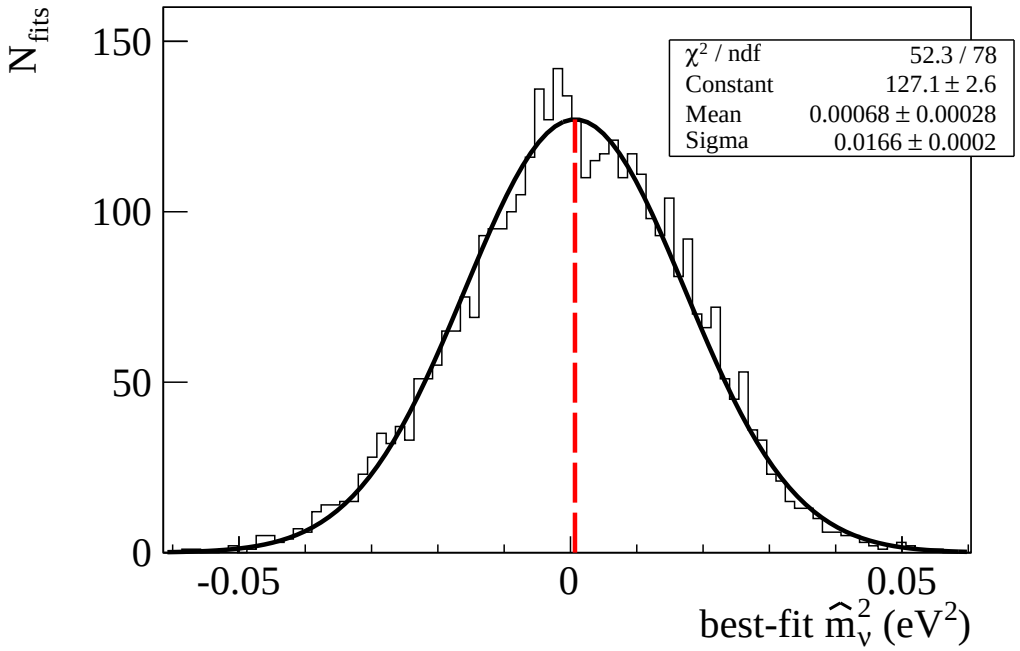

Figure 8.4: **Ensemble simulation with varying the absolute temperature to calculate the FSD.** The Monte-Carlo truth is $T_0^{\mathrm{sim}} = 30\,\mathrm{K}$; the analysis assumed $T_0^{\mathrm{fit}} = 33\,\mathrm{K}$. The shift of the resulting distribution from input neutrino mass $m_\nu^{2,\mathrm{sim}} = 0.0\,\mathrm{eV}^2$ is barely visible.

To conclude this section, the implementation of the Doppler effect in SSC should be verified. It was explained in section 4.2.5.4 that two different approaches are implemented: A slow, accurate algorithm that directly broadens the differential β-spectrum and a fast, approximative approach that broadens the final state distribution that is then used to calculate the differential β-spectrum. The resulting spectra of these two approaches differed only marginally as was shown in figure 4.6, but nevertheless it needs to be known if a systematic shift is introduced by using the approximation. Ensemble simulations with the accurate description of the Doppler effect as Monte-Carlo truth and analysis with the approximation show no significant influence; the shift was found to be

$$\Delta m_\nu^2 = (2.4 \pm 2.3) \cdot 10^{-4}\,\mathrm{eV}^2, \tag{8.4}$$

which is consistent with zero. The approximation of the Doppler effect, the broadening of the FSD, can be used in future analyses.

8.3 Influence of tritium purity

So far, only changes of the column density ρd have been considered as systematic effect on m_ν^2. But since the activity S of the source (see eq. (3.3)) is also determined by the tritium purity ε_{T}, an uncertainty on ε_{T} should influence the determination of m_ν^2 as well. To investigate the effect of unaccounted shifts of ε_{T} ensemble simulations with results in figure 8.6 are carried out. The effect is compatible with investigations published in [65]. Please note that the influence of ε_{T} is smaller by approximately

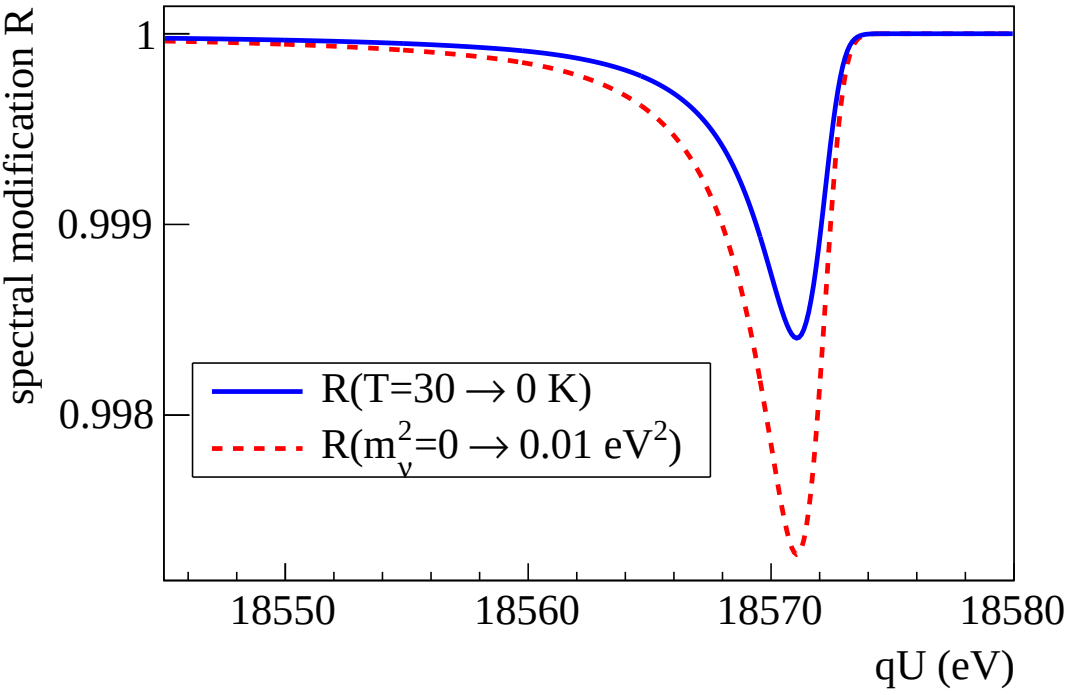

Figure 8.5: **Modification of the integrated spectrum of a non-vanishing neutrino mass or when neglecting the Doppler effect.** The spectral modification R is the ratio between the rates N of two integrated spectra where parameters have been modified from A to B: $R(A \to B) = N_A/N_B$. The influence of m_ν^2 on the integrated β-spectrum at KATRIN (red dashed line) is most prominent in the region a few eV below the endpoint energy that was set to 18,575 eV here. Very close to E_0 the background rate of 10^{-2} cps conceals the effect of m_ν^2. The blue solid line shows the ratio between a spectrum that considers the Doppler effect at $T = 30\,\mathrm{K}$ and a spectrum that neglects the effect. The influence is similar to a non-vanishing neutrino mass, clearly explaining the systematic influence of the Doppler effect on m_ν^2.

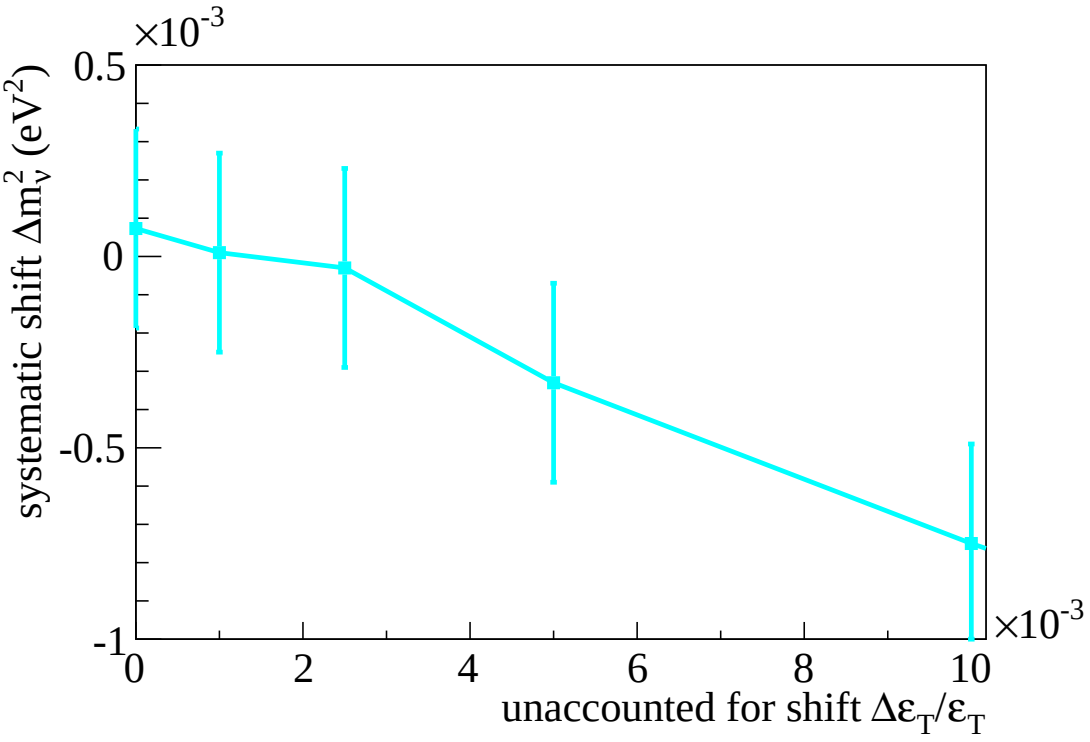

Figure 8.6: **Systematic shift Δm_ν^2 due to an unaccounted for shift of the tritium purity ε_T.** The effect is smaller by more than 1 order of magnitude than for shifts $\Delta\rho d/\rho d$ of figure 8.1.

one order of magnitude than an uncertainty of ρd. The reason is that ρd does not only change the activity, it also changes the scattering probabilities that have an impact on the shape of the spectrum - like m_ν^2. In the case of ε_T, to first order only the activity is changed. This causes an overall increase/decrease of the whole spectrum without influencing its shape. This scaling is absorbed during the analysis by a free fit parameter, the signal strength R_s of eq. (6.3), so that unaccounted for shifts of ε_T have no significant effect on the spectrum measurement.

Nevertheless, the small observable systematic shift in figure 8.6 occurs due to changes in the mixture of the different final state distributions of the daughter molecules of T_2, DT and HT. If a wrong ε_T is assumed for the analysis, the resulting FSD does not match the one that was used for the spectrum simulation and causes a small systematic shift Δm_ν^2. Further investigations on the trueness of ε_T and the connections to the calibration of the Laser Raman System to determine ε_T are already reported in [137] and will be discussed in detail in [71].

The knowledge of $\Delta\varepsilon_T/\varepsilon_T$ on the 10^{-3} level together with an activity monitoring (see section 2.6) of the source allows determining changes in the column density ρd. This is an independent measurement of $\Delta\rho d/\rho d$ next to the calibration measurements with an electron beam (see section 2.6) and is discussed in detail in [60].

8.4 Profile likelihood

The method of profile likelihood (see section 6.3.5) can be used to consider additional nuisance parameters that influence the spectrum measurement at KATRIN and

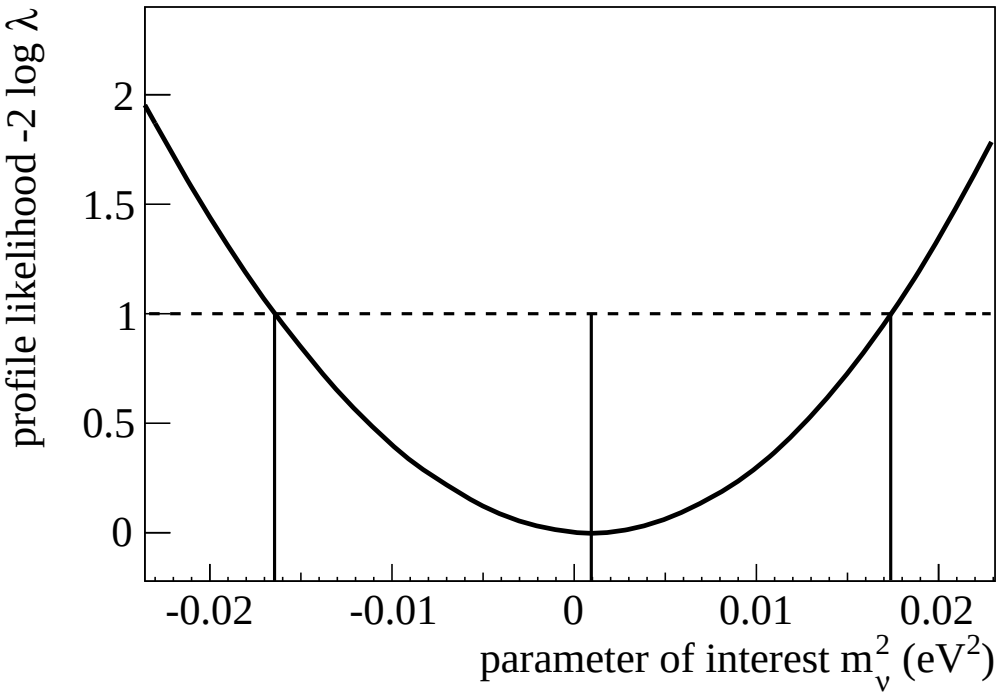

Figure 8.7: **Profile likelihood with constraint on ε_T.** In this case, a LARA measurement of $\overline{\varepsilon_T} = 0.90 \cdot \varepsilon_T^{sim} \pm 0.2\%$ is assumed. The minimum is shifted by $\Delta m_\nu^2 = 1.0{\cdot}10^{-3}\,\mathrm{eV}^2$. The statistical uncertainty determined by the function increase of 1 is unchanged compared to figure 7.2.

allows quantifying their systematic influence on m_ν^2. To present a prime example, the influence of ε_T is investigated in the following and can be compared to results obtained by ensemble simulations (see section 8.3).

First, eq. (6.30) is amended by ε_T as additional nuisance parameter. It is treated as a usual fit parameter with a lower limit of 0.5 that corresponds to pure DT in the source and an upper limit of 1.0 that stands for pure T_2[1]. The profile likelihood of m_ν^2 is shown in figure 7.2; it is not broadened significantly. The influence of ε_T on the statistical uncertainty of m_ν^2 is small.

In a second step, external measurements of ε_T provided by the Laser Raman system (LARA, see section 3.3) can be included in the analysis by adding constraint terms as in eq. (6.19) to the likelihood function respectively to the profile likelihood. In this test scenario, it is assumed that LARA reaches a precision on ε_T of 0.2%, but there is an uncertainty in the trueness of ε_T of -2%, -5% or -10%. This means that LARA would report $\overline{\varepsilon_T} = (0.931/0.905/0.855) \pm 0.2\%$, although the truth for the simulations was set to $\varepsilon_T^{sim} = 0.95$. The resulting systematic shifts are summarized in table 8.1.

This shows that if a wrong measurement of LARA was considered during the analysis by constraints to the likelihood, m_ν^2 would be shifted, but still within the allowed

[1]Other impurities like HT or non-tritiated impurities like H_2 are not considered in this first approach. Their fractions are expected to be very low due to the good purification processes of the Tritium Laboratory Karlsruhe (see section 3.3).

Table 8.1: **Systematic shifts Δm_ν^2 obtained by the profile likelihood method with shifted tritium purities $\overline{\varepsilon_\mathrm{T}}$ with simulation truth of $\varepsilon_\mathrm{T}^\mathrm{sim} = 0.95$.** $\overline{\varepsilon_\mathrm{T}}$ is assumed to be reported by a LARA measurement with an uncertainty of 0.2%.

$\overline{\varepsilon_\mathrm{T}}$	$\Delta m_\nu^2 (10^{-3}\,\mathrm{eV}^2)$
$0.98 \cdot \varepsilon_\mathrm{T}^\mathrm{sim}$	0.2
$0.95 \cdot \varepsilon_\mathrm{T}^\mathrm{sim}$	0.5
$0.90 \cdot \varepsilon_\mathrm{T}^\mathrm{sim}$	1.0

$7.5 \cdot 10^{-3}\,\mathrm{eV}^2$. In the presented case, the LARA measurement was set intentionally far off the true value what will not happen in the real experiment later due to calibration efforts of the LARA group [72].

The method of profile likelihood is suitable for KATRIN and can be used for various other parameters that systematically influence the measurement of KATRIN. A further example is an uncertainty of the retarding voltage of the KATRIN spectrometers as discussed in [121].

9. Measurements at the demonstrator

The aim of the demonstrator measurements is to prove the functionality of the WGTS cooling system by using original components (chapter 3), the original sensor system and the cryogenic facility of KATRIN. These tests provide first results of the source behaviour and allow for analyses regarding stability and homogeneity.

The demonstrator tests started at KIT in autumn 2010 with the first cool-down of the system and first heat load measurements [138]. During 2011, several dedicated tests were performed, starting with stability measurements in February and a long-term measurement at the end of April (section 9.1). In this work, additional analyses concerning Fourier transforms (section 9.2) and correlations (section 9.3) are presented. In section 9.4 results of the temperature homogeneity measurements are shown. This chapter ends with analysis and discussion of the implications of the demonstrator measurements in section 9.5. The demonstrator tests were completed in December 2012. Their results will also be published in [63].

During the demonstrator measurements two systems are responsible for taking data:

- The process control system PCS7 [139] for all processes, including the cryosystem, pressure measurements – especially the saturation pressure of neon – and some general temperature measurements. Measurements are typically recorded every second.
- The dedicated temperature measurement system TES [140] for all beam tube temperature sensors. The readout cycle of all Pt500 temperature sensors is adjustable and is set to 5 seconds if not stated otherwise. Measurements of the vapour pressure sensors are also managed by the TES, internally converting measured pressure values to temperatures. During the analysis this conversion is done by Mathematica [141] with an extension GASPAK [76].

9.1 Temperature stability

As shown in section 3.1 the requirements on the WGTS operating parameters are very strict and only allow temperature variations of the beam tube of $\Delta T_{\mathrm{stab}} <$

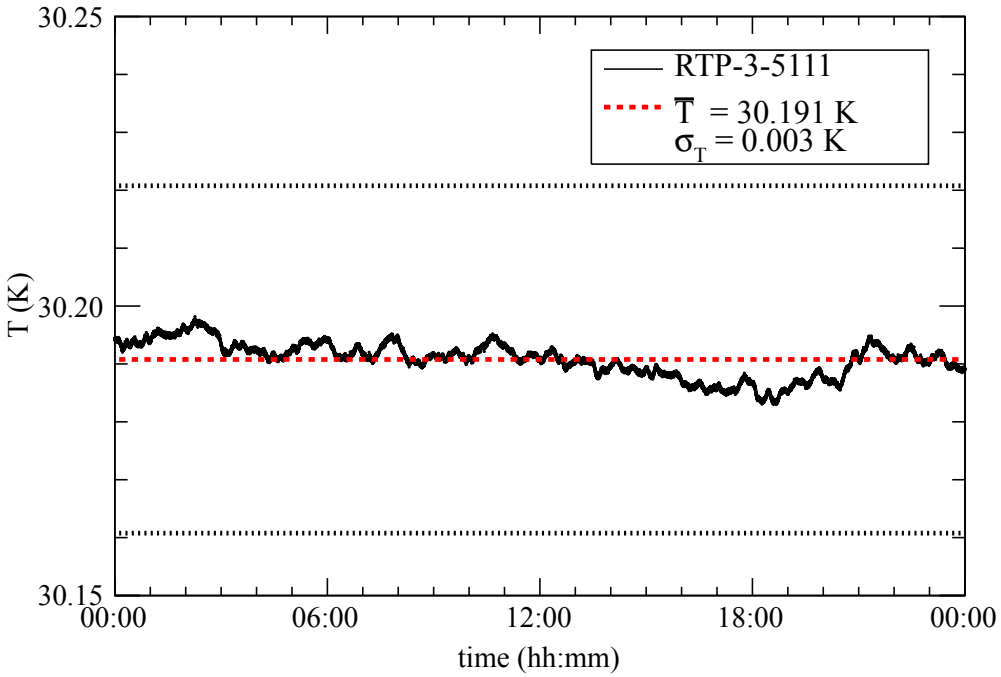

Figure 9.1: **Temperature of the demonstrator beam tube.** Shown is the measurement of a central Pt500 sensor (RTP-3-5111) in 24 hours. The standard deviation σ_T from the mean temperature $\overline{T} = 30.191\,\mathrm{K}$ is only 3 mK. The dotted lines show the requirements, a stability of $\pm 30\,\mathrm{mK}$ within one hour. Here, the cooling system of the beam tube is better than the requirement/specification by a factor of 10.

30 mK/h, corresponding to a 10^{-3} level. The required stability cannot be met by conventional cooling techniques for a system with dimensions of the WGTS. For the refrigerating plant used at KATRIN, fluctuations of $\pm 0.3\,\mathrm{K}$ have been measured during commissioning of the KATRIN cryogenic helium transfer line and infrastructure [74]. Together with the excellent shielding concept of the beam tube (see figure 3.5), the developed two-phase neon system with its improved condenser design (see section 3.3) allows to keep the temperature stable at 30 K.

The measured temperature of the demonstrator beam tube during 24 hours of undisturbed operation is shown in figure 9.1. The measuring points of one exemplary Pt500 sensor are shown for every second and represent the whole beam tube, since the behaviour of all sensors including the measured saturation pressure of the neon system is similar. The temperature fluctuations have a standard deviation of $\sigma_T = 3\,\mathrm{mK}$ during one day. During one hour of operation they do not exceed 1.5 mK. This proves the successful operation of the two-phase cooling system and its condenser. The beam tube temperature of the WGTS can be kept stable at the 10^{-4} level improving the required temperature stability by a factor of $10 - 20$ [63].

Further measurements characterize the long-term behaviour of the system (figure 9.2). On the scale of days larger variations – better called drifts – are visible in the whole system. Temperature changes of the cryogenic helium from the refrigerating plant are responsible for this behaviour. Its temperature depends on various

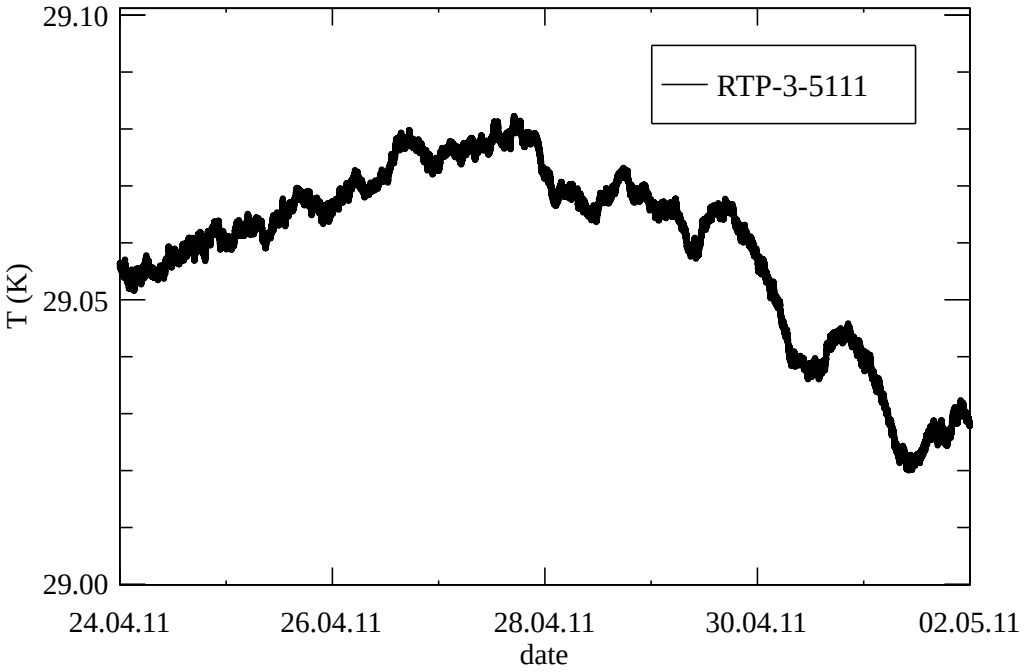

Figure 9.2: **Long-term measurement of the beam tube temperature.** During eight days of undisturbed operation of the demonstrator the temperature has been recorded and as an example a central Pt500 sensor (RTP-3-5111) is shown here. On that time scale slow global drifts are visible and low frequency oscillations might occur in the second part of this measuring period. The different average temperature compared to figure 9.1 is caused by a different operation of the refrigerating plant and a different set point of the neon system.

parameters, e.g. on the ambient temperature and results in changes of the mean temperature up to 0.3 K. The condenser reduces rapid temperature fluctuations of the refrigerating plant [74], but it follows the average temperature of the helium, which is used for its cooling. This causes slow drifts and is likely to be responsible for suspicious patterns in the temperature distribution during the last days of the shown long-term measurement. This motivates a dedicated search for periodicities in the system, a Fourier analysis of the temperature data in the following section. Nevertheless, long-term changes in the temperature are rather uncritical when looking at the planned measurement cycles at KATRIN: In [48], the measurement time is divided into several 2 hour intervals where the source has to be stable. Between these intervals, calibration measurements are foreseen, e.g. measurements with the electron gun of the rear-section (see section 2.6) to determine the column density of the source and detect changes. Long-term changes in temperature respectively column density can be resolved and considered when analysing the measured data.

9.2 Fourier analysis

Fourier analysis is a well-known method to check measurements on oscillatory behaviour and determine characteristic frequencies. The temperature at the demonstrator and later at the WGTS is an important parameter. It is monitored contin-

uously, 24 hours, all days. It is advisable to use the demonstrator measurements to investigate the behaviour of the cooling system and the beam tube temperature. This section will briefly explain the theory of Fourier analysis and apply it to measured temperatures at the demonstrator. The results of these analyses have already been reported in [142].

9.2.1 Theory

A physical process of a quantity h can be described in the time domain by values $h(t)$ for each time t, but it can also be represented in the frequency domain by amplitudes $H(f)$ for frequencies f [128]. A transformation rule called Fourier transformation exists between the two representations of the same process:

$$h(t) = \int_{-\infty}^{+\infty} H(f) e^{-2\pi i f t} \mathrm{d}f \tag{9.1}$$

$$H(f) = \int_{-\infty}^{+\infty} h(t) e^{2\pi i f t} \mathrm{d}f. \tag{9.2}$$

Taking measurements often moves away from continuous functions as in eq. (9.2) to discrete measurement points, so special emphasis should be given to Discrete Fourier transformations (DFT). If data is sampled every Δt seconds what corresponds to a sampling rate of $1/\Delta t$, the N discrete data points can be written as

$$h_k = h(k \cdot \Delta t), \quad k = 0, 1, \ldots N-1. \tag{9.3}$$

We can define frequencies

$$f_n = \frac{n}{N \cdot \Delta t}, \quad n = -\frac{N}{2}, \ldots, \frac{N}{2} \tag{9.4}$$

and use transformation rules for the DFT

$$h_k = \frac{1}{N} \sum_{n=0}^{N-1} H_n e^{-2\pi i k n/N} \tag{9.5}$$

$$H_n = \sum_{k=0}^{N-1} h_k e^{2\pi i k n/N}. \tag{9.6}$$

For eq. (9.6) the handling of the frequency range has been simplified. The numbering from $-N/2$ to $+N/2$ as in eq. (9.4) can be moved to 0 to $N-1$ because of the periodicity of the problem. The negative frequencies between $-1/2\Delta t$ and 0 are then represented by the f_n with $N/2+1 \leq n \leq N-1$, the positive frequencies between 0 and $1/2\Delta t$ by the usual numbers $1 \leq n \leq N/2-1$. Special cases are $n = 0$ that describes no frequency, i.e. a constant amplitude of the signal and $n = N/2$ that belongs to both frequency intervals as $f_{-N/2} = -\frac{1}{2\Delta t}$ and $f_{+N/2} = +\frac{1}{2\Delta t}$ (notation as in [128]).

In general, the transforms H_n are complex numbers. To present them, it is convenient to plot amplitudes $A(f_n)$

$$A(f_n) = \frac{2|H_n|}{N}. \tag{9.7}$$

Each data point h_k can be composed as a Fourier series by a superposition of cosine oscillations with discrete frequencies f_n and appropriate amplitudes $A(f_n)$

$$h_k = \frac{H_0}{N} + \sum_{n=1}^{N/2} A(f_n) \cos(2\pi f_n k \Delta t + \varphi). \tag{9.8}$$

Dedicated computer programs calculate Fourier transforms within split second. Nevertheless for large data samples or repeated transformations optimization of the routines are useful and save calculation time. Therefore algorithms called Fast Fourier Transformations (FFT) have been developed (e.g. [143]). "Normal" Fourier transformations for N discrete data points need $O(N^2)$ operations, but the FFT yields the transforms with $O(N \log_2 N)$ operations. That is remarkably faster for large samples. Since these methods are treated only as algorithms used to obtain the DFT, they will not be explained here. Details can be found in [128],[144] and [145]. The algorithms used for the following analyses are from the C library FFTW [146].

9.2.2 Analysis of temperature data

The demonstrator data used for the following Fourier analyses was taken during several measurement periods in 2011, especially during stability and the long-term measurements (see section 9.1). Motivated by visible temperature oscillations (figure 9.2) with periods of 1 day on the neon temperature, one should check the helium that is used for its cooling.

The helium from the KATRIN transfer line also cools the whole system, its shields and the pump ports. The helium temperatures shown in figure 9.3a show large fluctuation and expected oscillatory behaviour. A DFT of this data is shown right next to it. It reveals a broad band of frequencies with significant amplitudes up to 10 mK. These fluctuations also influence the neon condenser, and if they weren't dampened by some means, the beam tube temperature fluctuations would be impermissibly high. For this purpose, the neon condenser is equipped with a 3.7 kg lead core to increase its heat capacity and to smooth fluctuations of its temperature caused by varying helium temperature and throughput [74]. That this design is working has already been shown in figure 9.1 and can also be deduced from the comparison of the Fourier transforms of helium and neon in figure 9.4.

Actually, for this measurement period, there are some characteristic frequencies visible[1]. These frequencies and the broad band of amplitudes for low frequencies are strongly dampened by the condenser and are not visible in the DFT of neon. All amplitudes are significantly reduced as shown in figure 9.5, in case of the characteristic frequencies by 4 orders of magnitude, otherwise for frequencies $f > 0.3\,\mathrm{mHz}$ by typically 1-3 orders to amplitudes $< 0.1\,\mathrm{mK}$ [142]. Only the lowest frequencies corresponding to periodic times of several hours up to two days remain visible. This is consistent with the general temperature development shown before in figure 9.2.

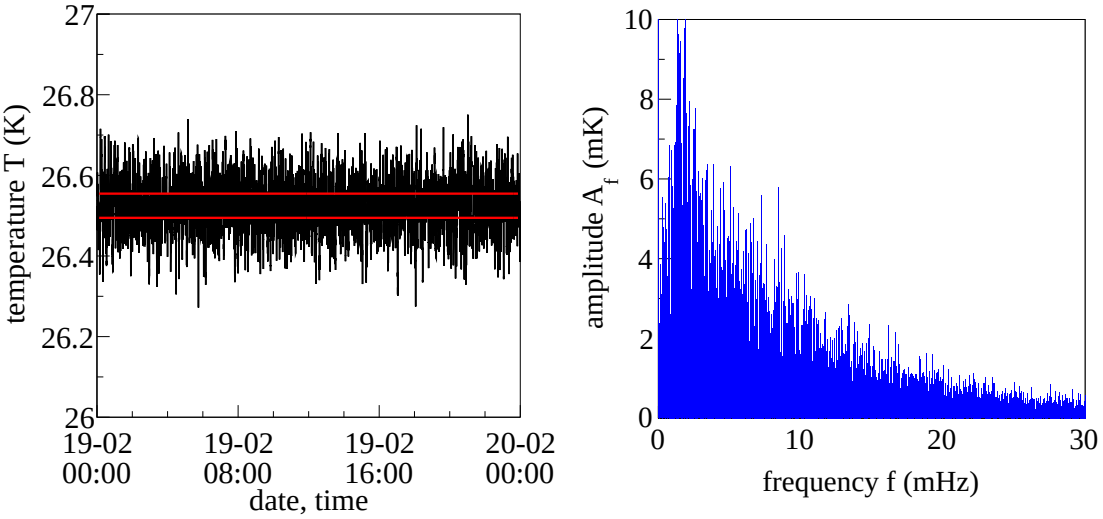

Figure 9.3: **a) Temperature of the gaseous helium entering the demonstrator.** The helium is provided by a refrigerating plant and does not meet the stability requirements ±30 mK drawn as red lines.
b) Discrete Fourier transform of the helium temperature. A broad band of low frequencies with non-negligible amplitudes (see eq. (9.7)) is visible. These oscillations add up to the temperature variations shown left.

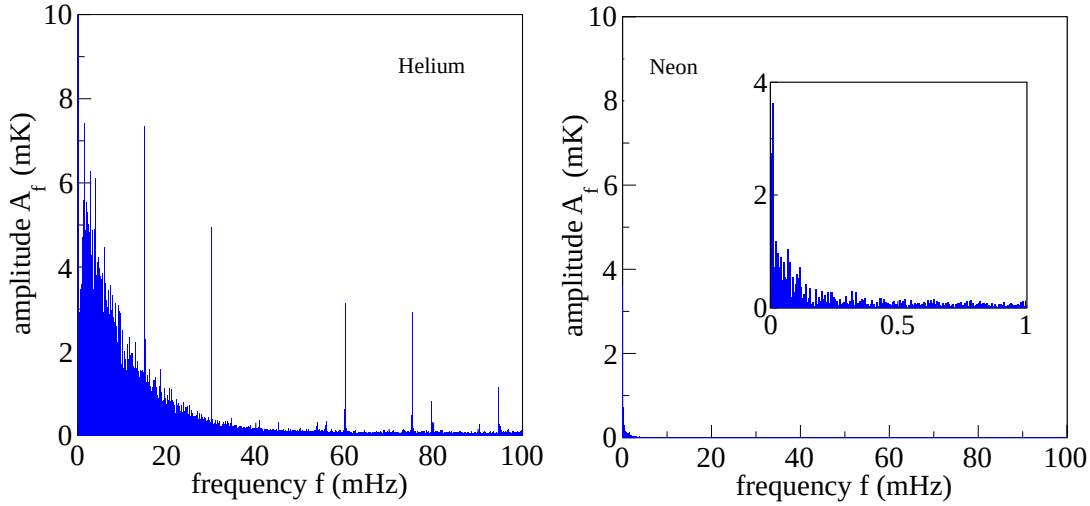

Figure 9.4: **a) Discrete Fourier transform of the helium temperature, February 26th and 27th 2011.** Besides the typical broad band of frequencies, several characteristic frequencies corresponding to periods between 10 and 60 seconds show up in this spectrum. **b) Discrete Fourier transforms of the neon respectively beam tube temperature.** The spectrum is strongly suppressed with low amplitudes only at very low frequencies (see inset) representing slow temperature drifts over days. Clearly no characteristic frequencies that are visible on the Fourier transform of the helium temperature in a) appear on the Fourier transform of the neon temperature. The condenser in the demonstrator, which is responsible for the heat transfer between helium and neon, dampens these frequencies (see figure 9.5).

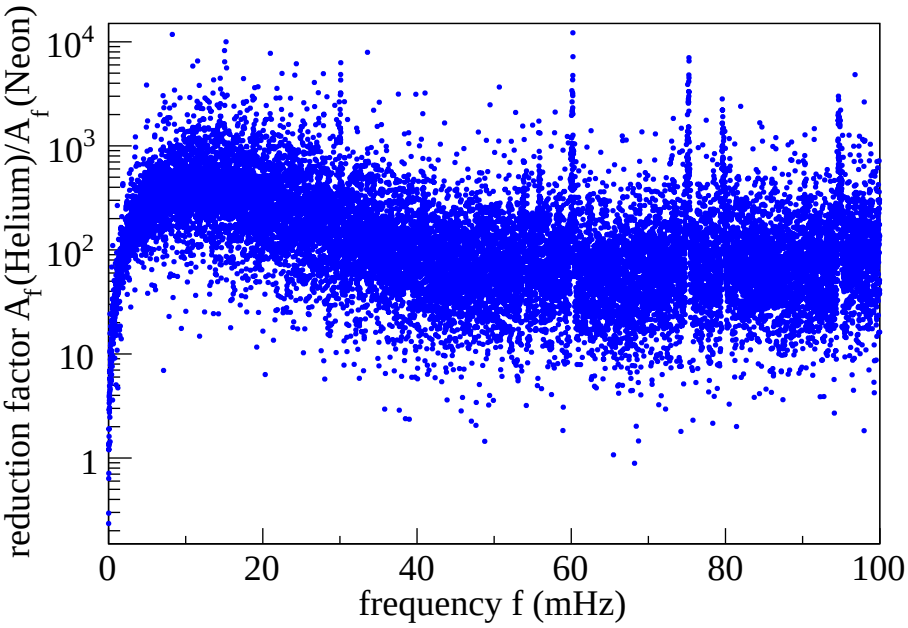

Figure 9.5: **Reduction factor in Fourier space between helium temperature and neon temperature.** Nearly all coefficients above 0.3 mHz are reduced by factors between 2 and 10^4. In particular, the peaks of the DFT of the helium temperature at characteristic frequencies are reduced by 4 orders of magnitude. For lower frequencies what corresponds to periods of 3 hours up to 2 days the reduction is weak.

To further investigate the correlation between helium and neon temperatures, the lowest frequencies are compared in figure 9.6, this time for the long-term measurement. Obviously, the amplitudes are similar and the expected daily variations show up in the frequency domain as well. The long-term drifts cannot be smoothed completely by the condenser, but variations on timescales larger than a data taking period in between column density calibration measurements (every 2 hours) are uncritical (see section 9.1).

9.3 Correlations

Checking for correlations between different measurements at the same time may give insight in the overall behaviour of the system. At the demonstrator, it is expected that the measured temperatures from different sensors are strongly correlated. Due to the defining temperature of the two-phase neon cooling system along its whole 10 m, overall temperature changes should occur at all sensors with strong correlations.

For these investigations the correlation coefficient ϱ_{xy} is useful e.g. [126]. It is defined as

$$\varrho_{xy} = \frac{\sigma_{xy}}{\sigma_x \cdot \sigma_y} \tag{9.9}$$

[1] Characteristic frequencies are only visible in some measuring periods. They correspond to periodic times between 10 and 60 seconds. They can be caused by automatically controlled valves or other regulating devices.

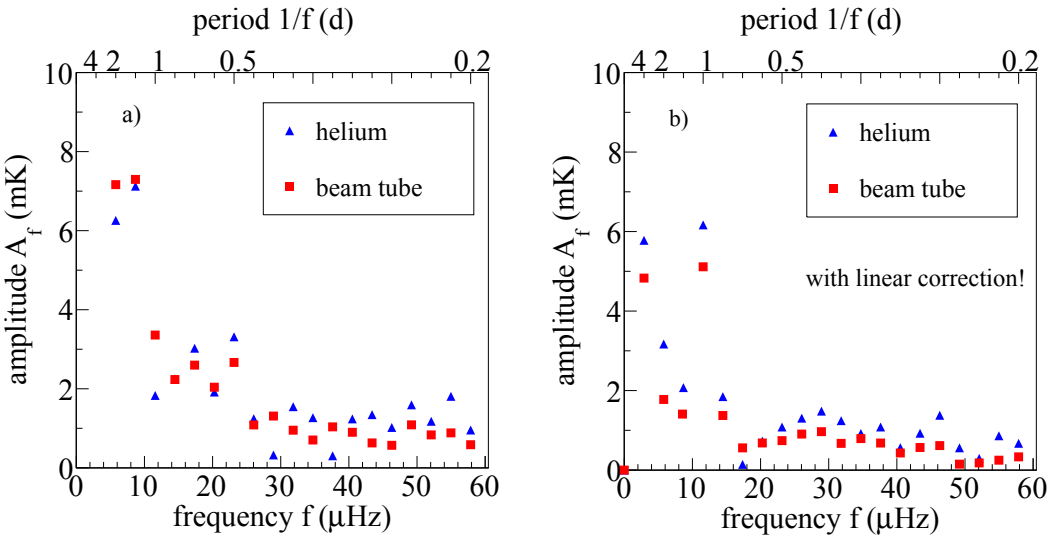

Figure 9.6: **a) Discrete Fourier transform of helium and beam tube temperature (RTP-3-5106).** Twenty lowest frequencies. The dataset is a 4 day measurement from April 28th to May 2nd 2011. The first coefficient for a period of 4 days is not shown, but is around 20 mK for both series. **b) Same as a), but a linear trend of the temperature signal has been subtracted before calculating the Fourier transforms.** This mainly reduces the amplitudes of the first few frequencies and focuses on oscillations instead of long-term drifts. Then it is even more evident that the beam tube temperature follows the behaviour of the defining helium temperature.

with standard deviations σ_x and σ_y of two random variables (here: two temperature measurements with values x and y) and the covariance

$$\sigma_{xy} = \langle (x - \langle x \rangle)(y - \langle y \rangle) \rangle \tag{9.10}$$

with expectation values $\langle x \rangle$ and $\langle y \rangle$ respectively. A coefficient of -1 shows a perfect anti-correlation, 0 states uncorrelated measurements, whereas +1 stands for a total correlation. Values in between show the extent of (anti-) correlation.

Another nice way to check for correlations are scatter plots x over y. In case of a correlation between those two variables, these scatter plots have tilted elliptical shape. Narrower ellipses imply stronger correlation.

In this section, only major results of the correlation analysis are presented. For a complete list of all correlation coefficients, please see [142]. Table 9.1 shows correlation coefficients between temperature measurements of the saturated neon, the beam tube at selected positions[2] and the helium (RTT-2-3107) used to cool the system. As expected, there is a very strong correlation between opposed Pt500 sensors (ϱ_{xy} is very close to +1) and also between sensors and the neon temperature. The neon temperature that governs the beam tube temperature on both sides along the whole 10 m is not perfectly stable as shown in section 9.1 due to external influences. The temperatures on top and bottom of the beam tube follow these changes of the neon temperature.

[2]Pt500 Sensor RTP-3-5101 is at the rear end at $z = -4.76$ m, at the bottom of the beam tube $\Phi = 270°$, RTP-3-5102 is at the top $\Phi = 90°$. RTP-3-5123 and RTP-3-5124 are at the front side ($z = +4.64$ m, $\Phi = 270°$ respectively $\Phi = 90°$ (cf. figures 3.8 and 3.9)).

Table 9.1: **Matrix of correlation coefficients between selected temperature measurements.** The sensors are Pt500 sensors on the rear side of the tube (RTP-3-5101 and RTP-3-5102), on the front side (RTP-3-5123 and RTP-3-5124), the neon temperature (converted from pressure measurements of RPI-2-5135) and the temperature of helium (RTT-2-3107) that is used to cool the system. Here, the correlation coefficients have been calculated for a 24 hour measurement on February 19th 2011, but they do not change significantly over time [142]. A strong correlation between the beam tube temperature measured by the Pt500-sensors and the defining neon temperature is obvious. The (anti-) correlation to the helium temperature is weak, since the condenser dampens strong fluctuations of the helium temperature leaving a slowly moving independent neon temperature and therefore beam tube temperature (see section 9.1).

KATRIN no.	RTP-3-5101	RTP-3-5102	RTP-3-5123	RTP-3-5124	RPI-2-5135
RTP-3-5102	0.9961				
RTP-3-5123	0.9712	0.9746			
RTP-3-5124	0.9906	0.9907	0.9874		
RPI-2-5135	0.9850	0.9828	0.9313	0.9672	
RTT-2-3107	−0.0600	−0.0610	−0.0403	−0.0442	−0.0933

This behaviour is also true for Pt500 sensors at the front side, but their correlation coefficients with the neon temperature are slightly smaller than for the rear side (0.93 and 0.96 compared to 0.98). This also stands for a strongly correlated behaviour, but shows differences between front and rear side.

This becomes obvious when looking at the scatter plots in figure 9.7. The left plot shows what is expected: An increase of the neon temperature causes an increase of the beam tube temperature at the rear side of the source. The Pt500 sensors there quickly follow the temperature changes; the result of a 24 hour measurement is a small tilted elliptical band. This is not the case for a sensor at the front side as shown on the right. There is a general tendency that an increase in the neon temperature also causes an increase of the front beam tube temperature. But there is some additional behaviour visible: Starting at $t = 0$ both temperatures increase and decrease simultaneously for some time, until the scatter points show some one-sided movement. They "leave" the former ellipse and settle inside a new ellipse around lower temperatures. This behaviour repeats itself during the whole measurement period. This means that generally the beam tube temperature at the front side follows the defining neon temperature, but there is a varying heat influx to the vicinity of the sensors, breaking the exact correlation. This behaviour can also be observed during other measurement periods, and during the long-term measurement [142]. How this time-dependent heat influx might occur will be discussed in the following section, where the difference between rear and front side of the source is investigated closely, when determining a temperature profile of the WGTS.

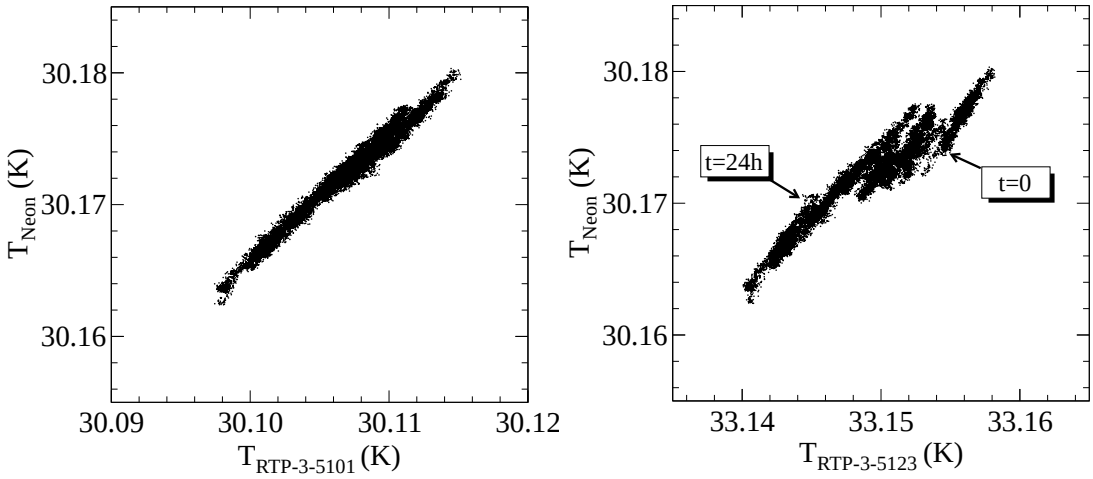

Figure 9.7: **a) Scatter plot of Pt500 temperature measurements at the beam tube rear side and the neon saturation temperature on February 19th 2011.** The neon defines the temperature of the beam tube on both sides. Changes in its temperature also show up at sensor positions on the rear end as strongly correlated measurements.
b) Scatter plot of Pt500 temperature measurements at the beam tube front side and the neon saturation temperature on February 19th 2011. There is also an evident correlation between the two measurements, but some external heat influences the Pt500 measurement, so that a "walk" of the scatter points during the 24 hours is visible. The difference on the x-axis of both plots will be explained in section 9.4.

9.4 Temperature homogeneity

Besides strict requirements on the temperature stability discussed in the previous sections, there are also specifications for the allowed temperature variations along the beam tube of $\Delta T_{\mathrm{hom}} < 30\,\mathrm{mK}$ for the inner 9.5 m, demanding a homogeneous temperature profile (see section 3.2). Regarding the physics of the source, a temperature profile directly influences the density profile [64], [116]. But in fact, if the profile is stable, this is no problem as will be shown in section 9.5. On the other hand, different temperatures in different parts of the source impose a different Doppler broadening on the emitted electrons (see section 4.2.5.4). Discussions on these effects will close this chapter.

Next to the physics, considerations on the temperature homogeneity arise from a rather technical motivation: The main heat influx occurs due to thermal radiation through the pumping chambers at the end of the beam tube. The photons hit the inner surface and slightly increase the temperature while the whole tube is cooled by the two-phase neon system. This setup will keep the temperature constant at 30 K at the connection of cooling tubes and beam tube (at 0°and 180°in figure 3.9), but will create an azimuthal temperature gradient towards top (90°) and bottom (270°) of the beam tube. These are the positions where most of the temperature sensors are measuring. Because the effect of thermal radiation rapidly decreases from the tube end to the center (view factor considerations), the magnitude of such an azimuthal temperature gradient depends on the longitudinal position. Therefore, it is also expected to obtain a temperature gradient from the ends of the beam tube towards the center: a longitudinal temperature profile. To demand a small longitudinal temperature gradient motivates a good shielding and cooling concept, but is not mandatory for a successful run of KATRIN as will be shown at the end of this section.

To determine the temperature profile, measurements in stand-alone operation of the system were carried out on November, 23rd and 24th 2011. The precise vapour pressure sensors were used. The resulting temperature profile is shown in figure 9.8.

On the rear side the temperature profile rises towards the end by up to 300 mK. On the front side, a stronger temperature gradient is visible. The temperature measured by sensors near the front end is higher by more than 850 mK than the neon saturation temperature. Additionally, on the front side, the temperatures measured by sensors at the top respectively at the bottom of the tube differ by up to 400 mK, although they are located at the same longitudinal position. The temperatures of sensors at 45° and 185° are between the extrema. At the rear side, the sensors on top are also slightly warmer than the sensors on the bottom.

To explain this effect, the pumping chamber geometries and its cooling are investigated closely. During cool-down of the system, it was observed that not all parts of the pumping chambers are cooled in full agreement with expectations. The flow impedance in the intermediate bellow cooling circuits at the pump ports (see figure 3.3) was underestimated. This resulted in insufficient liquid nitrogen flow rates through those circuits, which represented parallel branches in a common flow network with the outer liquid nitrogen shield. Thus, the upper parts of the pumping chambers nearly stayed at room temperature [74], so one expected an increased heat influx towards the beam tube. This helped to explain the difference between sensors

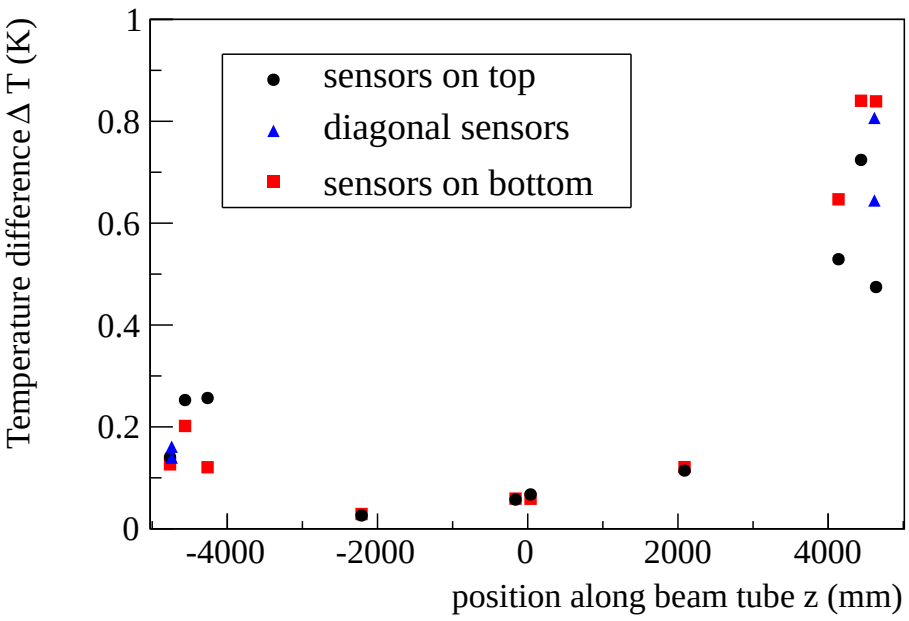

Figure 9.8: **Temperature profile measured at the demonstrator in stand-alone mode.** Shown are the temperature differences ΔT between the defining neon saturation temperature and the temperatures measured by the vapour pressure sensors at different positions z along the beam tube. The error bars are smaller than the used markers.

on top and bottom of the tube. But since this effect was true for both pumping chambers and no difference between front and rear chambers could be found, this cannot be the reason for the stronger temperature profile on the front side. Nevertheless, during reconstructioning the WGTS, additional valves will be installed to allow properly cooled pumping chambers, eliminating this additional unwanted heat influx.

The reason for the observed temperature profile is the small asymmetry of the system: At the front side, the neon condenser is located and most of the instrumentation lines enter the system there. Especially the 24 connection pipes from the vapour pressure sensors to the transducer outside of the source are guided inside the system near the front end (see figure 3.9b). These pipes are not sufficiently thermally isolated when entering the system and thus directly transfer heat to the measurement positions. The pipes run along the whole beam tube and branch off at different longitudinal positions. Their length varies from only 1 m for sensors at the front side to more than 10 m for sensors at the rear side of the source. Due to their different lengths, the effect is stronger at the front end, increasing the measured temperature significantly. At the rear side, the effect is reduced since the pipe is longer and it is guided along the beam tube inside the 30 K environment to adapt its temperature. In some way, this theory can also help to explain the temperature difference between sensors on top and bottom, since the heat incoming through different connection pipes might differ, additionally to the discussed thermal radiation from different warm parts of the pumping chamber.

Again, counteractive measures will be taken during reworking to the full WGTS by tying the vapour pressure pipes to a copper block kept slightly above 30 K before they enter the system. This will prevent heat influx through the capillaries and reduce the longitudinal temperature gradient considerably, leaving the aforementioned thermal radiation from the pump ports as main source for a longitudinal temperature profile.

9.4.1 Operation with heated blind flanges

When operating the WGTS at KATRIN, there will be additional heat sources that were not present at the demonstrator: The rotating turbomolecular pumps that are located at the pump ports at each end of the beam tube reach temperatures of more than 90°C when used in magnetic fields above 4 mT [80]. This heat increases the thermal radiation that reaches the beam tube through the pumping chambers. To simulate this effect at the demonstrator, where no pumps are used in the pump ports, electrical heaters have been installed at the eight blank flanges at the pump ports, each representing one warm pump up to 100°C.

The stability of the system is not influenced due to this additional heat influx as can be seen from figure 9.9. An 8 hour temperature measurement with a Pt500 sensor at the critical front end close to the pumping chamber shows variations on the mK-level that are completely consistent with the measured stability in stand-alone mode (see figure 9.1).

A measurement of the temperature homogeneity with heated blind flanges is shown in figure 9.10. This time the absolute temperatures were measured by Pt500 sensors[3] showing a strongly increased temperature gradient on the front side of more than 3 K.

[3]The sensors were uncalibrated during that measurement.

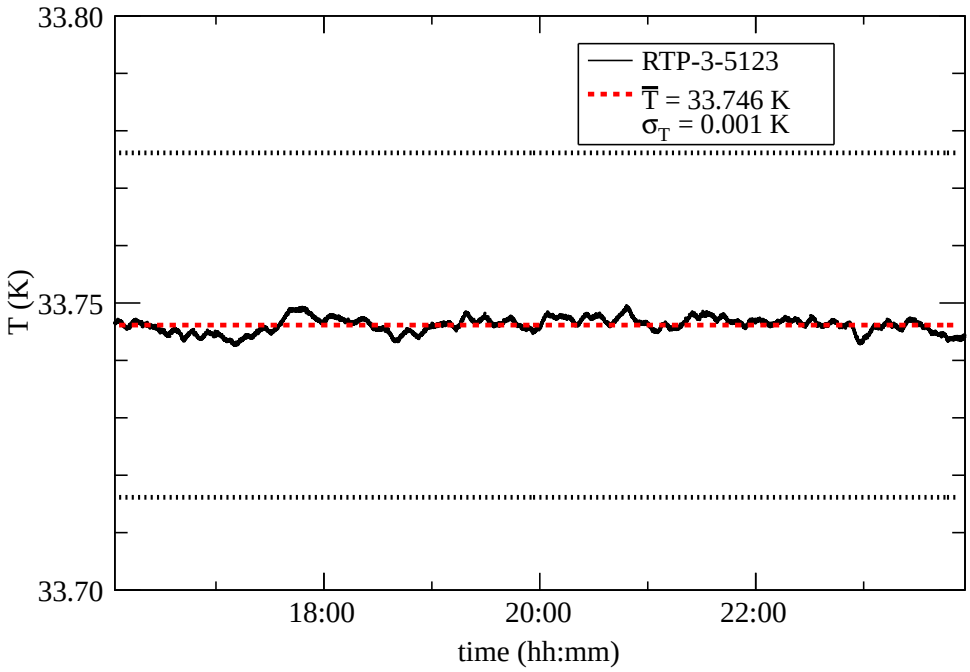

Figure 9.9: **Temperature stability when blind flanges were heated to 100°C.** Although the heat influx on the beam tube near the measuring position of sensor RTP-3-5123 ($\approx$ 30 cm away from beam tube end) is strongly increased due to the heated blind flanges, the temperature stability lies well inside the specification (dotted lines).

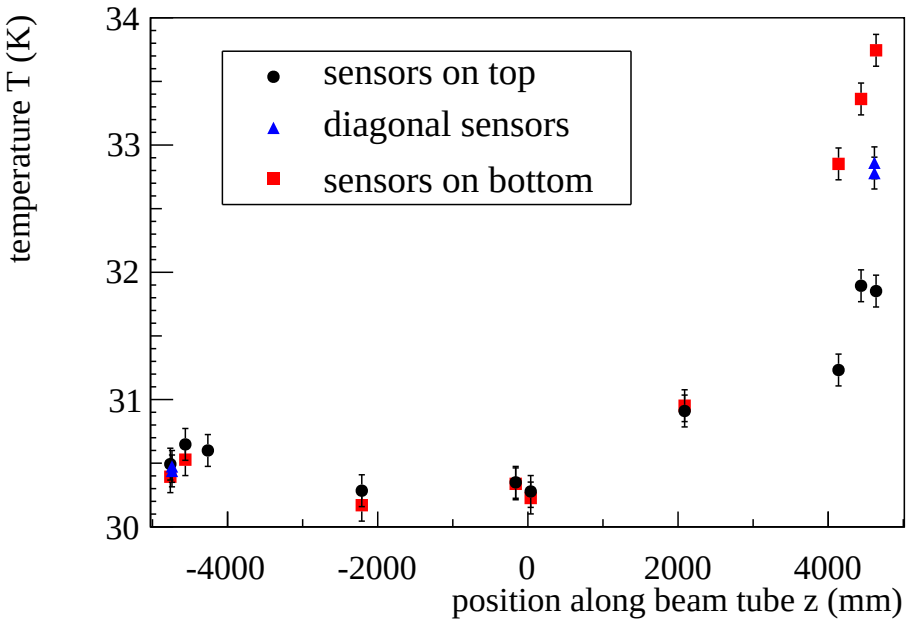

Figure 9.10: **Measured temperature profile when blind flanges were heated to 100°C.** Each Pt500 sensor distributed along the beam tube has a systematic uncertainty of 125 mK denoted by the error bars on the uncalibrated profile. The profile shows a strong rise towards the front side clearly exceeding the allowed homogeneity requirement of ±30 mK. In addition, there is a significant difference of up to 1.5 K between sensors attached to top (black circles) and bottom (red squares) of the beam tube at the front end.

The temperatures on the rear side of the beam tube are also increased by more than 0.5 K compared to the central part. Comparing this temperature profile with the one in stand-alone mode of figure 9.8 clearly shows that the extra heat load from the pump ports increases the temperature profile. Other features of the profile are visible again, for example that the sensors on bottom measure higher temperatures than those on top of the beam tube. At this point, one can conclude that it is necessary to keep the heat influx from the pumping section as small as possible to achieve a homogeneous temperature profile. As explained before, this will be improved in the WGTS by properly working intermediate bellow coolers. Other possibilities are a good magnetic shielding and dedicated cooling of the turbomolecular pumps to avoid increased heat influx at all [63].

9.5 Implications for KATRIN

The temperature stability of the beam tube cooling system was better by a factor of 20 than specified [63]. This is excellent, since the impact of temperature variations causing changes of the column density and thereby systematic shifts of the neutrino mass m_ν^2 is reduced (see section 8.2). Furthermore, in [60] was also reported that the injection pressure stabilization and tritium purity monitoring have met the requirements or the performance was even better. This means that the column density can

be stabilized and monitored at least on the required 0.2% level and allows for the wanted small systematic effect on m_ν^2 with possibilities to further reduce it.

Regarding the measured temperature homogeneity, a longitudinal temperature profile was expected due to incoming heat radiation at the beam tube ends. This gradient was required to be $< 30\,\mathrm{mK}$ (see eq. (3.8)). But the demonstrator tests show gradients of up to 0.85 K in stand-alone mode respectively 3 K with increased heat influx from the pumping chambers. Does this increased temperature profile harm KATRIN, since electrons from different parts of the source experience different Doppler broadenings, adding an uncertainty to the measurement?

This can be analysed by the methods similar to the analyses in chapters 7 and 8. Again, ensemble simulations are made. In this special case, the column density is fixed although the temperature is allowed to change. This allows observing the influence of the Doppler effect instead of the well-understood influence of column density changes. This approach corresponds to the case when the column density is determined with sufficient precision by electron gun measurements (see section 2.6) and does not rely on the information of the temperature profile. In this case, if one completely neglected the temperature profile with $\Delta T = 3\,\mathrm{K}$ that was used for the simulated measurement, assuming a flat distribution during the analysis, a shift of only

$$\Delta m_\nu^2 = (1.0 \cdot 10^{-4} \pm 2.3 \cdot 10^{-4})\,\mathrm{eV}^2 \tag{9.11}$$

would occur. This is not significant. The influence of shifts of the temperature gradient below 3 K is even less significant. It can be concluded that an increased temperature profile does not induce a significant systematic shift on the neutrino mass.

After the demonstrator measurements it was decided to turn around the cryostat and thus the beam tube. The main reason is a technical aspect, since turning the beam tube also turns the connection where the tritium injection line enters the WGTS. Thus, the length of the temperature stabilized transfer line from the pressure controlled buffer vessel of the inner loop (see figure 3.2) to the cryostat is nearly halved. This is easier to operate with the temperature stabilization and reduces costs by about 10000 € [147]. A shorter transfer line also reduces risks of damage. This is especially important for safety reasons, since a shorter line contains less tritium.

The inversion of the beam tube also shifts the strong temperature gradient from the front to the rear side of the source, since the connection tubes for temperature measurements that act as heat leaks into the system are also turned around (see section 9.4). This expects a less severe influence of the locally increased Doppler effect on the measurement, since electrons from the warmer rear side contribute less to the measured spectrum. Their probability to scatter inelastically on their way through the whole source is clearly increased compared to electrons emitted on the front side. Ensemble simulations on this influence cannot support this expected improvement when turning the WGTS. It doesn't matter if the temperature gradient is on the front or on the rear side[4] or if there is an uncertainty on the strength of the gradient. Each simulation was consistent with no systematic effect on m_ν^2. In terms

[4] Again, a measurement of the column density independent of the knowledge of $T(z)$ is assumed.

of sensitivity, a temperature profile on the rear side has to be favoured slightly, since it reduces the statistical uncertainty by

$$\frac{\Delta\sigma_{\mathrm{stat}}}{\sigma_{\mathrm{stat}}} = 0.65\%. \tag{9.12}$$

This improvement in statistical sensitivity could also be reached by accumulating more data, by extending the measurement time by roughly 2 weeks. Therefore, turning the beam tube is not necessary from the physics point of view.

10. Summary

The KATRIN experiment intends to measure the effective mass m_ν^2 of the electron antineutrino with an unprecedented sensitivity of $m_\nu < 0.2\,\mathrm{eV}$ (90% C.L.). For that purpose, a precise measurement of the tritium β-decay spectrum is intended. Compared to preceding experiments, KATRIN is required to improve the statistical accuracy on the observable m_ν^2 by two orders of magnitude and at the same time has to minimize systematic uncertainties at least by one order of magnitude. Both tasks immediately put the focus on the source of KATRIN, the windowless gaseous tritium source WGTS, since it provides the high β-electron flux and is responsible for systematic uncertainties. This also requires appropriate analysis tools to examine systematic effects for such a high precision measurement.

To understand and quantify the systematic uncertainties of the source, the work at hand presented the various models, simulations and measurements to describe the WGTS:

- Extensive gas dynamics simulations consider the gas flow, in particular the injection and pumping characteristics of the WGTS, and compute expected density and velocity distributions of the source. State of the art is a combination of one-dimensional calculations due to the large aspect ratio (>2000) of the source beam tube and small distortions that are considered by two-dimensional simulations. The implications of these radial and azimuthal inhomogeneities for the column density were found to be on the 10^{-5} level, i. e. too small to influence the measurement at KATRIN.

- The thermal behaviour of the beam tube has been measured in the "demonstrator experiment", a test experiment of the WGTS. The stability of the system was found to be on the 10^{-4} level, better by an order of magnitude than the requirement. The homogeneity measurements of the temperature along the 10 m of the beam tube showed an unexpected temperature gradient of $\Delta T > 1\,K$ on the front part of the beam tube due to an increased heat load on the system. Unaccounted for heat conduction through measuring capillaries was identified as reason of the asymmetric temperature profile and countermeasures have been identified to reduce the temperature gradient in the final

WGTS-assembly. Additionally, these measurements support the demand to keep the thermal radiation on the system through the pumping chambers as low as possible. In particular they demand a good magnetic shielding of the turbomolecular pumps.

- The description of the differential β-spectrum of tritium has been refined. Recently calculated final state distributions to consider rotational, vibrational and electronic excitations of the daughter molecules of the β-decay of molecular T_2 were considered. The contribution from other hydrogen isotopologues DT and HT to the measured spectrum has been taken into account according to the tritium purity of the WGTS. Due to the thermal movement and additional gas flow velocities due to the tritium circulation, the measured spectrum is broadened by the Doppler effect that is now considered within the KATRIN simulation in a consistent way.

- The calculation of expected integrated β-spectra at KATRIN has been improved to consider local inhomogeneities of physical parameters of the WGTS. In the simulation, the WGTS is divided into many small "voxels", which contain the local physical properties. The size of this partitioning can be chosen by the user to account for specific parameter profiles and required accuracy. The sum of the contributions of all these single voxels then results in the expected integrated spectrum at KATRIN.

The presented calculations of the KATRIN spectrum were then used to determine the statistical uncertainty of KATRIN. For that purpose, various analysis methods have been implemented and tested within the KATRIN analysis toolkit KASPER. Ensemble (Monte-Carlo) simulations and the method of profile likelihood were presented in this work. The obtained statistical uncertainty of KATRIN on m_ν^2 is consistent between all these methods with $\sigma_{\mathrm{stat}} = (0.017 \pm 0.001)\,\mathrm{eV}^2$ and in agreement with previous results from the KATRIN technical design report. The implementation of Feldman-Cousins Unified approach allowed converting the expected statistical uncertainty of KATRIN into a confidence belt that will be used to interpret a measurement later. The envisaged sensitivity of KATRIN of $m_\nu < 200\,\mathrm{meV}$ (90% C.L.) was confirmed.

The influence of systematic uncertainties of various source parameters was determined again by ensemble methods. It allowed confirming the requirements on the column density of the source that was known from former rudimentary analyses. This time, it was possible to directly determine the influence of experimental observables like the injection pressure or the tritium purity and not only the influence of a derived quantity, namely the column density. The results confirmed the required stability of $2 \cdot 10^{-3}$ on the named parameters. Systematic effects were also included into the analysis by the profile likelihood method. It was demonstrated how external measurements for example of the tritium purity can be added to the likelihood as constraint terms. The analysis then treated the tritium purity as additional fit parameter and evaluated its influence on the wanted neutrino mass. The method was shown to be promising for other parameters of KATRIN.

With the developed simulation software it was possible for the first time to investigate the effect of the density or temperature profile in the source, to account for

inhomogeneities in the source. This was especially important to evaluate the measured temperature profile at the demonstrator with a temperature spread $\Delta T > 1\,K$ at the beam tube ends. The simulation and analysis showed that the measured temperature profile does not spoil the sensitivity of KATRIN as long as it is stable and monitored by the precise temperature sensors.

All software and routines of the simulation and analysis that have been used throughout this work are provided within KASPER for members of the collaboration. The analysis routines are ready and can be used in upcoming test and commissioning measurements of the main spectrometer at the end of 2012. In the future, the analysis routines will be extended to include more systematic effects of the source into the analysis.

On the simulation side, a full 3-dimensional simulation of the gas dynamics in the WGTS is planned in collaboration with F. Sharipov. This is important to understand the situation at the pumping chambers especially on the front side of the WGTS. In fact, only $< 1\%$ of all T_2-decays are expected within this region, but due to their high probability to reach the detector without scattering their systematic influence must be understood.

The demonstrator measurements showed the need for minimal thermal radiation from the pumping chambers. Therefore, new efforts will improve the shielding of the turbomolecular pumps from magnetic fields and will establish a cooling system of the whole pumps to reduce the thermal radiation and improve the temperature homogeneity of the WGTS.

A. The krypton mode

The 'krypton mode' is a special operation mode of the WGTS [48]. Gaseous krypton ^{83m}Kr is added to the usual tritium gas and injected into the WGTS. During de-excitation, ^{83m}Kr emits conversion electrons with fixed energies [148]; the spectrum is a line spectrum with lines close to the tritium β-spectrum endpoint energy and above (see figure A.1a). These conversion electrons can be measured on top of the tritium β-electrons and create a step in the integrated spectrum (see figure A.1b).

On the one hand, the position of the steps depends on the potential difference U between point of emission in the source and the spectrometer. This allows comparing the measured line positions with those of other experiments and theory (e.g. [149]). On the other hand, a varying potential along the WGTS causes a broadening of the line (see figure A.2a). The krypton mode is therefore used to determine the potential distribution of the WGTS. To avoid freezing of ^{83m}Kr to the walls, the temperature of the source is temporarily increased to $T = 120\,\mathrm{K}$.

The basis for the implementation of the krypton mode into the existing source simulations SSC was achieved in [150]. There, information on the description of the krypton spectrum like line positions and natural widths was gathered, as well as descriptions of secondary effects like shake off/shake up electrons [151]. Additionally, the Doppler broadening due to the thermal motion of the ^{83m}Kr atoms was considered by using Voigt profiles, the convolution of a Lorentzian with a Gaussian. The work at hand unified these preliminary simulations to use the krypton spectrum in the same way as the tritium spectrum. The integrated spectrum is treated as superposition of Kr and T_2-spectrum. This is especially useful when considering the Doppler effect as presented in section 4.2.5.4. Special focus has also been given to simulations of the gas dynamics of the krypton mode. The higher temperature requires recalculations of some results that were obtained for $T = 30\,\mathrm{K}$. On the other hand, new calculations are needed to account for the large differences in the masses of the particles T_2 with 6 atomic units u respectively krypton with $83\,u$. They move with different mean speeds in the mixture and cause a separation effect respectively different concentrations along the source tube (see figure A.2b) [109, 110, 152]. This can be taken into account with the presented methods of SSC, i.e. the voxelization and description of density profiles.

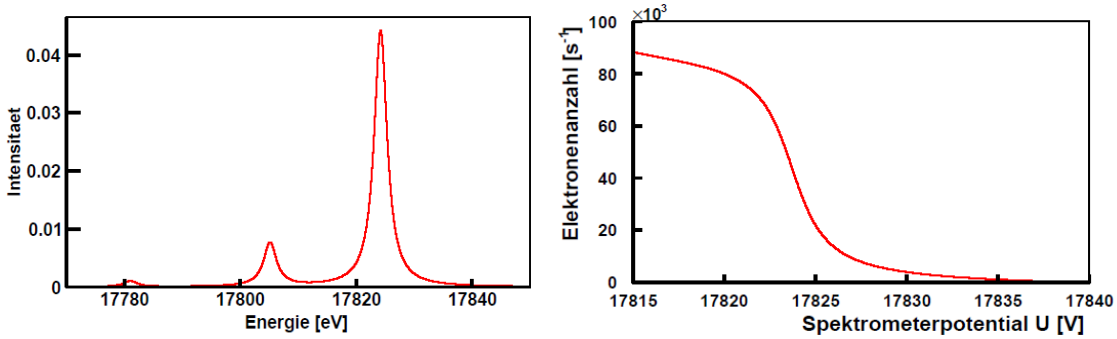

Figure A.1: **a) K-32 conversion line of ^{83m}Kr at 17.824 keV from [150]**. The main peak is the conversion line. Satellite lines occur, since the primary electron may lose energy with a certain probability when exciting another electron from a specific orbital to another (shake up) or even ionizing the atom (shake off).
b) Integrated K-32 conversion line of ^{83m}Kr from [150]. The lines of a) result in expected number of counts on the y-axis in an integral method; the electrons from higher lines as well as the existing tritium spectrum are neglected here. The K-32 line becomes a step in the integrated spectrum, the satellite lines cause a further increase at lower retarding energies U.

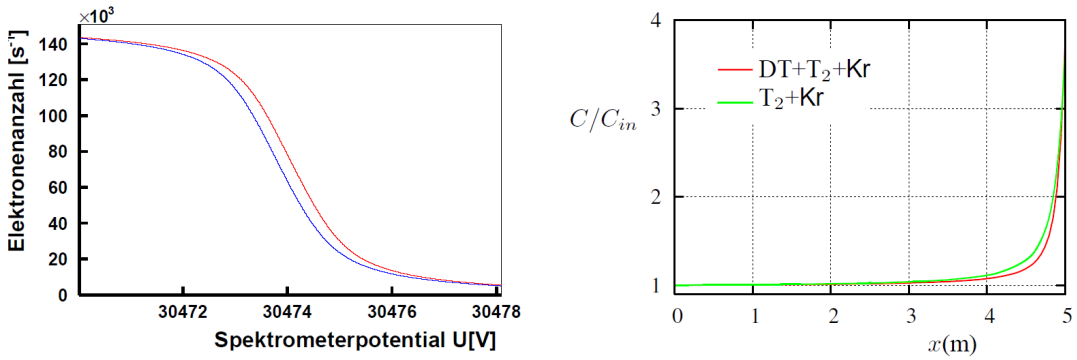

Figure A.2: **a) Broadened integrated krypton line at 30.474 keV from [150].** The plot shows the expected number of electrons on the y-axis for different retarding potentials U. The line for zero potential in the WGTS is shown in red whereas the blue line results from a linear potential from 0 V to 0.45 eV, rather large for illustration purposes. First, a shift can be observed, since here the source potential was chosen to be positive everywhere. Closer analysis shows that the line is also broadened.
b) Concentration of gaseous ^{83m}Kr in a mixture with T_2 ($DT+T_2$) relative to the concentration C_{in} at the injection from [110]. The molecules/atoms separate when streaming along the beam tube due to their different masses and therefore different mean speeds.

B. Cooling liquids at the demonstrator

The various cooling liquids and different cooling cycles at the demonstrator are shown in figure B.1. Please see caption for detailed description.

Of special importance for the demonstrator measurements is the two-phase neon cooling of the beam tube, since it defines the temperature stability of the system. It is cooled via the condenser by helium from the KATRIN refrigerating plant.

The measurements of the temperature homogeneity are influenced by thermal radiation through the pumping chambers onto the inner surface of beam tube. To minimize this effect, a cascade-like structure cools the pump ports: The outer parts are cooled by liquid nitrogen as well as the intermediate bellow coolers. The innermost parts are cooled by gaseous helium. During the demonstrator measurements, it was observed that the upper part of the nitrogen cooling is not working properly since the nitrogen uses parallel pipes (not shown) with less resistance, so that the upper part of the pumping chambers stayed at temperatures of about 230 K [63]. This means that the heat load on the gaseous helium at the pumping chamber and also on the beam tube will be higher; a stronger temperature gradient of the beam tube temperature from the center towards the pumping chambers is expected. This is especially true when using external heaters at the ends of the pump ports to simulate the effect of warm turbomolecular pumps that will be operated in strong magnetic fields at the WGTS later. Due to the weak shielding ability of the intermediate bellow coolers, the photons' impact on the beam tube temperature gradient is expected to be more severe than at the WGTS later where a proper cooling will be established.

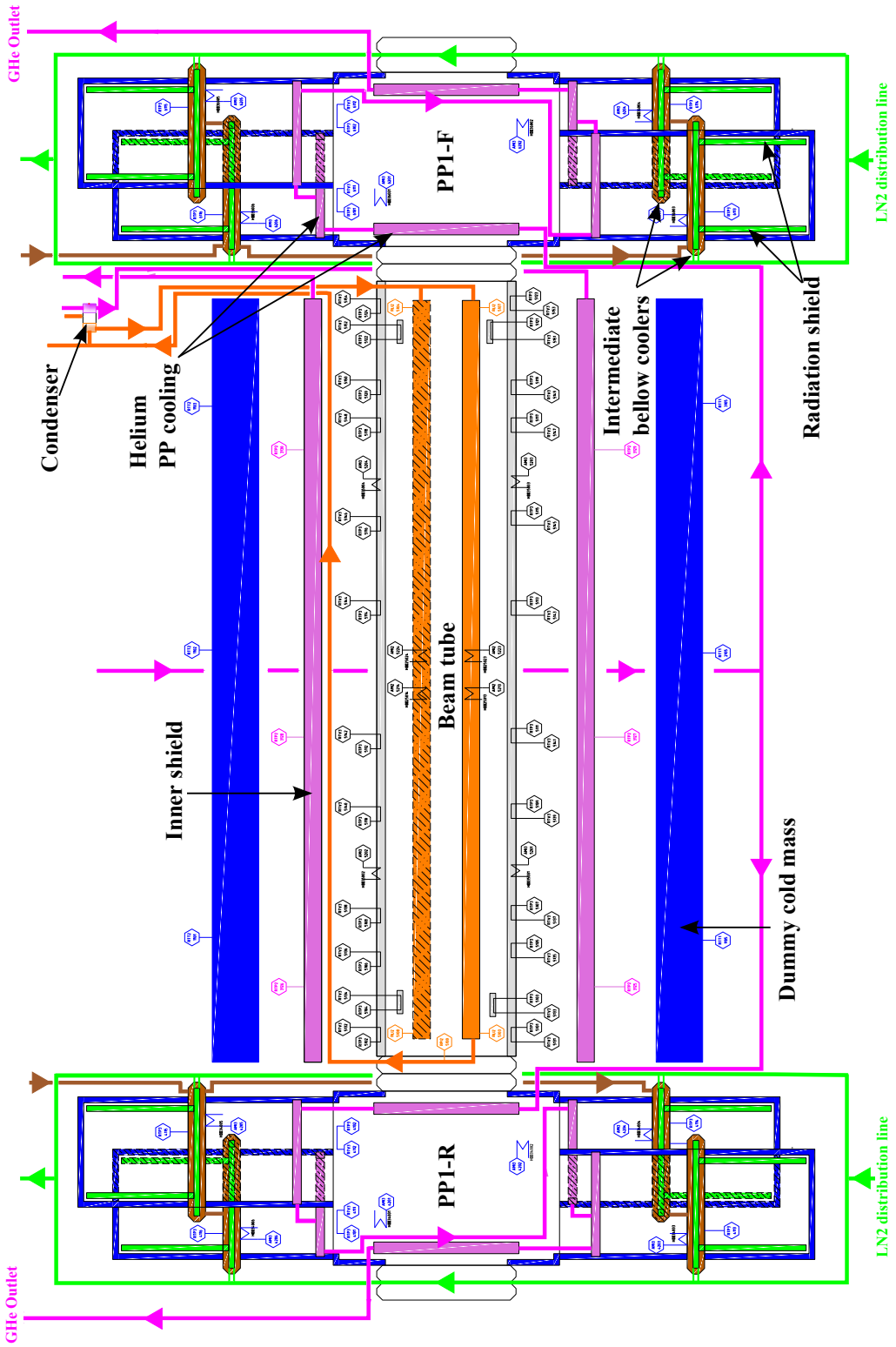

Figure B.1: **Scheme of cooling liquids in the demonstrator. From [153], modified for presentation purposes.** Neon (orange) is used to cool the beam tube at 30 K. The inner shield and the inner parts of the pumping chambers are cooled by gaseous helium (pink) also at 30 K, but with larger temperature fluctuations than the very stable neon system. Liquid nitrogen (brown) cools the intermediate bellow coolers between the inner part of the pumping chamber and the pump ports, whereas gaseous nitrogen (green) cools all outer parts of the pumping chambers and the radiation shields.

C. Calibration procedure of Pt500 sensors with vapour pressure sensors

The precision of the used Pt500 sensors with a total uncertainty of 0.125 mK [75] is not sufficient to continuously monitor the WGTS beam tube temperature with the requirements of $\Delta T < 30\,\mathrm{mK}$ on stability and homogeneity (see section 3.2). A big contribution to the uncertainty originates from the magnetic field dependence of the resistance measurement of the Pt500 sensors. The second type of used sensors, the vapour pressure sensors VPS, is insensitive to magnetic fields, but cannot be used continuously during KATRIN runs that will last up to 30 days. Therefore, the VPS will be used to calibrate the Pt500 sensors in situ whenever a major run of KATRIN starts or whenever the magnetic field changes. In the following, the calibration procedure with help of the temperature acquisition system TES [140] is explained:

1. The volumes (bulbs) of all VPS are filled simultaneously with gaseous neon, until the pressure is about 100 mbar below the saturation pressure p_{sat}. This turned out to be difficult at the demonstrator tests, where a large longitudinal temperature gradient at the front side of the beam tube automatically implied higher p_{sat} for those sensors. Thus, single sensor had to be adjusted manually.

2. Then, each sensor volume is filled individually with 350 mg of neon (measured by a mass flow meter) to obtain a half-filled sensor bulb.

3. The TES is then used to measure simultaneously with Pt500 and VPS. A difficulty of this calibration process is that there are only 3 pressure transducers for a block of 8 VPS. This means one has to open valves to connect the individual bulb volumes with the transducers. This causes a small pressure compensation to p_{sat} and therefore condensation respectively evaporation of neon. This is visible at the adjacent Pt500 sensors as a temperature increase/decrease. To calibrate, one has to wait approximately 15 minutes until the Pt500 temperature has stabilized again. Then, the saturation pressure of VPS number i

can be converted to T^i_{sat} and compared to the temperature T^i_{Pt500}, measured by Pt500 sensor with number i. The calibration coefficient is then calculated and stored by the TES

$$\Delta T^i = T^i_{\mathrm{Pt500}} - T^i_{\mathrm{sat}}. \tag{C.1}$$

4. The calibration coefficients are available in the TES or can be extracted from the calibration data in an offline analysis using Mathematica [141] and GASPAK [76]. This was done for analyses shown in this work (see section 9.4).

Deutsche Zusammenfassung

Das KATRIN Experiment hat das Ziel die effektive Masse des Elektron-Antineutrinos mit bisher unerreichter Genauigkeit $m_\nu < 0,2\,\mathrm{eV}$ (90% C.L.) zu bestimmen. In einer modell-unabhängigen direkten Messung wird das Spektrum der Tritium-β-Zerfallselektronen präzise vermessen um den Einfluss der Neutrinomasse auf die spektrale Form und damit die Masse selbst zu bestimmen. Im Vergleich zu Vorgängerexperimenten wird KATRIN die Sensitivität um einen Faktor 100 steigern, indem mehr Ereignisse für verbesserte Statistik analysiert werden und systematische Effekte minimiert werden. Beide Ansätze betreffen die Tritiumquelle bei KATRIN, die fensterlose gasförmige Tritiumquelle WGTS. Die WGTS stellt einerseits den hohen Fluss an β-Elektronen bereit, ist andererseits aber auch für systematische Unsicherheiten auf die Neutrinomasse verantwortlich.

In der vorliegenden Arbeit wurden die Modelle, Simulationen und Messungen beschrieben, die es dann ermöglichen systematische Effekte der WGTS zu untersuchen.

- Fortgeschrittene Simulationen der Gasdynamik der WGTS beschreiben einerseits die thermische Bewegung der Tritiummoleküle bei $T = 30\,\mathrm{K}$, andererseits die zusätzliche Geschwindigkeitskomponente aufgrund der Zirkulation zwischen Injektions- und Pumpkammern. Dies ergibt Dichte- und Geschwindigkeitsprofile der Moleküle. Aufgrund der Dimensionen der Quelle ($l = 10\,\mathrm{m}$, $d = 0,09\,\mathrm{m}$) ergeben ein-dimensionale Berechnungen das generelle Dichteprofil. Zwei-dimensionale Simulationen berücksichtigen den Einfluss radialer/azimutaler Asymmetrien des Systems und die Störungen des Profils im Bereich der Injektion und der Pumpkammern. Die dadurch verursachten Inhomogenitäten der Säulendichte der WGTS sind in der Größenordnung 10^{-5} und daher zu klein um die KATRIN Messung zu beeinflussen.

- Das Temperaturverhalten des WGST-Strahlrohrs wurde im sogenannten „Demonstrator“-Experiment ermittelt. Dabei wurde eine Temperaturstabilität auf dem 10^{-4} Niveau gemessen, was um eine Größenordnung besser als gefordert ist. Die Messung der Temperaturhomogenität des 10 m Strahlrohrs ergab allerdings einen unerwartet starken Temperaturgradienten $\Delta T > 1\,\mathrm{K}$ im Strahlrohr auf der dem Spektrometer zugewandten Seite der WGTS. Diese zusätzliche Wärmelast ließ sich durch Wärmeleitung durch die Messkapillaren der Temperatursensoren erklären, die das System nur einseitig belasten und ein asymmetrisches Temperaturprofil erzeugen. Beim Umbau des Demonstrators zur WGTS wird dieser Wärmeeintrag dann durch Anbindung an einen gekühlten Kupferblock verhindert. Außerdem wurde durch die Messungen gezeigt, dass die Wärmestrahlung durch die Pumpkammern auf das Strahlrohr minimiert

werden sollte. Deshalb werden weitere Anstrengungen unternommen, um die Erwärmung der Turbomolekularpumpen im starken Magnetfeld zu verringern.

- Die Beschreibung des differentiellen Tritium-β-Spektrums wurde verbessert. Dazu wurden aktuelle Berechnungen der Endzustandsverteilung der Tochtermoleküle von T_2, DT und HT verwendet, da Energie beim Zerfall in Rotations-, Vibrations- und elektronischen Anregungen verbleibt und nicht für das Elektron zur Verfügung steht. Desweiteren wurde der Dopplereffekt aufgrund der thermischen Bewegung und der zusätzlichen Gasflusskomponente berücksichtigt, was eine Verbreiterung des gemessenen β-Spektrums bewirkt.

- Auch die Berechnung des integrierten Spektrums, der Messgröße von KATRIN, wurde verbessert. Die neuen Berechnungen berücksichtigen lokale Inhomogenitäten der Quellparameter. Dabei wird die Quelle in der Simulation in viele kleine Volumina zerlegt, die die jeweils lokalen physikalischen Größen berücksichtigen. Je nach Parameterprofil kann die Unterteilung angepasst werden, um dann das integrierte Spektrum zu berechnen, indem die Beiträge aller Volumina zum integrierten Spektrum addiert werden.

Mit Hilfe dieses Quellmodells und der berechneten Spektren lässt sich dann die statistische Unsicherheit σ_{stat} von KATRIN bei der Bestimmung von m_ν^2 ermitteln. Dafür wurden verschiedene Analysemethoden in die KATRIN-Analyse Software KASPER implementiert. Durch „Ensemble Simulationen“, d.h. eine große Anzahl Monte-Carlo Simulationen des gesamten KATRIN-Experiments, und durch „Profile Likelihood“ Analysen konnte $\sigma_{\mathrm{stat}} = (0.017 \pm 0.001)\,\mathrm{eV}^2$ ermittelt werden, was in Übereinstimmung mit früheren Simulationen ist. Außerdem wurden mittels Feldman Cousins Unified Approach die Grundlagen geschaffen um σ_{stat} konsistent in eine Obergrenze bzw. einen Nachweis der Neutrinomasse zu übersetzen. Dabei konnte die anvisierte Sensitivität von KATRIN $m_\nu < 0,2\,\mathrm{eV}$ (90% C.L.) erneut bestätigt werden.

Daraufhin wurde der systematische Einfluss von Unsicherheiten der Parameter zur Quellbeschreibung auf die Analyse von m_ν^2 mittels genannter Ensemble Simulationen untersucht. Dadurch konnten die Anforderungen an die Säulendichtestabilität von $2 \cdot 10^{-3}$ bestätigt werden. Durch die neue Funktionalität der Quellsimulationen konnten die Einflüsse weiterer Messobservablen, zum Beispiel des Einlassdrucks und der Tritiumreinheit, bestimmt werden. Auch für diese Parameter wird eine Stabilität von $2 \cdot 10^{-3}$ gefordert. Im Rahmen der „Profile Likelihood“ Analysen wurde als Fallbeispiel die Tritiumreinheit ε_{T} als externe Messung durch das Laser Raman System (LARA) bei KATRIN in die Analysen mit einbezogen. Dadurch wurde ε_{T} als zusätzlicher freier Parameter in der Analyse auf m_ν^2 behandelt, der durch die LARA-Messung eingeschränkt („constrained“) ist.

Erstmals war es auch möglich, den Einfluss von Parameter-Inhomogenitäten in der Quelle, zum Beispiel des Dichte- oder Temperaturprofils, auf die Neutrinomassenanalyse zu ermitteln. Dies war besonders wichtig, um die Messungen am Demonstrator-Experiment mit einem longitudinalen Temperaturgradienten $\Delta T > 1\,\mathrm{K}$ einzuordnen. Die Simulationen und Analysen zeigten, dass ein solches Temperaturprofil die Sensitivität der KATRIN Messung nicht verschlechtert, solange es stabil ist und durch die präzisen Temperatursensoren genau bestimmt ist.

Die gesamten Simulations- und Analysemethoden sind im KATRIN-Analyse Paket KASPER zusammengefasst. Damit können die Routinen in den kommenden

Hauptspektrometer-Abnahmetests verwendet werden, um Messresultate direkt an Hand ihres Einflusses auf die Neutrinomassenanalyse bewerten zu können. Desweiteren werden die Analysen in der Zukunft um zusätzliche Fit-Parameter erweitert um die Einflüsse weiterer Experimentparameter auf m_ν^2 zu untersuchen.

Im Rahmen der Gasdynamik Simulationen sind drei-dimensionale Simulationen für die kritischen Pumpkammern geplant. Dort befinden sich zwar nur verhältnismäßig wenige Tritiummoleküle, doch von der dem Spektrometer zugewandten Pumpkammer erreichen die dort entstehenden β-Elektronen nahezu ungestört das Spektrometer und den Detektor.

Als ein Ergebnis der Demonstrator-Messungen zeigten die Homogenitätsmessungen, dass die identifizierten zusätzlichen Wärmeeinträge beim Umbau des Demonstrators zur WGTS beseitigt werden sollten. Insbesondere werden zukünftig weitere Anstrengungen unternommen um die magnetische Abschirmung und die Kühlung der Turbomolekularpumpen zu verbessern, um die Aufheizung im starken Magnetfeld und damit das Temperaturprofil der WGTS zu minimieren.

Danksagung/Acknowledgements

Ich möchte mich bei Prof. Dr. Guido Drexlin für die Möglichkeit bedanken, dass ich meine Doktorarbeit am KATRIN Experiment anfertigen konnte. Vielen Dank für Unterstützung bei der Durchführung der Arbeit.

Desweiteren bedanke ich mich bei Prof. Dr. Günter Quast, der die Arbeit als Korreferent betreut hat.

Der Dank für die alltäglichen Fragen, Diskussionen und Hilfen geht an Dr. Markus Steidl und Dr. Wolfgang Käfer. Vielen Dank für die gute Zusammenarbeit.

The same is true for the numerous physics discussions with Dr. Ferenc Glück and Dr. Nikita Titov. Thank you.

Vielen Dank an Amadeus Dieter, Stefan Groh, Marco Haag, Jiayu Hua, Dr. Susanne Mertens und Magnus Schlösser für die gute Zusammenarbeit bei vielen kleineren und größeren Projekten, Simulationen und Analysen.

I would like to thank Prof. Dr. Felix Sharipov for the good collaboration on the gas dynamics simulations, always providing me with new results and supporting me in adding them to the source simulations.

Danke auch an Prof. Dr. Steffen Grohmann, Tobias Bode, Thorben Wahl und das gesamte Demonstrator-Team für die Zusammenarbeit bei den Messungen am Demonstrator.

I would also like to thank Dr. Alan Poon for inviting me to visit Lawrence Berkeley National Laboratory and supporting me in analysis techniques during my stay.

In diesem Zusammenhang möchte ich auch dem Karlsruher House of Young Scientists (KHYS) danken, das mir diesen Auslandsaufenthalt durch finanzielle Förderung ermöglicht hat.

Auch den Korrekturlesern Dr. Markus Steidl, Dr. Alan Poon, Prof. Dr. Steffen Grohmann und Prof. Dr. Guido Drexlin möchte ich an dieser Stelle ausdrücklich danken für die vielen Verbesserungsvorschläge, Korrekturen und allgemeine Hinweise.

Außerdem möchte ich mich bei den Kolleginnen und Kollegen des KATRIN-Experiments für insgesamt über 4 Jahre gute Zusammenarbeit in angenehmer Arbeitsatmosphäre bedanken.

Und nicht zuletzt danke ich meiner Familie, die mich während des Studiums jederzeit unterstützt hat.

Bibliography

[1] W. Pauli. "Sehr geehrte radioaktive Damen und Herren". In R. Kronig and V. Weisskopf, editors, "Collected scientific papers : in 2 volumes", Interscience Publ., New York, 1964.

[2] F. Reines et al. "Detection of the free antineutrino". *Phys. Rev.*, 117 (1960) 159–173. doi:10.1103/PhysRev.117.159.

[3] G. Danby et al. "Observation of high-energy neutrino reactions and the existence of two kinds of neutrinos". *Phys. Rev. Lett.*, 9 (1962) 36–44. doi:10.1103/PhysRevLett.9.36.

[4] K. Kodama et al. (DONUT Collaboration). "Observation of tau neutrino interactions". *Phys. Lett. B*, 504(3) (2001) 218 – 224. doi:10.1016/S0370-2693(01)00307-0.

[5] N. Schmitz. *Neutrinophysik*. Teubner-Studienbücher : Physik. Teubner, Stuttgart, 1997.

[6] J. Beringer et al. (Particle Data Group). "2012 review of particle physics". *Phys. Rev. D*, 86(010001). http://pdg.lbl.gov/2012/reviews/contents_sports.html.

[7] J. N. Bahcall et al. "New solar opacities, abundances, helioseismology, and neutrino fluxes". *ApJ*, 621(1) (2005) L85. doi:10.1086/428929.

[8] R. Davis. "A review of the homestake solar neutrino experiment". *Prog. Part. Nucl. Phys.*, 32(0) (1994) 13 – 32. doi:10.1016/0146-6410(94)90004-3.

[9] Q. R. Ahmad et al. (SNO Collaboration). "Direct evidence for neutrino flavor transformation from neutral-current interactions in the Sudbury Neutrino Observatory". *Phys. Rev. Lett.*, 89 (2002) 011301. doi:10.1103/PhysRevLett.89.011301.

[10] S. N. Ahmed et al. (SNO Collaboration). "Measurement of the total active ^{8}B solar neutrino flux at the Sudbury Neutrino Observatory with enhanced neutral current sensitivity". *Phys. Rev. Lett.*, 92 (2004) 181301. doi:10.1103/PhysRevLett.92.181301.

[11] B. Aharmim et al. (SNO Collaboration). "Independent measurement of the total active ^{8}B solar neutrino flux using an array of ^{3}He proportional counters at the Sudbury Neutrino Observatory". *Phys. Rev. Lett.*, 101 (2008) 111301. doi:10.1103/PhysRevLett.101.111301.

[12] Y. Fukuda et al. (Super-Kamiokande Collaboration). "Evidence for oscillation of atmospheric neutrinos". *Phys. Rev. Lett.*, 81 (1998) 1562–1567. doi:10.1103/PhysRevLett.81.1562.

[13] P. Adamson et al. (MINOS Collaboration). "Measurement of the neutrino mass splitting and flavor mixing by MINOS". *Phys. Rev. Lett.*, 106 (2011) 181801. doi:10.1103/PhysRevLett.106.181801.

[14] F. P. An et al. (Daya Bay Collaboration). "Observation of electron-antineutrino disappearance at Daya Bay". *Phys. Rev. Lett.*, 108 (2012) 171803. doi:10.1103/PhysRevLett.108.171803.

[15] J. K. Ahn et al. (RENO Collaboration). "Observation of reactor electron antineutrinos disappearance in the RENO experiment". *Phys. Rev. Lett.*, 108 (2012) 191802. doi:10.1103/PhysRevLett.108.191802.

[16] Y. Abe et al. (Double Chooz Collaboration). "Reactor $\overline{\nu}_e$ disappearance in the Double Chooz experiment". *Phys. Rev. D*, 86 (2012) 052008. doi:10.1103/PhysRevD.86.052008.

[17] L. Bergström and A. Goobar. *Cosmology and particle astrophysics*. Springer-Praxis books in astrophysics and astronomy. Springer, Berlin, 2. edition, 2004.

[18] M. Roos. *Introduction to cosmology*. Wiley, Chichester [u.a.], 3. ed. edition, 2003.

[19] D. J. Fixsen. "The temperature of the cosmic microwave background". *ApJ*, 707(2) (2009) 916. doi:10.1088/0004-637X/707/2/916.

[20] D. Larson et al. "Seven-year Wilkinson Microwave Anisotropy Probe (WMAP) observations: Power spectra and WMAP-derived parameters". *ApJS*, 192(2) (2011) 16. doi:10.1088/0067-0049/192/2/16.

[21] "WMAP Internal Linear Combination Map", 2012. http://lambda.gsfc.nasa.gov/product/map/current/m_images.cfm.

[22] J. Lesgourgues and S. Pastor. "Massive neutrinos and cosmology". *Phys. Rep.*, 429(6) (2006) 307 – 379. doi:10.1016/j.physrep.2006.04.001.

[23] D. J. Eisenstein et al. "SDSS-III: Massive spectroscopic surveys of the distant universe, the milky way, and extra-solar planetary systems". *ApJ*, 142(3) (2011) 72. doi:10.1088/0004-6256/142/3/72.

[24] A. G. Sanchez et al. "The clustering of galaxies in the SDSS-III baryon oscillation spectroscopic survey: cosmological implications of the large-scale two-point correlation function". *Mon. Not. R. Astron. Soc.*, 425(1) (2012) 415–437. doi:10.1111/j.1365-2966.2012.21502.x.

[25] E. Komatsu et al. "Seven-year Wilkinson Microwave Anisotropy Probe (WMAP) observations: Cosmological interpretation". *ApJS*, 192(2) (2011) 18. doi:10.1088/0067-0049/192/2/18.

[26] S. R. Elliott and P. Vogel. "Double beta decay". *Annu. Rev. Nucl. Part. Sci.*, 52(1) (2002) 115–151. doi:10.1146/annurev.nucl.52.050102.090641.

[27] I. Abt et al. "A new ^{76}Ge double beta decay experiment at LNGS". *Letter of Intent*. http://www.mpi-hd.mpg.de/gerda/reportsLNGS/LoI.pdf.

[28] H. V. Klapdor-Kleingrothaus et al. "Evidence for neutrinoless double beta decay". *Mod. Phys. Lett. A*, 16(37) (2001) 2409–2420. doi:10.1142/S0217732301005825.

[29] S. Schönert. "The search for neutrino-less double beta decay with gerda lngs: status and perspectives". presentatation at "Astroparticle physics in Germany", Zeuthen, 2012. https://indico.desy.de/materialDisplay.py?contribId=20&sessionId=11&materialId=slides&confId=5709.

[30] M. Auger et al. (EXO Collaboration). "Search for neutrinoless double-beta decay in ^{136}Xe with EXO-200". *Phys. Rev. Lett.*, 109 (2012) 032505. doi:10.1103/PhysRevLett.109.032505.

[31] E. Fermi. "Versuch einer Theorie der β-Strahlen". *Zeitschrift für Physik A*, 88 (1934) 161–177. doi:10.1007/BF01351864.

[32] E. W. Otten and C. Weinheimer. "Neutrino mass limit from tritium β-decay". *Rep. Prog. Phys.*, 71(8) (2008) 086201. doi:10.1088/0034-4885/71/8/086201.

[33] M. Sisti et al. "New limits from the milano neutrino mass experiment with thermal microcalorimeters". *Nucl. Instr. Meth. Phys. A*, 520(1,2,3) (2004) 125 – 131. doi:10.1016/j.nima.2003.11.273.

[34] A. Nucciotti et al. "The Milano neutrino mass experiment with arrays of $AgReO_4$ microcalorimeters". *AIP Conference Proceedings*, 605(1) (2002) 453–456. doi:10.1063/1.1457684.

[35] F. Gatti et al. "MARE — Microcalorimeter Arrays for a Rhenium Experiment", 2006. Proposal, http://crio.mib.infn.it/wig/silicini/proposal/proposal_MARE_v2.6.pdf.

[36] A. D. Rújula and M. Lusignoli. "Calorimetric measurements of ^{163}Ho decay as tools to determine the electron neutrino mass". *Phys. Lett. B*, 118(4,5,6) (1982) 429 – 434. doi:10.1016/0370-2693(82)90218-0.

[37] P. Ranitzsch et al. "Development of metallic magnetic calorimeters for high precision measurements of calorimetric ^{187}Re and ^{163}Ho spectra". *J. Low Temp. Phys.*, 167 (2012) 1004–1014. doi:10.1007/s10909-012-0556-0.

[38] V. Lozza. "New approaches (C0BRA, ECHO, Q-value determinaton)". presentatation at "Astroparticle physics in Germany", Zeuthen, 2012. https://indico.desy.de/materialDisplay.py?contribId=20&sessionId=11&materialId=slides&confId=5709.

[39] K. Blaum et al. "Penning traps as a versatile tool for precise experiments in fundamental physics". *Contemporary Physics*, 51(2) (2010) 149–175. doi:10.1080/00107510903387652.

[40] G. Audi et al. "The AME2003 atomic mass evaluation: (II). Tables, graphs and references". *Nucl. Phys. A*, 729(1) (2003) 337 – 676. doi:10.1016/j.nuclphysa.2003.11.003.

[41] L. L. Lucas and M. P. Unterweger. "Comprehensive review and critical evaluation of the half-life of tritium". *J. Res. Natl. Inst. Stand. Technol. 105, 541 (2000)*, 105(4) (2000) 541 – 549. doi:10.6028/jres.105.043.

[42] K. Grotz and H. Klapdor. *Die schwache Wechselwirkung in Kern-, Teilchen- und Astroteilchenphysik*. Teubner, Stuttgart, 1989.

[43] J. J. Simpson. "Measurement of the β-energy spectrum of ^{3}H to determine the antineutrino mass". *Phys. Rev. D*, 23 (1981) 649–662. doi:10.1103/PhysRevD.23.649.

[44] C. Weinheimer et al. "Improved limit on the electron-antineutrino rest mass from tritium β-decay". *Phys. Lett. B*, 300(3) (1993) 210 – 216. doi:10.1016/0370-2693(93)90355-L.

[45] A. Belesev et al. "Results of the Troitsk experiment on the search for the electron antineutrino rest mass in tritium beta-decay". *Phys. Lett. B*, 350(2) (1995) 263 – 272. doi:10.1016/0370-2693(95)00335-I.

[46] C. Kraus et al. "Final results from phase II of the Mainz neutrino mass search in tritium β decay". *Eur. Phys. J. C*, 40 (2005) 447–468. doi:10.1140/epjc/s2005-02139-7.

[47] V. N. Aseev et al. "Upper limit on the electron antineutrino mass from the Troitsk experiment". *Phys. Rev. D*, 84 (2011) 112003. doi:10.1103/PhysRevD.84.112003.

[48] J. Angrik et al. (KATRIN Collaboration). "KATRIN Design Report 2004". *Wissenschaftliche Berichte FZKA 7090*. http://www.katrin.kit.edu/publikationen/DesignReport2004-12Jan2005.pdf.

[49] P. Kruit and F. H. Read. "Magnetic field paralleliser for 2π electron-spectrometer and electron-image magnifier". *J. Phys. E: Sci. Instrum.*, 16(4) (1983) 313. doi:10.1088/0022-3735/16/4/016.

[50] A. Picard et al. "A solenoid retarding spectrometer with high resolution and transmission for keV electrons". *Nucl. Instr. Meth. B*, 63(3) (1992) 345 – 358. doi:10.1016/0168-583X(92)95119-C.

[51] S. Groh. *Untersuchung von UV-Laser induziertem Untergrund am KATRIN Vorspektrometer*. Master's thesis, Karlsruhe Institute of Technology (KIT), 2010. http://www.katrin.kit.edu/publikationen/dth-groh.pdf.

[52] J. F. Wilkerson et al. "Limit on $\overline{\nu}_e$ mass from free-molecular-tritium beta decay". *Phys. Rev. Lett.*, 58 (1987) 2023–2026. doi:10.1103/PhysRevLett.58.2023.

[53] W. Stoeffl and D. J. Decman. "Anomalous structure in the beta decay of gaseous molecular tritium". *Phys. Rev. Lett.*, 75 (1995) 3237–3240. doi:10.1103/PhysRevLett.75.3237.

[54] S. Lukic et al. "Measurement of the gas-flow reduction factor of the KATRIN DPS2-F differential pumping section". *Vacuum*, 86(8) (2012) 1126 – 1133. doi:10.1016/j.vacuum.2011.10.017.

[55] A. Windberger. *Berechnungen und Simulationen zum Verhalten von Ionen in der differenziellen Pumpstrecke des KATRIN-Experiments*. Master's thesis, Karlsruhe Institute of Technology (KIT), 2011. http://www.katrin.kit.edu/publikationen/dth-windberger.pdf.

[56] M. Ubieto-Diaz. *Off-line commissioning of a non-destructive FT-ICR detection system for monitoring the ion concentration in the KATRIN beamline*. Ph.D. thesis, Ruprecht-Karls-Universität Heidelberg, 2011. http://pubman.mpdl.mpg.de/pubman/faces/viewItemFullPage.jsp?itemId=escidoc:1255588.

[57] B. Hillen. *Untersuchung von Methoden zur Unterdrückung des Spektrometeruntergrunds beim KATRIN Experiment*. Ph.D. thesis, Westfälische Wilhelms-Universität Münster, 2011. http://miami.uni-muenster.de/servlets/DerivateServlet/Derivate-6261/diss_hillen.pdf.

[58] F. Harms. *Assembly and first results of the KATRIN focal-plane detector system at KIT*. Master's thesis, Karlsruhe Institute of Technology (KIT), 2012. http://www.katrin.kit.edu/publikationen/dth_Fabian_Harms.pdf.

[59] M. Sturm et al. "Monitoring of all hydrogen isotopologues at Tritium Laboratory Karlsruhe using Raman spectroscopy". *Laser Physics*, 20(2) (2010) 493 – 507. doi:10.1134/S1054660X10030163.

[60] M. Babutzka et al. "Monitoring of the operating parameters of the KATRIN Windowless Gaseous Tritium Source". *New J. Phys.*, 14(10) (2012) 103046. doi:10.1088/1367-2630/14/10/103046.

[61] M. Erhard. *Untersuchung der Langzeitstabilität des nuklearen Standards für die Energieskala des KATRIN-Experiments*. Master's thesis, Karlsruhe Institute of Technology (KIT), 2012. http://www.katrin.kit.edu/publikationen/dth-erhard.pdf.

[62] B. Monreal et al. (KATRIN rear section working group). "KATRIN Rear Section conceptual design report v1.1", 2011. KATRIN internal report.

[63] S. Grohmann et al. "The thermal behaviour of the tritium source in KATRIN". *Cryogenics*. Submitted, 2012.

[64] F. Sharipov. "Calculations of tritium flow between the buffer vessel up to the first vacuum system", 2004. KATRIN internal report.

[65] N. Doss et al. "Molecular effects in investigations of tritium molecule β decay endpoint experiments". *Phys. Rev. C*, 73 (2006) 025502. doi:10.1103/PhysRevC.73.025502.

[66] N. Doss and J. Tennyson. "Excitations to the electronic continuum of $^3HeT^+$ in investigations of the T_2 β-decay experiments". *J. Phys. B: At. Mol. Opt. Phys.*, 41(125701). doi:10.1088/0953-4075/41/12/125701.

[67] A. Saenz et al. "Improved molecular final-state distribution of HeT^+ for the β-decay process of T_2". *Phys. Rev. Lett.*, 84 (2000) 242–245. doi:10.1103/PhysRevLett.84.242.

[68] S. Jonsell et al. "Neutrino-mass determination from tritium β decay: Corrections to and prospects of experimental verification of the final-state spectrum". *Phys. Rev. C*, 60 (1999) 034601. doi:10.1103/PhysRevC.60.034601.

[69] D. V. Sarantis Pantazis and F. Sharipov. "Numerical simulation of end effects in the WGTS unit", 2011. KATRIN internal report.

[70] ACCEL Instruments GmbH. "WGTS for KATRIN - injection chamber inner part". photograph, WGTS document server, 2007.

[71] M. Schloesser. *in preparation*. Ph.D. thesis, Karlsruhe Institute of Technology (KIT), 2013.

[72] M. Schloesser et al. "Accurate calibration of the Laser Raman System for the Karlsruhe Tritium Neutrino experiment". *J. Mol. Struc.* Submitted, 2012.

[73] S. Grohmann et al. "Cryogenic design of the KATRIN source cryostat". *AIP Conference Proceedings*, 985(1) (2008) 1277–1284. doi:10.1063/1.2908483.

[74] S. Grohmann. "Stability analyses of the beam tube cooling system in the KATRIN source cryostat". *Cryogenics*, 49(8) (2009) 413 – 420. doi:10.1016/j.cryogenics.2009.06.001.

[75] S. Grohmann et al. "Precise temperature measurement at 30 K in the KATRIN source cryostat". *Cryogenics*, 51(8) (2011) 438 – 445. doi:10.1016/j.cryogenics.2011.05.001.

[76] Cryodata Inc. "GASPAK User's Guide v. 3.45", 2007.

[77] A. Hobl. "Superconducting magnet system WGTS for KATRIN", 2006. Technical Design Report.

[78] A. Hervé and D. Hagedorn. "Proposal for a revised protection and operation scheme of WGTS", 2011. KATRIN internal report.

[79] S. Grohmann. "Ziele und Umfang der WGTS-Demonstratortests", 2010. ITEP colloquium, KIT.

[80] J. Wolf et al. "Investigation of turbo-molecular pumps in strong magnetic fields". *Vacuum*, 86(4) (2011) 361 – 369. doi:10.1016/j.vacuum.2011.07.063.

[81] M. Babutzka et al. *The comprehensive guide to KASSIOPEIA*, 2011. KATRIN internal document.

[82] W. Käfer. *Sensitivity studies for the KATRIN experiment*. Ph.D. thesis, Karlsruhe Institute of Technology (KIT), 2012. http://digbib.ubka.uni-karlsruhe.de/volltexte/1000026021.

[83] S. Mertens. *Study of Background Processes in the Electrostatic Spectrometers of the KATRIN Experiment*. Ph.D. thesis, Karlsruhe Institute of Technology (KIT), 2012. http://digbib.ubka.uni-karlsruhe.de/volltexte/1000027058.

[84] J. W. Liu. "Total cross sections for high-energy electron scattering by H_2 ($^1\sigma_g^+$), N_2 ($^1\sigma_g^+$), and O_2 ($^3\sigma_g^-$)". *Phys. Rev. A*, 35 (1987) 591–597. doi:10.1103/PhysRevA.35.591.

[85] J. W. Liu. "Total inelastic cross section for collisions of H_2 with fast charged particles". *Phys. Rev. A*, 7 (1973) 103–109. doi:10.1103/PhysRevA.7.103.

[86] S. Trajmar et al. "Electron scattering by molecules ii. experimental methods and data". *Phys. Rep.*, 97(5) (1983) 219 – 356. doi:10.1016/0370-1573(83)90071-6.

[87] T. Shirai et al. "Analytic cross sections for electron collisions with hydrocarbons: CH4, C2H6, C2H4, C2H2, C3H8, and C3H6". *Atomic Data and Nuclear Data Tables*, 80(2) (2002) 147 – 204. doi:10.1006/adnd.2001.0878.

[88] P. Renschler. *KESS - A new Monte Carlo simulation code for low-energy electron interactions in silicon detectors*. Ph.D. thesis, Karlsruhe Institute of Technology (KIT), 2011. http://digbib.ubka.uni-karlsruhe.de/volltexte/1000024959.

[89] M. Hötzel. *Berechnung von KATRIN Messspektren unter Einziehung der Eigenschaften der fensterlosen gasförmigen Tritiumquelle*. Master's thesis, University Karlsruhe, 2009. http://www.katrin.kit.edu/publikationen/dth-hoetzel.pdf.

[90] T. J. Corona. *in preparation*. Ph.D. thesis, University of North Carolina, 2013.

[91] ROOT development team. "ROOT v.5.32". Online documentation, 2012. http://root.cern.ch/drupal/content/documentation.

[92] V. Aseev et al. "Energy loss of 18 kev electrons in gaseous T_2 and quench condensed D_2 films". *Eur. Phys. J. D*, 10 (2000) 39–52. doi:10.1007/s100530050525.

[93] I. Wolff. *Entfaltung der Energieverlustfunktion beim KATRIN Experiment*. Master's thesis, Westfälische Wilhelms-Universität Münster, 2008. http://www.uni-muenster.de/Physik.KP/AGWeinheimer/Files/theses/Diplom_Irina_Wolff.pdf.

[94] C. Kranz. *Optimierung der Methoden und Messprozeduren zur Entfaltung der Energieverlustfunktion beim KATRIN-Experiment*. Master's thesis, Westfälische Wilhelms-Universität Münster, 2011. http://www.uni-muenster.de/Physik.KP/AGWeinheimer/Files/theses/Diplom_Christopher_Kranz.pdf.

[95] S. Ziegler. *in preparation*. Master's thesis, Karlsruhe Institute of Technology (KIT), 2013.

[96] J. Kaspar. *Influence of energy scale imperfections on neutrino mass sensitivity in the KATRIN experiment*. Master's thesis, Czech Technical University in Prague, 2003.

[97] S. Vöcking. *in preparation*. Ph.D. thesis, Westfälische Wilhelms-Universität Münster, 2012.

[98] N. Wandkowsky et al. "Main spectrometer commissioning document", 2011/2012. KATRIN internal report.

[99] W. W. Repko and C. Wu. "Radiative corrections to the end point of the tritium β decay spectrum". *Phys. Rev. C*, 28 (1983) 2433–2436. doi:10.1103/PhysRevC.28.2433.

[100] K. Jousten, editor. *Handbook of vacuum technology*. Wiley-VCH, Weinheim, 2008.

[101] F. Sharipov et al. "Influence of temperature variations and acoustic waves on the column density. Calculations of the velocity distribution function.", 2009. KATRIN internal report.

[102] N. Doss. *Calculated final state probability distributions for T_2 β-decay measurements*. Ph.D. thesis, University College London, 2007. http://www.tampa.phys.ucl.ac.uk/ftp/eThesis/NatashaDoss2007.pdf.

[103] D. A. Long. *The Raman Effect: A Unified Treatment of the Theory of Raman Scattering by Molecules*. Wiley, Chichester, 2002.

[104] C. Schwartz and R. J. L. Roy. "Nonadiabatic eigenvalues and adiabatic matrix elements for all isotopes of diatomic hydrogen". *J. Mol. Spec.*, 121(2) (1987) 420 – 439. doi:10.1016/0022-2852(87)90059-2.

[105] L. Asplund et al. "Vibrational structure and lifetime broadening in core-ionised methane". *J. Phys. B: At. Mol. Phys*, 18(8) (1985) 1569–1579. doi:10.1088/0022-3700/18/8/014.

[106] W. Greiner. *Classical mechanics : point particles and relativity*. Springer, New York, 2004.

[107] F. Sharipov. "Numerical calculations of tritium flow through the KATRIN beam line", 2003. KATRIN internal report.

[108] Y. Sone. *Molecular Gas Dynamics*. Birkhäuser, Boston, 2006.

[109] F. Sharipov and D. Kalempa. "Separation phenomena in the tritium source and numerical simulations of the turbo-molecular pumps", 2005. KATRIN internal report.

[110] D. Kalempa and F. Sharipov. "Separation phenomenon in the Windowless Gaseous Tritium Source of KATRIN experiment. Ternary mixture tritium-hydrogen-krypton", 2009. KATRIN internal report.

[111] F. Sharipov. "Tritium flow through a non-symmetrical source. simulation of gas flow through an injection hole.", 2010. KATRIN internal report.

[112] F. Sharipov and V. Seleznev. "Rarefied gas flow through a long tube at any pressure ratio". *J. Vac. Sci. Technol. A*, 12(5). doi:10.1116/1.578969.

[113] F. Sharipov. "Application of the Cercignani-Lampis scattering kernel to calculations of rarefied gas flows. III. Poiseuille flow and thermal creep through a long tube". *Eur. J. Mech. B*, 22(2) (2003) 145 – 154. doi:10.1016/S0997-7546(03)00018-9.

[114] F. Sharipov. "Rarefied gas flow through a long tube at arbitrary pressure and temperature drops". *J. Vac. Sci. Technol. A*, 15(4) (1997) 2434. doi:10.1116/1.580904.

[115] F. Sharipov. "Discussions on KATRIN gas dynamics reports". private communication, 2010.

[116] F. Sharipov. "Rarefied gas flow through a long tube at any temperature ratio". *J. Vac. Sci. Technol. A*, 14(4) (1996) 2627–2635. doi:10.1116/1.579991.

[117] C. Cercignani. *Theory and application of the Boltzmann equation*. Scottish Acad. Pr., Edinburgh, 1975.

[118] F. Sharipov. "Three-dimensional numerical simulation of tritium flow in the source outlet and the adjacent pumping chamber", 2012. KATRIN project proposal.

[119] KATRIN Collaboration. *KASPER documentation*, 2012. KATRIN internal document.

[120] M. Haag. "KATRIN analysis software - status report". presentatation at 22nd KATRIN collaboration meeting, 2012.

[121] M. Haag. *in preparation*. Ph.D. thesis, Karlsruhe Institute of Technology (KIT), 2013.

[122] D. Furse et al. *The KATRIN database*, 2011. KATRIN internal document.

[123] J. Kaspar. *Am/Co photoelectron source for energy scale monitoring of the KATRIN neutrino experiment*. Ph.D. thesis, Czech Technical University in Prague, 2008.

[124] F. Fränkle et al. "Radon induced background processes in the KATRIN pre-spectrometer". *Astroparticle Physics*, 35(3) (2011) 128 – 134. doi:10.1016/j.astropartphys.2011.06.009.

[125] S. Mertens et al. "Background due to stored electrons following nuclear decays in the KATRIN spectrometers and its impact on the neutrino mass sensitivity". *Astroparticle Physics*. doi:10.1016/j.astropartphys.2012.10.005.

[126] G. Cowan. *Statistical data analysis*. Oxford science publications. Clarendon Press, Oxford, 1998.

[127] F. James. *Statistical methods in experimental physics*. World Scientific, New Jersey, 2nd edition, 2008.

[128] W. H. Press et al. *Numerical Recipes: The art of numerical computing*. Cambridge University Press, New York, 3rd edition, 2007.

[129] G. J. Feldman and R. D. Cousins. "Unified approach to the classical statistical analysis of small signals". *Phys. Rev. D*, 57 (1998) 3873–3889. doi:10.1103/PhysRevD.57.3873.

[130] J. Neyman. “Outline of a theory of statistical estimation based on the classical theory of probability”. *Philosophical Transactions of the Royal Society of London. Series A, Mathematical and Physical Sciences*, 236(767) (1937) 333–380. http://www.jstor.org/stable/91337.

[131] R. Barlow. “A note on estimating errors from the likelihood function”. *Nucl. Instr. Meth. Phys. A*, 550 (2005) 392 – 396. doi:10.1016/j.nima.2005.05.047.

[132] T. M. Karbach. “Feldman-Cousins confidence levels - toy MC method”, 2011. http://arxiv.org/abs/1109.0714.

[133] W. A. Rolke et al. “Limits and confidence intervals in the presence of nuisance parameters”. *Nucl. Instr. Meth. Phys. A*, 551(2-3) (2005) 493–503. doi:10.1016/j.nima.2005.05.068.

[134] F. James and M. Winkler. *MINUIT User's guide*. CERN, 2004. http://seal.web.cern.ch/seal/documents/minuit/mnusersguide.pdf.

[135] K. Eitel. “Discussion on KATRIN spectrum calculation”. private communication, 2012.

[136] E. Otten. “The Mainz neutrino mass experiment”. *Prog. Part. Nucl. Phys.*, 32 (1994) 153–171. doi:10.1016/0146-6410(94)90016-7.

[137] M. Schloesser et al. “Accuracy of the Laser Raman system for KATRIN”. *Proceedings of the International School of Physics "Enrico Fermi", "Neutrino Physics and Astrophysics", Varenna*. http://arxiv.org/abs/1203.4099v1.

[138] T. Bode. *Experimentelle Untersuchung der thermischen Eigenschaften der KATRIN-Tritiumquelle am WGTS-Demonstrator*. Master's thesis, Karlsruhe Institute of Technology (KIT), 2011.

[139] Siemens. “SIMANTIC PCS 7”, 2010.

[140] C. Sackmann. “WGTS Temperaturerfassungssystem, version 1.6.0”. Technical documentation, confidential, 2011.

[141] Wolfram Research, Inc. “Mathematica”, 2010. http://www.wolfram.com/mathematica.

[142] A. Dieter. *Analyse ausgewählter Temperaturdaten des WGTS Demonstrators von KATRIN*. Bachelor's thesis, Karlsruhe Institute of Technology (KIT), 2011.

[143] J. W. Cooley and J. W. Tukey. “An algorithm for machine calculation of complex Fourier series”. *Mathematics of Computation*, 19 (1965) 297–301.

[144] E. O. Brigham. *FFT Schnelle Fourier-Transformation*. R. Oldenbourg Verlag GmbH, München, 5th edition, 1992.

[145] M. Clausen and U. Baum. *Fast Fourier Transforms*. BI-Wissenschaftsverlag, Mannheim, 1993.

[146] M. Frigo and S. G. Johnson. “FFTW 3.3.1”, 2011. http://www.fftw.org.

[147] M. Sturm. "Drehen des WGTS-Strahlrohrs um 180°", 2011. KATRIN internal report.

[148] T. Mayer-Kuckuk. *Kernphysik : eine Einführung*. Teubner-Studienbücher : Physik. Teubner, Stuttgart, 7th. edition, 2002.

[149] B. Ostrick. *Eine kondensierte ^{83m}Kr-Kalibrationsquelle für das KATRIN Experiment*. Ph.D. thesis, Westfälische Wilhelms-Universität Münster, 2008. http://miami.uni-muenster.de/servlets/DerivateServlet/Derivate-5046/diss_ostrick.pdf.

[150] J. Hua. *Simulation des Kryptonmodus der Tritiumquelle WGTS im KATRIN Experiment*. Master's thesis, Karlsruhe Institute of Technology (KIT), 2010. http://www.katrin.kit.edu/publikationen/dth-hua.pdf.

[151] T. Mukoyama and S. Shimizu. "Electron shakeoff accompanying internal conversion". *Phys. Rev. C*, 11 (1975) 1353–1363. doi:10.1103/PhysRevC.11.1353.

[152] F. Sharipov and D. Kalempa. "Separation phenomena for gaseous mixture flowing through a long tube into vacuum". *Phys. Fluids*, 17(127102). doi:10.1063/1.2140290.

[153] A. Reiner. "Demonstrator P&I diagram", 02-18-2010. KATRIN internal document.